Dissertation im Fachbereich Geowissenschaften
der Freien Universität Berlin

Development and evaluation of a double-canyon urban canopy scheme, and estimation of urban heat island mitigation effects

Sebastian Alfred Schubert

2013

Erstgutachter:	Prof. Dr. Uwe Ulbrich
Zweitgutachter:	Prof. Dr. Friedrich-Wilhelm Gerstengarbe
Tag der Disputation:	12. Juli 2013

Typeset in Adobe Minion Pro with MnSymbol and Adobe Myriad Pro with MdSymbol using LaTeX 2_ε.

Für Ingeborg, Renate und Alfred, für Adine, Jörg und Nadja,
und für Ruth mit unserem Töchterchen

Abstract

This work presents the development of a double-canyon urban canopy scheme (DCEP) based on the Building Effect Parametrization (BEP). The new scheme calculates the incoming and outgoing longwave and shortwave radiation for roof, wall and ground surfaces of an urban street canyon characterized by its street and building width as well as its canyon length, and the height distribution of buildings. The scheme introduces the radiative interaction of two neighbouring urban canyons allowing for the full inclusion of roofs into the radiation exchange, both, within the canyons and with the sky. In contrast to BEP, direct and diffuse shortwave radiation from the sky are treated independently, thus allowing for the calculation of the effective parameters representing the urban diffuse and direct shortwave radiation budget in the mesoscale model. Also, the energy balance of incoming longwave and diffuse shortwave radiation from the sky is closed, so that the new scheme is physically more consistent than BEP. Sensitivity tests show that these modifications are important for urban regions with a large variety of building heights. Moreover, the online coupling of DCEP with the mesoscale climate and weather model CCLM is explained in detail.

An extensive evaluation of CCLM/DCEP is done against Basel Urban Boundary Layer Experiment data. The urban canopy parameters required for this purpose are based on a 3-D building data-set of the canton of Basel-Stadt (Switzerland) and land-use data of Basel and its surroundings. The simulated radiative and energy fluxes as well as near-surface air temperatures and wind velocities are compared with measurements. The results indicate a good online performance of the model system comparable to the offline one of other urban canopy schemes in terms of the fluxes.

Furthermore, CCLM/DCEP is applied to investigate possible adaption measures to extreme heat events for the city of Berlin (Germany). The emphasis is on the effects of a modified urban vegetation cover and roof albedo on near-surface air temperatures. Five extreme heat events with a duration of 5 days or more are identified for the period 2000 to 2009. A reference simulation is carried out for each of them with current vegetation cover, roof albedo and urban canopy parameters, and is evaluated with temperature observations from weather stations in Berlin and its surroundings. The derivation of the urban canopy parameters from an impervious surface map and a 3-D building data set is detailed. Characteristics of the simulated urban heat island for each extreme heat event are analysed in terms of these canopy parameters. In addition, six sensitivity runs are examined with a modified vegetation cover of each urban grid cell by −25 %, +5 % and +15 %, with a roof albedo increased to 0.40 and 0.65, and with a combination of the largest vegetation cover and roof albedo, respectively. At the weather stations' grid cells, the results show a maximum of the average diurnal change in air temperature during each extreme heat event of 0.82 K

and −0.48 K for the −25 % and +15 % vegetation covers, −0.50 K for the roof albedos of 0.65, and −0.63 K for the combined vegetation and albedo case. The largest effects on the air temperature are detected during midday.

Zusammenfassung

In dieser Arbeit wird die Entwicklung eines Doppel-Canyon basierten städtischen Bestandsschichtsschemas (DCEP) auf der Grundlage der Building Effect Parametrization (BEP) vorgestellt. Das neue Schema berechnet die ein- und ausgehende lang- und kurzwellige Strahlung für Dach-, Wand- und Bodenflächen einer städtischen Häuserschlucht, die durch ihre Straßen- und Gebäudebreite sowie ihre Länge und die Höhenverteilung der Gebäude charakterisiert ist. Das Schema führt den Strahlungsaustausch benachbarter Häuserschluchten ein, wodurch die Einbeziehung der Dächer in den Strahlungsaustausch möglich wird – sowohl innerhalb der Häuserschluchten als auch mit dem Himmel. Direkte und diffuse kurzwellige Himmelsstrahlung werden im Gegensatz zu BEP getrennt behandelt, was eine Berechnung der effektiven Parameter für die städtische diffuse und kurzwellige Strahlungsbilanz im mesoskaligen Modell erlaubt. Weiterhin wird die Energiebilanz der einfallenden langwelligen und der diffusen kurzwelligen Himmelsstrahlung geschlossen, so dass das neue Schema physikalisch konsistenter als BEP ist. Sensitivitätsstudien zeigen die Wichtigkeit der Änderungen für urbane Regionen mit großen Gebäudehöhenunterschieden. Außerdem wird die Online-Kopplung von DCEP an das mesoskalige Klima- und Wettermodell CCLM ausführlich dargestellt.

Des Weiteren wird eine umfangreiche Evaluierung von CCLM/DCEP im Vergleich zu Basel-Urban-Boundary-Layer-Experiment-Daten unternommen. Die benötigten Häuserschluchtparameter basieren auf einem 3-D Gebäudedatensatz des Kantons Basel-Stadt (Schweiz) sowie Landnutzungsdaten von Basel und Umgebung. Die simulierten Strahlungs- und Energieflüsse sowie die bodennahen Lufttemperaturen und Windgeschwindigkeiten werden mit Messungen verglichen. Die Resultate weisen auf eine gute Online-Leistungsfähigkeit des Modellsystems im Vergleich zu Offline-Anwendungen anderer städtischer Bestandsschichtsschemata bezüglich der Flüsse hin.

Weiterhin werden mögliche Anpassungsmaßnahmen für Hitzewellen in der Stadt Berlin (Deutschland) mit Hilfe des mesoskaligen Modells CCLM/DCEP untersucht. In dieser Studie betrachten wir die Auswirkung der Änderungen der städtischen Vegetation und der Dach-Albedo auf die bodennahe Lufttemperatur. Fünf Hitzewellen mit einer Länge von mindestens fünf Tagen wurden in den Jahren 2000 bis 2009 identifiziert. Für jede dieser Hitzewellen wird eine Referenzsimulation mit der aktuellen Pflanzenbedeckung und Dach-Albedo und den aktuellen Häuserschluchtparametern durchgeführt und mit Stationsmessungen aus Berlin und Umgebung evaluiert. Die Ableitung dieser Parameter aus einer Versiegelungskarte und aus 3-D Gebäudedaten wird erklärt. Die simulierte städtische Wärmeinsel jeder Referenzsimulation wird anhand dieser Parameter analysiert. Weiterhin werden sechs Simulationsläufe mit einer

um −25 %, +5 % und +15 % geänderten Vegetationsbedeckung in jeder städtischen Gitterzelle, einer erhöhten Dachalbedo von 0.40 bzw. 0.65 und einer Kombination der größten Pflanzenbedeckung und Dachalbedo ausgewertet. Die Ergebnisse zeigen ein Maximum der durchschnittlichen Lufttemperaturänderung im Tagesverlauf während jeder Hitzewelle in den Stationsgitterzellen von 0.82 K und −0.48 K für die −25 % und +15 % Vegetationsbedeckungsänderung, −0.50 K für die Dachalbedos von 0.65 und −0.63 K für die kombinierte Vegetations- und Albedomodifikation. Der stärkste Effekt auf die Lufttemperatur wurde zur Tagesmitte simuliert.

Contents

List of Figures

List of Tables

1. Introduction

There is an increasing need of representing urban areas in regional climate models due to a progressing urbanization worldwide: While in 2010, more than 50 % of the world's population lived in cities, this number is projected to increase to more than 67 % in 2050 (UN 2011). This growing population (Martine et al. 2007) is accommodated by the expansion of cities leading to global, regional and local effects on weather and climate due to land-use and land-cover (LULC) changes. These changes, in turn, are propagated to the physical processes governing energy, momentum and mass exchange between land surfaces and the atmosphere (e.g. Pielke et al. 2002; Kabat et al. 2004; Cotton and Pielke 2007; C. L. Zhang et al. 2009; Mahmood et al. 2010). The probably most well documented effect of anthropogenic climate modification is the urban heat island (UHI) effect (Arnfield 2003). It can result in up to 15 K warmer urban air temperatures than in the rural surroundings in mid-latitude cities (Kuttler 2004). During extreme heat events for example, these higher urban temperatures further increase the population's mortality and the risk of hospitalization (cf. Koppe et al. 2004; Michelozzi et al. 2009). Thus, it is crucial to understand and provide reliable predictions of the meteorological conditions most of the people live in.

This study focuses on modelling meteorological quantities in urban areas with the regional or mesoscale climate model COSMO-CLM (COSMO in CLimate Mode (CCLM); Rockel, Will et al. 2008) with the finest resolution of about 1 km. The CCLM is a non-hydrostatic model (i.e. it does not use the hydrostatic assumption), which is a necessary prerequisite for working at the targeted scales (e.g. Orlanski 1981; Kato 1997). Furthermore, it has been the community model of the German climate research since 2005 (Rockel, Will et al. 2008). As a possible application, the quantities simulated by CCLM can be used as input for determining biometeorological indices like the physiological equivalent temperature (Muthers et al. 2010). Up to now, models on the micro-scale or local scale such as ENVI-met (Bruse and Fleer 1998) or UBIKLIM (Urbanes Bioklima Modell; Friedrich et al. 2001) are used for short-term fair weather simulations. Due to the increasing resolution of regional or mesoscale climate models (e.g. Rummukainen 2010), more urban effects can be represented in these models. However, since the airflow around individual buildings and roads still cannot be spatially resolved in these models, parametrization schemes are applied to represent urban surfaces.

In the simplest approach, cities are parametrized by means of a bulk-transfer scheme. In this scheme, the urban form is represented as a flat horizontal surface with appropriate bulk radiative, aerodynamic and thermal characteristics (Grimmond et al.

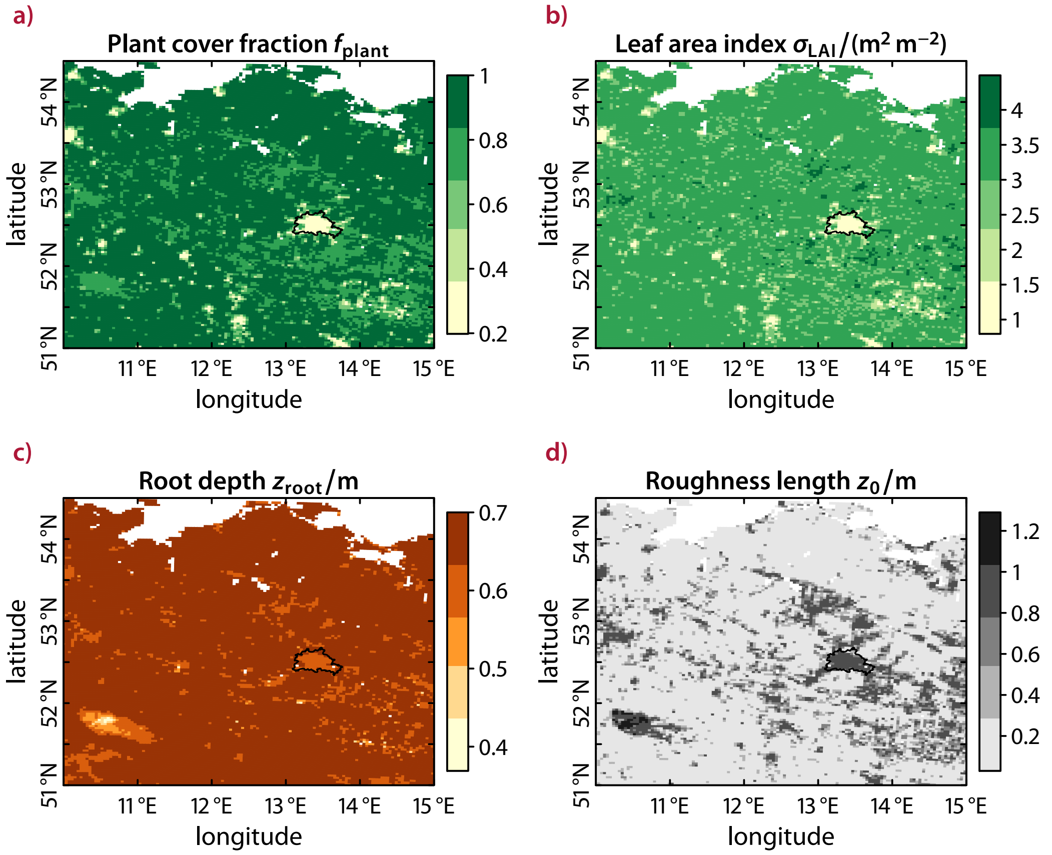

Figure 1.1. Default input parameters of the bulk scheme in COSMO-CLM at a resolution of about 2.8 km: vegetation parameters in a), b) and c) as well as the aerodynamic roughness length in d). The area of the city of Berlin (Germany) is marked.

2010). A basic version of this scheme is currently also the default in CCLM: cities are represented by natural land surfaces but with an increased surface roughness length, a reduced plant cover fraction, leaf area index and root depth (fig. 1.1). This is done in order to account for the increased vertical momentum and heat flux, and a reduced evapotranspiration, respectively. The exact parameter values depend on the data set chosen as input. The advantage of this bulk approach is the relatively low demand on input parameters and the simplicity of its coupling with the atmospheric model (Masson 2006). However, this simple parametrization is not able to fully represent the characteristics of urban areas that influence the atmosphere (e.g. Best 2005): examples are a considerable increase in heat storage and also small negative values of the nocturnal sensible heat flux directed towards the urban surfaces or even positive values directed towards the atmosphere. Therefore, characteristics of the urban planetary boundary layer such as the UHI as well as a near-neutral nocturnal vertical temperature profile and its downwind advection cannot be simulated sufficiently well

(Best 2005). Also, bulk-transfer schemes do not resolve the vertical effects of buildings on the urban canopy air and often do not differentiate between several urban LULC classes (e.g. Liu et al. 2006).

In order to better represent the urban surfaces, the basic bulk scheme was extended with, for example, an additional canopy layer above the soil surface (Best 2005). While this approach simulated the net radiation well in the study by Best et al. (2006), it showed larger discrepancies in the partitioning of turbulent and storage heat fluxes resulting, for example, in an underprediction of the latent heat flux by about one order of magnitude. Another strategy employed, for example, by Taha (1999) uses a statistical description of the increased storage flux in urban areas. In general, theses statistical approaches are primarily based on relations obtained from observations of the surface energy balance. This is realized, for example, in the NARP-LUMPS scheme consisting of three components: the NARP (Net All-wave Radiation Parametrization; Offerle et al. 2003) estimates the net radiation from solar and atmospheric forcings as well as surface radiative properties; the storage flux is estimated with the OHM (Objective Hysteresis Model; Grimmond et al. 1991) depending on the land-cover; the sensible and latent heat fluxes, finally, are calculated with the LUMPS (Local-scale Urban Meteorological Parametrization Scheme; Grimmond and Oke 2002). However, these schemes are only applicable to conditions encountered during the original reference measurements (Masson 2006).

Consequently, in analogy to vegetation canopy schemes, urban canopy models (UCMs) were developed with different levels of complexity (Grimmond et al. 2010; Grimmond et al. 2011). In these models, the urban surfaces are represented by long street canyons for which the radiation budget as well as the exchange of momentum and heat with the atmosphere is calculated. The underlying physical approaches are presented in detail by Brown (2000), and an update on more recent developments and challenges of urban regional modelling can be found in Masson (2006) and Martilli (2007). Amongst other things, UCMs differ in the number of height levels they take into account. In single-layer schemes, the canyons of one grid cell have the same height and the canopy air is parametrized; the canopy interacts directly only with the lowest atmospheric layer. Examples for this scheme are the Town Energy Balance (TEB) scheme by Masson (2000) and the scheme by Kusaka et al. (2001). In multi-layer schemes, buildings protrude into the lower atmosphere and thus vertically distribute the calculated energy fluxes in the lower levels of the main atmospheric model; drag forces are considered in the momentum equations of the atmospheric model. Representatives of this approach are the Building Effect Parametrization (BEP; Martilli et al. 2002) as well as the schemes by Dupont et al. (2004) and Kondo et al. (2005). Another distinguishing feature of UCMs is the treatment of vegetation in the urban area. While many schemes do not directly incorporate the effect of vegetation, each grid cell of the driving model can divided into a vegetated part and an urban part treated by the UCM (tile approach; e.g. Masson 2000; Kusaka et al. 2001; Best et al.

2006; Hamdi and Schayes 2007). In doing so, vegetated and urban fluxes contribute to the total surface flux weighted by the plan area fraction of the respective part, thus, the vegetated and urban part interact over the lowest mesoscale model level. A more realistic description of the interaction between the urban surfaces and the vegetation is achieved by the integration of vegetation in the urban canyon formulation (e.g. S.-H. Lee and Park 2008; Lemonsu et al. 2012). This approach, however, might need more parameters and increase the computation time (Grimmond et al. 2010).

In this study, the multi-layer Double-Canyon Effect Parametrization (DCEP) UCM based on BEP (Martilli et al. 2002) is developed and is fully online coupled with the CCLM. The development of DCEP is done such as to ensure a proper modelling of the impact of building height variability on the shortwave and longwave radiation budget at the urban surfaces. The presence of buildings of different heights generates shadowing and radiation trapping that may extend to several urban canyons. For example, a building exceeding surrounding buildings in height may cast its shadow not only on the buildings across the street but also on those of other nearby street canyons. This shadowing effect influences the distribution of the radiation energy (both shortwave and longwave) to horizontal (roofs, road) and vertical surfaces (walls). In the urban schemes developed so far roofs do not fully interact with the other urban surfaces: the roofs either always receive the full radiation from the sky and do not exchange radiation with the other urban surfaces or the radiation exchange between urban surfaces is limited (refer to Grimmond et al. (2010) and Grimmond et al. (2011) for a list of urban schemes).

Based on these considerations, the model development part of this study focuses on the following research questions:

- How does the integration of roofs in the radiation exchange, achieved by the combination of two street canyons, affect the effective urban albedo, emissivity and radiative surface temperature?
- How do these effects depend on the building height variability in urban areas?

To investigate these questions, modifications are introduced to the radiation scheme of BEP. The choice of the highly detailed BEP is motivated by the fact that it is a multi-layer scheme in which buildings vertically distribute sources and sinks of heat, moisture and momentum throughout the urban canopy layer. Any number of road orientations is possible and an unlimited number of reflections are taken into account in BEP's radiation scheme. These properties allow for a thorough investigation of the research questions. Within the current BEP scheme, roofs at all height levels in the urban canyon receive the full radiation from the sky, i.e. shadowing effects from walls and other roofs are neglected. The roofs' reflected radiation is also fully emitted into the sky. Moreover, in the BEP scheme, the incoming radiation as received from the mesoscale model is not conserved. This is due to shadow effects on low wall elements and the way in which the incoming diffuse radiation from the sky is distributed inside the urban canyon. The new scheme presented here closes the radiative energy balance. This scheme also differentiates between diffuse and direct shortwave radiation, which is not the case in BEP but in other urban schemes e.g. Masson (2000) or S.-H. Lee and Park (2008). Furthermore, the basic street canyon element of the radiative part of BEP is extended from a single canyon to a double canyon in order to include roofs consistently in the radiation exchange. In the single-canyon approach, the radiation budget of each urban surface is calculated based on the morphology of one street canyon consisting of two buildings and the street in between. In the double-canyon approach, two neighbouring canyons are considered in the calculation of the urban radiative processes.

A sensitivity study is carried out to determine for which urban geometries the modifications of BEP's radiation scheme are particularly important. To assess the impact of the modifications on the meteorology, CCLM/DCEP runs are conducted for various urban geometries.

The coupled CCLM/DCEP is evaluated with data from the 2001–2002 Basel Urban Boundary Layer Experiment (BUBBLE; Rotach et al. 2004; Rotach et al. 2005; Christen and Vogt 2004). The aim of BUBBLE was to investigate in detail the boundary layer structure of the city of Basel (Switzerland) and its surroundings by combining near-surface and remote sensing instrumentation. During the intensive observation period (IOP) between 10 June to 10 July 2002, the radiation and energy balance as well as wind velocity and air temperature were measured among other quantities at several urban, suburban and rural sites. The observations of 20 continuous days during the IOP are compared with the simulation with emphasis on the radiative and surface energy fluxes. Also the performance in terms of the air temperature and wind velocity is analysed. In addition, the simulation is compared with a simulation with the bulk scheme to assess the model improvement with DCEP. The difference between single-canyon and double-canyon approach is analysed as well for the realistic setting of Basel.

Masson (2006) proposed to evaluate UCMs offline using measurements of the surface energy budget. That way, the UCM is not influenced by the errors of the atmospheric model. For example, this approach was considered by Masson et al. (2002), Lemonsu et al. (2004), Hamdi and Masson (2008), S.-H. Lee and Park (2008), Lemonsu et al. (2010), Grimmond et al. (2010), Grimmond et al. (2011), Bueno et al. (2011) and Loridan and Grimmond (2012). In particular, BEP was evaluated offline by Hamdi and Schayes (2007) and coupled to the Building Energy Model (BEM; Salamanca et al. 2010) by Salamanca and Martilli (2010). Due to the offline coupling, these studies obviously cannot model the feedback effects from the atmospheric model. Thus, Best et al. (2006) suggested that a UCM needs to be also evaluated in an online coupled framework, with a comprehensive observational data-set to be able to separate out errors from the atmospheric model and the errors from the UCP. Other studies that used online coupled models simulated only for short time spans, and compared mainly with temperature and wind speed measurements (e.g. Dupont et al. 2004; Chin et al. 2005; Kondo et al. 2005; Grossman-Clarke et al. 2010). The BEP scheme was evaluated online by Martilli et al. (2003) and coupled with BEM by Salamanca et al. (2011). The evaluation of DCEP closes this gap by analysing online coupled simulations over a longer time span. Since the sensitivity study of the changes introduced by DCEP shows only negligible differences between DCEP and BEP for the typical height distributions of Basel, the reader is referred to Hamdi and Schayes (2007) for an offline evaluation.

Furthermore, the coupled CCLM/DCEP is applied to estimate the influence of possible mitigation measures to extreme heat events (EHE) for the city of Berlin (Germany) in the years 2000–2009. For a given building composition, the major strategies to reduce urban air temperatures include the increase of urban vegetation cover, roof top greening and reducing the albedo of impervious surfaces (Rosenzweig et al. 2009). This can lead to a reduced sensible heat flux and the amount of heat stored in urban surfaces, with a subsequent cooling of the urban air (Rosenzweig et al. 2009). Here, the study concentrates on the modifications of the vegetation cover as well as the roof albedo, which influence urban air temperatures through evapotranspiration and reflection of radiation, respectively.

Several studies demonstrated the potential use of regional atmospheric modelling for UHI mitigation and air quality regulatory purposes by means of applying state-of-the-art UCMS with mesoscale meteorological and air quality models (e.g. Taha 2008; Kikegawa et al. 2003; Sailor and Dietsch 2007; Rosenzweig et al. 2009; Krayenhoff and Voogt 2010; Salamanca et al. 2011; Masson et al. 2012). For example, Taha (2008) showed for Sacramento (California, USA) a potential UHI mitigation of up to 3 K in response to an increased albedo of roofs, walls and roads. Also according to these simulations, the ozone concentration could be reduced in most areas of the city. Krayenhoff and Voogt (2010) estimated the reduction of the maximum daytime air temperature in downtown Chicago (Illinois, USA) during a clear summer day connected to a change of the roof albedo from 0.06 to 0.65 to be about 1 K. Salamanca et al. (2011) showed a considerable reduction in the simulated summer UHI and energy consumption for Madrid (Spain) due to a reduction in roof albedos and anthropogenic heating.

First, a reference simulation for each analysed EHE, based on the current spatial distribution of the vegetation cover and surface albedo of Berlin, is evaluated with temperature measurements of six surface stations in and around Berlin. Also the spatial structure of the simulated UHI is analysed. In order to estimate the cooling effect of vegetation in Berlin, results of the reference simulations are compared with those from simulations that are characterized by increased or decreased vegetation fractions. Furthermore, the reference simulations are compared with simulations representing the application of high-albedo roof surface coatings (Bretz and Akbari 1997).

For all simulations of Basel and Berlin, urban canopy parameters (UCPs) that describe the simplified form of the urban street canyons (e.g. street width and building height) are derived from extensive 3-D building data sets. In many studies, however, the derivation of these UCPs are based on LULC classifications, which originate from medium resolution remote sensing data (e.g. Dupont et al. 2004; H. Zhang et al. 2008; Grossman-Clarke et al. 2010; Chen et al. 2011; Salamanca et al. 2011). Usually, in these kinds of classifications only one or very few urban LULC classes are foreseen, thus not accurately reflecting the spatial and structural heterogeneity of the urban landscape. Each urban LULC class can be characterized by an individual set of UCPs, which are commonly estimated from typical values or from field surveys of small parts of the city in question. However, since the urban structures still vary within a region represented by one urban LULC class, a representative value for each UCP can only roughly be determined (e.g. Grossman-Clarke et al. 2010; Schubert et al. 2010; Chen et al. 2011). For example, the "Industrial or commercial units" class of the CORINE land-use data (Coordinated Information on the European Environment; Büttner et al. 2012) is assigned to an almost completely impervious area with large buildings in the centre of Berlin as well as to a green space with isolated buildings at the border of Berlin. While Ratti et al. (2002) estimated some UCPs for $0.2\,\mathrm{km}^2$ of London (UK), Toulouse (France) and Berlin (Germany) as well as for larger areas of Los Angeles and Salt Lake City (both USA), more extensive data-sets are to the author's knowledge only available for US cities in the National Urban Database with Access Portal Tool (NUDAPT; Burian et al. 2008; Burian and Jason 2009; Ching et al. 2009). Furthermore, algorithms developed for simplifying complex urban morphology data usually aim at reducing the storage need of this data but keep the visual appearance when rendered (e.g. Fan et al. 2009). This work, however, presents algorithms designed to calculate effective UCPs from the two technically distinct building data-sets of Basel and Berlin.

Note that Neunhäuserer et al. (2007) modified a former version of the CCLM to better represent urban areas. In addition to the parameters employed for urban areas in the bulk scheme (fig. 1.1), they introduced a soil type "city" with a modified pore volume, field capacity, plant wilting point, hydraulic conductivity/diffusivity, heat capacity, heat conductivity and albedo. Also, they introduced an additional anthropogenic heat source at the surface. This scheme, however, does not account for the vertical structure of the urban canopy and thus does not include shadowing effects of the urban surfaces. Furthermore, at the time of this study, a group at the German weather service implemented the single-layer TEB into the CCLM, which is currently evaluated.

This work is structured as follows: in chapter 2, those governing equations and parametrization approaches of CCLM are outlined that concern the formulation and implementation of DCEP. In chapter 3, the DCEP scheme is explained in detail, and the changes introduced to the radiation scheme are discussed. The description of DCEP is completed with a summary of the radiation exchange equations in appendix A and a detailed formulation of the (sky) view factors in appendix B. Chapter 4 presents the evaluation of CCLM/DCEP with BUBBLE measurements and in chapter 5, the influence of mitigation strategies in Berlin during extreme heat events is analysed. Chapter 6, finally, gives a short outlook on future model developments and studies, and concludes this work.

2. Physics of the mesoscale model COSMO-CLM

This chapter introduces the underlying physics of the mesoscale model COSMO-CLM (CCLM). It describes the basic principles and governing equations of CCLM and explains the parametrization of the physical processes as far as they concern the development of the urban scheme detailed in the next chapter. The urban parametrization scheme extends the approaches described in the following to enhance the performance of the model in urban areas. Furthermore, the basic physics of COSMO-CLM is similar to that of other mesoscale meteorological models (e.g. the WRF model; Skamarock et al. 2008) so the description here is likely to apply also to these models.

The COSMO model is a non-hydrostatic limited-area atmospheric prediction model on the meso-β and meso-γ scale as defined by Orlanski (1975). The original version of the model designed for operational numerical weather prediction has been developed by Germany's National Meteorological Service DWD (Steppeler et al. 2003) and it is now developed further by the Consortium for Small-Scale Modelling (COSMO). The COSMO model in climate mode (COSMO-CLM or CCLM) includes modifications allowing the application on time scales up to centuries (Böhm et al. 2006; Rockel, Will et al. 2008). These modifications comprise for example the introduction of an annual cycle to vegetation parameters like the plant cover and the leaf area index as well as an externally prescribed, time-dependent CO_2 concentration in the atmosphere.

2.1. Basic model equations

In the following, the main approaches of CCLM involved in the derivation of the basic model equations and concerned with the formulation of the urban scheme are illustrated by the example of the momentum equation. At the end of this section, a list of these basic model equations is given. The principle content is based on the manual of CCLM (Doms, Schättler et al. 2011), which should be consulted for a complete description.

The continuous momentum equation for the air masses is given by

$$\rho \frac{\mathrm{d}\boldsymbol{u}}{\mathrm{d}t} = -\nabla p + \rho \boldsymbol{g} - 2\boldsymbol{\Omega} \times (\rho \boldsymbol{u}) - \nabla \cdot \mathbf{t}\,, \tag{2.1}$$

where ρ is the total density of the air mixture, $\boldsymbol{u}$ is the barycentric wind velocity relative to rotating earth, t is time, p is the air pressure, $\boldsymbol{g} \equiv \boldsymbol{G} - \boldsymbol{\Omega} \times (\boldsymbol{\Omega} \times \boldsymbol{r})$ is the apparent acceleration of gravity including the gravity $\boldsymbol{G}$ and the centripetal force, which depends on the position $\boldsymbol{r}$ as measured from the earth's centre, $\boldsymbol{\Omega}$ is the constant angular velocity of the earth's rotation, and $\mathbf{t}$ is the stress tensor due to the viscosity of the air mixture.

The explicit numerical simulation of mesoscale atmospheric flows governed by the basic equation in (2.1) and the continuous forms of the equations at the end of this section is not possible nowadays due to the high cost in computation time. Therefore, the equations are averaged over finite space and time intervals which can be identified with the spatial grid spacing and the time step of the simulation. Any variable $\psi(\boldsymbol{x}, t)$ is decomposed in the following way:

$$\psi(\boldsymbol{x}, t) = \overline{\psi}(\boldsymbol{x}, t) + \psi'(\boldsymbol{x}, t) \tag{2.2}$$

with the moving average

$$\overline{\psi}(\boldsymbol{x}, t) = \frac{1}{\Delta x\, \Delta y\, \Delta z\, \Delta t} \int_x^{x+\Delta x} \int_y^{y+\Delta y} \int_z^{z+\Delta z} \int_t^{t+\Delta t} \psi(\boldsymbol{x}, t)\, \mathrm{d}t\, \mathrm{d}z\, \mathrm{d}y\, \mathrm{d}x\,. \tag{2.3}$$

Thus, $\overline{\psi}(\boldsymbol{x}, t)$ represents the average over the finite time increment Δt and space intervals Δx, Δy and Δz; $\psi'(\boldsymbol{x}, t)$ is the deviation from that average. In the following, arguments are omitted for the sake of readability. The space and time intervals are chosen such that $\overline{\psi}$ varies much more slowly than ψ'. Let ϕ be another function of $\boldsymbol{x}$ and t, then this scale separation[*] is expressed in the Reynolds conditions (Reynolds 1895; Monin and Yaglom 1971), especially,

$$\overline{\overline{\psi}\phi} = \overline{\psi}\,\overline{\phi}\,, \tag{2.4}$$

$$\overline{\frac{\partial \psi}{\partial x_i}} = \frac{\partial \overline{\psi}}{\partial x_i} \quad \text{and} \quad \overline{\frac{\partial \psi}{\partial t}} = \frac{\partial \overline{\psi}}{\partial t}\,, \tag{2.5}$$

which results in

$$\overline{\overline{\psi}} = \overline{\psi}\,, \quad \overline{\psi'} = 0 \quad \text{and} \quad \overline{\overline{\psi}\phi'} = 0\,. \tag{2.6}$$

Raupach and Shaw (1982) showed that (2.5) is only valid in (urban) canopies if ψ is constant at the air/canopy element interfaces. For example, this is not the case for $\psi = p$, which results in additional drag terms in the momentum equations. They are taken into account in the urban parametrization (cf. section 3.2) but are not considered here.

In addition to the Reynolds decomposition in (2.2), the mass weighted average $\widehat{\psi}$ (Favre 1965) is defined as

$$\widehat{\psi} \equiv \overline{\rho\psi}/\overline{\rho} \quad \text{with} \quad \psi = \widehat{\psi} + \psi''\,. \tag{2.7}$$

---

[*] Galmarini and Thunis (1999) and Galmarini et al. (2000) discuss the errors for the case when the scale separation is not possible and thus the Reynolds assumptions are not valid.

From that,

$$\overline{\rho\psi''} = 0 \quad \text{and} \quad \widehat{\psi''} = 0 \,. \tag{2.8}$$

The Favre averaging reduces the number of terms resulting from density fluctuation, e.g.

$$\overline{\rho\psi\phi} = \overline{\rho}\,\overline{\psi}\,\overline{\phi} + \overline{\rho}\,\overline{\psi'\phi'} + \overline{\psi}\,\overline{\rho'\phi'} + \overline{\phi}\,\overline{\rho'\psi'} + \overline{\rho'\psi'\phi'} \qquad \text{(only Reynolds averages)} \tag{2.9a}$$

$$= \overline{\rho}\,\widehat{\psi}\,\widehat{\phi} + \overline{\rho\psi''\phi''} \,. \qquad \text{(with Favre averages)} \tag{2.9b}$$

The mean values $\overline{\psi}$ and $\widehat{\psi}$ are called grid values of ψ describing the slowly varying, resolvable part of the flow while the subgrid scale perturbations ψ' and ψ'' describe the strongly fluctuating, non-resolvable part. For grid spacings Δx, Δy and Δz of the order of 100 m, the fluctuating part of the flow can be identified with purely turbulent motion. For larger horizontal grid spacings, however, subgrid scale fluxes include additional processes showing organized structures. Shallow and moist convection, for example, have to be parametrized for grid spacings of the order of 10 km (Frank 1983).

Applying the averaging operator (2.3) to (2.1) yields the prognostic equation for the mean values:

$$\overline{\rho}\frac{\widehat{\mathrm{d}}\widehat{\boldsymbol{u}}}{\mathrm{d}t} = -\nabla\overline{p} + \overline{\rho}\boldsymbol{g} - 2\boldsymbol{\Omega}\times\left(\overline{\rho}\,\widehat{\boldsymbol{u}}\right) - \nabla\cdot\left(\overline{\mathbf{t}} + \boldsymbol{\tau}\right) , \tag{2.10}$$

where the total derivative $\widehat{\mathrm{d}}/\mathrm{d}t$ is to be taken with respect to the mass weighted velocity $\widehat{\boldsymbol{u}}$, i.e.

$$\frac{\widehat{\mathrm{d}}}{\mathrm{d}t} \equiv \frac{\partial}{\partial t} + \widehat{\boldsymbol{u}}\cdot\nabla \,. \tag{2.11}$$

In addition to the average molecular fluxes and source terms in the continuous equations, the averaging procedure introduces new terms which describe subgrid scale transport processes. In the momentum equation, this is the turbulent flux of momentum represented by Reynolds stress tensor $\boldsymbol{\tau}$ with

$$\boldsymbol{\tau} \equiv \overline{\rho\boldsymbol{u}''\boldsymbol{u}''} \,. \tag{2.12}$$

For the application on the meso-scale, certain terms in the averaged governing equations are approximated by simplified expressions valid on this scale. In general, the turbulent fluxes of momentum, heat and moisture are much larger than the corresponding molecular fluxes (Garratt 1992). Thus, the latter are neglected except for precipitation fluxes of liquid and solid water; in particular, the stress due to the viscosity of the air mixture is disregarded:

$$\mathbf{t} \simeq 0\,. \tag{2.13}$$

In the atmosphere, the water constituents contribute very little to the total mass of the volume of air. Thus, the specific heat of moist air at constant pressure and at constant volume can be approximated by the respective values of dry air, c_{Pd} and c_{Vd} (Wong and Embleton 1984). Furthermore, the latent heat of vaporization and of sublimation is estimated by their constant values $\lambda \equiv \lambda_{\mathrm{vap}}$ and λ_{sub}, respectively, at reference temperature $T_0 = 273.15\,\mathrm{K}$.

With these approximations, the final version of the momentum equation is given by

$$\rho \frac{\mathrm{d}\boldsymbol{u}}{\mathrm{d}t} = -\nabla p + \rho \boldsymbol{g} - 2\boldsymbol{\Omega} \times (\rho \boldsymbol{u}) - \nabla \cdot \boldsymbol{\tau}\,, \tag{2.14}$$

where here and in the following, the averaging symbols $\bar{}$ and $\widehat{}$ on single variables are omitted for convenience. With a similar averaging procedure applied to the prognostic equations for pressure and temperature as well as further approximations (see Doms, Schättler et al. 2011), which, however, do not directly concern the formulation of the urban scheme, the final version of these equations is

$$\frac{\mathrm{d}p}{\mathrm{d}t} = -\frac{c_{\mathrm{Pd}}}{c_{\mathrm{Vd}}} p \nabla \cdot \boldsymbol{u} + \left(\frac{c_{\mathrm{Pd}}}{c_{\mathrm{Vd}}} - 1\right) Q_{\mathrm{h}}\,, \tag{2.15}$$

$$\rho c_{\mathrm{Pd}} \frac{\mathrm{d}T}{\mathrm{d}t} = \frac{\mathrm{d}p}{\mathrm{d}t} + Q_{\mathrm{h}}\,. \tag{2.16}$$

Here, Q_{h} represents the rate of diabatic heating,

$$Q_{\mathrm{h}} = \lambda_{\mathrm{vap}} I_{\mathrm{l}} + \lambda_{\mathrm{sub}} I_{\mathrm{f}} - \nabla \cdot (\boldsymbol{H} + \boldsymbol{R})\,, \tag{2.17}$$

where I_{l} and I_{f} are the sources of liquid and frozen water, respectively, and $\boldsymbol{R}$ is the flux density of solar and thermal radiation. The sensible heat flux $\boldsymbol{H}$ is given by[†]

$$\boldsymbol{H} \simeq \widehat{c_{\mathrm{P}}}\overline{\rho \boldsymbol{u}'' T''} \approx c_{\mathrm{Pd}} \overline{\pi}\,\overline{\rho \boldsymbol{u}'' \theta''}\,, \tag{2.18}$$

where θ is the potential temperature defined as

$$\theta \equiv \frac{T}{\pi} \quad \text{with} \quad \pi \equiv \left(\frac{p}{p_0}\right)^{R_{\mathrm{d}}/c_{\mathrm{Pd}}}\,. \tag{2.19}$$

[†] The terms listed here correspond to the ones in Doms, Schättler et al. (2011) because $\overline{\rho \boldsymbol{u}'' \widehat{\psi}} = \widehat{\psi}\overline{\rho \boldsymbol{u}''} = 0$.

p_0 is a constant reference pressure usually set to 1000 hPa. The density ρ is diagnosed via the equation of state,

$$\rho = p\{R_\mathrm{d}[1 + (R_\mathrm{v}/R_\mathrm{d} - 1)q_\mathrm{v} - q_\mathrm{l} - q_\mathrm{f}]T\}^{-1}\,, \tag{2.20}$$

where R_d and R_v are the gas constants for dry air and water vapour, and q_v, q_l and q_f are the mass fraction of water vapour, liquid water and frozen water, respectively, in the air mixture. The respective prognostic equations for the mass fractions are given in Doms, Schättler et al. (2011), which together with (2.14) to (2.16) and (2.20) form a complete set to predict the grid scale variables of state ($\boldsymbol{u}$, p, T, ρ, q_v, q_l, q_f) once the radiative, micro-physical and subgrid scale fluxes are determined. The next subsection describes the parametrization of some of these processes.

2.2. Physical parametrizations

In the following, the radiation scheme and the parametrization of the turbulent fluxes as well as the calculation of the surface fluxes and the 2 m temperature in CCLM are explained. The approaches will be modified by the urban parametrization scheme in urban areas. Details of the multi-layer soil model, vegetation parametrization and the Kessler-type microphysic scheme (Kessler 1969) including precipitation formation in water, mixed phase and ice clouds are given in Doms, Förstner et al. (2011) on which also most of this section is based.

2.2.1. Radiation scheme

The radiative transfer scheme is based on the δ-two-stream solution of the radiative transfer equation (Ritter and Geleyn 1992). The equations are solved for three spectral intervals in the solar (shortwave) part covering wavelengths from 0.25 µm to 4.64 µm and for five spectral intervals in the thermal (longwave) part covering 4.64 µm to 104.5 µm. Three components of the radiative flux are considered: the diffuse upward and downward fluxes as well as (in the case of shortwave radiation) the parallel, direct solar flux.

The lower boundary condition of longwave radiation is characterized by the surface emissivity ϵ and the surface temperature T,

$$L^\uparrow = (1 - \epsilon)L^\downarrow + \epsilon\sigma T^4\,, \tag{2.21}$$

where $L^\downarrow$ and $L^\uparrow$ are the incoming and outgoing diffuse longwave radiation at the ground, and σ is the Stefan-Boltzmann constant. A value of $\epsilon = \epsilon_\mathrm{nat} = 0.996$ is assigned to all surface types. The index “nat” indicates that the values here will represent only the grid cell’s natural surface fraction as explained in section 3.5.1.

The lower boundary condition for shortwave radiation is given by

$$K^{\uparrow} = \alpha^{\downarrow} K^{\downarrow} + \alpha^{\Downarrow} K^{\Downarrow} \,, \tag{2.22}$$

where $K^{\downarrow}$ with $\alpha^{\downarrow}$ and $K^{\Downarrow}$ with $\alpha^{\Downarrow}$ are the incoming diffuse and direct shortwave radiation with the corresponding solar or shortwave albedo. The reflected shortwave radiation $K^{\uparrow}$ is assumed to be completely diffuse. The albedo $\alpha^{\downarrow}$ for diffuse radiation is divided into the albedo $\alpha^{\downarrow}_{\text{snow}}$ for snow, the albedo $\alpha^{\downarrow}_{\text{plant}}$ for the snow-free ground covered by plants and the albedo $\alpha^{\downarrow}_{\text{soil}}$ for the snow-free bare soil,

$$\alpha^{\downarrow} = \alpha^{\downarrow}_{\text{nat}} = f_{\text{snow}} \alpha^{\downarrow}_{\text{snow}} + (1 - f_{\text{snow}}) \left[f_{\text{plant}} \alpha^{\downarrow}_{\text{plant}} + (1 - f_{\text{plant}}) \alpha^{\downarrow}_{\text{soil}} \right] , \tag{2.23}$$

where f_{snow} is the snow covered fraction and f_{plant} is the plant cover fraction of the corresponding mesoscale grid cell. The snow albedo depends on the age of the snow, and the soil albedo depends on the soil type and the soil water content. Constant values are assigned to the albedo for dry soil depending on the soil type (e.g. 0.25 for loam) and to the albedo for plants ($\alpha^{\downarrow}_{\text{plant}} = 0.15$). The albedo for direct shortwave radiation depends on the zenith angle Z and $\alpha^{\downarrow}$:

$$\alpha^{\Downarrow} = \alpha^{\Downarrow}_{\text{nat}} = \frac{1 + \frac{1}{2}\left(\frac{1}{\alpha^{\downarrow}_{\text{nat}}} - 1\right) \cos Z}{\left[1 + \left(\frac{1}{\alpha^{\downarrow}_{\text{nat}}} - 1\right) \cos Z\right]^2} \,. \tag{2.24}$$

Thus, $\alpha^{\Downarrow}_{\text{nat}}$ increases with Z and reaches a value of 1 for $Z = 90°$ independently of $\alpha^{\downarrow}_{\text{nat}}$.

2.2.2. Parametrization of turbulent fluxes

As explained above, the subgrid scale double correlation terms in (2.14) to (2.16) include contributions from small-scale turbulent motion as well as other contributions such as moist convection. In the following, only the parametrization of the purely turbulent part of the correlations is described. Prognostic equations for these double correlations or second statistical moments can be formulated but include additional triple correlations (third moments). In general, a prognostic equation for an nth moment includes terms of $(n + 1)$st moments or higher due to the non-linear characteristics of turbulence (closure problem; Keller and Friedmann 1924; Stull 1988). Therefore, the correlation terms are diagnosed from grid scale values. In CCLM, the second moments are based on the two-and-one-half level model by Mellor and Yamada (1982), which uses a prognostic equation for the turbulent kinetic energy (TKE).

Furthermore, CCLM assumes horizontal scales of motion much larger than the vertical scales (boundary layer approximation). Here, contributions from horizontal turbulent fluxes become negligible when compared to the vertical fluxes (Yi et al.

2000; Markowski and Richardson 2010), thus leaving only turbulent fluxes of the form $\overline{\rho w''\psi''}$ in the prognostic equations. Here, w is the vertical component of the wind speed. Furthermore, applying the Boussinesq approximation in the correlation terms, i.e. neglecting density fluctuations ρ' (Boussinesq 1897), the mass weighted Favre average reduces to the Reynolds average (cf. (2.9)):

$$\overline{\rho w''\psi''} \simeq \overline{\rho}\,\overline{w'\psi'} \,. \tag{2.25}$$

In analogy to the molecular stress in a Newtonian fluid, which is characterized by the fluid's viscosity, the turbulent kinematic Reynolds stress is parametrized by

$$\overline{w'u'}\Big|_{\text{turb}} = -K_{\text{m}}\frac{\partial u}{\partial z} \,, \tag{2.26}$$

$$\overline{w'v'}\Big|_{\text{turb}} = -K_{\text{m}}\frac{\partial v}{\partial z} \,, \tag{2.27}$$

where the turbulent diffusion coefficient for momentum, K_{m}, replaces the viscosity. Here, however, K_{m} is a function of the flow and thus is not constant in time or space. This closure approximation is called gradient transport theory or K-theory (Stull 1988). In order to avoid moisture source term correlations due to cloud condensation and evaporation, the turbulent kinematic flux of heat is expressed in terms of the liquid water potential temperature $\theta_{\text{l}} \equiv \theta - (\lambda_{\text{vap}}/c_{\text{Pd}})q_{\text{c}}$, where q_{c} is the cloud water content. Thus,

$$\overline{w'\theta_{\text{l}}'}\Big|_{\text{turb}} = -K_{\text{h}}\frac{\partial \theta_{\text{l}}}{\partial z} \,. \tag{2.28}$$

Here, K_{h} is the turbulent diffusion coefficient for heat. The kinematic buoyant heat flux $\overline{w'\theta_{\text{v}}'}\big|_{\text{turb}}$ is calculated subsequently with the statistical cloud scheme of Deardorff and Sommeria (1977).

The diffusion coefficients K_{m} and K_{h} are computed from the mean turbulent kinetic energy e_{t} and the turbulent length scale l as

$$K_{\text{h}} = lS_{\text{h}}e_{\text{t}}^{1/2} \,, \tag{2.29}$$

$$K_{\text{m}} = lS_{\text{m}}e_{\text{t}}^{1/2} \,, \tag{2.30}$$

depending on the stability of the atmosphere expressed in the stability functions S_{h} and S_{m}. The approach of Blackadar (1962) is used to estimate l:

$$\frac{1}{l} = \frac{1}{\kappa z} + \frac{1}{l_\infty} \quad \Rightarrow \quad l = \frac{\kappa z}{1 + \kappa z/l_\infty} \longrightarrow \begin{cases} \kappa z \text{ for } z \ll l_\infty/\kappa \\ l_\infty \text{ for } z \gg l_\infty/\kappa \end{cases} . \tag{2.31}$$

With this approach, the length scale l increases linearly with height z close to the ground and approaches a fixed value l_∞ at large heights. κ is the von Kármán constant with $\kappa \approx 0.40$ (Högström 1996). The turbulent kinetic energy is predicted via

$$\frac{\mathrm{d}e_\mathrm{t}}{\mathrm{d}t} = \frac{g}{\theta_\mathrm{v}}\overline{w'\theta'_\mathrm{v}}\Big|_\mathrm{turb} - \frac{\partial u}{\partial z}\overline{w'u'}\Big|_\mathrm{turb} - \frac{\partial v}{\partial z}\overline{w'v'}\Big|_\mathrm{turb} - \frac{1}{\rho}\frac{\partial}{\partial z}\overline{\rho w' e'_\mathrm{t} + w'p'}\Big|_\mathrm{turb} - \frac{e_\mathrm{t}^{3/2}}{\alpha_\mathrm{M} l} \,. \qquad (2.32)$$

The first term on the right-hand side represents the buoyant production or consumption term, the second and third term represent the shear production, and the fourth term represents the combined turbulent transport of TKE with the pressure correlation term. The latter is parametrized as

$$\overline{\rho w' e'_\mathrm{t} + w'p'}\Big|_\mathrm{turb} = -\rho \alpha_\mathrm{T} l e_\mathrm{t}^{1/2} \frac{\partial e_\mathrm{t}}{\partial z} \,. \qquad (2.33)$$

The last term in (2.32) gives the dissipation of the TKE. α_T and α_M are model constants[‡].

2.2.3. Surface fluxes and 2 m temperature

In CCLM, the air from the surface up to the first main model layer is conceptually divided into the roughness layer and above the constant-flux layer. For both layers, separate transfer resistances for scalars (heat and moisture) and momentum are defined, which depend on the surface roughness z_0 and on the stability of the atmosphere. When calculating the sensible and latent heat flux from the surface, the resistances for scalars of both layers are taken into account whereas for the momentum fluxes, the roughness layer resistance for momentum is not considered (Doms, Förstner et al. 2011; Raschendorfer 2012).

Analogously, the 2 m temperature is calculated from the surface temperature T_S and the air temperature of the lowest model, T_1, using the resistance for scalars of the roughness layer, $r^\mathrm{h}_{S\to 0}$, and the resistance for scalars of the constant-flux layer up to a height of 2 m, $r^\mathrm{h}_{0\to 2\,\mathrm{m}}$,

$$T_{2\,\mathrm{m}} = T_S + \frac{r^\mathrm{h}_{S\to 0} + r^\mathrm{h}_{0\to 2\,\mathrm{m}}}{r^\mathrm{h}_{S\to 1}}\left(T_1 - T_S\right) . \qquad (2.34)$$

The resistance $r^\mathrm{h}_{S\to 1}$ for both layers is given by $r^\mathrm{h}_{S\to 1} = r^\mathrm{h}_{S\to 0} + r^\mathrm{h}_{0\to 1}$. Here, $r^\mathrm{h}_{0\to 1}$ is the total resistance of the complete constant-flux layer up to the height of the first model layer. Note that for the diagnosis of $T_{2\,\mathrm{m}}$, the resistances are calculated for the typical roughness length of a synoptic station of 0.2 m.

[‡] In S_h, S_m and α_T, a factor of $2^{1/2}$ has been absorbed for convenience compared to Doms, Förstner et al. 2011; α_M includes a factors of $2^{-5/2}$.

3. The urban Double-Canyon Effects Parametrization scheme (DCEP)

The multi-layer Double-Canyon Effects Parametrization scheme (DCEP) is an urban canopy parametrization scheme based on the Building Effect Parametrization (BEP) by Martilli et al. (2002). Both schemes use the incoming shortwave and longwave radiation, and the wind velocity, air density, temperature and pressure near the surface as input to calculate, at each urban level, the momentum and sensible heat fluxes for roofs, walls and for roads. Furthermore, the schemes calculate the reflected and emitted radiation of each urban surface, which are used to define the effective radiative properties of the urban land surface in the mesoscale model.

The basic canyon element of BEP and of the DCEP part concerning non-radiative processes is a quasi two-dimensional street canyon that consists of one road (ground) surface, one row of buildings on one side of the road except its far wall and the wall of the building on the opposite side of the street (black outlines in fig. 3.1). Each canyon element is characterized by the building width B, the street width W and the building height distribution $\gamma_i \equiv \gamma(z_{i+1/2})$ which is the fraction of buildings of height $z_{i+1/2}$

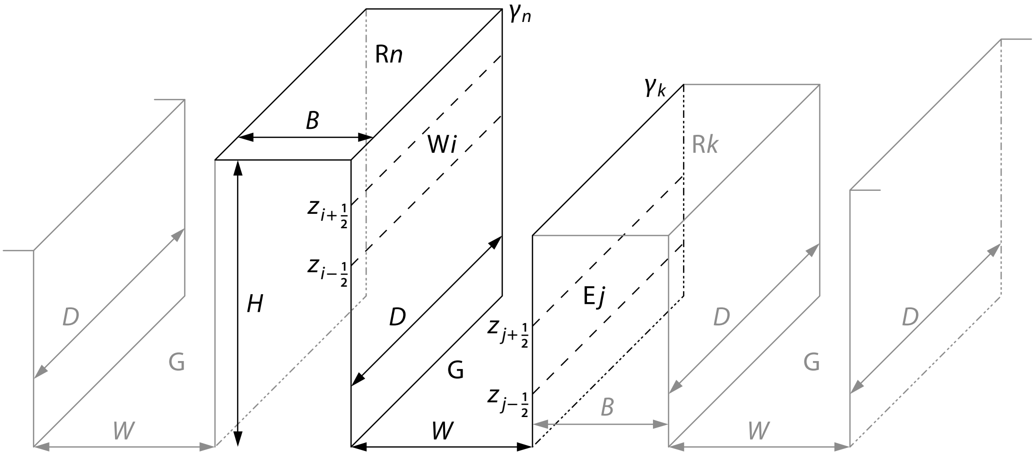

Figure 3.1. The basic street canyon element is characterized by the building width B, the street width W and the building height distribution γ_i. The canyon length D is assumed to be much larger than B and W. $H \equiv z_{n+1/2}$ is the height of the largest building. Depicted is also the ith west wall element Wi, the jth east wall element Ej, the ground surface G and the roof surface Rn at the height H (the height levels z_i are explained in fig. 3.2). Several identical neighbouring street canyons fill the mesoscale grid cell (as indicated by the grey building parts).

in the urban part of a mesoscale grid cell. The canyon length D is assumed to be much larger than B or W and has thus very little influence on the physical results. In all following illustrations of the street canyon, D appears shortened for display purposes. Furthermore, every street canyon is characterized by its street direction, i.e. alignment angle ζ relative to the north south axis. Independent of the street direction, the left-hand side wall elements are called west walls and the right-hand side walls east walls. This is indicated by adding either W or E to the height index at which the wall element is situated.

For every considered street direction, the mesoscale grid cell is *independently* assumed to be filled by several identical neighbouring street canyon elements all with the same set of parameters B, W, γ_i and D (as indicated by the grey building parts in fig. 3.1). For example, for street canyon elements with $B = 10\,\mathrm{m}$ and $W = 15\,\mathrm{m}$, and a mesoscale grid cell size of 1 km this leads to 40 neighbouring canyons. (This number is effectively reduced when vegetation is considered in the grid cell, as explained below.) It is assumed that all fluxes and radiative properties of all neighbouring street canyons are equal. In particular, the street canyon imagined at the border of the mesoscale grid cell is supposed to feature the same radiation budget and fluxes as a street canyon in the middle of the grid cell. Thus, both urban schemes calculate the radiation budget, and the sensible and momentum fluxes for each west wall element Wi, each east wall element Ej, each roof element Rk and the ground surface G of one representative canyon element. Here, the canyons of *different* street directions do not influence each other directly but via the mesoscale grid cell's average atmosphere. To this end, the results for different street directions are weighted with the fraction of the respective street direction and scaled with the urban fraction f_{urb} of the mesoscale grid cell to yield the average effect from the urban surfaces on the mesoscale grid cell.

The different real building heights in the area of the mesoscale grid cell are modelled by applying the height distribution γ_i to each row of buildings. Every row assumes every building height and the height-dependent variables are weighted with γ_i or the sum Γ_i thereof: Since γ_i expresses the fraction of buildings with a height $z_{i+1/2}$ (cf. fig. 3.2), the fraction of wall elements located between the half levels $z_{i-1/2}$ and $z_{i+1/2}$, i.e. inside the urban layer i with a thickness $\Delta z_i \equiv z_{i+1/2} - z_{i-1/2}$, is given by $\Gamma_i \equiv \sum_{j=i}^{n} \gamma_j$ with n being the total number of urban vertical levels. In comparison with Martilli et al. (2002), the numbering of height indices in DCEP has been changed to start with 0 at the ground level. Roof levels, roof temperatures and the radiation budgets for roofs as well as γ and Γ are defined at the half levels. All wall properties are defined at the urban main levels z_i (fig. 3.2).

The main difference between the BEP and the DCEP scheme is in the formulation of the radiative processes in the street canyon. In the BEP scheme, roof surfaces always receive the full radiation from the sky independent of their height and do not interact with the other urban surfaces. With the introduction of the double-canyon approach in the DCEP scheme, shadowing effects on roofs are possible and the roof surfaces

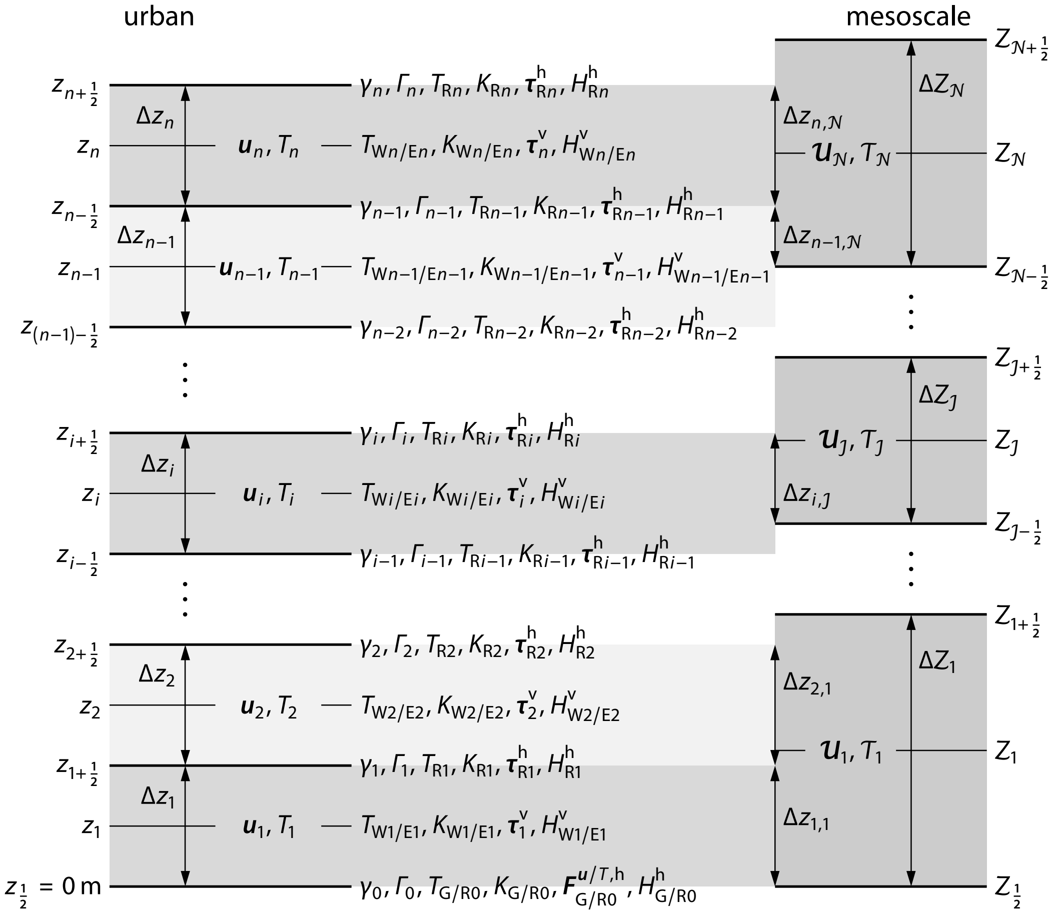

Figure 3.2. Labelling of the urban height layers i on the left-hand side and of the layers $\mathcal{J}$ of the mesoscale model on the right-hand side. Also shown is the overlap $\Delta z_{i,\mathcal{J}}$ of the respective urban and mesoscale layers. In the urban part of the mesoscale grid cell, the ground surface G and the lowest possible roof surface R0 are located at the lowest half level $z_{1/2}$. In general, the roof surface Ri, and its fluxes and radiation budget are located at the height $z_{i+1/2}$. The wall surfaces Wi and Ei are situated between the half levels $z_{i-1/2}$ and $z_{i+1/2}$, and their fluxes and radiation budgets are defined at the main level z_i. The mesoscale fields located at the heights $Z_{\mathcal{J}}$ of the mesoscale main levels $\mathcal{J}$ are interpolated to the fields at the heights z_i as explained in section 3.5.

interact with their neighbouring wall surfaces. Furthermore, DCEP closes the radiative energy balance and differentiates between diffuse and direct shortwave radiation. Full details including an explanation of all considered aspects of the radiative processes are given in section 3.1, and appendix A lists a short summary of the radiation budget equations of every urban surface element (comparable to the list of equations in Martilli et al. 2002). Section 3.6 analyses the closure of the energy balance and the extension to the double-canyon approach by comparing BEP and DCEP output for different urban morphologies.

While the formulation of the sensible heat and momentum fluxes induced by every single urban surface element of DCEP in section 3.2 follows the approaches in BEP, the TKE production has been slightly modified to include the stability of the atmosphere. Furthermore, the notation has been adjusted to follow the convention in this work and some additional pieces of explanation concerning the parametrization are given.

The storage of heat in the urban surfaces in DCEP also uses the proposition by Martilli et al. (2002) but with a modified inner boundary condition (section 3.3). The numerical implementation is explained in detail. The modification of the turbulent length scales by the presence of the buildings as well as the effective height above the surface are explained in section 3.4. Necessary normalization coefficients are added compared to Martilli et al. (2002).

The coupling of DCEP with a mesoscale model, in particular CCLM, is explained in section 3.5. First, this section describes the calculation of the effective urban surface albedo, emissivity and temperature, which represent the total urban radiation budget and which are used by the mesoscale radiation scheme. This part of the coupling is not described in Martilli et al. (2002). Furthermore, this section explains the interpolation of the mesoscale fields used as input to DCEP as well as the aggregation of urban surface fluxes and the averaging with fluxes from the natural surfaces. These average fluxes enter the basic model equations of the mesoscale model and represent the average effect of urban *and* natural surfaces on the mesoscale atmosphere. While natural surfaces are not accounted for in the original version of BEP by Martilli et al. (2002), Hamdi and Schayes (2007) introduced an additional parameter describing the urban fraction of a mesoscale grid cell. In this work, the aggregation and mixing of fluxes extend these concepts and adjust them to the specific formulation of CCLM. As in the majority of other UCMs (e.g. Masson 2000; Kusaka et al. 2001; Best et al. 2006), however, vegetation is only considered in a separate part of the mesoscale grid cell and not in the urban canyon. Finally, the coupling of DCEP with CCLM is summarized in a flow chart and its computational requirements are estimated.

Note that in order to distinguish between average values of the urban part, the natural surface part and the total mesoscale grid cell in the following, the indices "urb" and "nat" are added and/or lower case symbols are used when referring to the respective parts. Upper case swash letters and/or no indices are used for the total grid cell average. For example, while $K^{\uparrow}_{\mathrm{urb}}$ and $K^{\uparrow}_{\mathrm{nat}}$ represent the reflected shortwave radiation of the urban and the rural part, respectively, $\mathcal{K}^{\uparrow}$ indicates the total grid cell average of this quantity. Similarly, α_{urb} and α_{nat} are the albedo of the urban and the rural part, respectively, and α is the total grid cell averaged albedo. Furthermore, the grid cell average air temperature $\mathcal{T}_{\mathcal{J}}$ and wind velocity $\mathcal{U}_{\mathcal{J}}$ are defined on the $\mathcal{J}$th mesoscale main level at a height of $\mathcal{Z}_{\mathcal{J}}$ whereas the urban average air temperature T_i and wind velocity u_i are defined on the ith urban main level at a height of z_i (fig. 3.2).

Note also that the contents of sections 3.1, 3.5.1 and 3.6 have been published in Schubert et al. (2012).

3.1. Urban radiation budget

In this section, the formulation of the radiation budget of each urban surface element in DCEP is given and it is explained in detail how the scheme differs from the approaches in BEP. The different sources of radiation incident on each surface element are identified and described separately in the subsections 3.1.1 and 3.1.2.

The radiation budget of all urban surfaces is described by the incoming longwave radiation vector

$$L \equiv (L_{\mathrm{W}1}, \dots, L_{\mathrm{W}n}, L_{\mathrm{E}1}, \dots, L_{\mathrm{E}n}, L_{\mathrm{R}0}, \dots, L_{\mathrm{R}n}, L_{\mathrm{G}}) , \tag{3.1}$$

the incoming shortwave radiation vector

$$K \equiv (K_{\mathrm{W}1}, \dots, K_{\mathrm{W}n}, K_{\mathrm{E}1}, \dots, K_{\mathrm{E}n}, K_{\mathrm{R}0}, \dots, K_{\mathrm{R}n}, K_{\mathrm{G}}) , \tag{3.2}$$

and the vector of surface temperatures

$$T \equiv (T_{\mathrm{W}1}, \dots, T_{\mathrm{W}n}, T_{\mathrm{E}1}, \dots, T_{\mathrm{E}n}, T_{\mathrm{R}0}, \dots, T_{\mathrm{R}n}, T_{\mathrm{G}}) \tag{3.3}$$

of the surface elements. Here, the indices Wi, Ei and Ri indicate the respective values for the ith west wall, east wall and roof element, and G is the index for the ground element. Let μ indicate one of these elements, e.g. $\mu = \mathrm{W}i, \mathrm{E}i, \mathrm{R}i, \mathrm{G}$, then the incoming shortwave and longwave radiation on the μth surface element is given by

$$L_\mu = S_\mu^{\mathrm{l},\downarrow} + E_\mu^{\mathrm{l}} + H_\mu^{\mathrm{l}} , \tag{3.4}$$

$$K_\mu = S_\mu^{\mathrm{k},\downarrow} + S_\mu^{\mathrm{k},\Downarrow} + E_\mu^{\mathrm{k}} , \tag{3.5}$$

with $S_\mu^{\mathrm{l},\downarrow}$, $S_\mu^{\mathrm{k},\downarrow}$ and $S_\mu^{\mathrm{k},\Downarrow}$ being the incoming longwave, diffuse and direct shortwave radiation from the sky. Here and in the following, ↓ and ⇓ indicate diffuse and direct radiation, respectively. E_μ^{k} and E_μ^{l} are the reflected shortwave and longwave radiation from other urban surfaces and H_μ^{l} is the emitted longwave radiation from those surface elements. In the original BEP scheme, the complete incoming shortwave radiation from the sky is assumed to be direct radiation, thus $S_\mu^{\mathrm{k},\downarrow} = 0$. In DCEP also diffuse incoming shortwave sky radiation is considered. Both components of the diffuse incoming sky radiation, $S_\mu^{\mathrm{k},\downarrow}$ and $S_\mu^{\mathrm{l},\downarrow}$, are treated equally but with different amounts of input sky radiation: $\mathcal{K}^\downarrow$ for diffuse shortwave and $\mathcal{L}^\downarrow$ for longwave radiation, respectively. Thus, $S_\mu^{\mathrm{k},\downarrow}$ and $S_\mu^{\mathrm{l},\downarrow}$ for the μth surface element can be obtained by means of the same function $S_\mu^\downarrow$ that depends only on the urban morphology:

$$S_\mu^{\mathrm{k},\downarrow} = S_\mu^\downarrow(\mathcal{K}^\downarrow) , \tag{3.6}$$

$$S_\mu^{\mathrm{l},\downarrow} = S_\mu^\downarrow(\mathcal{L}^\downarrow) . \tag{3.7}$$

Furthermore, it is assumed that shortwave and longwave radiation is reflected by an urban surface at the same rate in all directions (Lambertian scatterer). Therefore, the shortwave and longwave radiation exchanges between urban surfaces, E^{k}_{μ} and E^{l}_{μ}, are characterized by the same function, M_{μ}, but with different surface parameters, i.e. the shortwave albedos α_t with $t = \mathrm{W}, \mathrm{R}, \mathrm{G}$ and the longwave emissivities ϵ_t:

$$E^{\mathrm{k}}_{\mu} = M_{\mu}(\{K_{\kappa}\}, \{\alpha_t\}), \tag{3.8}$$

$$E^{\mathrm{l}}_{\mu} = M_{\mu}(\{L_{\kappa}\}, \{1 - \epsilon_t\}). \tag{3.9}$$

For every urban surface element μ, the incoming radiation from all other surfaces κ needs to be calculated and therefore all surface parameters t need to be given. This is indicated by the set braces in (3.8) and (3.9). In addition, the longwave radiation that is emitted by an urban surface κ is also assumed to be equal in all directions. Therefore, the longwave radiation H^{l}_{μ} received by the urban surface μ from all other surfaces κ can also be expressed in terms of the function M_{μ}:

$$H^{\mathrm{l}}_{\mu} = M_{\mu}(\{\sigma(T_{\kappa})^4\}, \{\epsilon_t\}) \tag{3.10}$$

with the Stefan–Boltzmann constant σ.

The direct shortwave radiation $S^{\mathrm{k},\Downarrow}_{\mu}$ depends on the position of the sun and is described separately in section 3.1.2. In the following, two different possibilities to define the functions $S^{\downarrow}_{\mu}$ and M_{μ} are explained, which, together with (3.4) and (3.5), describe a linear system of equations in terms of L_{μ} and K_{μ} (cf. appendix A for a complete listing). The system can be solved with standard methods such as Gauss-Jordan Elimination or LU decomposition (Press et al. 1992). This has to be done only once because the system's coefficients are constant over time.

3.1.1. Diffuse radiation

Modified BEP scheme

In the original BEP formulation, the area of the sky directly above the basic street canyon element acts as a source of diffuse sky radiation (cf. fig. 3.3a). Obviously, this area does not cover the complete sky. However, extending this area over a large number of neighbouring canyon is not feasible due to the many building height combinations and view factors involved. Thus, to include the radiation from the missing part of the sky, the areas at the side of the canyon above the roof depicted in fig. 3.3b also act as a radiation source. In general, this leads to an overestimation of the total radiative energy. In the following, the details of this mechanism as well as a solution are presented.

In BEP, all roofs at all height levels receive the full radiation from the sky surface element Sr and the reflected radiation from roofs is completely emitted into the sky.

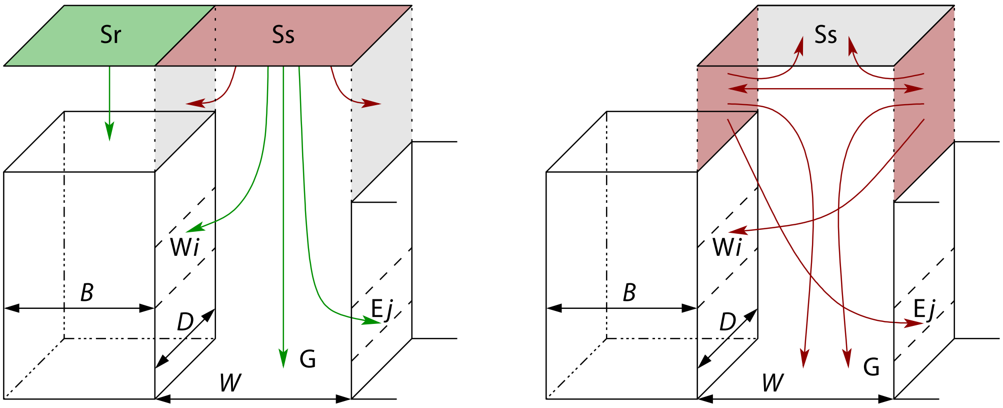

a) Radiation from the sky surface element Sr above the roofs is completely received by the roofs. Radiation from the single-canyon sky surface element Ss above the road surface is distributed within the canyon. The energy that leaves the canyon through the grey areas is not accounted for.

b) The open canyon sides also act as a radiation source. This radiation is distributed inside the canyon. The radiation that leaves through the canyon sides and Ss is not accounted for.

Figure 3.3. Distribution of diffuse radiation from the sky on the urban surfaces in the original BEP scheme (Martilli et al. 2002). In general, the combined incoming radiation from a) and b) is larger than the sky radiation. The introduction of the correction factor c in (3.13) solves that problem.

Consequently, no radiation from other surfaces (reflected or emitted) is received by the roofs:

$$S^{\downarrow}_{\mathrm{R}i}(\mathcal{R}) = \mathcal{R}\,, \quad \text{with} \quad \mathcal{R} = \mathcal{L}^{\downarrow}, \mathcal{K}^{\downarrow} \tag{3.11}$$

$$M_{\mathrm{R}i}(\{\,R_\kappa\,\},\{\,r_t\,\}) = 0\,, \tag{3.12}$$

for each type of diffuse sky radiation $\mathcal{R}$, the incoming diffuse radiation R_κ at all other surfaces κ and their respective reflectivity parameters r_t. Thus, energy is conserved for this part of the sky-surface interaction.

Inside the canyon, the probability for a wall element j to be present is given by Γ_j. If the wall element is present, it receives radiation from the sky surface element Ss. However, it is absent with a probability $(1-\Gamma_j)$ and, in this case, the energy of the incoming radiation from the sky is not accounted for (see fig. 3.3a: here, red arrows indicate unaccounted energy). Instead, the area with no wall element present acts as a diffuse radiation source with the same flux density as from the top sky (see fig. 3.3b). Each surface element inside the canyon receives radiation from both sources, the top sky and the areas where wall elements are not present. As indicated above, this leads to the problem that, in general, the total calculated amount of radiative energy received by the canyon is larger than the incoming radiation at the top of the canyon calculated by the mesoscale model. In order to solve that problem, a factor c is introduced into the BEP scheme that scales the radiative flux from the missing wall areas to ensure energy conservation. Since the radiation budget is assumed to be equal for each of the large number of neighbouring canyons, energy conservation has to be ensured in every street canyon separately. Thus, the incoming radiative energy from the mesoscale model, $\mathcal{R}DW$ (radiation per unit area times canyon surface), has to equal the total energy distributed in the canyon. Therefore, the factor c is defined by the relation

$$\begin{aligned}\mathcal{R}DW\,\Psi_{\mathrm{Ss}\to\mathrm{G}} &+ 2\mathcal{R}DW\sum_{j=1}^{n}\Psi_{\mathrm{Ss}\to j}\Gamma_j \\ &+ 2\sum_{i=1}^{n}(1-\Gamma_i)\,c\,\mathcal{R}D\,\Delta z_i\left(\Psi_{i\to\mathrm{G}} + \sum_{j=1}^{n}\Psi_{i\to j}\Gamma_j\right) \stackrel{!}{=} \mathcal{R}DW\,,\end{aligned} \tag{3.13}$$

where $\Psi_{\mathrm{Ss}\to\mathrm{G}}$ is the sky-view factor for diffuse radiation from the single-canyon sky surface element Ss above the street canyon (named sky in the following) to the ground, i.e. it describes the *energy* fraction of the diffuse radiation from the sky that is received by the ground (see appendix B for details on (sky) view factors). Thus, the first term in (3.13) expresses the energy received by the ground and the second term gives the total energy received by all wall elements inside the street canyon; $\Psi_{\mathrm{Ss}\to j}$ is the sky view factor for radiation from the sky to the wall element j. Therefore, the sum of the first two terms in (3.13) gives the total received energy inside the street canyon from the sky (corresponding to fig. 3.3a); $\Psi_{i\to\mathrm{G}}$ and $\Psi_{i\to j}$ are the view factors for radiation from the ith wall element received by the ground and the jth wall element, respectively. Thus, the third term corresponds to the distributed energy inside the canyon that originates from the open canyon sides where wall elements are not present (compare with fig. 3.3b). The factor c in (3.13) only depends on morphological parameters of the canyon, and hence it is a simulation constant. The effect of the overestimation of energy is analysed further in section 3.6. Now, the diffuse radiation from the sky as received by the ith wall elements and the ground is given by

$$S^{\downarrow}_{\mathrm{W}i}(\mathcal{R}) = S^{\downarrow}_{\mathrm{E}i}(\mathcal{R}) = \mathcal{R}\tilde{\Psi}_{\mathrm{Ss}\to i} + \sum_{j=1}^{n} c\mathcal{R}\tilde{\Psi}_{j\to i}(1-\Gamma_j)\,, \tag{3.14}$$

$$S^{\downarrow}_{\mathrm{G}}(\mathcal{R}) = \mathcal{R}\tilde{\Psi}_{\mathrm{Ss}\to\mathrm{G}} + 2\sum_{j=1}^{n} c\mathcal{R}\tilde{\Psi}_{j\to\mathrm{G}}(1-\Gamma_j)\,. \tag{3.15}$$

The modified view factors $\tilde{\Psi}_{\mu\to\kappa}$ describe the energy of the diffuse radiation *per unit area* that is received by κ from surface μ, thus, (3.14) and (3.15) give the received radiative flux.

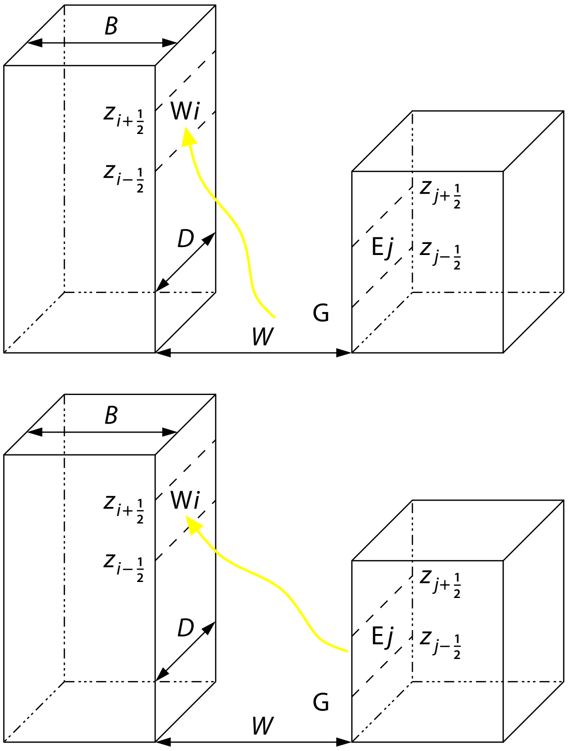

a) Radiation received from the ground G

b) Radiation received from the jth east wall element Ej

Figure 3.4. Diffuse radiation received by the ith west wall element Wi from other urban surfaces inside the urban street canyon in the single-canyon approach in the BEP scheme

Furthermore, the urban surfaces inside the street canyon receive radiation reflected or emitted from the other urban surfaces in the canyon. As an example, fig. 3.4 shows the corresponding sources of radiation for the west wall element Wi. In the single-canyon approach of BEP, no radiation is received from the roof surfaces. Thus, the exchange functions are given by:

$$M_{\mathrm{W}i}(\{R_\kappa\},\{r_t\}) = \underbrace{r_{\mathrm{G}} R_{\mathrm{G}} \tilde{\Psi}_{\mathrm{G}\to i}}_{\text{ground}} + \underbrace{\sum_{j=1}^{n} r_{\mathrm{W}} R_{\mathrm{E}j} \tilde{\Psi}_{j\to i} \Gamma_j}_{\text{east wall}}, \tag{3.16}$$

$$M_{\mathrm{E}i}(\{R_\kappa\},\{r_t\}) = \underbrace{r_{\mathrm{G}} R_{\mathrm{G}} \tilde{\Psi}_{\mathrm{G}\to i}}_{\text{ground}} + \underbrace{\sum_{j=1}^{n} r_{\mathrm{W}} R_{\mathrm{W}j} \tilde{\Psi}_{j\to i} \Gamma_j}_{\text{west wall}}, \tag{3.17}$$

$$M_{\mathrm{G}}(\{R_\kappa\},\{r_t\}) = \underbrace{\sum_{j=1}^{n} r_{\mathrm{W}} (R_{\mathrm{E}j} + R_{\mathrm{W}j}) \tilde{\Psi}_{j\to i} \Gamma_j}_{\text{east and west walls}}. \tag{3.18}$$

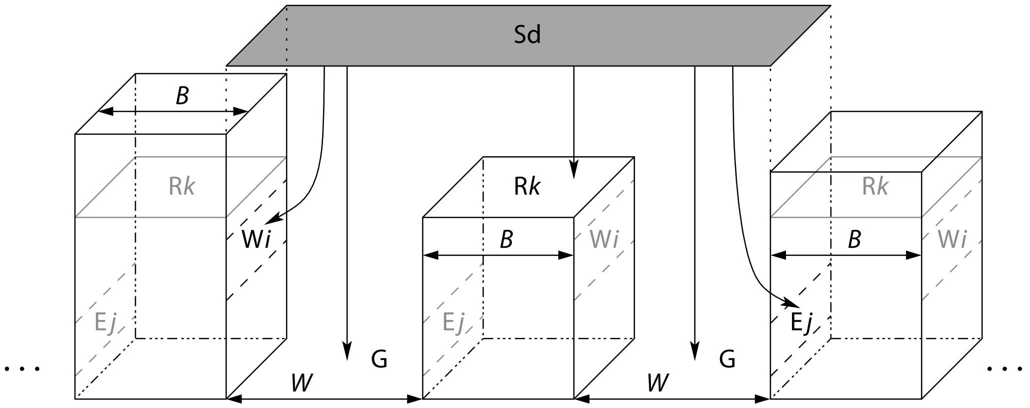

Figure 3.5. Extended double-canyon morphology for distribution of diffuse radiation from the sky and the radiation between the surfaces. The equations are formulated for the black labelled surface elements (e.g. the western wall element *i* always represents the W*i* on the left). Sd is the double-canyon sky surface element.

Here, the first summand in (3.16) corresponds to fig. 3.4a and the second summand corresponds to fig. 3.4b. Furthermore, an infinite number of reflections of radiation by the urban surface inside the canyon are taken into account with this formulation.

Inclusion of roofs in DCEP

In order to include the roofs consistently into the radiation exchange between surfaces, the basic street canyon element is extended from one road and two rows of buildings on either side to include an additional road and a row of buildings (fig. 3.5). Neglecting boundary effects (as described in the introduction of this chapter), it is assumed that the ground surfaces of both canyons receive the same radiation L_{G} and K_{G}, and have the same temperature T_{G}. Furthermore, the radiation budget of all west wall elements at a particular height level i is described by $L_{\mathrm{W}i}$, $K_{\mathrm{W}i}$ and $T_{\mathrm{W}i}$; of all east wall elements at level j by $L_{\mathrm{E}j}$, $K_{\mathrm{E}j}$ and $T_{\mathrm{E}j}$; and of all roofs at level k by $L_{\mathrm{R}k}$, $K_{\mathrm{R}k}$ and $T_{\mathrm{R}k}$, respectively. As far as the reception of energy from the sky is concerned, the ground element can either be inside the western or the eastern canyon. With that morphology, the double-canyon sky surface element Sd above the extended canyon element is larger than the single-canyon sky surface element Ss in the original BEP scheme. As a result, the view from the urban surfaces on Sd is partly obstructed by the building in the middle. This is taken into account by view factors $\tilde{\Psi}_{\mu \xrightarrow{k} \kappa}$ for radiation from surfaces μ to κ that consider buildings at a level k in the middle (appendix B.2.3). Therefore, the diffuse radiation from the sky is distributed to the wall, street and now also roof elements inside the canyon as follows:

$$S^{\downarrow}_{\mathrm{W}i}(\mathcal{R}) = S^{\downarrow}_{\mathrm{E}i}(\mathcal{R}) = \sum_{k=0}^{n} \gamma_k \mathcal{R} \tilde{\Psi}_{\mathrm{Sd}\xrightarrow{k} i} + \sum_{k=0}^{n} \gamma_k \sum_{j=1}^{n} c \mathcal{R} \tilde{\Psi}_{j \xrightarrow{k} i} (1 - \Gamma_j) \,, \tag{3.19}$$

$$\begin{aligned} S^{\downarrow}_{\mathrm{G}}(\mathcal{R}) = \sum_{k=0}^{n} \gamma_k \mathcal{R} \tilde{\Psi}_{\mathrm{Sd}\xrightarrow{k} \mathrm{G}} &+ \sum_{j=1}^{n} c \mathcal{R} \tilde{\Psi}_{j \to \mathrm{G}} (1 - \Gamma_j) \\ &+ \sum_{k=0}^{n} \gamma_k \sum_{j=1}^{n} c \mathcal{R} \tilde{\Psi}_{j \xrightarrow{k} \mathrm{G}} (1 - \Gamma_j) \,, \end{aligned} \tag{3.20}$$

$$S^{\downarrow}_{\mathrm{R}i}(\mathcal{R}) = \mathcal{R} \tilde{\Psi}_{\mathrm{Sd} \to \mathrm{R}i} + 2 \sum_{j=i+1}^{n} c \mathcal{R} \tilde{\Psi}_{j \to \mathrm{R}i} (1 - \Gamma_j) \,. \tag{3.21}$$

With the new canyon geometry, the correction factor c has to be adjusted to fulfil the equation

$$\begin{aligned} &\mathcal{R} D (2W + B) \sum_{k=0}^{n} \gamma_k \Big(\Psi_{\mathrm{Sd}\xrightarrow{k} \mathrm{G}} + 2 \sum_{j=1}^{n} \Psi_{\mathrm{Sd}\xrightarrow{k} j} \Gamma_j + \Psi_{\mathrm{Sd} \to \mathrm{R}k} \Big) \\ &+ \sum_{k=0}^{n} \gamma_k \sum_{i=1}^{n} (1 - \Gamma_i) c \mathcal{R} D \, \Delta z_i \Big(\Psi_{i \to \mathrm{G}} + \Psi_{i \xrightarrow{k} \mathrm{G}} + 2 \sum_{j=1}^{n} \Psi_{i \xrightarrow{k} j} \Gamma_j + 2 \Psi_{i \to \mathrm{R}k} \Big) \overset{!}{=} \mathcal{R} D (W + B) \,, \end{aligned} \tag{3.22}$$

where the first term describes, for the two combined canyons, the total radiation from the sky, and the second term is the total radiation from the canyon sides where wall elements are not present.

The exchange functions are extended to include not only the interaction of surface elements inside one canyon but also the radiation from the neighbouring canyon. For symmetry reasons and consistency, the equation for the ground surface includes the radiation from the neighbouring canyons on both, the west and east side. Thus, in addition to the terms in (3.16) to (3.18) depicted in fig. 3.4, the terms represented in fig. 3.6 are added to the functions:

$$\begin{aligned} M_{\mathrm{W}i}(\{R_\kappa\}, \{r_t\}) = &\underbrace{r_{\mathrm{G}} R_{\mathrm{G}} \tilde{\Psi}_{\mathrm{G} \to i}}_{\text{ground}} + \underbrace{\sum_{k=0}^{n} \gamma_k r_{\mathrm{G}} R_{\mathrm{G}} \tilde{\Psi}_{\mathrm{G} \xrightarrow{k} i}}_{\text{ground other canyon}} + \underbrace{\sum_{k=0}^{i-1} r_{\mathrm{R}} R_{\mathrm{R}k} \tilde{\Psi}_{\mathrm{R}k \to i} \gamma_k}_{\text{roofs}} \\ &+ \underbrace{\sum_{j=1}^{n} r_{\mathrm{W}} R_{\mathrm{E}j} \tilde{\Psi}_{j \to i} \Gamma_j}_{\text{east wall}} + \underbrace{\sum_{k=0}^{n} \gamma_k \sum_{j=1}^{n} r_{\mathrm{W}} R_{\mathrm{E}j} \tilde{\Psi}_{j \xrightarrow{k} i} \Gamma_j}_{\text{east wall other canyon}} \,, \end{aligned} \tag{3.23}$$

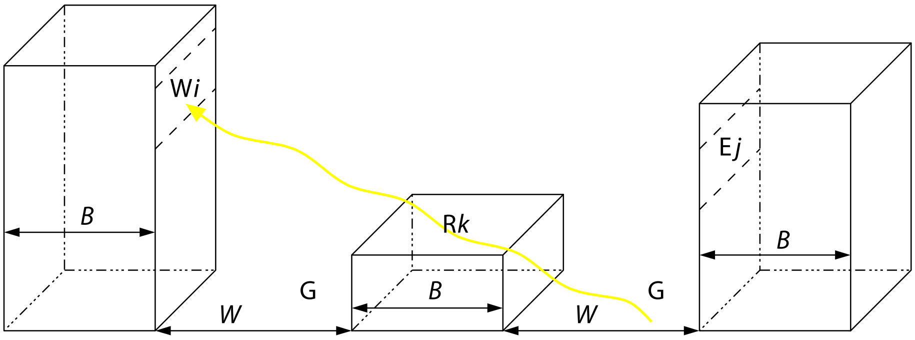

a) Radiation received from the ground surface G of a neighbouring canyon

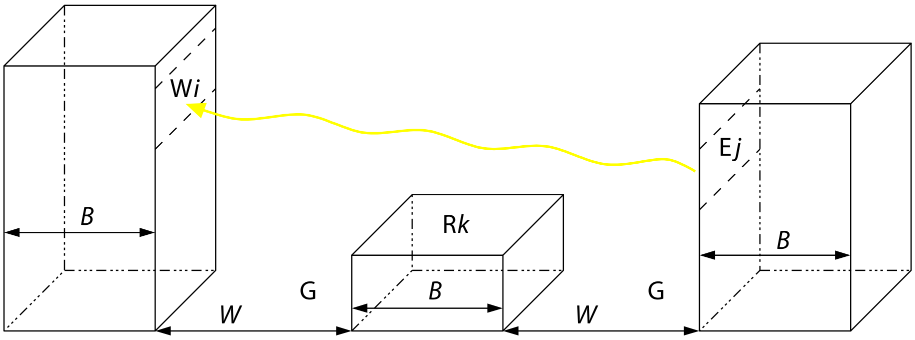

b) Radiation received from the *j*th east wall element Ej of a neighbouring canyon

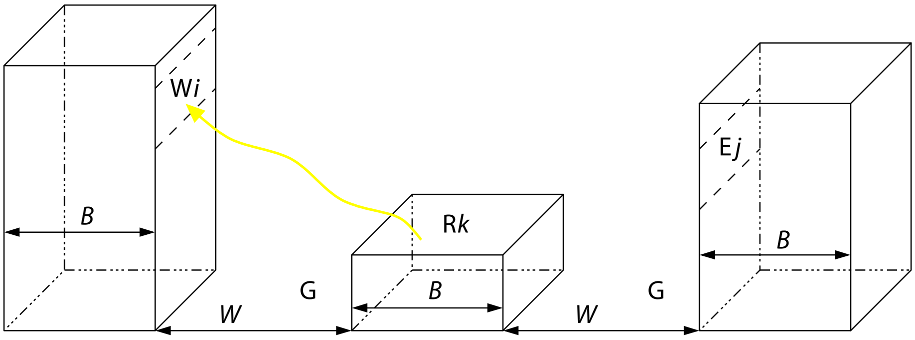

c) Radiation received from the *k*th roof surface

Figure 3.6. Additional sources of diffuse radiation taken into account by the double-canyon approach of DCEP. Depicted is the additional radiation received by the *i*th west wall element Wi from the other urban surfaces inside a neighbouring street canyon (in a) and b)) as well as from the roof surfaces (in c)).

$$\begin{aligned} M_{\mathrm{E}i}(\{R_\kappa\},\{r_t\}) = {} & \underbrace{r_\mathrm{G} R_\mathrm{G} \tilde{\Psi}_{\mathrm{G}\to i}}_{\text{ground}} + \underbrace{\sum_{k=0}^{n} \gamma_k r_\mathrm{G} R_\mathrm{G} \tilde{\Psi}_{\mathrm{G}\xrightarrow{k} i}}_{\text{ground other canyon}} + \underbrace{\sum_{k=0}^{i-1} r_\mathrm{R} R_{\mathrm{R}k} \tilde{\Psi}_{\mathrm{R}k\to i} \gamma_k}_{\text{roofs}} \\ & + \underbrace{\sum_{j=1}^{n} r_\mathrm{W} R_{\mathrm{W}j} \tilde{\Psi}_{j\to i} \Gamma_j}_{\text{west wall}} + \underbrace{\sum_{k=0}^{n} \gamma_k \sum_{j=1}^{n} r_\mathrm{W} R_{\mathrm{W}j} \tilde{\Psi}_{j\xrightarrow{k} i} \Gamma_j}_{\text{west wall other canyon}} , \end{aligned} \tag{3.24}$$

$$M_\mathrm{G}(\{R_\kappa\},\{r_t\}) = \underbrace{\sum_{j=1}^{n} r_\mathrm{W}(R_{\mathrm{E}j} + R_{\mathrm{W}j}) \tilde{\Psi}_{j\to i} \Gamma_j}_{\text{east and west wall}} + \underbrace{\sum_{k=0}^{n} \gamma_k \sum_{j=1}^{n} r_\mathrm{W}(R_{\mathrm{E}j} + R_{\mathrm{W}j}) \tilde{\Psi}_{j\xrightarrow{k} i} \Gamma_j}_{\text{east and west wall other canyon}} , \tag{3.25}$$

$$M_{\mathrm{R}i}(\{R_\kappa\},\{r_t\}) = \underbrace{\sum_{j=i+1}^{n} r_\mathrm{W}(R_{\mathrm{E}j} + R_{\mathrm{W}j}) \tilde{\Psi}_{j\to \mathrm{R}i} \Gamma_j}_{\text{east and west wall}} . \tag{3.26}$$

This extension ensures that every piece of radiation reflected or emitted by an urban surface is received by another surface. A simpler, yet consistent solution to include the interaction of roofs has not been found by the author of this work.

3.1.2. Direct radiation

The following subsection describes the calculation of the direct solar radiation received by every urban surface element. The single-canyon formulation (based on Martilli et al. 2002) allows shadows on wall and ground surfaces; roof surfaces always receive the full solar radiation independent of their height. The combination of two canyons extends the single-canyon formulation to allow shadows on roofs. Both approaches were developed with Alberto Martilli (private communication) and published in Schubert et al. (2012).

The position of the sun relative to the street canyon has to be known to calculate the sunlit part of every urban surface element. The solar azimuth angle ψ, which is the angle between the projection of the sun on the earth's surface and the north-south direction (fig. 3.7a), is given by

$$\cos\psi = \frac{\cos Z \sin\varphi - \sin\delta}{\sin Z \cos\varphi} \tag{3.27}$$

with Z being the zenith angle, φ the geographic latitude and δ the declination of the sun (Iqbal 1983). The equation used in Pielke (2002) and also in Martilli et al. (2002) gives, according to Iqbal (1983), improper values for $\psi > 90°$. For a positive value of

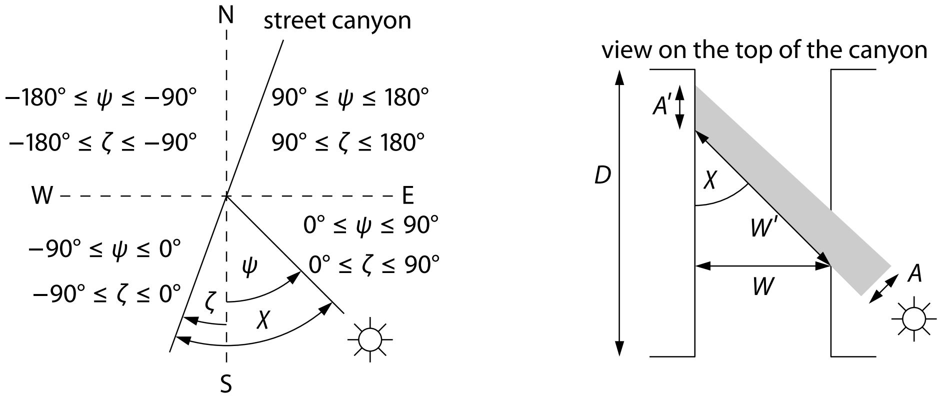

a) Geometry of the solar azimuth angle ψ and street canyon angles ζ

b) Modification of street width W and beam area A

Figure 3.7. Calculation and influence of the angle between the street direction and the sun beams

the hour angle, ψ is positive, for a negative value, ψ is negative. With that, the angle between the face of the wall and the sun direction is given by

$$\chi = \psi - \zeta\,. \tag{3.28}$$

In general, both directions are not perpendicular (i.e. $\chi \neq 90°$) so the street and building width W and B, respectively, and the direct insolation $\mathcal{K}^{\Downarrow}$ have to be adjusted accordingly. Referring to fig. 3.7b,

$$\tilde{W} = W / \sin\chi\,, \tag{3.29}$$

$$\tilde{B} = B / \sin\chi\,, \tag{3.30}$$

and with a reference area A enlarged to $\tilde{A} = A/\sin\chi$,

$$\tilde{\mathcal{K}}^{\Downarrow} = \mathcal{K}^{\Downarrow} \sin\chi\,. \tag{3.31}$$

The angle of the opposite canyon side is given by $\chi_{\mathrm{opp}} = \chi + \pi$, so that $\sin\chi_{\mathrm{opp}} = -\sin\chi$. In the case of $\sin\chi \leq 0$, this side of the canyon receives no direct solar radiation, and (3.29) to (3.31) has to be evaluated for the other canyon side with an angle of χ_{opp}.

An infinite number of height combinations of neighbouring canyons has to be taken into account to calculate the fraction of an urban surface that is sunlit by direct radiation. In the following, two possible simplifications of the number of height combinations are presented.

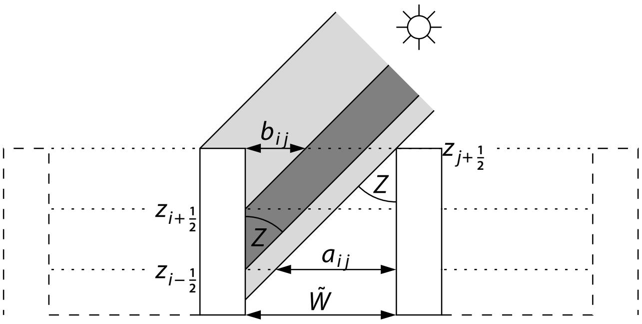

Figure 3.8. Shadow calculation of direct solar radiation in a single canyon: all buildings are at the same height. The surfaces of the left building directly insolated by the sun are indicated by the light grey shaded area. In addition, the dark grey shaded area indicates the sunlit fraction of the ith wall surface situated between the heights $z_{i-1/2}$ and $z_{i+1/2}$. Z is the zenith angle, a_{ij} and b_{ij} are the helper variables in (3.32), and $\tilde{W}$ denotes the effective street width.

Shadow calculation based on a single canyon

The simplest assumption is that all buildings have the same height (fig. 3.8); thus, the incoming direct radiation on the western wall element Wi is given by

$$\begin{aligned} S^{\mathrm{k},\Downarrow}_{\mathrm{W}i} &= \frac{\tilde{K}^{\Downarrow}}{\Delta z_i} \frac{1}{\sum_{j=i}^{n} \gamma_j} \sum_{j=i}^{n} \gamma_j \left[\tilde{W} - b_{ij} - (\tilde{W} - a_{ij}) \right] \\ &= \frac{\tilde{K}^{\Downarrow}}{\Delta z_i} \frac{1}{\Gamma_i} \sum_{j=i}^{n} \gamma_j (a_{ij} - b_{ij}) \, , \end{aligned} \tag{3.32a}$$

with

$$a_{ij} = \min\left[(z_{j+1/2} - z_{i-1/2}) \tan Z, \tilde{W} \right] \, , \tag{3.32b}$$

$$b_{ij} = \min\left[(z_{j+1/2} - z_{i+1/2}) \tan Z, \tilde{W} \right] \, . \tag{3.32c}$$

This corresponds to the original formulation in Martilli et al. (2002) except for the $1/\Gamma_i$ factor, which ensures energy conservation. This factor is necessary because a building that includes a wall element Wi has to have at least the height $z_{i+1/2}$ (cf. fig. 3.2), and thus, all buildings must reach at least level i. The incoming direct shortwave radiation for the ith east wall segment $S^{\mathrm{k},\Downarrow}_{\mathrm{E}i}$ is obtained by substituting χ by χ_{opp}. The road receives the following radiation:

$$S^{\mathrm{k},\Downarrow}_{\mathrm{G}} = \frac{\tilde{K}^{\Downarrow}}{W} \sum_{j=0}^{n} \gamma_j \max(0, \tilde{W} - z_{j+1/2} \tan Z) \tag{3.33}$$

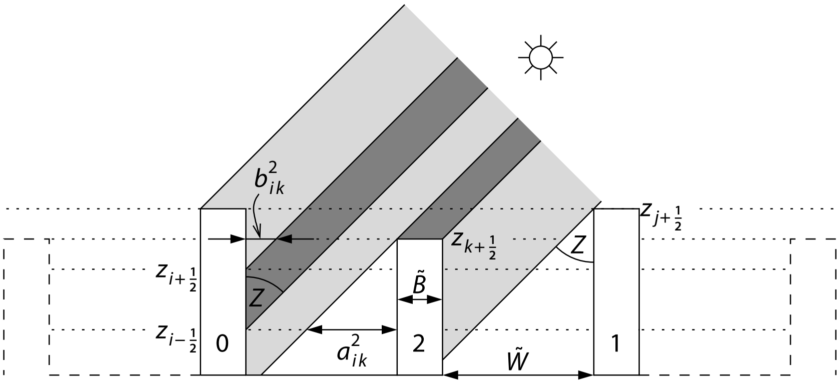

Figure 3.9. Shadow calculation of direct solar radiation in a double canyon: every second building has the same height. The surfaces of the left and central buildings directly insolated by the sun are indicated by the light grey shaded area. In addition, the dark grey shaded areas indicate the sunlit fractions of the ith wall surface situated between the heights $z_{i-1/2}$ and $z_{i+1/2}$ on the left building as well as of the kth roof surface at the height $z_{k+1/2}$ on the central building. Z is the zenith angle, a^2_{ij} and b^2_{ij} are helper variables in (3.35), and $\tilde{W}$ and $\tilde{B}$ denote the effective street width and the effective building width, respectively.

and the roofs, in this simple approach, receive full radiation:

$$S^{\mathrm{k},\Downarrow}_{\mathrm{R}i} = \mathcal{K}^{\Downarrow} . \tag{3.34}$$

In the next subsection, a more realistic approach that takes shadows on roof surfaces into account is presented.

Shadow calculation based on two combined canyons

The restriction that every building has the same height is replaced by the less strict assumption that every *second* building has the same height. Thus, in fig. 3.9, the two neighbouring buildings 1 and 2 may cast a shadow on building 0. The approach of the single canyon with summands a^1_{ij} and a^1_{ij} is utilized to calculate the shadow by building 1 and a^2_{ik} and a^2_{ik} for the shadow by building 2:

$$\begin{aligned} S^{\mathrm{k},\Downarrow}_{\mathrm{W}i} &= \frac{\tilde{\mathcal{K}}^{\Downarrow}}{\Delta z_i} \frac{1}{\sum_{k=0}^{n} \gamma_k \sum_{j=i}^{n} \gamma_j} \sum_{k=0}^{n} \gamma_k \sum_{j=i}^{n} \gamma_j \omega_{i,j,k} \\ &= \frac{\tilde{\mathcal{K}}^{\Downarrow}}{\Delta z_i} \frac{1}{\Gamma_i} \sum_{k=0}^{n} \gamma_k \sum_{j=i}^{n} \gamma_j \omega_{i,j,k} \end{aligned} \tag{3.35a}$$

with

$$\omega_{ijk} = \begin{cases} \min\left(a^1_{ij} - b^1_{ij}, a^2_{ik} - b^2_{ik}\right), & i \leq k \\ a^1_{ij} - b^1_{ij}, & i > k \end{cases} \tag{3.35b}$$

and

$$a^1_{ij} = \min\left[\left(z_{j+1/2} - z_{i-1/2}\right) \tan Z, 2\tilde{W} + \tilde{B}\right], \tag{3.35c}$$

$$b^1_{ij} = \min\left[\left(z_{j+1/2} - z_{i+1/2}\right) \tan Z, 2\tilde{W} + \tilde{B}\right], \tag{3.35d}$$

$$a^2_{ik} = \min\left[\left(z_{k+1/2} - z_{i-1/2}\right) \tan Z, \tilde{W}\right], \tag{3.35e}$$

$$b^2_{ik} = \min\left[\left(z_{k+1/2} - z_{i+1/2}\right) \tan Z, \tilde{W}\right]. \tag{3.35f}$$

For roads, the radiation flux is given by

$$S_{\mathrm{G}}^{\mathrm{k},\Downarrow} = \frac{\tilde{\mathcal{K}}^{\Downarrow}}{W} \sum_{k=0}^{n} \gamma_k \sum_{j=0}^{n} \gamma_j \max\left(0, \min\left(\tilde{W} - z_{k+1/2} \tan Z, 2\tilde{W} + \tilde{B} - z_{j+1/2} \tan Z\right)\right) \tag{3.36}$$

and for roofs by

$$S_{\mathrm{R}i}^{\mathrm{k},\Downarrow} = \frac{\tilde{\mathcal{K}}^{\Downarrow}}{B} \sum_{j=0}^{n} \gamma_j \min\left(\tilde{B}, \max\left(0, \tilde{W} + \tilde{B} - \left(z_{j+1/2} - z_{i+1/2}\right) \tan Z\right)\right). \tag{3.37}$$

3.2. Building induced fluxes and TKE production

In this section, the parametrization of the momentum and sensible heat fluxes induced by the urban surface elements and the resulting production of TKE is described (fig. 3.2 on page 35 shows the heights where the urban surfaces and the fluxes are defined). Here, every urban surface element is treated *separately*; the aggregated effect on the mesoscale grid cell is described in section 3.5. It is explicitly noted when the following differs from the formulation in Martilli et al. (2002).

3.2.1. Fluxes from horizontal surfaces: roofs and street

In order to calculate the momentum and sensible heat fluxes from *individual* horizontal urban surfaces, BEP and DCEP use the formulation by Louis (1979), which is based on the Monin-Obukhov similarity theory (MOST; Monin and Obukhov 1954). To this end, roof and street surfaces are characterized by their roughness lengths $z_{0\mathrm{R}}$ and $z_{0\mathrm{G}}$. This formulation corresponds to a simplified version of the bulk approach described in section 2.2.3 but it is applied to each horizontal urban surface element separately. Applying MOST to the complete urban surface layer characterized by only one roughness length for the ensemble of the city was shown to not properly reproduce the vertical structure in the urban roughness layer (e.g. Rotach 1993).

With that, the momentum flux $\boldsymbol{\tau}^{\mathrm{h}}_{\mu}$ induced by the roof surface on the ith level ($\mu = \mathrm{R}i$) or the ground surface ($\mu = \mathrm{G}$ with $i = 0$) is given by

$$\boldsymbol{\tau}^{\mathrm{h}}_{\mu} = -\rho \frac{\kappa^2}{\left[\ln\left(\frac{\Delta z_{i+1}/2}{z_{0\mu}}\right)\right]^2} f_{\mathrm{m}}\left(\frac{\Delta z_{i+1}/2}{z_{0\mu}}, Ri_{\mathrm{B}\mu}\right) u^{\mathrm{h}}_{i+1} \boldsymbol{u}^{\mathrm{h}}_{i+1}, \tag{3.38}$$

where $\Delta z_i \equiv z_{i+1/2} - z_{i-1/2}$ is the thickness of the ith urban layer and $\boldsymbol{u}^{\mathrm{h}}_i \equiv (u_i, v_i, 0)$ is the horizontal wind velocity with $u^{\mathrm{h}}_i \equiv \sqrt{u_i^2 + v_i^2}$. f_{m} is the stability function for momentum exchange according to Louis (1979), in which the bulk Richardson number Ri_{B} determines the stability of the atmosphere. Ri_{B} approximates the negative ratio of buoyant and shear production of TKE (cf. (2.32)), and is given by

$$Ri_{\mathrm{B}} \equiv \frac{g\,\Delta\theta_{\mathrm{v}}\,\Delta z}{\theta_{\mathrm{v}}\left[(\Delta u)^2 + (\Delta v)^2\right]}, \tag{3.39}$$

with $\Delta\theta_{\mathrm{v}}$, Δu and Δv being the differences in virtual potential temperature, zonal and meridional wind velocity, respectively, over a distance of Δz; θ_{v} is the mean virtual potential temperature. Here, Ri_{B} is expressed as

$$Ri_{\mathrm{B}\mu} \approx \frac{g\,(T_{i+1} - T_{\mu})\,\Delta z_{i+1}/2}{\frac{1}{2}(T_{i+1} + T_{\mu})(u^2_{i+1} + v^2_{i+1})}. \tag{3.40}$$

T_i is the atmospheric temperature at height z_i. As expected, the direction of the momentum flux $\boldsymbol{\tau}^{\mathrm{h}}_{\mu}$ is opposite to that of the mean wind velocity $\boldsymbol{u}^{\mathrm{h}}_{i+1}$ and thus reduces u^{h}_{i+1}.

The sensible heat flux is parametrized analogously to the momentum flux and is proportional to the difference between the temperatures of the atmosphere and the surface:

$$H^{\mathrm{h}}_{\mu} = -\rho c_{\mathrm{Pd}} \frac{\kappa^2}{\left[\ln\left(\frac{\Delta z_{i+1}/2}{z_{0\mu}}\right)\right]^2} f_{\mathrm{h}}\left(\frac{\Delta z_{i+1}/2}{z_{0\mu}}, Ri_{\mathrm{B}\mu}\right) u^{\mathrm{h}}_{i+1}(T_{i+1} - T_{\mu}), \tag{3.41}$$

where f_{h} is the stability function for heat. Heat flows from the urban surface into the atmosphere, if the latter is cooler than the surface. The atmosphere warms the surface, if the surface is cooler than the atmosphere.

Sensible heat and turbulent momentum fluxes from the urban surfaces modify the TKE production. In the following, it is assumed that the x-axis of the coordinate system points in the direction of the mean wind velocity $\boldsymbol{u}^{\mathrm{h}}$. With this and (2.32), the production of TKE is given by

$$P = \frac{g}{\theta_\mathrm{v}} \overline{w'\theta_\mathrm{v}'} - \frac{\partial u^\mathrm{h}}{\partial z} \overline{w' u^{\mathrm{h}\prime}} \,. \tag{3.42}$$

The first summand is expressed in terms of the air temperature neglecting the influence of water constituents in the flux $\overline{w'\theta_v'}$. For the second summand, the formulation of the logarithmic wind profile by Louis (1979) is used;

$$u^\mathrm{h} = u_\star \frac{\ln\left(\frac{z}{z_0}\right)}{\kappa f_\mathrm{m}^{1/2}} \,, \tag{3.43}$$

where the friction velocity $u_\star$ is given by

$$u_\star^2 \equiv \frac{|\boldsymbol{\tau}^\mathrm{h}|}{\rho} \equiv \frac{\tau^\mathrm{h}}{\rho} = \left|\overline{w' u^{\mathrm{h}\prime}}\right| = -\overline{w' u^{\mathrm{h}\prime}} \,. \tag{3.44}$$

Thus, the gradient of the wind velocity averaged over the interval z_0 to z is given by

$$\overline{\frac{\partial u^\mathrm{h}}{\partial z}} \equiv \frac{1}{z} \int_{z_0}^{z} \frac{\partial u^\mathrm{h}}{\partial z} \mathrm{d}z = \frac{1}{z} u^\mathrm{h}(z) = u_\star \frac{\ln\left(\frac{z}{z_0}\right)}{z\,\kappa f_\mathrm{m}^{1/2}} \,. \tag{3.45}$$

Assuming the validity of the logarithmic wind profile up to a height of half of the urban grid cell layer above the surface μ, $z = 1/2\,\Delta z_i$, the TKE production for half of the urban grid cell volume above the horizontal surfaces is given by

$$P_\mu^\mathrm{h} = \frac{g}{T_i} \frac{H_\mu^\mathrm{h}}{\rho c_\mathrm{Pd}} + \frac{\ln\left(\frac{\Delta z_{i+1}/2}{z_{0\mu}}\right)}{\kappa \frac{\Delta z_{i+1}}{2} f_\mathrm{m}} \left(\frac{\tau_i^\mathrm{h}}{\rho}\right)^{3/2} \,. \tag{3.46}$$

In comparison with the formulation in the BEP scheme, the stability of the atmosphere is taken into account.

3.2.2. Fluxes from vertical surfaces: walls

Buildings induce pressure and viscous drag forces on the flow (Raupach and Shaw 1982). Analogously to the horizontal surfaces, every vertical wall surface element is treated separately here. The momentum flux at the wall surface element Wi or Ei (depending on the wind direction) is parametrized (Raupach et al. 1991) by

$$\boldsymbol{\tau}_i^\mathrm{v} = -\rho C_\mathrm{drag} u_i^\perp \boldsymbol{u}_i^\perp \,, \tag{3.47}$$

where $\boldsymbol{u}_i^{\perp}$ is the wind velocity perpendicular to the street canyon wall and the drag coefficient C_{drag} is set to 0.4 (Raupach 1992). Thus, the momentum flux is zero for a street canyon which is aligned with the wind direction. For a non-vanishing $u_i^{\perp}$ the momentum flux is attributed to the side of the canyon which results in a reduction of the wind speed u_i due to the flux.

The parametrization of the sensible heat flux H_μ^{v} of each wall surface element $\mu = \mathrm{W}i$ or $\mu = \mathrm{E}i$ is based on the formulation of wind forced convection by Clarke (1985):

$$H_\mu^{\mathrm{v}} = -h_i(T_i - T_\mu) \tag{3.48}$$

with the empirical forced convection coefficient

$$h_i = 5.678\,\mathrm{W\,m^{-2}\,K^{-1}}\left[1.09 + 0.23\left(\frac{u_i^{\mathrm{h}}}{0.3048\,\mathrm{m\,s^{-1}}}\right)\right]. \tag{3.49}$$

The direction of the heat flow is analogous to that of the horizontal surfaces.

For the horizontal fluxes here, only the shear production of TKE is considered. Assuming a wind velocity of $\boldsymbol{u}_i^{\perp}$ at a distance W from the wall* and a vanishing wind velocity at the wall, the TKE production is given by

$$P_i^{\mathrm{v}} = \frac{C_{\mathrm{drag}}}{W}(u_i^{\perp})^3\,. \tag{3.50}$$

3.3. Heat storage in urban surfaces

Every urban surface element μ consists of several layers to represent the storage of heat (fig. 3.10). A one-dimensional heat equation describes the heat conduction between the layers with depth d:

$$\frac{\partial T_\mu}{\partial t} = \frac{\partial}{\partial d}\left(k_\mu \frac{\partial T_\mu}{\partial d}\right), \tag{3.51}$$

where the thermal diffusivity k is given by $k_\mu = \nu_\mu/(\rho_\mu c_\mu)$ with the thermal conductivity ν_μ, the specific heat capacity c_μ and the material density ρ_μ. The discretization used for (3.51) for a time step from t to $t+1$ (Crank and Nicolson 1947) is given by

$$\begin{aligned}\frac{T_{\mu,i}^{t+1} - T_{\mu,i}^{t}}{\Delta t} = \frac{1}{\Delta d_{\mu,i}}\Bigg\{ & \frac{k_{\mu,i+1/2}}{2\,\Delta d_{\mu,i+1/2}}\left[(T_{\mu,i+1}^{t+1} - T_{\mu,i}^{t+1}) + (T_{\mu,i+1}^{t} - T_{\mu,i}^{t})\right] \\ & - \frac{k_{\mu,i-1/2}}{2\,\Delta d_{\mu,i-1/2}}\left[(T_{\mu,i}^{t+1} - T_{\mu,i-1}^{t+1}) + (T_{\mu,i}^{t} - T_{\mu,i-1}^{t})\right]\Bigg\}.\end{aligned} \tag{3.52}$$

---

[*] The value assumed here is not important for the physical result of the model because it cancels out in the aggregation to the mesoscale levels in section 3.5.

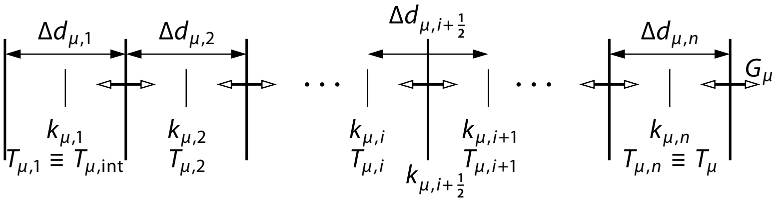

Figure 3.10. Layers of the urban surface element μ and the fluxes between them. Every layer i is characterized by its thickness $\Delta d_{\mu,i}$, thermal diffusivity $k_{\mu,i}$ and temperature $T_{\mu,i}$.

Here, $\Delta d_{\mu,i+1/2} \equiv \frac{1}{2}(\Delta d_{\mu,i} + \Delta d_{\mu,i+1})$ is the distance between the centres of two adjacent layers i and $i+1$, and $k_{\mu,i+1/2} = (\frac{1}{2}\Delta d_{\mu,i} k_i + \frac{1}{2}\Delta d_{\mu,i+1} k_{i+1}) / \Delta d_{\mu,i+1/2}$ is the effective thermal diffusivity between the centres.

Two possible boundary conditions for the temperature of the innermost layer have been analysed: either a fixed temperature

$$T_{\mu,1} \equiv T_{\mu,\mathrm{int}} = \mathrm{const.}\,, \qquad \text{(Dirichlet boundary condition)} \qquad (3.53)$$

which has been proposed in Martilli et al. (2002), or a vanishing inner heat flux

$$\left.\frac{\partial T_\mu}{\partial d}\right|_{\mathrm{int}} = 0 \Rightarrow \frac{T^t_{\mu,1} - T^t_{\mu,0}}{\Delta d_{\mu,1/2}} = 0, \forall t\,. \qquad \text{(Neumann boundary condition)} \qquad (3.54)$$

Throughout this work, the latter is used. For a realistic surface thickness of approx. 0.5 m and the realistic heat conduction parameters listed in section 5.3 (cf. Holman 1986; Kuttler 2004), a fixed innermost temperature influences the outer temperature of the surface and thereby also the atmosphere. For the wall surfaces, this fact has been interpreted by Martilli et al. (2002) as part of the anthropogenic heat flux, e.g. due to heating. However, in a simulation of Berlin (Germany) and its surroundings for the summer 2003 with the settings in section 5.3, a fixed temperature of 22 °C produced an urban *cooling* effect of several Kelvin for Berlin during daytime and nighttime. An increased inner temperature would solve this issue but would be unrealistic when applied to the wintertime and, in general, the indoor temperature is not constant anyway. For example, Wright et al. (2005) measured varying indoor temperatures in Manchester and London (UK) during the extreme heat event of 2003: while the external temperature varied between 14.2 °C and 32.1 °C in Manchester between 4 August and 13 August, indoor temperatures varied between 19.0 °C and 36.0 °C depending on the considered house and room. The hottest room featured temperatures between 23.0 °C and 36.0 °C. Similar results have been found for London. With the external temperature varying between 19.2 °C and 37.4 °C between 6 August and 14 August, the hottest measured flat had indoor temperatures between 26.0 °C and 39.2 °C. In DCEP, the fixation of the inner flux allows the innermost surface temperatures to vary with time. Furthermore, it ensures energy conservation and allows to treat anthropogenic heat completely separately (and thus in a controlled way, see section 6.1).

The energy balance of a simple plane surface (e.g. Doll et al. 1985; Arnfield 2003) is given by

$$R^* = H + \lambda E + G\,, \tag{3.55}$$

where R^* is the net radiation, H and λE are the sensible and latent heat flux, and G is the storage flux of heat into the surface. Since the latent heat flux from urban surfaces is currently not considered in DCEP, the storage flux at the exterior boundary of the surface μ is given by

$$G_\mu = (1-\alpha_\mu)K_\mu + \epsilon_\mu L_\mu - \epsilon_\mu \sigma T_\mu^4 - H_\mu\,. \tag{3.56}$$

Thus, the temperature $T_{\mu,n} = T_\mu$ has to fulfil Neumann boundary conditions:

$$\frac{T_\mu^{t+1}-T_\mu^t}{\Delta t} = \frac{1}{\Delta d_{\mu,n}}\left\{\frac{G_\mu^t}{\rho_{\mu,n}c_{\mu,n}} - \frac{k_{\mu,n-1/2}}{2\,\Delta d_{\mu,n-1/2}}\left[\left(T_\mu^{t+1}-T_{\mu,n-1}^{t+1}\right) + \left(T_\mu^t - T_{\mu,n-1}^t\right)\right]\right\}. \tag{3.57}$$

3.4. Urban turbulent length scales

In DCEP, the assumption of the BEP scheme that buildings generate turbulent vortices of the size of the height of the buildings is adopted (cf. fig. 3.11). The average building induced turbulent length scale l_J^{b} in the mesoscale layer J of CCLM is given by the harmonic mean of the building heights affecting that layer. This is analogous to the approach in (2.31) and adds additional dissipation terms of TKE (cf. (2.32)) for each building. Since the turbulent length scales are defined on half levels in CCLM, only buildings that are larger than the respective half level are considered†:

$$\frac{1}{l^{\mathrm{b}}_{J+1/2}} = \frac{1}{N^{(\mathrm{I})}_{J+1/2}} \sum_{\substack{i\\ z_{i+\frac12}\ge z_{J+\frac12}}} \gamma_i \frac{1}{z_{i+\frac12}} \tag{3.58a}$$

with

$$N^{(\mathrm{I})}_{J+1/2} \equiv \sum_{\substack{i\\ z_{i+\frac12}\ge z_{J+\frac12}}} \gamma_i\,. \tag{3.58b}$$

---

†The averaging over the street directions is omitted in the equations for the sake of readability. See the following section for details.

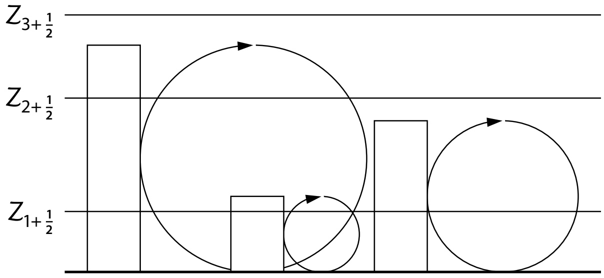

Figure 3.11. Turbulent vortices generated by the buildings. Lower levels are influenced by higher buildings, while it is assumed that higher levels are not influenced by lower buildings.

Similarly, the presence of the buildings result in a reduced effective height above the ground. The effective height $\tilde{z}_{J+1/2}$ of the half level $J+1/2$ is given by

$$\frac{1}{\tilde{z}_{J+1/2}} = \left(\frac{W}{W+B}\right)\frac{1}{Z_{J+1/2}} + \left(\frac{B}{W+B}\right)\frac{1}{N^{(\mathrm{II})}_{J+1/2}} \sum_{\substack{i \\ z_{i+\frac{1}{2}} \le Z_{J+\frac{1}{2}}}} \gamma_i \frac{1}{Z_{J+1/2} - z_{i+1/2}} \tag{3.59a}$$

with

$$N^{(\mathrm{II})}_{J+1/2} \equiv \sum_{\substack{i \\ z_{i+\frac{1}{2}} \le Z_{J+\frac{1}{2}}}} \gamma_i \,. \tag{3.59b}$$

Both normalization coefficients, $N^{(\mathrm{I})}$ and $N^{(\mathrm{II})}$, are necessary because the sums in (3.58a) and (3.59a) do not consider all building heights; $N^{(\mathrm{I})}$ and $N^{(\mathrm{II})}$ are not present in Martilli et al. (2002), though. The total urban length scale is then given by the harmonic mean of the building induced length scale and the traditional formulation in (2.31):

$$\frac{1}{l^{\mathrm{urb}}_{J+1/2}} = \frac{1}{l^{\mathrm{b}}_{J+1/2}} + \frac{1}{\kappa \tilde{z}_{J+1/2}} + \frac{1}{l_\infty} \,. \tag{3.60}$$

3.5. Coupling with a mesoscale model

The coupling of the presented urban scheme with a regional atmospheric numerical model requires the preprocessing of appropriate input data such as the building height distribution, the roof and road width as well as the fraction of natural and man-made surfaces in a model grid cell. The specific algorithm to estimate these parameters of the simplified urban morphology presented here depends on the available data. Two exemplary approaches are presented in section 4.1 for Basel (Switzerland) and in section 5.1 for Berlin (Germany). In general, however, the area fractions of roofs, walls and street surfaces should be equal in reality and in the model (Martilli 2009).

In the simulation, effective urban surface radiation parameters have to be derived to represent the urban surface in the mesoscale radiation scheme. Furthermore, the input fields of DCEP like the wind speed and the air temperature need to be interpolated from the corresponding mesoscale fields. The subsequently calculated urban sensible heat and momentum fluxes have to be aggregated from the urban height levels onto the mesoscale vertical levels and averaged with the fluxes from the natural surface. These averages enter the mesoscale model's prognostic equations for wind speed, temperature and TKE in (2.14), (2.16) and (2.32), respectively. This procedure of independently calculating surface fluxes of different parts of a grid cell (here natural and urban parts) and subsequent averaging is called *tile approach*.

As explained in the introduction of this chapter, the urban radiation budget, the urban momentum and sensible heat fluxes, and the urban heat storage described in sections 3.1 to 3.3 are calculated for each street direction independently. In order to calculate the average effect on the mesoscale atmosphere, the urban length scales and the urban fluxes from different street directions are averaged, weighted with the corresponding fraction f_{dir} of the street direction. This is omitted in the equations in this section for the sake of readability.

3.5.1. Effective surface radiation parameters

In the DCEP scheme, the fraction of a mesoscale model grid cell that is covered by impervious surfaces is conceptualized as multiple series of identical street canyon elements. The scheme calculates the reflected and emitted radiation components of every urban surface element; CCLM, however, characterizes the surface by the surface albedos for diffuse and for direct radiation, by the surface emissivity, and by the surface temperature (cf. section 2.2.1). In the following, the definition of the corresponding effective radiation properties of the *total* urban surface is explained. Subsequently, the averaging of these radiative surface parameters of the urban and natural surfaces is shown.

The effective urban albedo α_{urb} and its components for diffuse and direct shortwave radiation, $\alpha^{\downarrow}_{\mathrm{urb}}$ and $\alpha^{\Downarrow}_{\mathrm{urb}}$, are defined by the relation

$$K^{\uparrow}_{\mathrm{urb}} = \alpha_{\mathrm{urb}}(\mathcal{K}^{\downarrow} + \mathcal{K}^{\Downarrow}) = \alpha^{\downarrow}_{\mathrm{urb}}\mathcal{K}^{\downarrow} + \alpha^{\Downarrow}_{\mathrm{urb}}\mathcal{K}^{\Downarrow}\,, \tag{3.61}$$

with $K^{\uparrow}_{\mathrm{urb}}$ being the total reflected shortwave radiative flux from all urban surfaces into the sky. Combining (3.6) with (3.11), (3.14) and (3.15) or (3.19) to (3.21) shows that $\alpha^{\downarrow}_{\mathrm{urb}}$ is constant and depends only on the urban morphology as well as the albedos of the urban surface elements in the case of dry and snow-free surfaces. The albedo for direct radiation, however, depends on the solar azimuth ψ and the zenith angle Z and is thus not constant.

The sum of the emitted and reflected longwave radiation fluxes into the sky, $L^{\uparrow}_{\mathrm{urb}}$, the effective urban emissivity ϵ_{urb} and the effective radiative surface temperature T_{urb} are connected by

$$L^{\uparrow}_{\mathrm{urb}} = (1 - \epsilon_{\mathrm{urb}})\mathcal{L}^{\downarrow} + \epsilon_{\mathrm{urb}}\sigma T^{4}_{\mathrm{urb}}\,, \tag{3.62}$$

where the emissivity ϵ_{urb} can be understood as the mean emissivity of the surface:

$$\epsilon_{\mathrm{urb}} \equiv \sum_{i=0}^{n}\sum_{j=0}^{n}\gamma_i\gamma_j\frac{\epsilon_{\mathrm{R}}B + \epsilon_{\mathrm{G}}W + \epsilon_{\mathrm{W}}(z_{i+1/2} + z_{j+1/2})}{B + W + z_{i+1/2} + z_{j+1/2}}\,. \tag{3.63}$$

Therefore, T_{urb} can be easily obtained from (3.62). Note that T_{urb} is not a direct measure for temperatures inside the urban canopy but only describes the radiation budget of the urban canyon (cf. also section 3.6.3).

The surface radiation parameters from both the urban and the natural surfaces, along with their respective fractions of cover, f_{urb} and $f_{\mathrm{nat}} \equiv 1 - f_{\mathrm{urb}}$, are then used to define the total fluxes from a mesoscale model grid cell. The reflected shortwave radiation of the grid cell is given by

$$\mathcal{K}^{\uparrow} \equiv \alpha^{\downarrow}\mathcal{K}^{\downarrow} + \alpha^{\Downarrow}\mathcal{K}^{\Downarrow} = f_{\mathrm{urb}}K^{\uparrow}_{\mathrm{urb}} + f_{\mathrm{nat}}K^{\uparrow}_{\mathrm{nat}}\,. \tag{3.64}$$

Thus the grid cell albedos fulfil the relation

$$\alpha^{\downarrow} = f_{\mathrm{urb}}\alpha^{\downarrow}_{\mathrm{urb}} + f_{\mathrm{nat}}\alpha^{\downarrow}_{\mathrm{nat}}\,, \tag{3.65}$$

$$\alpha^{\Downarrow} = f_{\mathrm{urb}}\alpha^{\Downarrow}_{\mathrm{urb}} + f_{\mathrm{nat}}\alpha^{\Downarrow}_{\mathrm{nat}}\,. \tag{3.66}$$

Analogously, the grid cell reflected longwave radiation $\mathcal{L}^{\uparrow}$, the grid cell emissivity ϵ and the grid cell effective surface temperature $\mathcal{T}_{\mathrm{rad}}$ are defined by

$$\mathcal{L}^{\uparrow} \equiv (1 - \epsilon)\mathcal{L}^{\downarrow} + \epsilon\sigma\mathcal{T}^{4}_{\mathrm{rad}} = f_{\mathrm{urb}}L^{\uparrow}_{\mathrm{urb}} + f_{\mathrm{nat}}L^{\uparrow}_{\mathrm{nat}}\,. \tag{3.67}$$

Thus

$$\epsilon = f_{\text{urb}}\epsilon_{\text{urb}} + f_{\text{nat}}\epsilon_{\text{nat}}\,, \tag{3.68}$$

$$\mathcal{T}_{\text{rad}}^4 = \frac{1}{\epsilon}\left(f_{\text{urb}}\epsilon_{\text{urb}}T_{\text{urb}}^4 + f_{\text{nat}}\epsilon_{\text{nat}}T_{\text{nat}}^4\right). \tag{3.69}$$

The radiation that is emitted into the sky in the urban part of a grid cell is computed by means of an energy conservation equation. The fraction of the incoming shortwave or the incoming longwave and emitted longwave radiation, respectively, that is not absorbed by the urban surfaces is reflected back into the sky:

$$L_{\text{urb}}^{\uparrow} = \mathcal{L}^{\downarrow} + L_{\text{urb}}^{\text{emitt}} - L_{\text{urb}}^{\text{abs}}\,, \tag{3.70}$$

$$K_{\text{urb}}^{\uparrow} = \mathcal{K}^{\Downarrow} + \mathcal{K}^{\downarrow} - K_{\text{urb}}^{\text{abs}} \tag{3.71}$$

with $L_{\text{urb}}^{\text{emitt}}$ being the total emitted longwave and $L_{\text{urb}}^{\text{abs}}$ and $K_{\text{urb}}^{\text{abs}}$ the total absorbed longwave and shortwave radiation, respectively.

3.5.2. Interpolation of fields from mesoscale to urban height levels and grid cell averaged fluxes

Since DCEP operates on a grid different from the mesoscale model, the mesoscale atmospheric input parameters have to be interpolated to the usually finer urban grid whereas the urban fluxes computed by DCEP have to be aggregated to the mesoscale levels. To this end, the vertical overlap $\Delta z_{i,\mathcal{J}}$ of the urban layer i and the mesoscale layer $\mathcal{J}$ (cf. fig. 3.2 on page 35) is given by

$$\Delta z_{i,\mathcal{J}} = \max\left[\min(\mathcal{Z}_{\mathcal{J}+1/2}, z_{i+1/2}) - \max(\mathcal{Z}_{\mathcal{J}-1/2}, z_{i-1/2}), 0\right]. \tag{3.72}$$

Similarly, the overlap $\delta z_{i,\mathcal{J}}$ of the lower half of the urban layer i and the mesoscale layer $\mathcal{J}$ is calculated as

$$\delta z_{i,\mathcal{J}} = \max\left[\min(\mathcal{Z}_{\mathcal{J}+1/2}, z_i) \quad - \max(\mathcal{Z}_{\mathcal{J}-1/2}, z_{i-1/2}), 0\right], \tag{3.73}$$

which will be used in the formulation of the total urban TKE production.

Following the approach of BEP, an atmospheric field $\mathcal{X}$ is taken to be constant in the whole layer $\mathcal{J}$ of the mesoscale grid cell. Thus, the urban value x_i of the urban layer i is given by the averaged $\mathcal{X}_{\mathcal{J}}$ weighted with the overlap of layer $\mathcal{J}$ with layer i:

$$x_i = \frac{1}{\Delta z_i}\sum_{\mathcal{J}=1}^{\mathcal{N}} \Delta z_{i,\mathcal{J}}\mathcal{X}_{\mathcal{J}} \quad \text{with} \quad x = \boldsymbol{u}, T, \rho\,, \tag{3.74}$$

where $\mathcal{N}$ is indicates the highest mesoscale layer that has an overlap with an urban

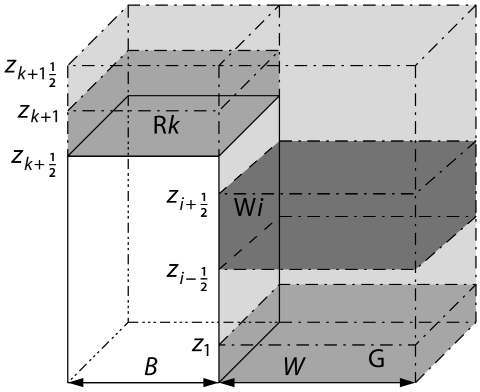

Figure 3.12. TKE production in the urban part of the grid cell. The shear and buoyant production due to fluxes from horizontal surfaces is considered in half of the urban grid cell above the respective surface (middle grey) instead of the traditional TKE production of the CCLM in section 2.2.2 (light grey). The shear production due to the fluxes from the wall surfaces (dark grey) is considered in addition to the traditional approach.

layer. The urban atmospheric values are used in the calculation of the fluxes from the urban surfaces in section 3.2.

To calculate the effect of these fluxes on the mesoscale mean fields, the fluxes have to be aggregated on the mesoscale grid. A flux from a *horizontal* urban surface is contained completely in the mesoscale layer $\mathcal{J}$ that includes that surface. This is expressed through the term $\tilde{\delta}_{i,\mathcal{J}}$ which indicates that the horizontal surface i is situated in the layer $\mathcal{J}$:

$$\tilde{\delta}_{i,\mathcal{J}} \equiv \begin{cases} 1 & \text{if } \mathcal{Z}_{\mathcal{J}-1/2} \leq z_{i+1/2} < \mathcal{Z}_{\mathcal{J}+1/2} \\ 0 & \text{otherwise} \end{cases} . \tag{3.75}$$

A flux from a *vertical* urban surface of layer i is attributes to the layer $\mathcal{J}$ according to the overlap of both layers expressed in $\Delta z_{i,\mathcal{J}}$. With that, the total momentum and sensible heat flux of the urban part in layer $\mathcal{J}$ from horizontal and vertical urban surfaces are given by

$$\boldsymbol{\tau}_{\mathcal{J}}^{\mathrm{urb}} = \frac{1}{B+W}\left(\sum_{i=0}^{n} \tilde{\delta}_{i,\mathcal{J}} \boldsymbol{\tau}_{\mathrm{R}i}^{\mathrm{h}} B \gamma_i + \tilde{\delta}_{0,\mathcal{J}} \boldsymbol{\tau}_{\mathrm{G}}^{\mathrm{h}} W + \sum_{i=1}^{n} \boldsymbol{\tau}_i^{\mathrm{v}} \Delta z_{i,\mathcal{J}} \Gamma_i\right), \tag{3.76}$$

$$H_{\mathcal{J}}^{\mathrm{urb}} = \frac{1}{B+W}\left(\sum_{i=0}^{n} \tilde{\delta}_{i,\mathcal{J}} H_{\mathrm{R}i}^{\mathrm{h}} B \gamma_i + \tilde{\delta}_{0,\mathcal{J}} H_{\mathrm{G}}^{\mathrm{h}} W + \sum_{i=1}^{n} (H_{\mathrm{W}i}^{\mathrm{v}} + H_{\mathrm{E}i}^{\mathrm{v}})\, \Delta z_{i,\mathcal{J}} \Gamma_i\right). \tag{3.77}$$

The resulting total tendencies of the model grid cell combining the fluxes from the urban and rural part are discussed after the TKE production in the following.

The TKE production is volumetric, thus it is multiplied with the respective volume and then divided by the air volume of the mesoscale grid cell. The air volume in layer $\mathcal{J}$

is reduced by the presence of the building, thus the fraction of air in the layer J,

$$V_J = 1 - \frac{B}{B+W}\frac{1}{\Delta Z_J}\sum_{i=1}^{n}\Delta z_{i,J}\Gamma_i\,, \tag{3.78}$$

is less than 1. Assuming that the TKE production due to the momentum and heat fluxes from roof and ground surfaces is described by (3.46) up to a height of half of the urban layer above the surface, and that the TKE production due to the walls fills the complete urban layer in the street canyon (cf. fig. 3.12), the total urban TKE production relative to the layer $J+1/2$ (defined between the heights Z_J and Z_{J+1}) is given by

$$P^{\mathrm{urb}}_{J+1/2} = \frac{1}{(B+W)\,\Delta Z_{J+1/2}V_{J+1/2}}\Bigg(B\sum_{i=0}^{n}P^{\mathrm{h}}_{\mathrm{R}i}\,\delta z_{i+1,J+1/2}\gamma_i + WP^{\mathrm{h}}_{\mathrm{G}}\,\delta z_{1,J+1/2} + W\sum_{i=1}^{n}P^{\mathrm{v}}_{i}\,\Delta z_{i,J+1/2}\Gamma_i\Bigg)\,. \tag{3.79}$$

In the air fraction of the urban part that is not covered by the TKE production from (3.79),

$$V^{\mathrm{trad}}_J = V_J - \frac{1}{B+W}\frac{1}{\Delta Z_J}\left(B\sum_{i=0}^{n}\delta z_{i+1,J}\gamma_i + W\,\delta z_{1,J}\right)\,, \tag{3.80}$$

the traditional production P^{trad} of the mesoscale model in (2.32) is used. Since CCLM does not consider the shear production due to vertical momentum fluxes, the TKE production in the third summand of (3.79) does not substitute the traditional TKE production. Thus the total TKE production of the grid cell is given by

$$\mathcal{D}^{e_t}_{J+1/2} = f_{\mathrm{nat}}P^{\mathrm{trad}}_{J+1/2} + f_{\mathrm{urb}}\frac{V^{\mathrm{trad}}_{J+1/2}}{V_{J+1/2}}P^{\mathrm{trad}}_{J+1/2} + f_{\mathrm{urb}}P^{\mathrm{urb}}_{J+1/2}\,. \tag{3.81}$$

Consequently, the traditional turbulent fluxes for momentum and temperature, $\boldsymbol{\tau}^{\mathrm{trad}}$ and H^{trad}, described in section 2.2.2 are considered in the rural part of the grid cell as well as in the V^{trad} fraction of the urban part. To calculate the total tendencies substituting the gradient of turbulent fluxes in the mesoscale prognostic equations (2.14) and (2.16), the fluxes are multiplied with the respective source area and divided by the volume of the mesoscale layer. Thus, the tendencies are given by

$$\boldsymbol{\mathcal{D}}^{\boldsymbol{u}}_J = \frac{f_{\mathrm{nat}}}{\Delta Z_J}\left(\boldsymbol{\tau}^{\mathrm{trad}}_{J-1/2} - \boldsymbol{\tau}^{\mathrm{trad}}_{J+1/2}\right) + \frac{f_{\mathrm{urb}}}{\Delta Z_J}\left(\frac{V^{\mathrm{trad}}_{J-1/2}}{V_{J-1/2}}\boldsymbol{\tau}^{\mathrm{trad}}_{J-1/2} - \frac{V^{\mathrm{trad}}_{J+1/2}}{V_{J+1/2}}\boldsymbol{\tau}^{\mathrm{trad}}_{J+1/2}\right) + \frac{f_{\mathrm{urb}}}{\Delta Z_J V_J}\boldsymbol{\tau}^{\mathrm{urb}}_J\,, \tag{3.82}$$

$$\mathcal{D}^{T}_{\mathcal{J}} = \frac{f_\text{nat}}{\Delta Z_{\mathcal{J}}}\left(H^\text{trad}_{\mathcal{J}-1/2} - H^\text{trad}_{\mathcal{J}+1/2}\right) + \frac{f_\text{urb}}{\Delta Z_{\mathcal{J}}}\left(\frac{V^\text{trad}_{\mathcal{J}-1/2}}{V_{\mathcal{J}-1/2}} H^\text{trad}_{\mathcal{J}-1/2} - \frac{V^\text{trad}_{\mathcal{J}+1/2}}{V_{\mathcal{J}+1/2}} H^\text{trad}_{\mathcal{J}+1/2}\right) + \frac{f_\text{urb}}{\Delta Z_{\mathcal{J}} V_{\mathcal{J}}} H^\text{urb}_{\mathcal{J}} . \tag{3.83}$$

Furthermore, it is informative to calculate the summed momentum, sensible heat and storage flux from all urban surfaces, $\boldsymbol{\tau}_\text{urb}$, H_urb and G_urb. They express the total effect of the urban part of the grid cell on the atmosphere and are given by

$$\boldsymbol{\tau}_\text{urb} = \frac{1}{B+W}\left(\sum_{i=0}^{n} \boldsymbol{\tau}^\text{h}_{\text{R}i} B\gamma_i + \boldsymbol{\tau}^\text{h}_\text{G} W + \sum_{i=1}^{n} \boldsymbol{\tau}^\text{v}_i \,\Delta z_i \varGamma_i\right) = \sum_{\mathcal{J}=1}^{\mathcal{N}} \boldsymbol{\tau}^\text{urb}_{\mathcal{J}} , \tag{3.84}$$

$$H_\text{urb} = \frac{1}{B+W}\left(\sum_{i=0}^{n} H^\text{h}_{\text{R}i} B\gamma_i + H^\text{h}_\text{G} W + \sum_{i=1}^{n} \left(H^\text{v}_{\text{W}i} + H^\text{v}_{\text{E}i}\right) \Delta z_i \varGamma_i\right) = \sum_{\mathcal{J}=1}^{\mathcal{N}} H^\text{urb}_{\mathcal{J}} , \tag{3.85}$$

$$G_\text{urb} = \frac{1}{B+W}\left(\sum_{i=0}^{n} G^\text{h}_{\text{R}i} B\gamma_i + G^\text{h}_\text{G} W + \sum_{i=1}^{n} \left(G^\text{v}_{\text{W}i} + G^\text{v}_{\text{E}i}\right) \Delta z_i \varGamma_i\right) . \tag{3.86}$$

Here, the urban storage fluxes $G^\text{h/v}_{\mu}$ are calculated with (3.56). The diagnostic grid cell average momentum, sensible heat and storage flux at the surface are then given by

$$\boldsymbol{\tau} = f_\text{nat} \boldsymbol{\tau}^\text{trad}_{1/2} + f_\text{urb} \boldsymbol{\tau}_\text{urb} , \tag{3.87}$$

$$\mathcal{H} = f_\text{nat} H^\text{trad}_{1/2} + f_\text{urb} H_\text{urb} , \tag{3.88}$$

$$\mathcal{G} = f_\text{nat} G_\text{nat} + f_\text{urb} G_\text{urb} . \tag{3.89}$$

Since water processes are neglected in DCEP, the grid cell average latent heat flux at the surface, $\lambda\mathcal{E}$, is given by the reduced rural latent heat flux $\lambda E^\text{nat}_{1/2}$ at the surface:

$$\lambda\mathcal{E} = f_\text{nat} \lambda E^\text{nat}_{1/2} . \tag{3.90}$$

As described in section 2.2.3, the 2 m temperature is diagnosed from the air temperature of the lowest mesoscale model layer and the surface temperature. While the air temperature $\mathcal{T}_1$ of the mesoscale model represents the average of both the rural and the urban part of the grid cell, the rural surface temperature T_S is calculated independently from the urban ground temperature T_G. Thus, the grid cell average 2 m temperature is estimated by

$$\mathcal{T}_{2\,\text{m}} = \left(f_\text{nat} T_S + f_\text{urb} T_\text{G}\right) + \frac{r^\text{h}_{\text{S}\to 0} + r^\text{h}_{0\to 2\,\text{m}}}{r^\text{h}_{\text{S}\to 1}} \left[\mathcal{T}_1 - \left(f_\text{nat} T_S + f_\text{urb} T_\text{G}\right)\right] . \tag{3.91}$$

Here, the atmospheric resistances of CCLM representing a typical synoptic station are not modified.

3.5.3. Flow chart and computational requirements

The online coupling of DCEP with CCLM is illustrated in the flow chart of fig. 3.13. All CCLM routines involved are listed by means of the relevant calculated variables, and the relationships to the routines of DCEP are indicated. The figure is subdivided into the routines of the initialization step and of an arbitrary time step t; the following time step $t+1$ is also shown and resembles the time step t. It indicates which results of time step t are used in step $t+1$.

The conceptual computational complexity of DCEP resembles the one of the original BEP. The main difference lies in the radiation part. Here, both schemes calculate the longwave and shortwave radiation budget of a street canyon: While each respective linear system of equations of DCEP includes $3n+2$ unknowns ($2n$ east and west wall elements, $n+1$ roof elements, 1 ground element), BEP's system does not include the roof surfaces and has, therefore, only $2n+1$ unknowns. This difference would, in principle, result in a rather small increase of computational time for DCEP because the matrix of coefficients of both systems is constant and needs to be inverted only once (cf. section 3.1). However, the implementation of BEP used as starting point of this work does not exploit this possibility. In this study, the inversion is not repeated and also due to further performance-oriented programming, the author's implementation of DCEP is expected to run faster than the current available one of BEP under the same circumstances.

The amount of additional run-time needed by CCLM/DCEP as compared to the bulk CCLM depends on the particular set-up of CCLM. For example, simulations on the finest grid described in section 5.3 take about 6 % to 10 % longer with DCEP than with the bulk scheme in the area of Berlin. On a system with multiple CPUs (central processing units), the additional time consumption currently does not directly depend on the *total* number of urban grid cells in the domain but on the *largest* number of urban grid cells calculated by a single CPU (cf. section 6.1).

Furthermore, DCEP increases the memory requirements. In the following, it is assumed that 50 mesoscale vertical layers, 10 urban vertical layers and 10 layers in each urban surface as well as 8 B double-precision floating-point numbers are used in the calculations. Then, the double-canyon approach needs about 19 KiB of additional memory[‡] per grid cell and street direction while the single-canyon approach needs about 6 KiB per grid cell and street direction. The increase of storage space is due to the additional view factors (see appendices B.2.2 and B.2.3). If the inverted radiation matrices are stored as discussed previously, the above requirements increase to about 35 KiB and 13 KiB, respectively. In all cases, an additional 4 KiB per grid cell are required for the coupling of the urban scheme with CCLM. Assuming a domain size of 150 × 150 grid cells and 4 street directions, this means total additional memory requirements of up to 3 GiB, which is divided among the computational nodes.

[‡] 1 KiB = 1024 B, 1 GiB = 1024^3 B

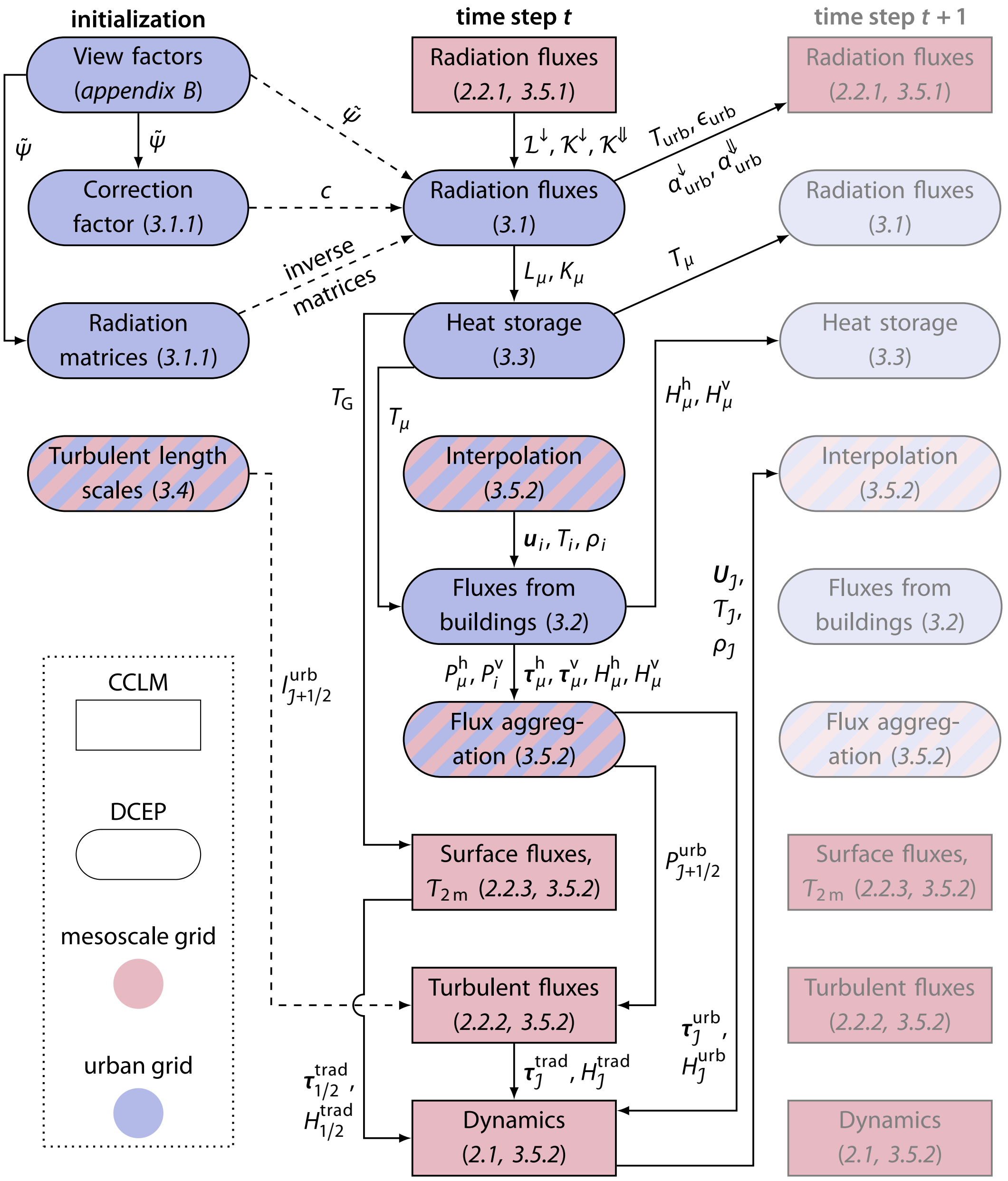

Figure 3.13. Flow chart of the online coupling of DCEP with CCLM. The necessary routines of CCLM (listed by the relevant variables) are given in rectangles, DCEP's urban routines are shown with rounded edges. Light red indicates operation on the mesoscale grid, light blue on the urban grid; striped routines connect both grids. The variables on the arrows denote which results are used in later routines. The routines are explained in the given sections. The first column of the figure lists the calculation of urban run-time constants, the second column gives the routines of a model time step and the third column indicates which results are used in the following time step. Depending on the set-up, CCLM's radiation fluxes are not calculated in every time step, thus $\mathcal{L}^{\downarrow}$, $\mathcal{K}^{\downarrow}$ and $\mathcal{K}^{\Downarrow}$ are kept constant.

3.6. Sensitivity analysis of the modifications in the radiation scheme in DCEP

3.6.1. Influence of the urban morphology on the distributed diffuse energy

It is informative to investigate for which canyon geometries the distributed to the incoming radiative energy deviates most in the original BEP scheme and subsequently the closure of the energy balance in DCEP is particularly important. Of interest is also for which building height distributions the total radiative energy from the sky received by the roof surfaces is minimized. Since roofs always receive the full sky radiation in the original BEP, the largest differences between BEP and DCEP simulations of urban surface temperatures are expected for those building height distributions.

In the original BEP scheme, the total energy of diffuse radiation $S^{\downarrow}_{\text{tot}}(\mathcal{R})$ that is distributed inside the street canyon depends on the height distribution and is given by

$$S^{\downarrow}_{\text{tot}}(\mathcal{R}) \equiv \sum_i [S^{\downarrow}_{\text{W}i}(\mathcal{R}) D\, \Delta z_i \Gamma_i + S^{\downarrow}_{\text{E}i}(\mathcal{R}) D\, \Delta z_i \Gamma_i] + S^{\downarrow}_{\text{G}}(\mathcal{R}) D W\,. \tag{3.92}$$

The ratio of the distributed to the incoming radiative energy, η, is a measure of the violation of energy conservation and is given with (3.14) and (3.15) by

$$\eta \equiv \frac{S^{\downarrow}_{\text{tot}}(\mathcal{R})}{\mathcal{R} D W} = \sum_{i,j} \gamma_j M_{ji} \gamma_i + \sum_i \gamma_i \nu_i\,. \tag{3.93}$$

where the coefficients M_{ij} and ν_i depend only on Δz_i, W, B and D. Thus, η is independent of the incoming radiation $\mathcal{R}$ and only a function of γ_i for fixed values Δz_i, W, B and D. The correction factor c is defined to yield $\eta = 1$.

In the following, urban height levels are assumed every 5 m starting at 0 m up to 50 m and $D \approx 2$ km. Using a null-space active-set quadratic programming solver (Eaton et al. 2008), η in (3.93) is maximized with the constraints $0 \leq \gamma_i \leq 1$ and $\sum_i \gamma_i = 1$. This results in a canyon geometry in which, for 50 % of the buildings, the roofs are on the lowest model level, while the roofs of the other 50 % of the buildings are on the highest level. This building height distribution is called $\gamma^{\max}$ in the following (tab. 3.1) and is used, although unrealistic, to estimate the maximum effect of the closure of the energy balance for a building height distribution with a maximum height of 50 m. Since there have to be buildings on at least two different urban height levels to violate the energy conservation in the original BEP scheme, $\gamma^{\max}$ is also one of the simplest height configurations that exhibit this issue. The asymptotic behaviour of η for $\gamma^{\max}$ and small street widths, which does not incorporate the calculation of view factors, is explained below.

The dependence of η and c on the street width W is depicted in fig. 3.14a for $\gamma^{\max}$ and two other building height distributions, $\gamma^{\min}$ and γ^{mid}, respectively. The

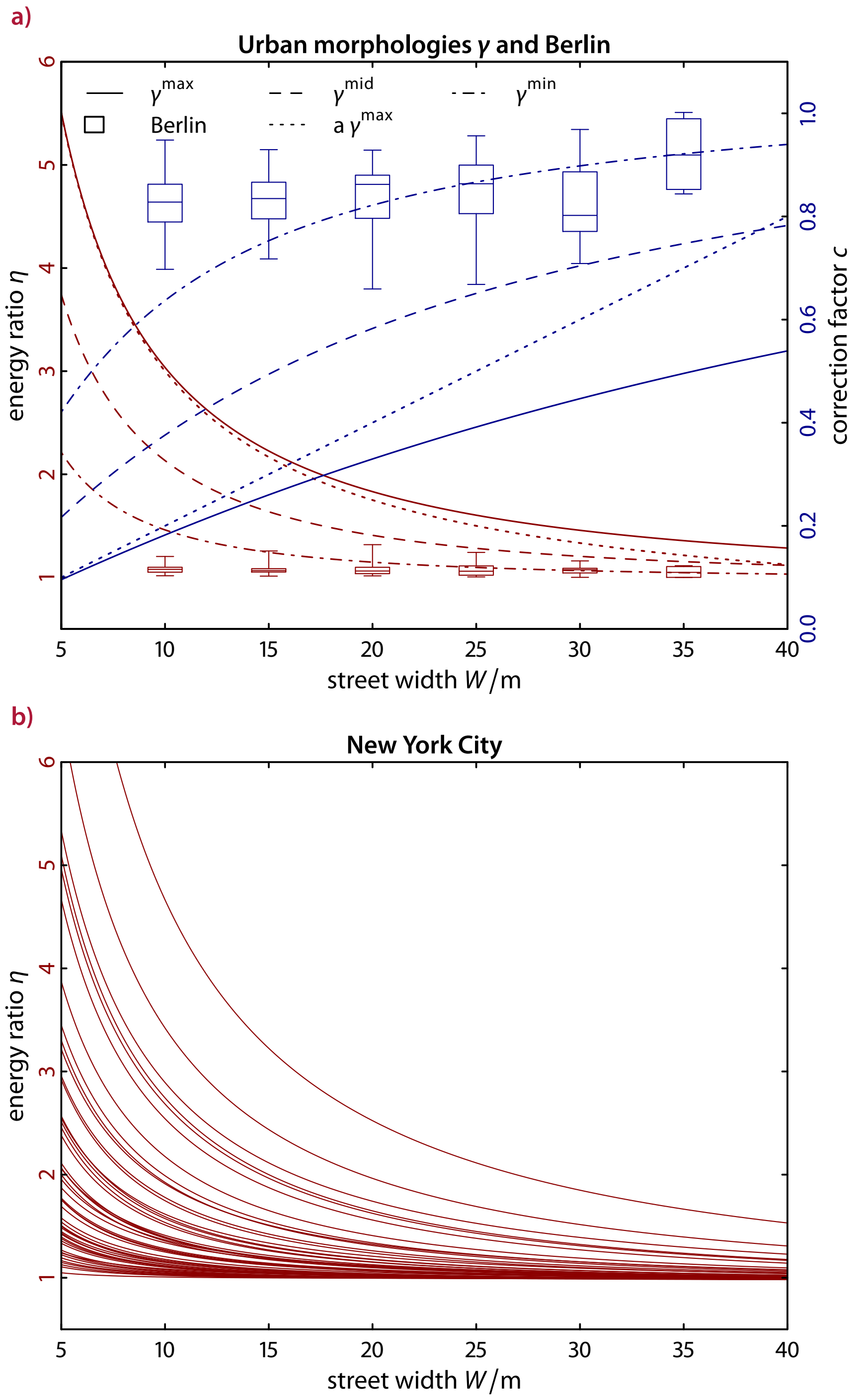

Figure 3.14. Energy ratio η and correction factor c dependence on the street width W. In a), the curves are calculated for the different urban morphologies in tab. 3.1. The boxes are based on data of the city of Berlin. The asymptotic behaviour of η and c for γ^{max} is depicted by curves labelled "a γ^{max}". In b), η is shown for 50 grid cells of New York City with a size of 1 km × 1 km.

distribution γ^{min} is more realistic than γ^{max}, and corresponds to a sample height distribution in the centre of Berlin (Germany) and is characterized by the majority of buildings having heights between 15 m and 20 m, i.e. a relatively low spread in roof heights (cf. section 5.1). The building height distribution γ^{mid} is chosen to lie between γ^{min} and γ^{max} and is characterized by a larger spreading of heights yet not as extreme as for γ^{max} (tab. 3.1).

As was expected from the optimization procedure, η values are largest for γ^{max} and relatively smaller for γ^{mid} and γ^{min} (fig. 3.14a). For all three building height distributions, the ratio η increases with decreasing road widths, especially for road widths below 10 m. The incoming radiative energy for the street canyon given by the mesoscale model, $\mathcal{R}DW$, obviously decreases with decreasing W whereas the horizontal area where no wall is present stays constant. The energy from the side area that is radiated into the sky at the top of the canyon decreases with decreasing W. The remainder, which is partly received by the ground and wall elements and partly by the area where no wall is present, is thus increasing at every wall element. Therefore, η increases for decreasing W.

For γ^{max}, small W and a large maximum building height $H \equiv z_{n+1/2}$, the energy received by the ground surface and radiated into the sky can be neglected. With $\gamma_0^{\mathrm{max}} = 0.5$ and $\gamma_n^{\mathrm{max}} = 0.5$, walls are present in 50 % of the cases. Therefore, 50 % of the radiation from the sky and 50 % of the radiation from the side area with no wall present are received by the present walls. The radiation from the side is present in 50 % of the cases at the west and east walls, respectively. In summary, the energy ratio and correction factor for γ^{max} and $W \ll H$ are given by

$$\eta_{\mathrm{asymp}}^{\mathrm{max}}(W) = \frac{\frac{1}{2}\mathcal{R}DW + 2\frac{1}{2}\frac{1}{2}\mathcal{R}Dh}{\mathcal{R}DW} = \frac{1}{2} + \frac{1}{2}\frac{H}{W} \tag{3.94}$$

and

$$c_{\mathrm{asymp}}^{\mathrm{max}}(W) = W/H\,. \tag{3.95}$$

Both functions are plotted in fig. 3.14a and describe the behaviour of η and c for small W well. For a street width of 5 m, this gives $\eta(5\,\mathrm{m}) \approx 5.5$. In general, this means that depending on the street canyon geometry, more than five times the incoming energy from diffuse radiation can potentially be distributed inside the street canyon. The values for η are much smaller in the case of γ^{min}, nonetheless clearly larger than 1 for small W. For buildings of equal height, η would equal 1, independent of the road width (not shown). The distribution γ^{mid} results in η values between those for γ^{min} and γ^{max}.

As a realistic example, fig. 3.14a also shows the distribution of η and c for different street widths based on an extensive data set for the city of Berlin (cf. section 5.1).

Height z/m	γ^{min}	γ^{mid}	γ^{max}	γ^{minroof}
0	0.01	0.01	0.50	0.61
5	0.07	0.17	0.00	0.00
10	0.05	0.05	0.00	0.00
15	0.35	0.25	0.00	0.00
20	0.37	0.17	0.00	0.00
25	0.03	0.03	0.00	0.00
30	0.03	0.03	0.00	0.00
35	0.04	0.04	0.00	0.00
40	0.01	0.01	0.00	0.00
45	0.00	0.10	0.00	0.00
50	0.04	0.14	0.50	0.39

Table 3.1. Height distributions used to assess the influence of the correction factor c for energy conservation

The street widths as determined for all 128 model grid cells with an urban fraction $f_{\text{urb}} > 0$ (see section 3.6.2 for the grid specification of the mesoscale model) have been combined into bins of size 5 m. The top and bottom of the boxes at the centre of the bins are defined by the 25th and 75th percentile, with the whiskers bounded by the 2.5th and 97.5th percentile. Due to the relatively even building height distribution, for the majority of model grid cells, η is close to 1, with c between 0.8 and 0.9 (fig. 3.14a). A much larger spread of building heights is to be found in New York City (USA), which is included in the National Building Statistics Database (Burian et al. 2008). In this data set, the building height distribution of New York City is given on a 1 km × 1 km grid; the average street width is not included, though. Thus, fig. 3.14b shows the energy ratio of 50 grid cells with a building (plan area) fraction larger 0.35 calculated from their respective building height distribution for street widths of 5 m to 40 m. Six grid cells feature η values larger than those of γ^{mid}, two grid cells have η values even larger than those of γ^{max} with a maximum building height of 185 m and 212 m, respectively. Cities with such high buildings are beyond the scope of this study.

Furthermore, it is interesting for which height configuration the extension to a double canyon is most relevant. Using the average longwave and shortwave radiation for Berlin during the first week in August 2003 as input (see next subsection for details on the simulations), the received sky radiation on the roofs is minimized with fixed $B = 10$ m and $W = 20$ m. This minimization using a successive quadratic programming solver leads to the building height distribution γ^{minroof} in tab. 3.1. Since γ^{minroof} is very similar to γ^{max}, strong differences in the urban quantities are expected when comparing simulations with the one-canyon and the two-canyon approaches both with γ^{max}. Therefore, γ^{minroof} is not considered in the following.

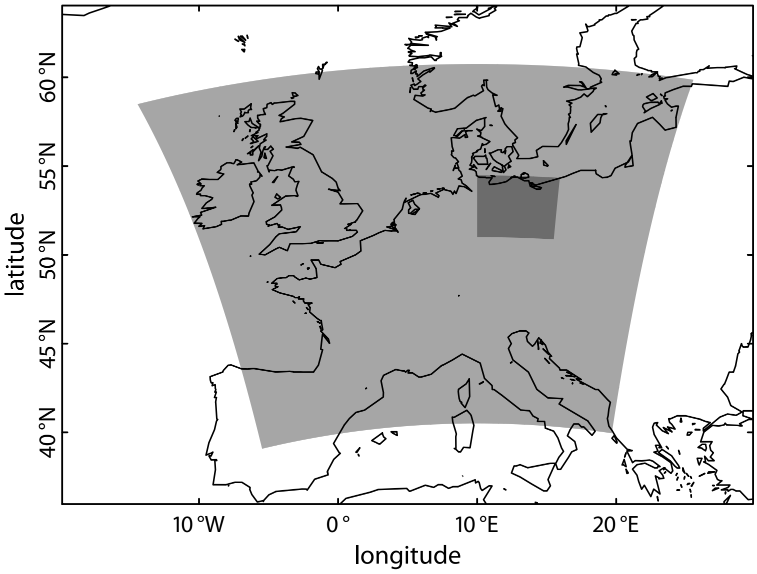

Figure 3.15. Nested domains for the analysis of the changes introduced in DCEP. For the large domain, a resolution of 7 km and for the smaller domain a resolution of 2.8 km is used.

3.6.2. Set-up of simulations

For the sensitivity analysis, CCLM simulations are conducted in order to investigate the effect of the changes introduced into the radiative part of the BEP scheme described section 3.1 on surfaces radiative properties such as albedo, emissivity and surface temperature as well as surface fluxes and air temperatures. CCLM version 4.8_clm11 is used for one way nested grids with a horizontal resolutions of approx. 7 km (without urban schemes) and 2.8 km (with urban schemes) for 1 August 2003 0000 UTC through 7 August 2003 0000 UTC (fig. 3.15). This period is characterized by predominantly clear sky and light wind conditions. The coarse resolution simulation covers Central Europe, Great Britain and Ireland, northern Spain and Italy, and southern Norway and Sweden. The simulation with the fine resolution is centred around Berlin with a domain size of approx. 550 km × 550 km. Initial and three-hourly boundary conditions are provided by output from the GME model of DWD and the orography, vegetation and soil parameters are provided by the preprocessor of CCLM (Smiatek et al. 2008). The nested finer resolution simulation uses 50 vertical levels with the lowest levels at approx. 10 m, 35 m, 73 m and 122 m above the ground. Details of the physics of CCLM are given in chapter 2.

In order to analyse the influence of the correction factor c in the BEP scheme, simulation results with c are compared to simulations with the original, uncorrected formulation. The correction factor c ensures energy conservation of the incoming diffuse radiation (as described in section 3.1.1) and is thus necessary for a correct formulation of the radiation scheme. Furthermore, the extension of BEP's single-canyon approach to the double-canyon approach introduced in the corresponding subsections of 3.1.1 and 3.1.2 is examined. Thus, simulations with the following three model settings are conducted:

1. without the correction factor (i.e. $c = 1$) using the original formulation of the radiation exchange in the BEP scheme but differentiated between diffuse and direct shortwave radiation; this setting is named "BEP" in the following,

2. utilizing (3.13) to calculate c and thus ensuring energy conservation; original formulation of radiation exchange for roofs; this setting is named "corr",

3. utilizing (3.22) to calculate c and thus ensuring energy conservation; modified formulation of radiation exchange between two neighbouring canyons to allow the interaction of roofs with the canyons; this setting is named "DCEP".

For each of the CCLM model settings, simulations are conducted with the three height distributions γ^{min}, γ^{mid}, γ^{max} and a fixed street width of $W = 20\,\mathrm{m}$ and a building width $B = 10\,\mathrm{m}$. Four different street canyon orientations are assumed in every grid cell: $\chi = -45°, 0°, 45°, 90°$. The canyon length is assumed to be as large as the average length in a grid cell at the angle of the canyon (cf. section 5.1), resulting in canyon lengths of about 2.8 km and 2 km, respectively. For this sensitivity study, the urban fraction $f_{\mathrm{urb}} = 1$ is used in the 128 urban grid cells in the territory of Berlin. Following the proposition of Martilli et al. (2002), the urban surface parameters are set to $\alpha_{\mathrm{R}} = \alpha_{\mathrm{W}} = \alpha_{\mathrm{G}} = 0.2$, $\epsilon_{\mathrm{R}} = \epsilon_{\mathrm{W}} = 0.90$, $\epsilon_{\mathrm{G}} = 0.95$ and a thermal diffusivity of $k_{\mathrm{R}} = K_{\mathrm{W}} = 0.67 \times 10^{-6}\,\mathrm{m}^2\,\mathrm{s}^{-1}$, $k_{\mathrm{G}} = 0.29 \times 10^{-6}\,\mathrm{m}^2\,\mathrm{s}^{-1}$ is used. For the volumetric specific heat an increased value of $c_{\mathrm{R}} = c_{\mathrm{W}} = c_{\mathrm{G}} = 2.3 \times 10^6\,\mathrm{J\,m^{-3}\,K^{-1}}$ is assumed.

3.6.3. Results and discussion

In this subsection, results from one grid cell at the centre of the modelled urban area are discussed. All urban grid cells share the same urban properties so this cell, being at the centre, represents the strongest influence of the modifications. In order to be comparable with the radiative temperature, all other temperature values are given in kelvin. (Later chapters use degree Celsius when comparing measured air temperatures with simulations.)

Roof surface temperatures averaged for specific hours of the day over the simulation period ($\bar{T}_{\mathrm{R}}$) are similar during the night and in the morning for the "BEP" and "corr" runs (fig. 3.16). In the afternoon, however, the "corr" run shows a higher $\bar{T}_{\mathrm{R}}$, particularly for the γ^{max} distribution (approx. 2 K). This is caused by the corrected effective albedo for diffuse radiation (see below and tab. 3.2). In both runs, $\bar{T}_{\mathrm{R}}$ shows only a small height dependence (fig. 3.16) due to the fact that the roof radiation budget

a) Simulations with the urban height distribution $\gamma^{\max}$

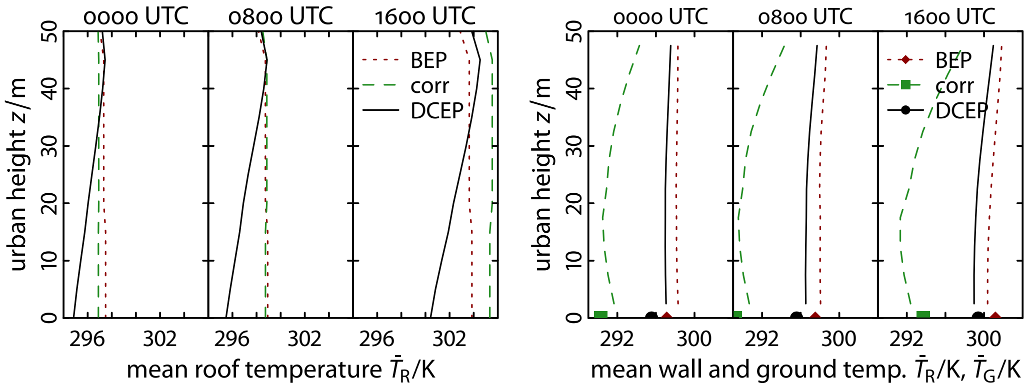

b) Simulations with the urban height distribution γ^{mid}

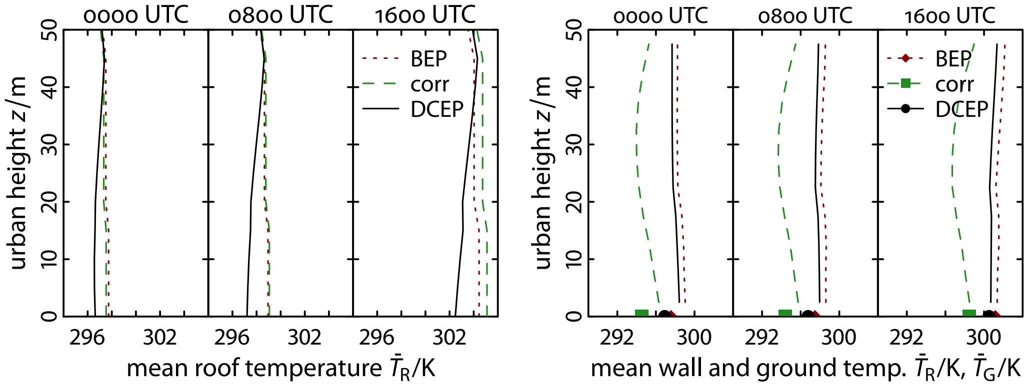

c) Simulations with the urban height distribution $\gamma^{\min}$

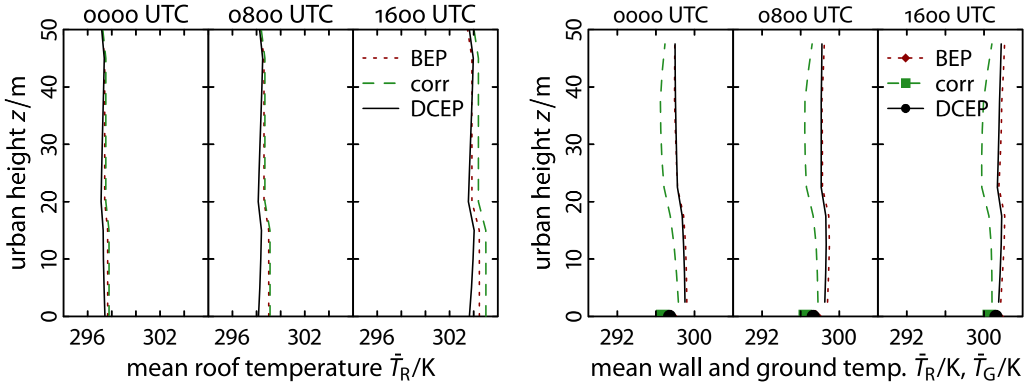

Figure 3.16. Simulated roof temperatures on the left-hand side, wall and ground temperatures on the right-hand side (ground temperatures are marked by symbols at $z = 0$ m) averaged at 0000 UTC, 0800 UTC and 1600 UTC over the simulation period. Note the different temperature range for the left-hand and right-hand plots.

	γ^{min}	γ^{mid}	γ^{max}
BEP	0.04	-0.11	-0.34
corr	0.13	0.14	0.15
DCEP	0.12	0.12	0.12

Table 3.2. Effective urban albedo for diffuse radiation for different building height distributions and different ways to distribute the radiation energy inside the canyon. The original BEP scheme produces negative values because of the overestimation of the diffuse radiation distributed in the street canyon.

is independent of the roof height in these BEP versions (sections 3.1.1 and 3.1.2). The small $\bar{T}_{\text{R}}$ differences are caused by differences in the sensible heat fluxes, which in turn are due to vertically different atmospheric conditions in the lowest CCLM model grid cells. In the "DCEP" run, roofs receive less radiation especially at lower levels. During daytime, this results in lower $\bar{T}_{\text{R}}$ of approx. 4 K, 2 K and 1 K for the γ^{max}, γ^{mid} and γ^{min} distributions, respectively. At night the magnitude of the $\bar{T}_{\text{R}}$ differences between the "corr" and the "DCEP" run is about half the above values (fig. 3.16).

Average wall and ground surface temperatures, $\bar{T}_{\text{wall}} \equiv 1/2(\bar{T}_{\text{W}} + \bar{T}_{\text{E}})$ and $\bar{T}_{\text{G}}$, are notably lower in the "corr" runs than in the "BEP" runs (fig. 3.16) for all γ distributions and times of day. Maximum $\bar{T}_{\text{wall}}$ differences of approx. 8 K are detected for γ^{max} at a height of 17.5 m. Differences in $\bar{T}_{\text{G}}$ have similar magnitudes. In the "BEP" runs, the total incoming diffuse radiation on walls and the ground is overestimated (section 3.1.1). In the "corr" runs, the energy balance is closed and, therefore, the incoming diffuse radiation on these surfaces is reduced, resulting in lower surface temperatures. In the "DCEP" run, less sky radiation is received by roof surfaces and consequently more radiation by ground and wall surfaces. Consequently, $\bar{T}_{\text{wall}}$ and $\bar{T}_{\text{G}}$ are larger in that run compared to "corr".

The albedo $\alpha^{\downarrow}_{\text{urb}}$ for diffuse radiation is a run-time constant and is shown in tab. 3.2. The original formulation results in negative values for the runs with γ^{mid} and γ^{max}; these unphysical values can be explained by the overestimation of the total distributed radiation inside the urban canyon. For the calculation of $\alpha^{\downarrow}_{\text{urb}}$, the *direct* shortwave radiation $\mathcal{K}^{\Downarrow}$ is neglected in (3.71) and the shortwave *diffuse* radiation $\mathcal{K}^{\downarrow}$ is given by the mesoscale model. However, the total absorbed energy $K^{\text{abs}}_{\text{urb}}$ is calculated using an overestimated incoming radiation (cf. section 3.1.1). This leads to a lower and eventually even negative reflected radiation $K^{\uparrow}_{\text{urb}}$ for increasing energy ratios η. Dividing $K^{\uparrow}_{\text{urb}}$ by $\mathcal{K}^{\downarrow}$ gives the albedo for diffuse radiation, which, therefore, can also be negative. The introduction of the correction factor c solves that issue by correcting the total received radiation inside the canyon and therefore also $K^{\text{abs}}_{\text{urb}}$. When combining two canyons in the canyon model, less radiation is received by the roofs and therefore more radiation by the street and wall surface elements. Furthermore, due to the inter-

a) Simulations with the urban height distribution γ^{max}

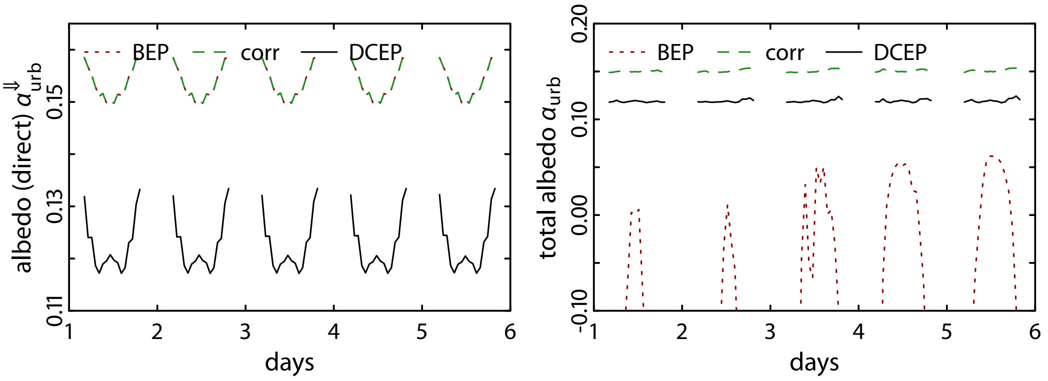

b) Simulations with the urban height distribution γ^{mid}

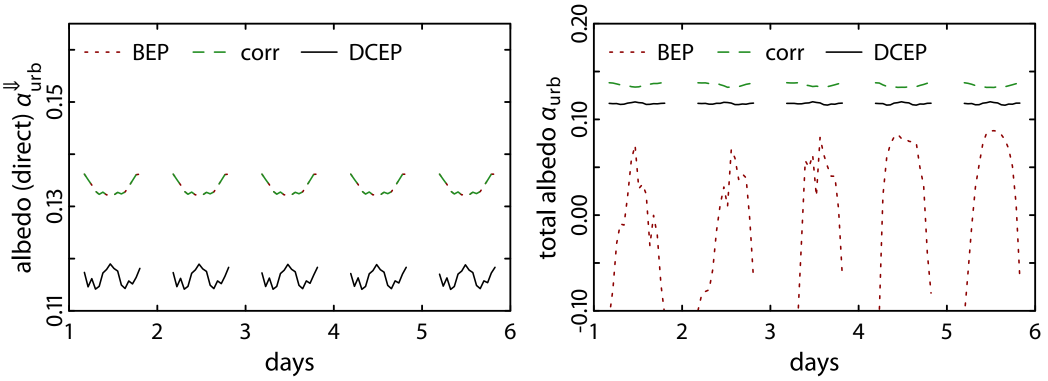

c) Simulations with the urban height distribution γ^{min}

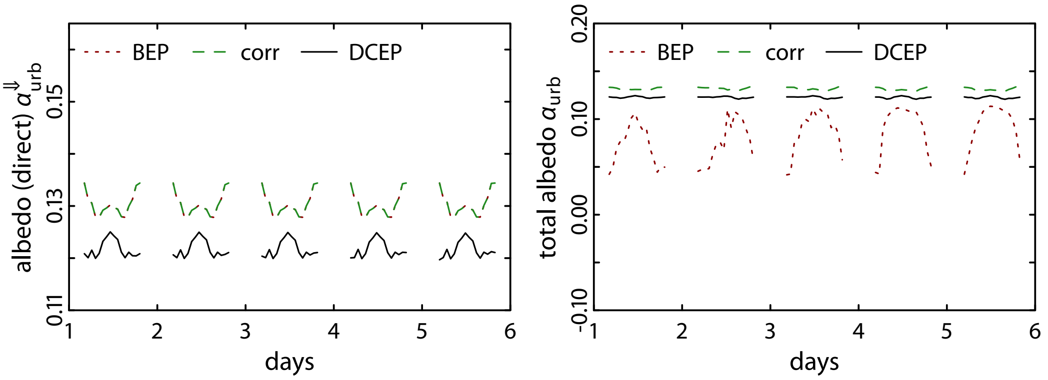

Figure 3.17. Simulated effective urban albedo for direct solar radiation, $\alpha_{\mathrm{urb}}^{\Downarrow}$, and the total effective albedo for complete incoming shortwave radiation, α_{urb}. Since these parameters are defined by the ratio of reflected to incoming radiation, they can only be calculated for hours with non-vanishing insolation. The value of $\alpha_{\mathrm{urb}}^{\Downarrow}$ is the same for the "BEP" and the "corr" run.

action of the roofs with the elements inside the canyon, less radiation is reflected into the sky. Thus, this results in a lower albedo in the "DCEP" run in comparison with the "corr" runs (tab. 3.2). The difference of $\alpha_{\mathrm{urb}}^{\downarrow}$ for the three height distributions in the "DCEP" runs is less than 0.01, thus $\alpha_{\mathrm{urb}}^{\downarrow}$ is less sensitive to the height distribution in this case than in the other runs. Since there is no difference in the treatment of direct solar radiation in the "BEP" and in the "corr" runs, the albedos for direct shortwave radiation, $\alpha_{\mathrm{urb}}^{\Downarrow}$, are equal in both runs for the three γ distributions (fig. 3.17). Because of the same reasons mentioned above, $\alpha_{\mathrm{urb}}^{\Downarrow}$ is lower in the "DCEP" run. In addition, fig. 3.17 shows also the resulting total urban albedo α_{urb} over the course of the simulation period. Since the solar radiation was assumed to be completely direct in previous regional atmospheric modelling studies using the original BEP scheme (Martilli et al. 2003; Hamdi and Schayes 2007; Grimmond et al. 2010; Salamanca et al. 2010; Salamanca and Martilli 2010), no negative values of the urban albedo have been observed so far.

The behaviour of the effective radiative temperature T_{urb} is similar to that of the diffuse albedo. The values of the corrected runs are higher compared to the "BEP" runs because the absorbed radiation in (3.70) is not overestimated in the "corr" runs. The radiation trapping effect is increased in the "DCEP" configuration resulting in lower radiative temperatures.

The urban influence on the simulated air temperature consists to a large part of the sensible heat fluxes from the surrounding street, wall and roof surfaces in a particular mesoscale model layer. Therefore, the air temperature differences between the three model runs result from differences in the radiation balance of roof, wall and road surfaces and subsequent sensible heat differences. Since the wall surface temperature differences are larger than that of the roofs (cf. fig. 3.16), their influence dominates. The introduction of the correction factor in the "corr" runs reduces the air temperature T_1 of the lowest CCLM level at approximately 10 m (fig. 3.18). The strongest differences between "corr" and "DCEP"/"BEP" runs occur at night for γ^{max} (up to 4 K). Differences in T_1 of approx. 2 K are simulated during daytime. As expected, the T_1 differences are larger for configurations with a larger energy ratio η, i.e. γ^{max} and γ^{mid}. In the "DCEP" run, a higher amount of radiation is received inside the canyon and, due to the inclusion of roofs into the radiation exchange, more energy is retained inside the urban canopy. In short, the radiation trapping effect is increased by this modification, which leads to a higher air temperature near the ground (fig. 3.18). The effective radiative temperature T_{urb}, however, is lower in the "DCEP" runs than in the "corr" runs (fig. 3.18). T_{urb} is obtained from (3.62) by means of the total incoming longwave radiation from the sky and the outgoing longwave radiation, and so T_{urb} is not a direct measure for the surface temperatures inside the canyon. Note that T_{urb} together with $\alpha_{\mathrm{urb}}^{\downarrow}$ and $\alpha_{\mathrm{urb}}^{\Downarrow}$ is used by the mesoscale model's radiation scheme to determine the outgoing longwave and shortwave radiation of the urban surface, respectively.

a) Simulations with the urban height distribution γ^{max}

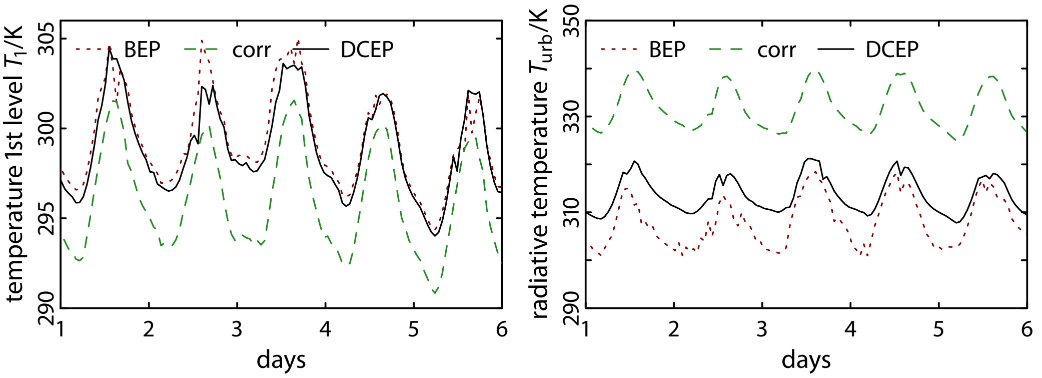

b) Simulations with the urban height distribution γ^{mid}

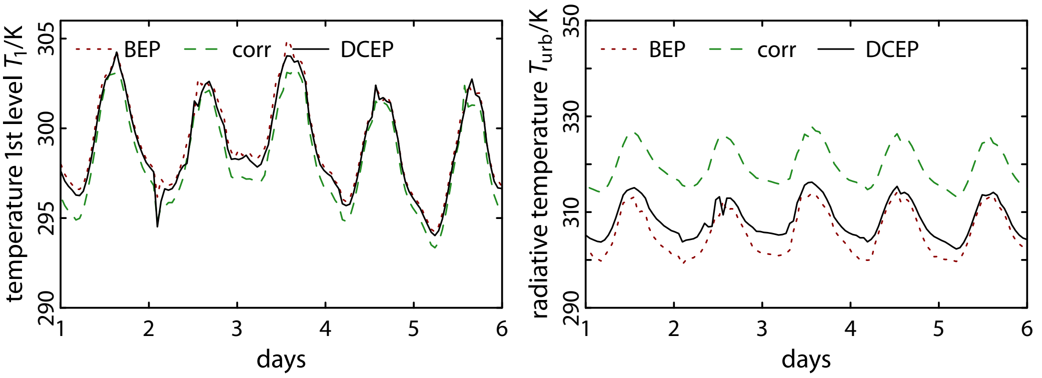

c) Simulations with the urban height distribution γ^{min}

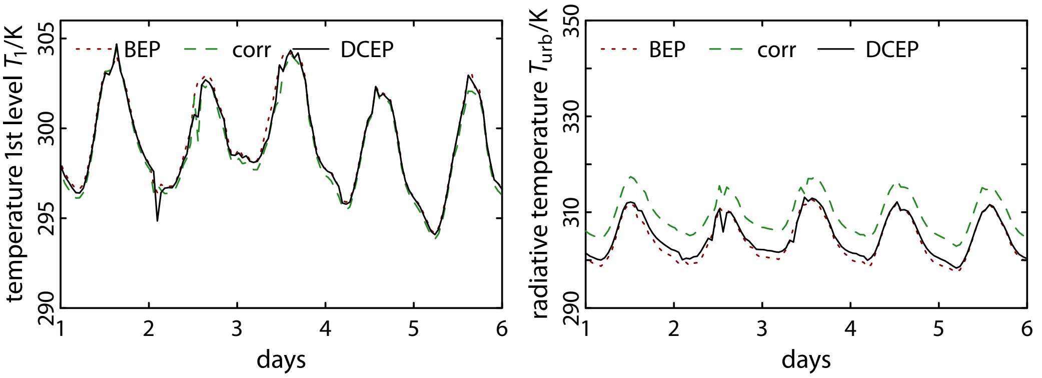

Figure 3.18. Simulated air temperature T_1 at the lowest CCLM level (approx. 10 m) and the effective urban radiative temperature T_{urb} for different fixed height distributions

Maximum differences in T_{urb} between the "corr" and "DCEP"/"BEP" runs amount to approx. 25 K, 15 K and 10 K for γ^{max}, γ^{mid} and γ^{min}, respectively.

The total sensible heat flux H_{urb} for the urban surfaces is positive during daytime, i.e. the urban surface warms the air, and negative during nighttime (fig. 3.19). Due to lower wall surface temperatures, the total sensible heat flux is higher in the "corr" run than in the other runs. The storage flux G_{urb} is approximately equal for all runs.

3.7. Summary and conclusion

This chapter described the urban Double-Canyon Effect Parametrization scheme (DCEP), which is based on the Building Effect Parametrization scheme (BEP) by Martilli et al. (2002). The new scheme adopts BEP's basic canyon element for non-radiative processes: This canyon element consists of two rows of buildings, and is characterized by its street and building width while the canyon length is assumed to be much larger than the former.

In DCEP, the building induced fluxes and the turbulent length scales modified by the presence of the building are formulated similarly to the ones in BEP. Also the storage of heat in the urban surfaces is implemented in DCEP according to Martilli et al. (2002) but with a modified inner boundary condition: instead of defining a constant inner (building) temperature over the complete duration of the simulation, the exchange of energy with the interior is set to zero. This ensures energy conservation and decouples the storage of heat in the urban surfaces from anthropogenic heating or cooling.

The main differences of BEP and DCEP, residing in the radiation scheme, were analysed in a sensitivity study with the different version of the urban scheme coupled to CCLM as described in detail in this chapter. The following three modifications were introduced into the radiation scheme:

1. Differentiation between diffuse and direct shortwave radiation from the sky by treating diffuse shortwave radiation like the longwave radiation. In contrast, in the original BEP scheme it is assumed that all incoming shortwave radiation from the sky is direct radiation. These model changes allow to calculate urban albedos for diffuse and direct radiation, $\alpha^{\downarrow}_{\mathrm{urb}}$ and $\alpha^{\Downarrow}_{\mathrm{urb}}$, respectively. This model version simulates air temperatures inside the canyon on the lowest model level T_1 similar to those obtained with the BEP version of Martilli et al. (2002), especially during nighttime. This can be expected since the magnitude of the diffuse shortwave radiation is always considerably smaller than the amount of the thermal radiation and it is zero at night. However, these changes result in negative values of $\alpha^{\downarrow}_{\mathrm{urb}}$ for building height configurations with a larger variation in roof heights. The unphysical values of $\alpha^{\downarrow}_{\mathrm{urb}}$ are due to an overestimation of the incoming diffuse shortwave and longwave radiation from the sky in the

a) Simulations with the urban height distribution γ^{max}

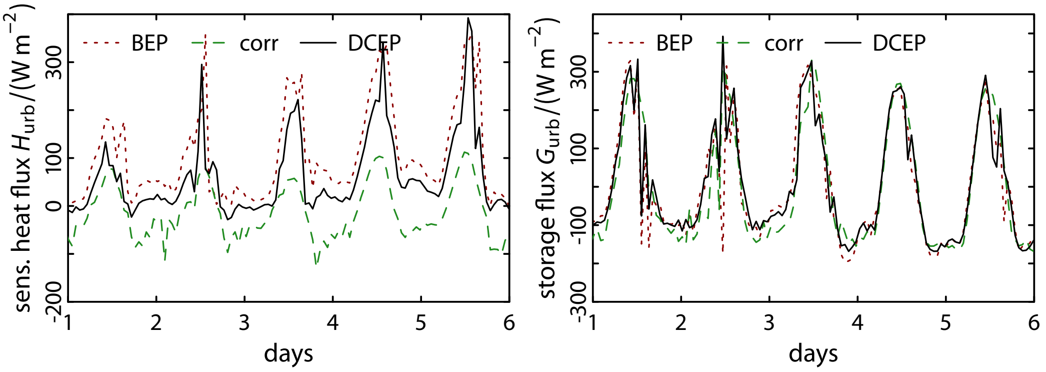

b) Simulations with the urban height distribution γ^{mid}

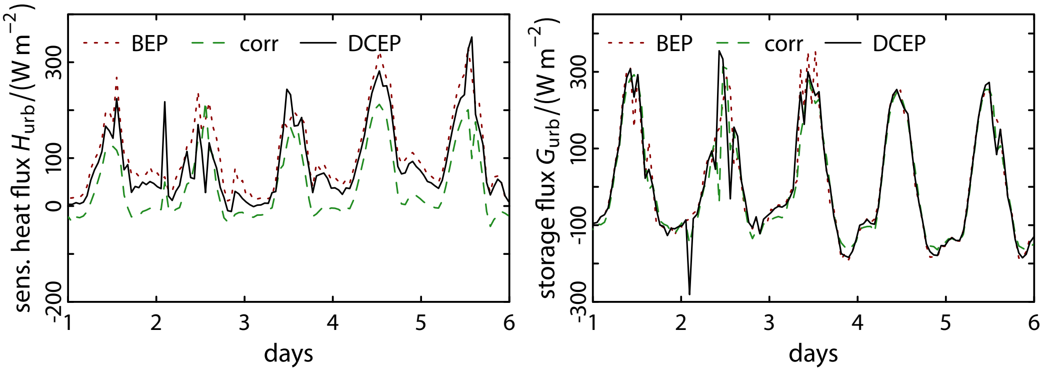

c) Simulations with the urban height distribution γ^{min}

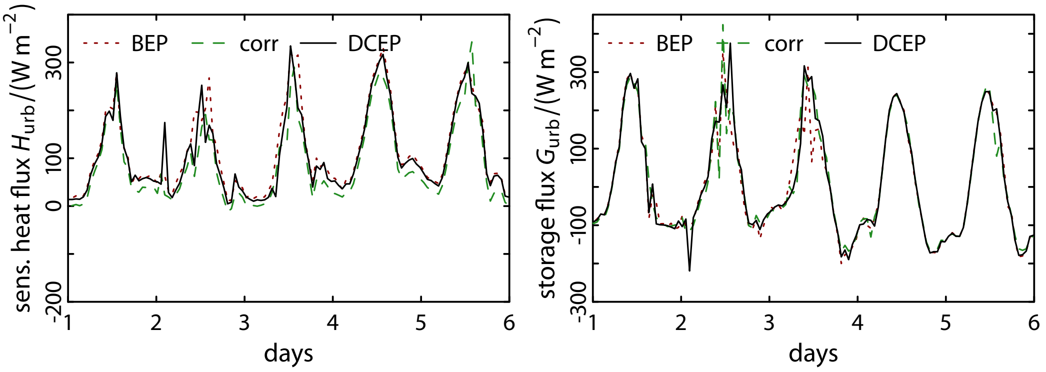

Figure 3.19. Simulated urban sensible heat and storage flux for different fixed height distributions

original BEP. Consequently, the effective radiative temperature T_{urb} – although not showing unphysical values – does not represent the longwave radiation budget in the original BEP.

2. Closure of the energy balances for longwave and shortwave diffuse radiation. This was achieved by scaling the radiation that is distributed in the canyon in such a way that it equals the amount of the incoming components from the mesoscale model. According to the sensitivity study, the corrected scheme resulted in considerably lower simulated surface and air temperatures inside the urban canyon in comparison with those from the original BEP (with and without considering diffuse shortwave radiation) for urban morphologies with a large building height variability. The effective radiative temperatures of the urban canyon, T_{urb}, were considerably higher in the corrected BEP version. The BEP scheme is officially included in the Weather Research and Forecasting (WRF) model. Thus, current WRF simulations for city centres with tall buildings, relatively narrow streets and a large building height variability are particularly affected by this overestimation of energy input.

3. The original BEP and the aforementioned set-ups use a single canyon as a basic element. Within that formulation, roof surfaces receive the full sky radiation and do not interact with surrounding urban surfaces independent of their height. This is changed by the extended canyon model DCEP. The inclusion of roofs in the radiation exchange increases the temperatures inside the urban canyon, both of urban surfaces and the air temperature, because more energy is distributed inside the canyon and remains longer within the canyon: the radiation trapping effect is increased. The roof temperatures, on the other hand, are lower because of shadowing effects on these surfaces. Furthermore, this modification alleviates the deviations in the magnitudes of simulated air and radiative temperatures caused by correcting the energy balance in modification 2.

The sensitivity analysis of temperatures, albedo and sensible heat fluxes to the building height variability shows that the effects of roofs are stronger for larger building height variability. The inclusion of the roofs' radiative interactions in DCEP lead to a good agreement with the results for the original BEP scheme which was tested in previous studies and found to successfully simulate urban conditions (Martilli et al. 2003; Hamdi and Schayes 2007). However, DCEP is physically more consistent than BEP because it conserves the incoming radiative energy and it accounts for more than one street canyon.

In the next chapter, DCEP is evaluated with measurements from Basel (Switzerland). Furthermore, the differences between the single-canyon and the double-canyon approach are analysed for this realistic setting.

4. Evaluation of DCEP with data from the Basel Urban Boundary Layer Experiment 2002

The Basel UrBan Boundary Layer Experiment (BUBBLE; Christen and Vogt 2004; Rotach et al. 2005) was conducted in 2001–2002 as part of the COST (European Co-operation in Science and Technology) action 715 – *Meteorology applied to urban pollution problems* (Fisher et al. 2001). The aim of BUBBLE was to investigate in detail the boundary layer structure of the city of Basel and its surroundings by combining near-surface and remote sensing instrumentation. Basel is a mid-size town (23 km^2) and consists together with its surrounding of a built-up area of approximately 130 km^2 (30 km^2 dense urban, 80 km^2 suburban and 20 km^2 industrial areas) and a population of 400 000 (Christen and Vogt 2004).

The experimental efforts of BUBBLE considered both, the exchange near the surface as well processes in the lower troposphere. Over a period of approximately one year, turbulent fluxes were measured at two towers up to a height of at least twice the average building height in the city centre. Furthermore, a wind profiler and a LIDAR (Light Detection And Ranging) system were operated to measure the relative variations of the atmospheric aerosol vertical profile in the city centre. Additional measurements took place during the intensive observation period (IOP) between 10 June to 10 July 2002. Among other quantities, the radiation and energy balance as well as wind velocity and air temperature were measured at several urban, suburban and rural sites. Furthermore, a Doppler SODAR / RASS (SOnic Detection And Ranging / Radio Acoustic Sounding System) was used to measure wind and temperature profiles. Other measurements and experiments in the context of BUBBLE not used in this work are described in Rotach et al. (2005).

In this chapter, data from the IOP is used to evaluate the performance of the coupled CCLM/DCEP model with the emphasis on the radiative and surface energy fluxes. First, the derivation of urban canopy parameters for Basel and its surroundings is explained. Second, the selected BUBBLE measurements sites are introduced. Subsequently, the set-up of the simulations is explained and finally the comparison of simulations and measurement data is presented.

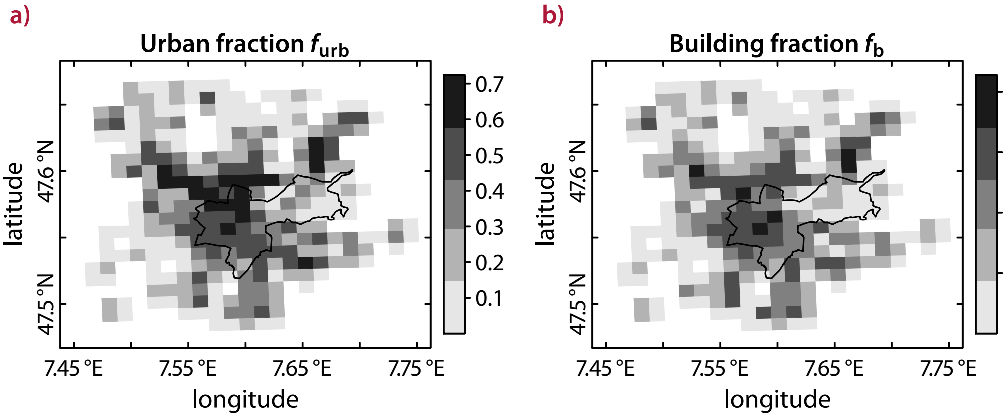

Figure 4.1. Urban fraction in a) and building fraction in b) of Basel and its surroundings at a resolution of 1 km based on land-use data of the cantons Basel-Stadt and Basel-Landschaft as well as CORINE. The area of the canton Basel-Stadt is outlined in black.

4.1. Derivation of urban canopy parameters of Basel and surroundings

Specific urban canopy parameters for each mesoscale grid cell are derived for the area of Basel and its surroundings. To this end, detailed land-use data of the cantons of Basel-Stadt (*gva.bs* 2012) and Basel-Landschaft (*geo.bl* 2012) as well as the CORINE land-use data (Coordinated Information on the European Environment; Büttner et al. 2012) for France and Germany are used. Furthermore, building parameters for the area of the canton Basel-Stadt including the city of Basel, and municipalities Riehen and Bettingen are derived from a 3-D building data set (*3D-Stadtmodelle Basel-Stadt* 2012) in the 3-D shapefile format. The polygons in this data set are separated into roof, wall and terrain surfaces. However, unlike the polygons in the 3-D building data set of Berlin described in section 5.1, the surfaces are not combined to complete houses, which makes the analysis more challenging.

The percentages of the urban fraction f_{urb} and the building fraction f_b of each grid cell (fig. 4.1) are derived from the land-use data by assigning particular percentages of both to every land-use class. The comprehensive data set of the canton Basel-Stadt features 32 land-use classes. The particular values of f_{urb} and f_b assigned to each class (tab. 4.1) are based on an optical evaluation of aerial photographs of Basel. A similar approach is used for the land-use data of the municipalities of the canton Basel-Landschaft that are situated next to the city of Basel. However, in this data set more than 100 classes are defined, which are not listed here. In contrast to the set of classes of Basel-Stadt, there is no dedicated class for buildings and thus every class consists of a mixture of buildings, streets and other surfaces. These fractions vary from $f_{urb} = 0.80$ and $f_b = 0.60$ for industrial zones to $f_{urb} = 0.40$ and $f_b = 0.36$

Type index	Type label	f_{urb}	f_{str}	f_b
0	Gebaeude.Gebaeude	1.00	0.00	1.00
1	Gebaeude.Ueberdachung	1.00	0.00	1.00
3	Gebaeude.Gebaeude_im_Wald	1.00	0.00	1.00
4	Gebaeude.Tank	1.00	0.00	1.00
5	befestigt.Strasse_Weg.Strasse_Weg	1.00	1.00	0.00
6	befestigt.Strasse_Weg.Waldstrasse_Waldweg	0.60	0.60	0.00
7	befestigt.Trottoir.Trottoir	1.00	1.00	0.00
8	befestigt.Trottoir.Rabatte	0.00	0.00	0.00
9	befestigt.Verkehrsinsel	0.40	0.40	0.00
10	befestigt.Bahn.Bahnareal	0.60	0.60	0.00
11	befestigt.Bahn.Tramareal	0.40	0.40	0.00
13	befestigt.Wasserbecken.Wasserbecken	0.00	0.00	0.00
14	befestigt.Wasserbecken.Wasserbecken_im_Wald	0.00	0.00	0.00
15	befestigt.uebrige_befestigte.Hafenareal	0.95	0.95	0.00
16	befestigt.uebrige_befestigte.Fabrikareal	0.95	0.95	0.00
17	befestigt.uebrige_befestigte.Gewaesservorland	0.70	0.70	0.00
18	befestigt.uebrige_befestigte.Sportanlage	0.10	0.10	0.00
19	befestigt.uebrige_befestigte.uebrige_befestigte	0.10	0.10	0.00
20	humusiert.Acker_Wiese_Weide	0.00	0.00	0.00
21	humusiert.Intensivkultur.Reben	0.00	0.00	0.00
23	humusiert.Gartenanlage.Gartenanlage	0.00	0.00	0.00
24	humusiert.Gartenanlage.Parkanlage_Spielplatz	0.00	0.00	0.00
25	humusiert.Gartenanlage.Friedhof	0.00	0.00	0.00
26	humusiert.Gartenanlage.Schrebergarten	0.15	0.10	0.05
27	humusiert.Gartenanlage.Tierpark	0.00	0.00	0.00
28	humusiert.Gartenanlage.Sportanlage_humusiert	0.00	0.00	0.00
30	humusiert.uebrige_humusierte.Gewaesservorland	0.00	0.00	0.00
31	humusiert.uebrige_humusierte.uebrige_humusierte	0.00	0.00	0.00
33	Gewaesser.fliessendes.fliessendes	0.00	0.00	0.00
34	Gewaesser.fliessendes.fliessendes_im_Wald	0.00	0.00	0.00
36	bestockt.geschlossener_Wald	0.00	0.00	0.00
39	bestockt.uebrige_bestockte	0.00	0.00	0.00

Table 4.1. Classes of the land-use data set of the canton Basel-Stadt (Switzerland) and the assigned urban fraction f_{urb}. The urban fraction of the areas consists of street surfaces (indicated by the street surface fraction f_{str}) and buildings (indicated by the building fraction f_b). The corresponding values are assigned by optically analysing aerial photographs of Basel.

for living zones. A value of $f_{\mathrm{urb}} = 0.00$ is assigned to zones with natural surfaces only. The CORINE land-use classes in the area north of Basel located in France and Germany include only two urban classes: *Discontinuous urban fabric* and *Industrial or commercial units*. For both classes, an urban fraction of $f_{\mathrm{urb}} = 0.70$ with equal proportions of buildings and streets (or other flat impervious) surfaces is assumed. Finally, the values of f_{urb} and f_{b} are aggregated to the mesoscale model grid cells (fig. 4.1). This results in a maximum value of f_{urb} of approx. 0.72 and a maximum f_{b} of approx. 0.43. Finally, the fraction of street surfaces in a grid cell is given by $f_{\mathrm{str}} = f_{\mathrm{urb}} - f_{\mathrm{b}}$.

For the main study area, the canton of Basel-Stadt, the 3-D building data set is used to estimate the height distribution of buildings, the street width and the distribution of street directions. The heights of buildings – given by the height of the roof surfaces above the ground – are aggregated into the mesoscale grid cells (fig. 4.2). The average street width W in a grid cell is estimated from the average distance of wall elements to other walls in that grid cell (fig. 4.3a). For the area of Basel-Stadt, this results in an average street width of $\overline{W}^f \approx 21\,\mathrm{m}$. Here, the values of the grid cells are weighted with the respective urban fraction f_{urb} of the grid cell. The distribution of street directions is estimated from the average orientation of wall elements (fig. 4.4). For the present study, four street directions are considered: north-west–south-east, north–south, north-east–south-west and east–west. With the definition of correlation in (5.1) on page 126, fractions of perpendicular street directions are highly correlated with $r \approx 0.88$ and for non-perpendicular street directions $r \approx -0.94$. Thus, streets are mostly perpendicular to each other. The building width follows from the assumption that surface fractions (buildings, street, vegetation) are equal in reality and in the simplified model of DCEP (Martilli 2009). In the model, the urban part of the grid cell is completely covered by street and building surfaces. Thus, the building width B is given by

$$B = \frac{f_{\mathrm{b}}}{f_{\mathrm{str}}} W \,. \tag{4.1}$$

For the area of Basel-Stadt, the average building width weighted with the respective urban fraction is $\overline{B}^f \approx 20\,\mathrm{m}$.

For the area surrounding the canton Basel-Stadt described by the land use data of CORINE and the canton Basel-Landschaft, an average height distribution of 0.05, 0.20, 0.40, 0.30 and 0.05 for buildings of height 0 m, 5 m, 10 m, 15 m and 20 m is used (fig. 4.2). The distribution of street directions (fig. 4.4) is assumed equal for all directions, and the street width is set to 25 m (fig. 4.3a). The building width is calculated as described above (fig. 4.3b). This prescription results in unrealistic building widths of 25 m for the grid cells with $f_{\mathrm{str}} \approx f_{\mathrm{b}}$ due to neglecting the vegetation fraction in the urban canyon. The large street width is required, however, to limit the radiative interaction between opposite buildings in these areas and necessarily leads to a large

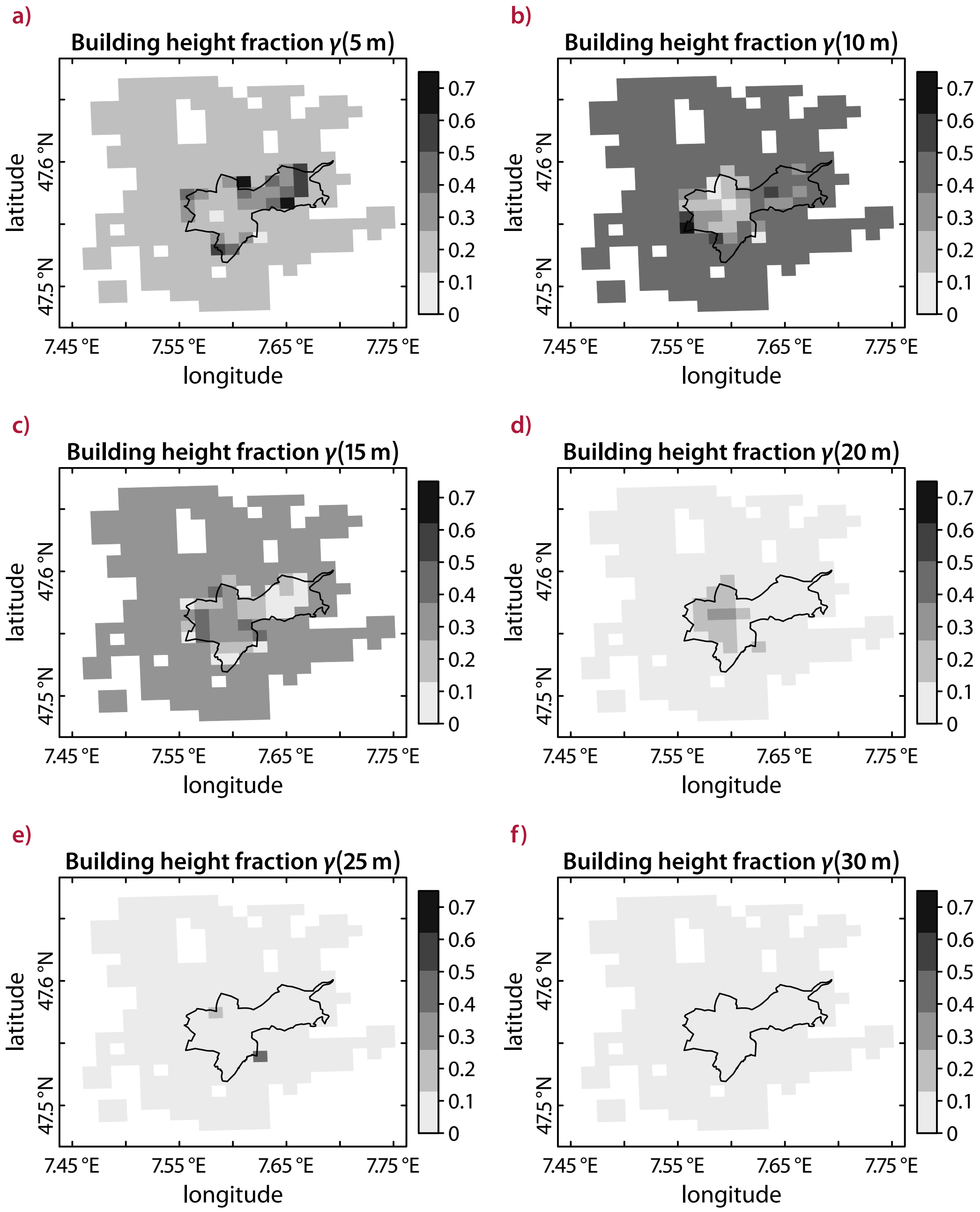

Figure 4.2. Building height distribution of Basel and surroundings for the lowest heights at a resolution of 1 km based on the 3-D building data set. The respective figures include buildings of a height ±2.5 m and the same values are assumed for every street direction. The area of the canton Basel-Stadt is outlined in black.

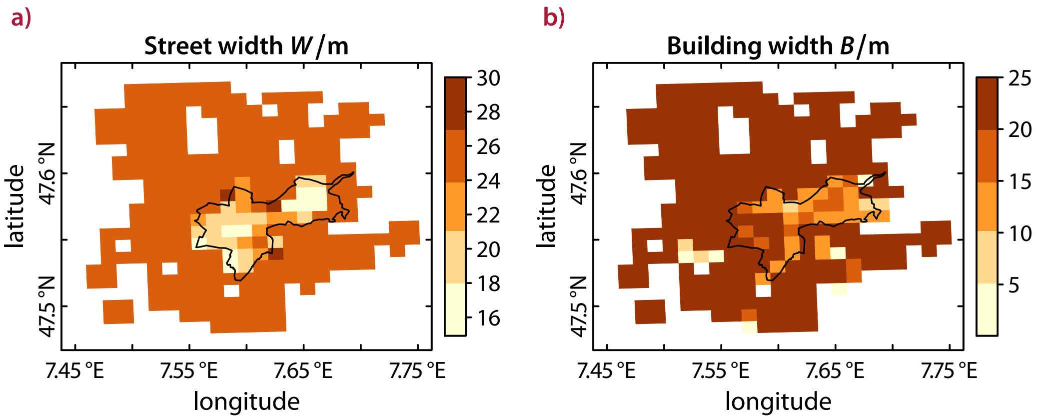

Figure 4.3. Street width in a) and building width in b) of Basel and surroundings at a resolution of 1 km. The former is based on the 3-D building data set resulting with (4.1) in the latter. The same values are assumed for every street direction. The area of the canton Basel-Stadt is outlined in black.

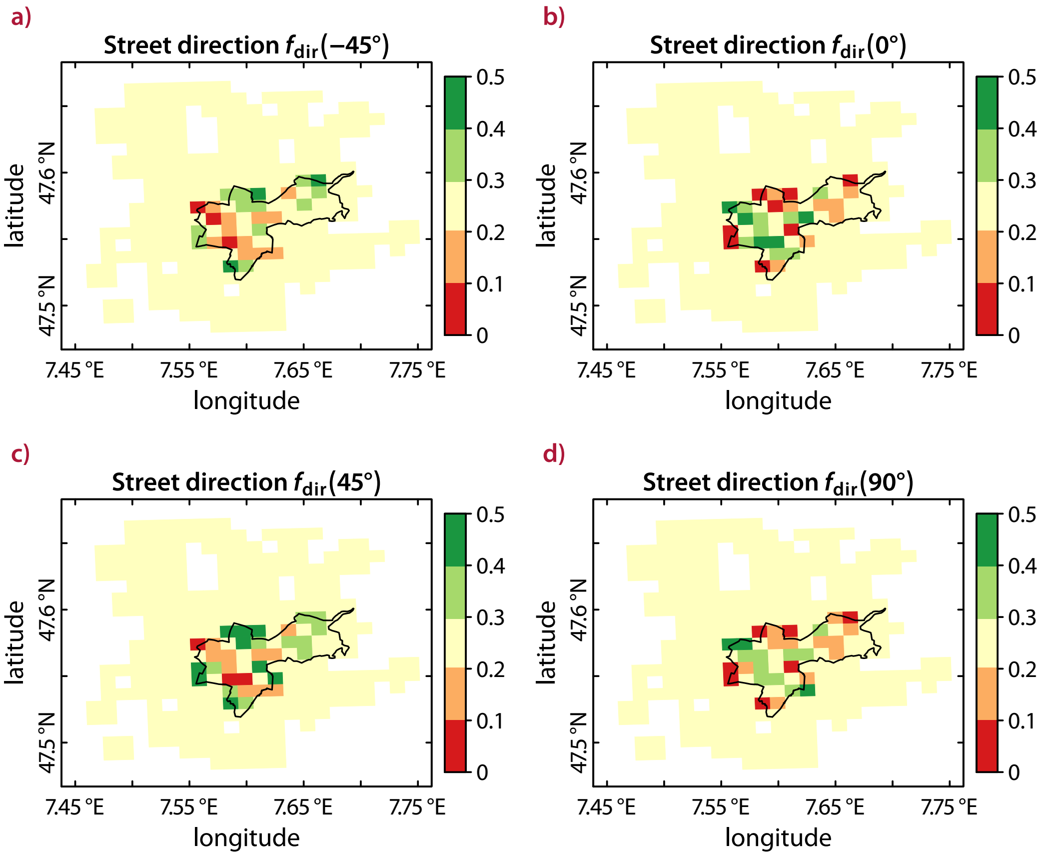

Figure 4.4. Distribution of street directions $f_{\mathrm{dir}}(\zeta)$ of Basel and surroundings at a resolution of 1 km based on the 3-D building data set. The convention of the street canyon angle is explained in fig. 3.7a. The area of the canton Basel-Stadt is outlined in black.

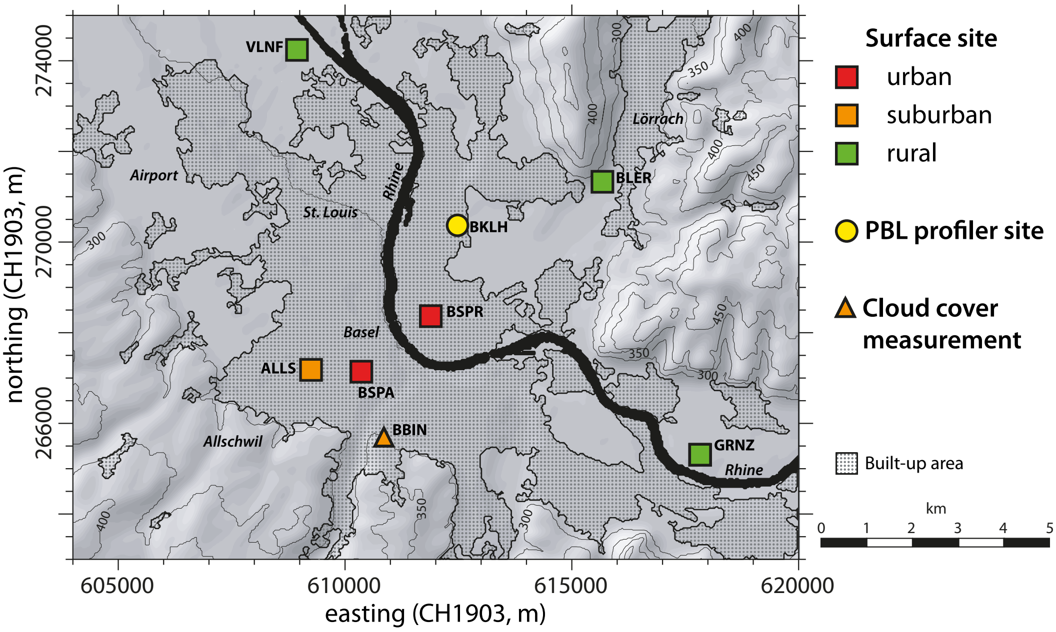

Figure 4.5. Locations of measurement sites in Basel and vicinity from which data is used for CCLM evaluation. The map is based on the official station map of the BUBBLE campaign (*BUBBLE* 2004).

building width if building and street fractions are to be equal in reality and in the urban canopy model. Due to the large distance between buildings, roofs do not interact with the other urban surfaces; thus, the large building width does not produce unphysical results.

4.2. Description of measurement sites

The results of the CCLM simulation are compared with measurements from six surface stations, planetary boundary layer profiles and cloud cover measurements. Figure 4.5 shows the locations of the measurement sites used for comparison. All sites operated continuously during the IOP on which is focused here; the two *urban* surface stations measured during the complete BUBBLE campaign of one year. These urban stations were situated in the densely built-up city core of Basel: the tower at Basel-Sperrstraße (BSPR, fig. 4.6a) and the tower at Basel-Spalenring (BSPA, fig. 4.6b). These areas are characterized by building heights larger than 10 m, high building fractions and a low vegetation cover. Most houses are residential multi-storey row houses enclosing either open (green spaces) backyards or one-storey garages, car parking or flat commercial buildings (Christen and Vogt 2004). The *suburban* tower in Allschwil (ALLS, fig. 4.7a) was situated in a vegetated backyard within a uniform residential neighbourhood consisting of two to three storey single and semi-detached houses. The *rural* sites in

a) Tower in Basel-Sperrstraße (BSPR)

b) View on and from the tower at Basel-Spalenring (BSPA)

Figure 4.6. Urban surface stations in Basel operating during the complete BUBBLE campaign. The pictures are taken from the official BUBBLE website (*BUBBLE* 2004) or were supplied by Roland Vogt.

a) Tower in a vegetated backyard in Allschwil (ALLS)

b) Measurements above non-irrigated grassland in Grenzach (GRNZ)

c) Mast above crop land in Village Neuf (VLNF)

d) Mast above non-irrigated grassland in Basel Lange Erlen (BLER)

Figure 4.7. Suburban (in a)) and rural surface stations (in b), c) and d)) in the surroundings of Basel operating during the complete BUBBLE campaign (only d)) or the IOP (the rest). The pictures are taken from the official BUBBLE website (*BUBBLE* 2004) or were supplied by Roland Vogt.

Grenzach (GRNZ, fig. 4.7b) and Basel Lange Erlen (BLER, fig. 4.7d) were both located above non-irrigated agricultural grassland. The mast at the *rural* Village Neuf site (VLNF, fig. 4.7c) was situated above crop land.

Table 4.2 lists the heights z at which different quantities were measured at the surface stations. All measurements of the radiation budget components, and the latent and sensible heat flux were conducted above the canopy. Where measurements of the sensible heat flux were available at different heights, data from the highest measurement is chosen for analysis. Thus, at the urban and suburban stations, the sensible and latent heat fluxes were measured at a height of at least twice the mean building height. The measurement height has to be above the roughness sublayer height z_* to avoid local effects of the roughness elements (Rotach 1999; Rotach 2002).

Site	K^*, L^*		λE		H		T		u	
	z	z/h	z	z/h	z	z/h	z	z/h	z	z/h
BSPR	31.5 m	2.15	31.7 m	2.17	31.7 m	2.17	13.9 m	0.95	31.7 m	2.17
BSPA	32.9 m	2.63	29.9 m	2.40	37.6 m	3.01	15.8 m	1.26	37.6 m	3.01
ALLS	15.1 m	2.01	15.8 m	2.11	15.8 m	2.11	15.0 m	2.00	15.8 m	2.11
GRNZ	1.4 m	–	28.0 m	–	28.0 m	–	1.5 m	–	28.4 m	–
VLNF	2.0 m	–	3.3 m	–	3.3 m	–	2.0 m	–	2.0 m	–
BLER	2.0 m	–	–	–	–	–	2.0 m	–	10.0 m	–

Table 4.2. Height of the devices of BUBBLE measuring the components of the shortwave and longwave radiation budget K^* and L^*, the air temperature T, the wind velocity u, and eddy correlations from which the latent and sensible heat flux λE and H are derived. When measurements at different heights are available, the height best supporting the present evaluation is chosen. Given is the absolute height z above the ground and the height z/h relative to the average building height h. The latter is not defined for the rural sites. The fluxes λE and H were not measured at BLER. The values are based on Christen and Vogt (2004) and the information given in the BUBBLE data.

While Roth (2000) lists different estimates of z_* in terms of the mean roughness element height h, which corresponds to the mean building height in the present case, with up to $z_* = 5h$ (or higher depending on the horizontal spacing of the roughness elements), Rotach et al. (2001) suggest $z_* = 2h$ for typical European cities.

At both urban stations, BSPR and BSPA, the 90 % source areas of the eddy correlation instrumentation for turbulent flux measurements were calculated to reach approx. 300 m to 500 m upwind under typical summertime convective situations. Furthermore, downward looking radiation sensors have an approximate field of view with a radius of 100 m (Christen and Vogt 2004). The corresponding radius of the field of view of the suburban and rural stations is 50 m and 5 m, respectively. Where available, temperature measurements from a height of about 10 m are chosen for analysis, the height of the lowest atmospheric CCLM model level. These values can be directly compared to the *prognostic* atmospheric temperature at this level. Otherwise, the temperature measurements are compared with the simulated *diagnostic* 2 m temperature. Wind velocity measurements are only available at the given height.

In addition, soil heat flux measurements are available at the three rural sites. The fluxes were measured with three heat plates each at GRNZ, VLNF and BLER at a depth of 5 cm, 4 cm and 7 cm, respectively. Due to the large amount of heterogeneous surfaces at the urban sites, the measurement of the fluxes in the urban surfaces was not feasible.

Table 4.3 lists the urban parameters described in the previous section for the mesoscale grid cells which include the surface stations at a resolution of 1 km (see next section for details). Also shown are site parameters as derived from average param-

Site	f_{urb}	W/m	B/m	h/m	γ						
					0 m	5 m	10 m	15 m	20 m	25 m	30 m
BSPR	0.71	18.1	27.8	15.4	0.01	0.15	0.11	0.33	0.31	0.08	0.01
	0.84	*11.8*	*21.3*	*14.6*				—			
BSPA	0.54	18.2	18.4	12.6	0.02	0.16	0.28	0.39	0.15	0.00	0.00
	0.69	*12.9*	*14.9*	*12.5*				—			
ALLS	0.47	19.5	36.7	9.6	0.02	0.25	0.55	0.15	0.01	0.01	0.00
	0.47	*11.9*	*17.5*	*7.5*				—			
GRNZ	0.03	25.0	25.0	10.5	0.05	0.20	0.40	0.30	0.05	0.00	0.00
	0.09	–	–	–				—			
BLER	0.24	18.3	14.4	8.6	0.07	0.34	0.40	0.19	0.01	0.00	0.00
	0.06	–	–	–				—			

Table 4.3. Parameters of the grid cells that include BUBBLE measurement stations as derived in section 4.1. Listed are the urban fraction f_{urb}, the street and building width W and B, and the average building height h. In addition, the building height distribution of the 7 lowest urban model levels is given. The italic values are estimates derived from the local parameters from the area 250 m around the measurement sites given in Christen and Vogt (2004). VLNF is treated completely rural in the simulations and the measurement site does not have any buildings in its direct surroundings.

eters in Christen and Vogt (2004) of an area 250 m around the sites. Estimates of the building and street width, B and W, are calculated from the average building (or plan area) fraction f_{b} and the average building frontal area index f_{f} according to a modified approach of Martilli (2009) taking the vegetation cover into account. Following the definitions in Grimmond and Oke (1999a) and using the effective two-dimensional description of the urban part of the grid cell in DCEP (cf. fig. 3.1 on page 33), the building fraction is given by

$$f_{\mathrm{b}} \equiv \frac{A_{\mathrm{b}}}{A_{\mathrm{tot}}} = \frac{B}{W+B} f_{\mathrm{urb}} \,, \tag{4.2}$$

and the building frontal area index is given by

$$f_{\mathrm{f}} \equiv \frac{A_{\mathrm{proj}}}{A_{\mathrm{tot}}} = \frac{h}{W+B} f_{\mathrm{urb}} \,. \tag{4.3}$$

A_{b} is the plan area of buildings at ground level, A_{proj} is the total vertical extended building area projected into the plane normal to the approaching wind direction and A_{tot} is the total reference plan area. Here, it is imagined that the street canyons extend perpendicular to the wind direction. The mean building height is denoted with h as before. Thus, the building and street width are given by

$$B = \frac{f_\mathrm{b}}{f_\mathrm{f}} h \,, \tag{4.4}$$

$$W = \left(\frac{f_\mathrm{urb}}{f_\mathrm{b}} - 1 \right) B \,, \tag{4.5}$$

respectively. Note, however, that the exact expressions depend on the definition of the reference area A_tot. Therefore, a one-to-one correspondence of f_b and f_f, and W and B does not exist. Nonetheless, the model grid cell characteristics represent the site conditions relatively well. The urban fractions of BSPR and BSPA are slightly lower in the model grid cell, in part because the areas for which the site specific parameters were derived are considerably smaller than the areas of the corresponding grid cells.

In Basel-Kleinhüningen (BKLH) in the northern part of Basel, a Doppler SODAR / RASS was operated to measure wind and temperature profiles between a height of 40 m and 500 m with a vertical resolution of 20 m (Rotach et al. 2005). The cloud cover was measured at the Basel-Binningen (BBIN) station south of Basel.

4.3. Set-up of simulations and description of the weather conditions

Simulations with CCLM/DCEP are conducted to assess the performance of the coupled model system for the area of Basel, June–July 2002. The results are compared with the output of the default bulk approach in CCLM and the output of CCLM with the single-canyon approach of the corrected BEP (corresponding to the “corr” run in section 3.6.2). CCLM version 4.8_clm11 is used for one way nested grids of resolutions of approx. 25 km (without urban schemes), 7 km (without urban schemes), 2.8 km (with and without urban schemes) and 1 km (with and without urban schemes) for 15 June 2002 0000 UTC through 10 July 2002 0000 UTC (fig. 4.8). The 25 km simulations cover Europe, and the Mediterranean and Black Sea region; the 7 km Central Europe, southern Great Britain, western Spain and Italy; the 2.8 km simulation the Alpine Region including western France and southern Germany. The 1 km simulation is centred around Basel with a domain size of approx. 300 km × 300 km.

The integration time step is with increasing resolution 150 s, 40 s, 25 s and 4 s, respectively. The comparably low time step in the finest resolution is necessary to avoid numerical instabilities due to the steep orography in the alpine region. Filtering of steep slopes in the preprocessor of CCLM allows larger time steps (cf. Fuhrer 2012).

The two finest resolution runs use 50 vertical levels. The lowest levels are at approx. 10 m, 35 m, 73 m and 122 m above ground.

The initial and six-hourly boundary conditions are provided by ERA-Interim reanalysis data (Dee et al. 2011) and all nesting steps use spectral nudging (Rockel,

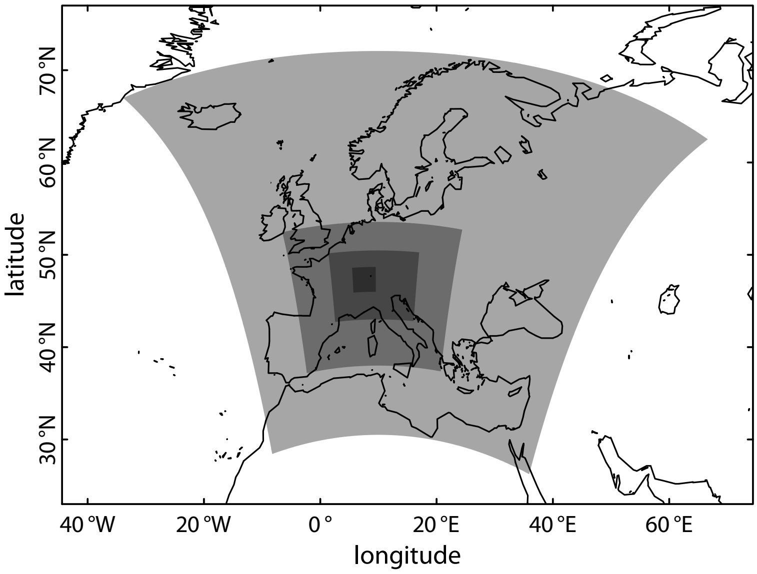

Figure 4.8. Nested domains of the downscaling for Basel. The resolutions are with decreasing domain size 25 km, 7 km, 2.8 km and 1 km.

Castro et al. 2008). The initial soil water content for the 25 km resolution domain, however, is taken from a simulation with the same set-up but starting in January 1995. Without this spin up, CCLM simulations with the interpolated soil water content of ERA-Interim resulted in air temperatures that were considerably too low during the BUBBLE IOP period.

The orography, monthly vegetation and soil parameters are provided by the preprocessor of CCLM (Smiatek et al. 2008). This data set provides vegetation parameters and roughness length in the area of Basel appropriate for the bulk-transfer scheme, i.e. adjusted for an urban area. With DCEP, the preprocessor parameters represent the vegetation part in a grid cell only. Therefore, the data in Basel is substituted with parameters for June and July from the surroundings of Basel: a leaf area index of $3.49\,\mathrm{m^2\,m^{-2}}$ and $3.4\,\mathrm{m^2\,m^{-2}}$; a plant cover fraction of 0.8847 and 0.8779; a root depth of 1.53 m; a roughness length of 0.23 m and 0.22 m.

For the simulation with DCEP, the urban canopy parameters as derived in section 4.1 are used. The urban surface parameters for roof (R), wall (W) and street surfaces (G) follow the propositions by Martilli et al. (2002): an emissivity of $\epsilon_R = \epsilon_W = 0.90$, $\epsilon_G = 0.95$ and an thermal diffusivity of $k_R = k_W = 0.67 \times 10^{-6}\,\mathrm{m^2\,s^{-1}}$, $k_G = 0.29 \times 10^{-6}\,\mathrm{m^2\,s^{-1}}$. Furthermore, an increased value of the volumetric specific heat capacity $c_R = c_W = c_G = 2.3 \times 10^6\,\mathrm{J\,m^{-3}\,K^{-1}}$ is used. The albedo for roof and street surfaces is motivated by typical values listed in Loridan and Grimmond (2012): $\alpha_R = 0.15$ and $\alpha_G = \alpha_W = 0.1$.

Furthermore, anthropogenic heat emissions are neglected for the following reasons: Christen and Vogt (2004) found a yearly total energy surplus when summing up $\mathcal{R}^* - \mathcal{H} - \lambda\mathcal{E}$ at the urban stations, i.e. the net radiation reduced by the sensible and the latent heat flux. Furthermore, they argued that the yearly total heat storage in the urban surfaces is zero. Thus, with the energy balance equation in (4.12) on page 108, they attributed the energy surplus to the anthropogenic heat flux, and were able to approximate its yearly average to 20 W m^{-2} and 10 W m^{-2} at BSPR and BSPA, respectively. At ALLS, they estimated the anthropogenic heat flux to be about 50 % of the value at BSPA, thus approx. 5 W m^{-2} (Christen and Vogt 2004, personal communication). It can be expected that the respective values are higher during winter due to heating and consequently lower during summer as was found e.g. for Łódź (Poland; Kłysik 1996; Offerle et al. 2005), and London (UK; I. G. Hamilton et al. 2009).

During the IOP, which is almost completely covered by the simulations, the mean air temperature was 20 °C, the total rainfall was 65 mm mostly from thunderstorms and the winds were on average 2.0 m s^{-1} (Christen and Vogt 2004). Thus, the IOP was significantly warmer and slightly drier than the 30 year average with 16.8 °C and 89 mm, respectively (Christen and Vogt 2004). The low amount of precipitation concentrated on small time scales justifies the disregard of precipitation on the urban surfaces in DCEP (cf. section 3.5.2).

4.4. Results

In the following, the performance of CCLM/DCEP and CCLM with the bulk scheme is evaluated for the period 20 June 2002 0000 UTC – 9 July 2002 2300 UTC (20 complete days), respectively. In order to avoid possible spin up effects of the urban surfaces, the first 5 days of the simulation are not considered in the analysis. Assuming that the initialized urban surface temperatures deviate not more than 10 K from the equilibrium urban surface temperatures, the 2 m temperature error due to spin-up processes is expected to be less than 0.1 K (cf. section 5.3, in particular fig. 5.11 on page 135). Since the measuring sensors of BUBBLE are influenced by both urban and natural surfaces, simulated grid cell averaged values are compared with the measurements. The plots of this section show the average diurnal course of the simulated grid cell averages of the mesoscale grid cells in which the respective site was situated. Where appropriate the corresponding values of the urban part of the grid cells is also included. The observations are shown in red if at most 30 % of the hourly values are missing, and in grey if more than 30 % of the hourly values are missing.

The models are assessed in terms of the mean-bias error (MBE) and the root-mean-square error (RMSE). Both measures are widely used to determine the quality of a UCM (e.g. Masson et al. 2002; Hamdi and Schayes 2007; Grimmond et al. 2010; Grimmond et al. 2011; Loridan and Grimmond 2012). They are defined as

$$\mathrm{MBE}(O,P) \equiv \frac{1}{N}\sum_{i=1}^{N}(P_i - O_i) \tag{4.6}$$

and

$$\mathrm{RMSE}(O,P) \equiv \sqrt{\frac{1}{N}\sum_{i=1}^{N}(P_i - O_i)^2}\,, \tag{4.7}$$

respectively. Here, O are the N observation values, P are the corresponding model predictions. In this work, O and P are the hourly values of the evaluated variables during the analysed period. The MBE and the RMSE, however, do not describe the source of error. Therefore, as proposed by Willmott (1981), the RMSE is furthermore divided into a systematic and an unsystematic part,

$$\mathrm{RMSE_S}(O,P) \equiv \sqrt{\frac{1}{N}\sum_{i=1}^{N}(\hat{P}_i - O_i)^2}\,, \tag{4.8}$$

$$\mathrm{RMSE_U}(O,P) \equiv \sqrt{\frac{1}{N}\sum_{i=1}^{N}(P_i - \hat{P}_i)^2}\,, \tag{4.9}$$

where $\hat{P}$ is derived from a least square fit assuming P as a linear function of O resulting in $\hat{P}_i \equiv mO_i + n$ with m and n being the slope and intercept of this fit, respectively. Since both $\sum_i^N(P_i - \hat{P}_i) = 0$ and $\sum_i^N(P_i - \hat{P}_i)O_i = 0$ due to the minimization of the residual squares in the fit, the overall RMSE is given by

$$\mathrm{RMSE}^2(O,P) = \mathrm{RMSE}^2_\mathrm{S}(O,P) + \mathrm{RMSE}^2_\mathrm{U}(O,P)\,. \tag{4.10}$$

The systematic RMSE is a measure for a constant *linear* deviation of the model predictions from the measurements whereas the unsystematic RMSE indicates random errors or errors due to higher order deviations. Note that in the following, RMSE values are rounded for printing, thus the relationship (4.10) is only approximately fulfilled.

4.4.1. Surface radiation budget

In this subsection, the simulations are evaluated in terms of the components of the shortwave and longwave radiation near the surface. Table 4.4 on page 103 lists the total, systematic and unsystematic RMSE as well as the MBE for all components.

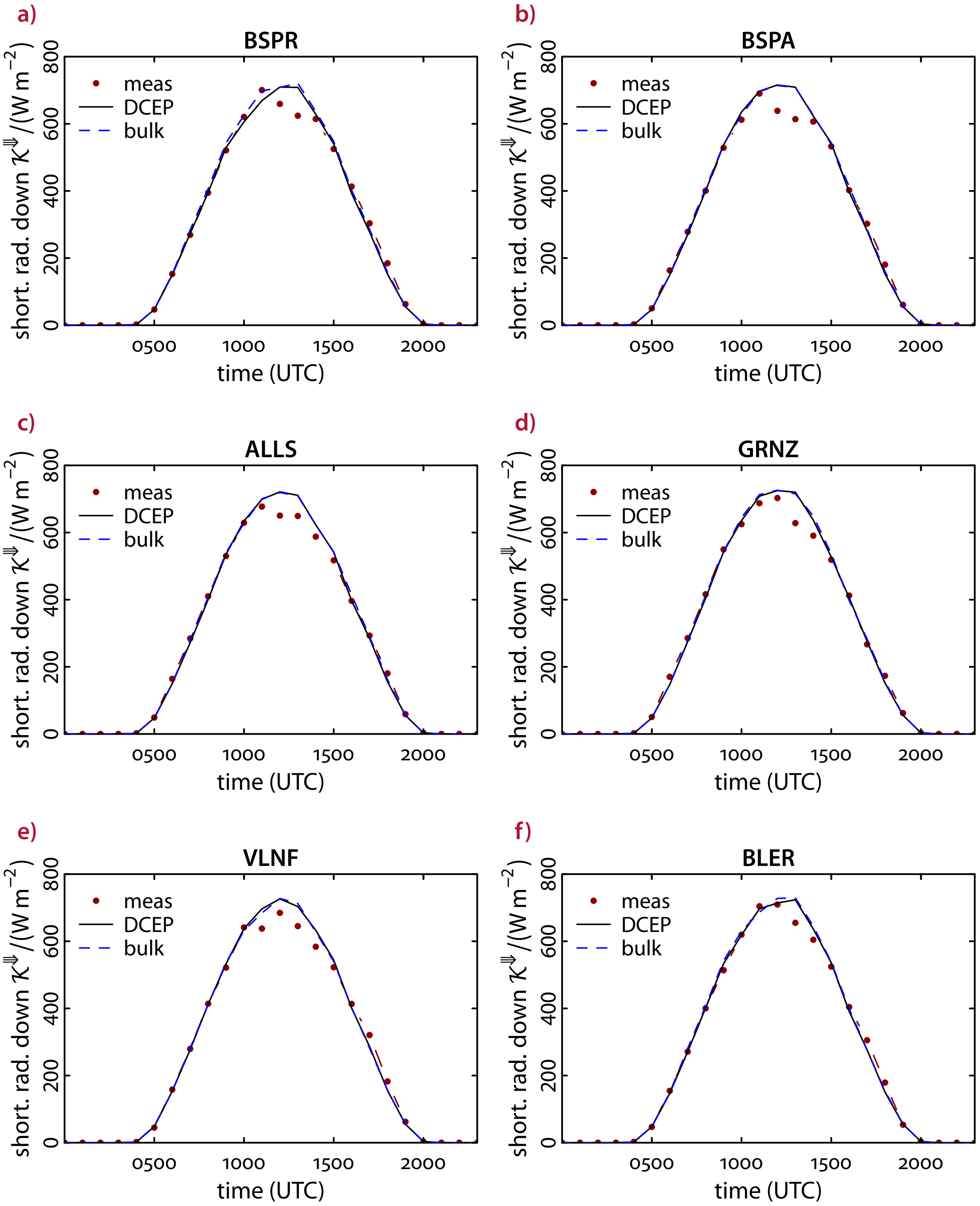

Figure 4.9. Measured and simulated average diurnal cycle of the direct and diffuse shortwave irradiance $\mathcal{K}^{\Downarrow}$ near the surface between 20 June 2002 and 9 July 2002. The simulations are conducted with either the DCEP or the bulk scheme and represent the mesoscale grid cell average.

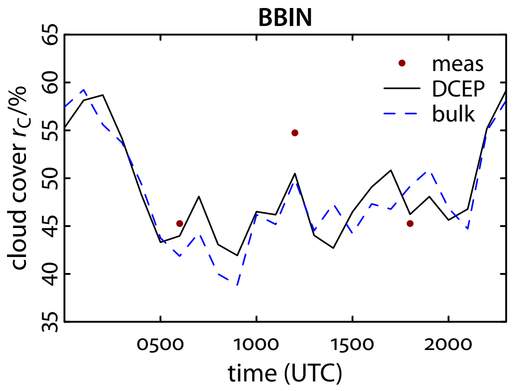

Figure 4.10. Measured and simulated average diurnal cycle of the cloud cover at the Basel Binningen station between 20 June 2002 and 9 July 2002. The measurements took place in 1/10 units. The simulations are conducted with either the DCEP or the bulk scheme and represent the mesoscale grid cell average.

The simulated **direct and diffuse shortwave irradiance** $\mathcal{K}^{⤋} \equiv \mathcal{K}^{\Downarrow} + \mathcal{K}^{\downarrow}$ is similar at all urban and rural measurement sites (fig. 4.9) and shows only very small changes due to the urban modifications in CCLM. The DCEP scheme as well as the bulk approach do not consider anthropogenic aerosols. These aerosols can lead to an attenuation of $\mathcal{K}^{⤋}$ in mid-latitude cities of up to 10 % (Kuttler 2004). The mid-size city Basel, however, does not show a considerable difference between urban and rural stations, which might be due to the limited instrument resolution or the close distance of the stations (Christen and Vogt 2004). Thus, the simulations represent the measurements well at all stations with an MBE of at most 7 W m^{-2} except at 1200–1300 UTC when the measurements show a lower irradiance of up to 95 W m^{-2}. This overestimation is the reason for the large RMSE of approx. 100 W m^{-2}, which is mainly unsystematic due to the temporary error. An underestimation of the cloud cover could be the reason for this. In fact, the optically observed cloud cover at the Basel-Binningen station (measured in 1/10 units three times a day) is on average approx. 4 % higher than the simulated cloud cover at 1200 UTC (fig. 4.10) with an RMSE at 1200 UTC of approx. 26 %. During the evaluation period, the cloud cover at 1200 UTC is underestimated four times by at least 20 % with a maximum of approx. 64 % but overestimated only two times by at least 20 % with a maximum of 57 %. Given the uncertainty of the measurements of at least 5 %, the small average underestimation does not allow to draw a clear conclusion but the frequency of extreme underestimation of the cloud cover indicates that the cloud cover is the reason for the overestimation of the shortwave irradiance.

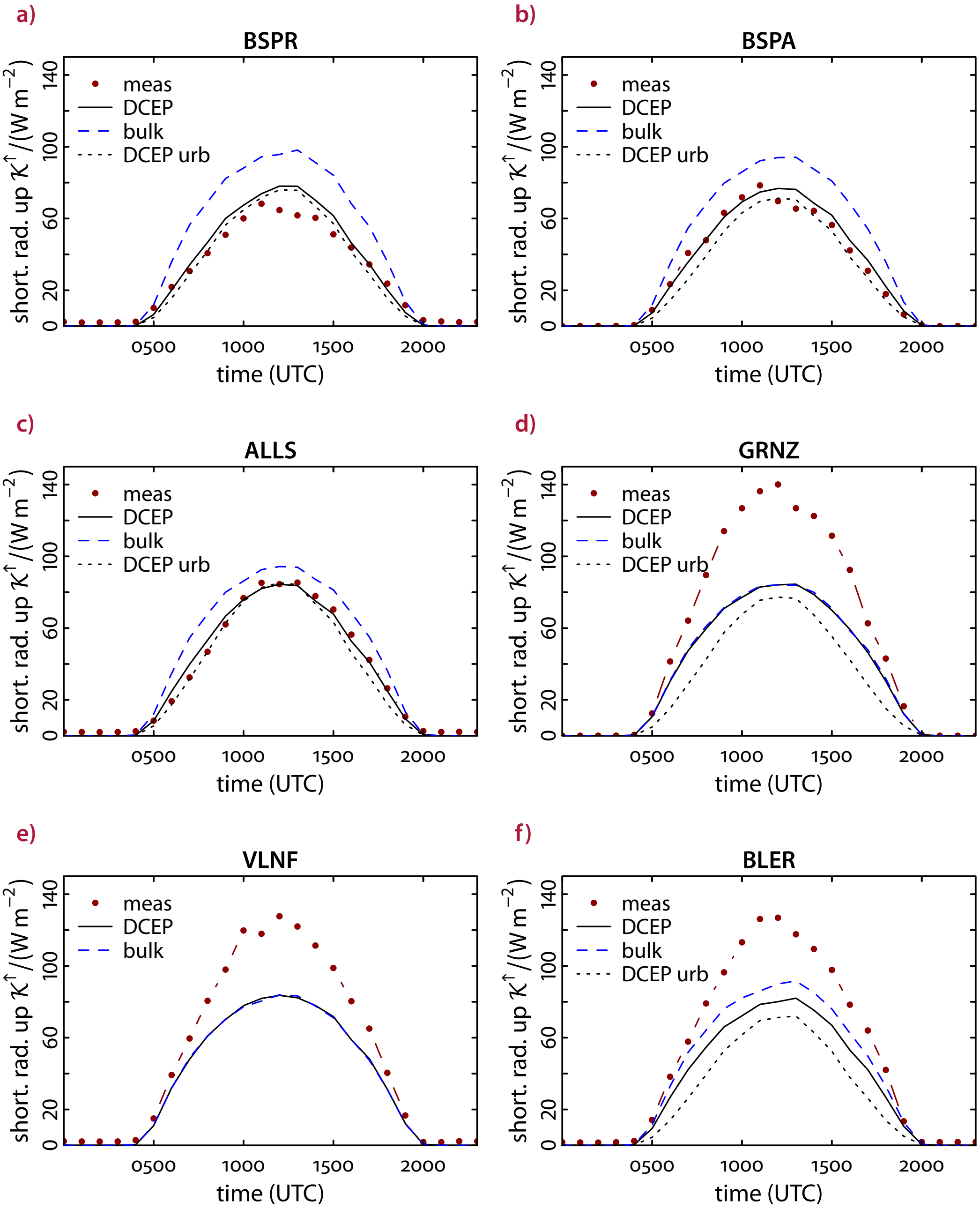

Figure 4.11. Measured and simulated average diurnal cycle of the reflected shortwave radiation $\mathcal{K}^{\uparrow}$ near the surface between 20 June 2002 and 9 July 2002. The simulations are conducted with either the DCEP or the bulk scheme. The "DCEP urb" values represent only reflected shortwave radiation of the urban part of the corresponding mesoscale grid cell, $K^{\uparrow}_{\text{urb}}$; otherwise the simulated values represent the mesoscale grid cell average.

The **reflected shortwave radiation** $\mathcal{K}^{\uparrow}$ is the component of the radiation budget that is most strongly modified in the urban area of Basel (Christen and Vogt 2004). This is due to the lower albedo of the urban surfaces as well as the multiple reflections at the different urban surfaces which effectively reduce the total albedo. Both effects are taken into account by DCEP (cf. (3.64) on page 57) but not by the bulk scheme. Thus, DCEP clearly leads to an improved $\mathcal{K}^{\uparrow}$ (fig. 4.11) for the urban and suburban stations in comparison with the bulk approach. While the bulk approach overestimates $\mathcal{K}^{\uparrow}$ by approx. $30\,\mathrm{W\,m^{-2}}$ at BSPR during midday, DCEP reduces the overestimation to approx. $10\,\mathrm{W\,m^{-2}}$ at midday. This remaining overestimation is mainly due to the overestimation of $\mathcal{K}^{\Downarrow}$ during midday as discussed above. The average RMSE reduces from $23\,\mathrm{W\,m^{-2}}$ with the bulk scheme to $12\,\mathrm{W\,m^{-2}}$ with DCEP, the MBE reduces from $14\,\mathrm{W\,m^{-2}}$ to $2\,\mathrm{W\,m^{-2}}$. Furthermore, the remaining RMSE in the simulation with DCEP is mainly unsystematic. Similar improvements are detected at BSPA and ALLS. The non-vanishing values of $\mathcal{K}^{\uparrow}$ during the night at BSPR, ALLS, VLNF and BLER with $\mathcal{K}^{\uparrow} \approx 2\,\mathrm{W\,m^{-2}}$ are probably due to measurement errors or due to light pollution, which is not considered in DCEP.

The largest deviations between simulations and measurements are found for the rural GRNZ, VLNF and BLER. Here, CCLM underestimates $\mathcal{K}^{\uparrow}$ by up to $50\,\mathrm{W\,m^{-2}}$, which leads, on average, to a MBE of up to $-19\,\mathrm{W\,m^{-2}}$ and a mainly systematic RMSE of up to $36\,\mathrm{W\,m^{-2}}$. Presently in CCLM, the surface **albedo** is given by (2.22) to (2.24) on page 30. In particular, the fixed albedo for diffuse radiation of the vegetation of 0.15 with the large vegetation fraction is the main reason for the underestimation of the albedo (fig. 4.12) and consequently $\mathcal{K}^{\uparrow}$ at the rural sites. However, the shape of the diurnal course of the simulation, which is mainly dominated by the zenith angle dependence of the albedo for direct radiation in (2.24), is similar to the measurements. In contrast to that, the simulated albedo of the urban part of the grid cell is nearly constant and, consequently, the grid cell average albedo at the urban sites exhibits a smaller diurnal variation than at the rural sites. The measurements at BSPR, BSPA and ALLS, however, show a diurnal variation similar to the rural sites. Aida (1982) found that a flat concrete surface also showed a similar albedo variation during the day. The albedo of more complex concrete surfaces was lower in general but with the same shape of the diurnal course. In DCEP the albedo for direct radiation of the urban surfaces is assumed constant, which is likely the cause for the almost constant urban albedo in the simulation. Nonetheless, the resulting absolute error of $\mathcal{K}^{\uparrow}$ is small due to the low irradiance at the time of the underestimation of the albedo.

The measurement of the **incoming longwave radiation** $\mathcal{L}^{\downarrow}$ is affected by larger uncertainties than the measurement of the solar irradiance, and the difference between urban and rural stations is in the order of measurement error (Christen and Vogt 2004). This difference amounts up to $10\,\mathrm{W\,m^{-2}}$ for the hourly average (fig. 4.13 on page 100) and up to $45\,\mathrm{W\,m^{-2}}$ for a single measurement at BSPA and VLNF. With this in mind, the CCLM/DCEP model shows a good performance for $\mathcal{L}^{\downarrow}$ with a slight over-

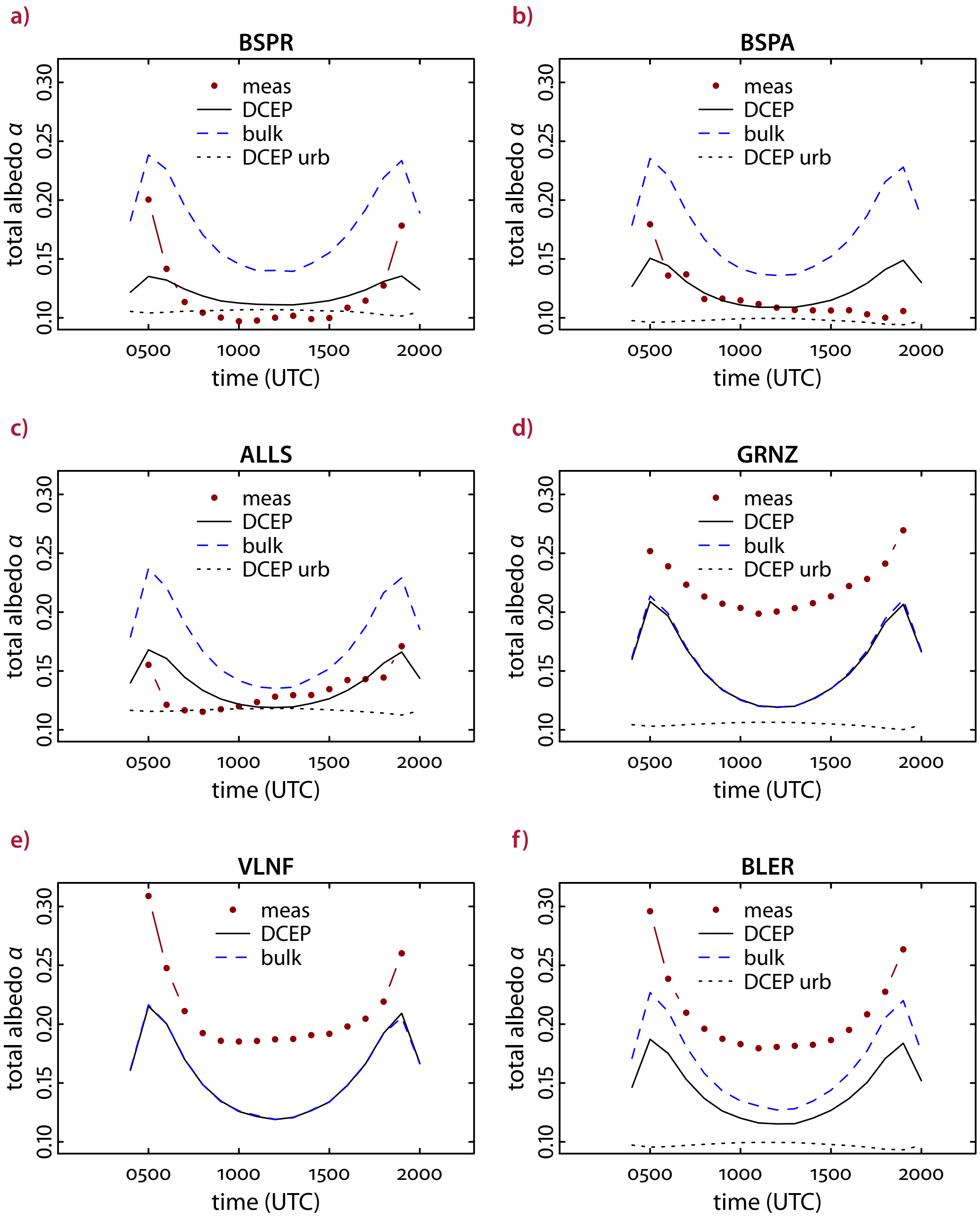

Figure 4.12. Measured and simulated average diurnal cycle of the total albedo α between 20 June 2002 and 9 July 2002. The simulations are conducted with either the DCEP or the bulk scheme. The "DCEP urb" values represent only the total albedo of the urban part of the corresponding mesoscale grid cell, α_{urb}; otherwise the simulated values represent the mesoscale grid cell average.

estimation by up to 16 $\mathrm{W\,m^{-2}}$ for the urban stations and an underestimation by up to 16 $\mathrm{W\,m^{-2}}$ for the rural stations. The mostly unsystematic RMSE is approx. 21 $\mathrm{W\,m^{-2}}$ for all stations with an absolute value of the MBE of up to 6 $\mathrm{W\,m^{-2}}$. The increased boundary layer temperature in the simulation with DCEP (see section 4.4.3) leads to the increase in $\mathcal{L}^{\downarrow}$ in the urban area compared with the bulk simulation. Similar effects of the urban surfaces were observed at Montreal (Canada; Oke and Fuggle 1972), Tokyo (Japan; Aida and Yaji 1979), Brandon (Canada; Suckling 1981), Toulouse (France; Estournel et al. 1983) and Cairo (Egypt; Frey et al. 2011). Nonetheless, the bulk simulation results in RMSE and MBE values similar to the ones of the simulation with DCEP, especially when considering the measurement error estimate.

The **emitted and reflected longwave radiation** $\mathcal{L}^{\uparrow}$ is larger for urban sites than for the rural sites mainly due to higher urban surface temperatures or different surface emissivities (Christen and Vogt 2004). The average difference of $\mathcal{L}^{\uparrow}$ between the urban BSPR and the rural VLNF or BLER of approx. 17 $\mathrm{W\,m^{-2}}$ is reproduced by DCEP but not by the bulk scheme. In DCEP, the higher urban surface temperatures increase $\mathcal{L}^{\uparrow}$ while the radiation trapping decreases $\mathcal{L}^{\uparrow}$ (cf. section 4.4.1). In total, the effects accumulate to an increase of $\mathcal{L}^{\uparrow}$ for the urban area of Basel. While this change improves the performance at BSPR in terms of $\mathcal{L}^{\uparrow}$ by reducing the RMSE from 17 $\mathrm{W\,m^{-2}}$ for the bulk scheme to 13 $\mathrm{W\,m^{-2}}$ and the MBE from −11 $\mathrm{W\,m^{-2}}$ to 2 $\mathrm{W\,m^{-2}}$, the performance at BSPA is slightly worse than by the bulk scheme with an by 1 $\mathrm{W\,m^{-2}}$ increased RMSE and a 5 $\mathrm{W\,m^{-2}}$ larger MBE. In general, at the urban stations, the sensors measure a mixture from different surface types (section 4.2), which does not necessarily represent the average of the mesoscale grid cell. This might explain the slight overestimation with DCEP at BSPA. At all stations except at GRNZ, DCEP tends to overestimate the nighttime $\mathcal{L}^{\uparrow}$. This is also true for the bulk scheme at ALLS, VLNF and BLER. The reason for this overestimation are probably too high surfaces temperatures, which are likely caused by the too high air temperatures (see section 4.4.3). At the suburban and rural sites, DCEP and the bulk scheme underestimate the midday $\mathcal{L}^{\uparrow}$.

The net radiation $\mathcal{R}^{*}$ calculated from the components of the radiation budget by means of

$$\mathcal{R}^{*} = \mathcal{K}^{\Downarrow} - \mathcal{K}^{\uparrow} + \mathcal{L}^{\downarrow} - \mathcal{L}^{\uparrow} \tag{4.11}$$

is depicted in fig. 4.15 on page 102 and summarizes the findings described above. $\mathcal{R}^{*}$ is measured to be up to 90 $\mathrm{W\,m^{-2}}$ larger at the urban sites than at the rural sites during daytime mainly due to the low urban albedo. During nighttime, however, the urban area (at the stations) emits up to 25 $\mathrm{W\,m^{-2}}$ more energy due to higher longwave emissions. While CCLM/DCEP overestimates $\mathcal{R}^{*}$ by up to 75 $\mathrm{W\,m^{-2}}$ at BSPR and BSPA, and up to 88 $\mathrm{W\,m^{-2}}$ at ALLS at 1200-1300 UTC mainly due to the overestimation of $\mathcal{K}^{\Downarrow}$ and captures it otherwise well, the deviations are larger for the other stations. Due to the underestimation of the local rural albedo in CCLM and the resulting underestimation of $\mathcal{K}^{\uparrow}$, $\mathcal{R}^{*}$ is overestimated there.

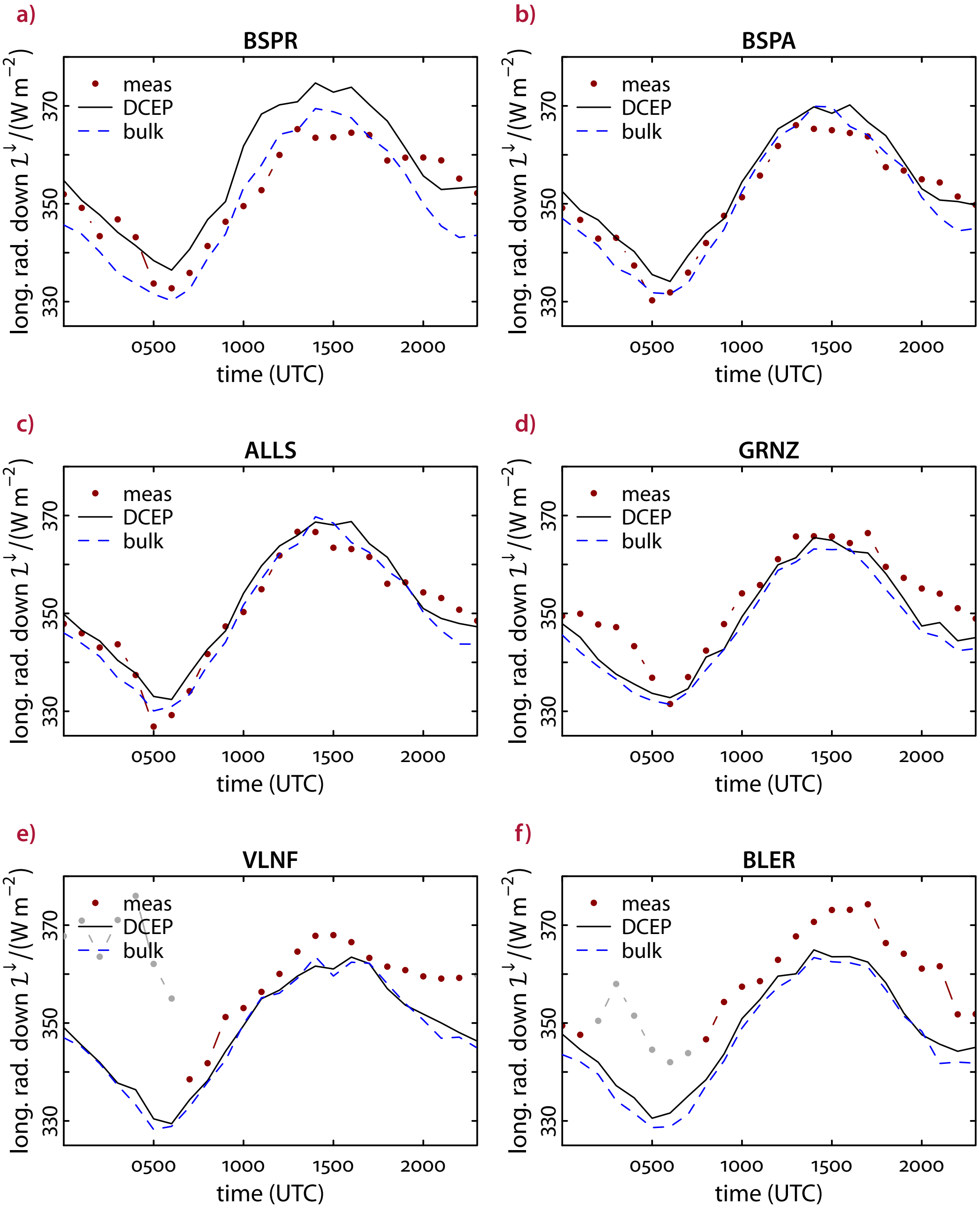

Figure 4.13. Measured and simulated incoming average diurnal cycle of the longwave radiation $\mathcal{L}^{\downarrow}$ near the surface between 20 June 2002 and 9 July 2002. The simulations are conducted with either the DCEP or the bulk scheme and represent the mesoscale grid cell average.

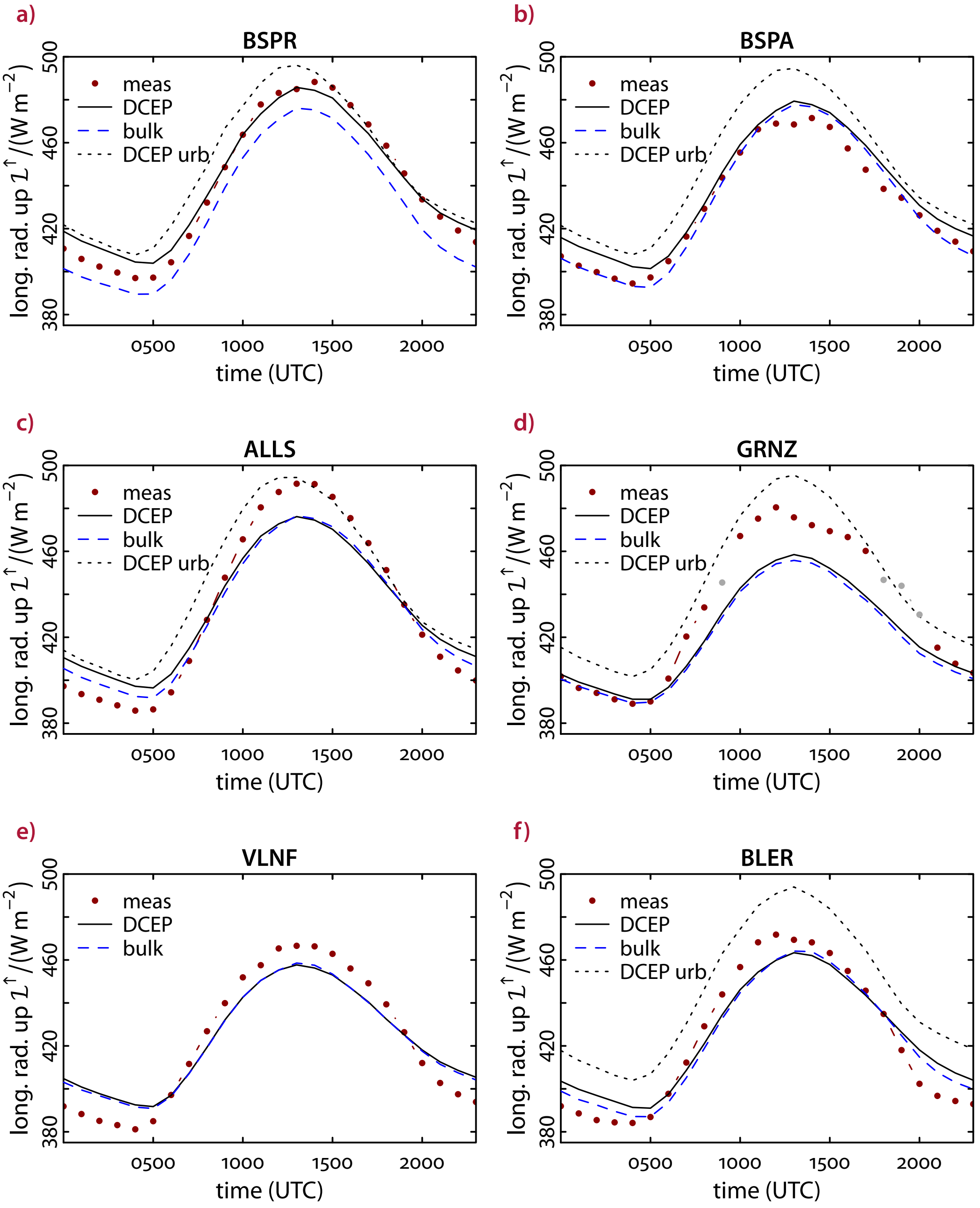

Figure 4.14. Measured and simulated average diurnal cycle of the reflected and emitted average longwave radiation $\mathcal{L}^{\uparrow}$ near the surface between 20 June 2002 and 9 July 2002. The simulations are conducted with either the DCEP or the bulk scheme. The "DCEP urb" values represent only the longwave radiation of urban part of the corresponding mesoscale grid cell, $L^{\uparrow}_{\text{urb}}$; otherwise the simulated values represent the mesoscale grid cell average.

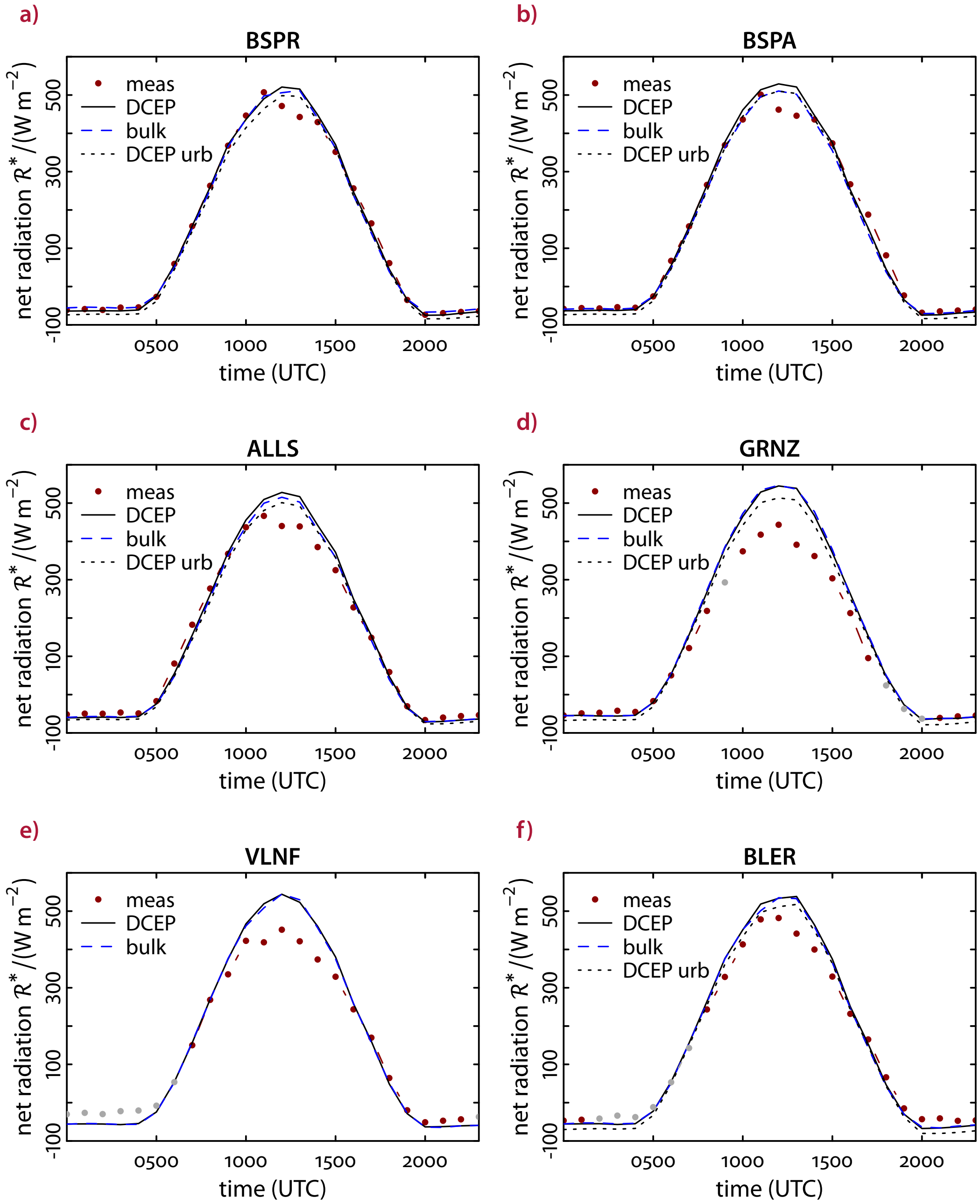

Figure 4.15. Average diurnal cycle of the net radiation $\mathcal{R}^*$ near the surface between 20 June 2002 and 9 July 2002 calculated from shortwave and longwave radiation budget. The simulations are conducted with either the DCEP or the bulk scheme. The "DCEP urb" values represent only the net radiation of the urban part of the corresponding mesoscale grid cell, R^*_{urb}; otherwise the simulated values represent the mesoscale grid cell average.

Site	$\mathcal{K}^{⤋}$		$\mathcal{K}^{\uparrow}$		$\mathcal{L}^{\downarrow}$		$\mathcal{L}^{\uparrow}$		$\mathcal{R}^{*}$	
	RMSEs (T/S/U)	MBE	RMSEs (T/S/U)	MBE	RMSEs (T/S/U)	MBE	RMSEs (T/S/U)	MBE	RMSEs (T/S/U)	MBE
BSPR	106 / 26 / 103	2	12 / 3 / 12	2	22 / 5 / 21	4	13 / 7 / 11	2	82 / 16 / 81	2
	102 / 21 / 100	*7*	*23 / 17 / 16*	*14*	*20 / 4 / 20*	*-3*	*17 / 12 / 12*	*-11*	*77 / 20 / 75*	*2*
BSPA	104 / 20 / 102	6	12 / 4 / 12	1	20 / 3 / 20	2	12 / 7 / 10	6	81 / 10 / 81	1
	103 / 20 / 101	*8*	*20 / 12 / 15*	*11*	*19 / 3 / 19*	*-1*	*11 / 1 / 11*	*1*	*79 / 19 / 77*	*-5*
ALLS	100 / 20 / 98	6	14 / 5 / 13	-1	20 / 2 / 20	1	18 / 14 / 11	0	79 / 8 / 79	8
	101 / 20 / 99	*8*	*18 / 6 / 16*	*6*	*19 / 2 / 19*	*-1*	*17 / 12 / 12*	*-2*	*77 / 4 / 77*	*2*
GRNZ	100 / 21 / 98	5	36 / 34 / 13	-19	20 / 4 / 19	-3	22 / 18 / 12	-11	94 / 43 / 84	37
	100 / 21 / 98	*7*	*36 / 33 / 13*	*-19*	*19 / 5 / 18*	*-5*	*23 / 20 / 12*	*-13*	*95 / 45 / 83*	*39*
VLNF	101 / 20 / 99	6	30 / 27 / 13	-15	22 / 6 / 22	-6	15 / 10 / 10	0	91 / 25 / 87	22
	101 / 20 / 99	*6*	*30 / 27 / 13*	*-15*	*22 / 7 / 21*	*-7*	*14 / 10 / 10*	*0*	*91 / 24 / 88*	*21*
BLER	99 / 23 / 96	2	30 / 28 / 12	-17	22 / 6 / 21	-5	14 / 10 / 11	2	82 / 17 / 80	12
	100 / 22 / 98	*5*	*26 / 22 / 14*	*-12*	*22 / 8 / 20*	*-7*	*14 / 8 / 11*	*-1*	*80 / 13 / 79*	*10*

Table 4.4. Root-mean-square errors (RMSE) and mean-bias errors (MBE) of the components of the radiation budget at the surface between 20 June 2002 and 9 July 2002 calculated from the hourly grid cell averaged model output at the mesoscale grid cells in which the sites were situated. All values are in $\mathrm{W\,m^{-2}}$. In addition to the total RMSE listed first (T), the systematic RMSE (S) and the unsystematic RMSE (U) are listed. The values are given for the total incoming shortwave radiation $\mathcal{K}^{⤋}$, the reflected shortwave radiation $\mathcal{K}^{\uparrow}$, the incoming longwave radiation $\mathcal{L}^{\downarrow}$, the reflected and emitted longwave radiation $\mathcal{L}^{\uparrow}$ and the total radiation budget $\mathcal{R}^{*}$. The first row of each site in upright font gives the values for the coupled CCLM/DCEP simulation while the second row in italics lists the results of the default bulk scheme of CCLM.

4.4.2. Surface energy budget

In this subsection, the model performance is evaluated in terms of the remaining components of the energy budget at the surface. The RMSE and MBE values are listed in tab. 4.5 on page 110. The latent and sensible heat flux are considered positive if energy flows from the surface into the atmosphere and negative in the opposite case. The storage flux, on the other hand, is positive if the surface stores energy and negative if the surface releases energy. In general, the measured fluxes are an average over their source area, which depends on the wind direction and the stability of the boundary layer (Schmid and Oke 1990). Thus, in contrast to the components of the radiation budget, this source area is not stationary in time. Furthermore, Christen and Vogt (2004) found an energy gap when comparing the measured soil fluxes with the residual storage fluxes calculated from (4.13) on page 108 at the rural sites. This gap amounted to approx. 18 % of the radiation budget $\mathcal{R}^*$ during daytime and to typically around 30 % of $\mathcal{R}^*$ during nighttime (see fig. 4.18 on page 109). A similar non-closed energy balance has been found by e.g. Wilson et al. (2002), Offerle et al. (2005), Oncley et al. (2007) and Frey et al. (2011). According to Christen and Vogt (2004), the reason for this energy gap is supposedly the underestimation of the absolute values of both, the sensible and the latent heat flux. Furthermore, they assumed that this effect is also present at the urban sites. Oncley et al. (2007) speculated that the horizontal advection of heat is the major issue. Foken (2008) argues further that the measurements of the turbulent fluxes with the eddy covariance method (e.g. Moncrieff et al. 1997) cannot detect energy transport by large scale eddies caused by the heterogeneity of the landscape. However, since the storage of energy in the plant canopy and in the photosynthetic products as well as in the soil above the heat plates measuring the soil fluxes is not negligible (Meyers and Hollinger 2004; Heusinkveld et al. 2004), the real storage flux might be larger than the measured soil heat flux. Therefore, the underestimation of the sensible and the latent heat flux might not be as severe as indicated by the figures before. In the following, the above mentioned sources of error have to be considered.

In general, mid-latitude cities with negligible irrigation feature less evapotranspiration than their rural surroundings due to the lower vegetation fraction (Christen and Vogt 2004; Offerle et al. 2006). In the bulk scheme, this is taken into account by a lower vegetation fraction and leaf area index in the urban area (cf. fig. 1.1) whereas DCEP treats separately a fully vegetated part and a purely urban part of the grid cell. In the latter, the **latent heat flux** $\lambda\mathcal{E}$ is neglected, thus the grid cell average $\lambda\mathcal{E}$ is the reduced latent heat flux of the vegetated part (cf. (3.90)). At BSPR, CCLM/DCEP capture $\lambda\mathcal{E}$ well with an RMSE of $29\,\mathrm{W\,m^{-2}}$, which is only a small improvement in comparison to the bulk scheme with a RMSE of $30\,\mathrm{W\,m^{-2}}$. Here, CCLM/DCEP results in a lower latent heat flux than the bulk scheme during the late evening, night and early afternoon, which agrees with observations. Thus, the average $\lambda\mathcal{E}$ is captured better by DCEP with a small MBE of $-2\,\mathrm{W\,m^{-2}}$ than by the bulk scheme with a MBE of $14\,\mathrm{W\,m^{-2}}$.

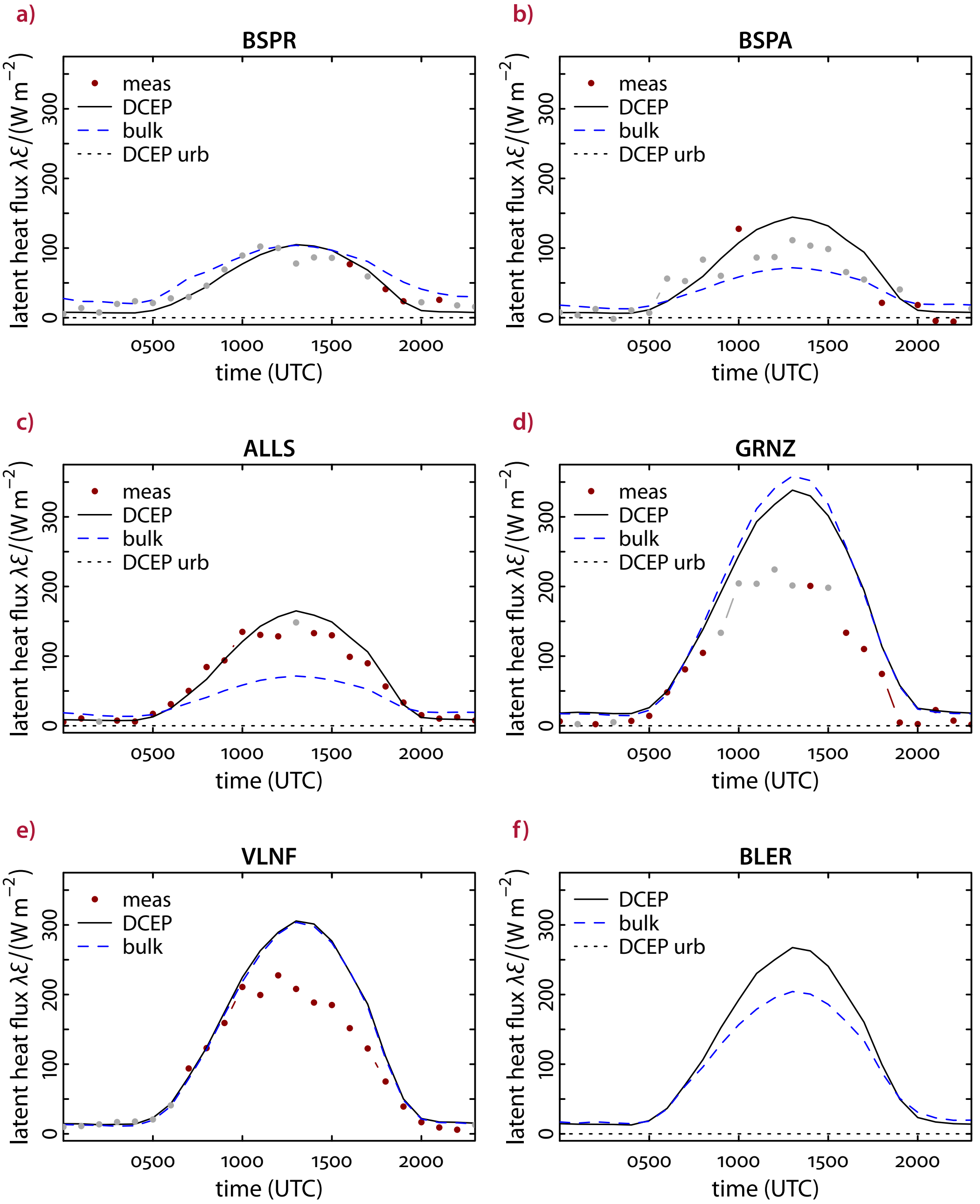

Figure 4.16. Measured and simulated average diurnal cycle of the latent heat flux $\lambda\mathcal{E}$ between 20 June 2002 and 9 July 2002. The simulations are conducted with either the DCEP or the bulk scheme and represent the mesoscale grid cell average. At BLER, the latent heat flux was not measured.

Due to the lower urban fraction, the simulated $\lambda\mathcal{E}$ is approx. 50 W m^{-2} larger at BSPA than at BSPR in the simulation with DCEP. While the bulk scheme underestimates $\lambda\mathcal{E}$ with a MBE of −8 W m^{-2}, DCEP overestimates it with a MBE of 15 W m^{-2}. Although the total RMSE increases by 3 W m^{-2} with DCEP, the systematic RMSE (27 W m^{-2}) is considerably lower than with the bulk scheme (45 W m^{-2}).

Interestingly, the tile approach of DCEP clearly improves the performance at the suburban station ALLS. The larger vegetation fraction and leaf area index in the vegetated part of the grid cell result in a latent heat flux of approx. 165 W m^{-2} at 1300 UTC, which is captured by CCLM/DCEP. The bulk scheme with the vegetation parameters assigned to the city produces only a flux of approx. 71 W m^{-2}. The mostly systematic RMSE of 45 W m^{-2} with the bulk scheme is improved to a mostly unsystematic RMSE of 31 W m^{-2}, and the MBE is improved from −23 W m^{-2} to 7 W m^{-2}.

At the rural stations GRNZ and VLNF, $\lambda\mathcal{E}$ is overestimated during daytime by up to 150 W m^{-2}. Analogue to the underestimation of the reflected shortwave radiation at these stations, the overestimation of $\lambda\mathcal{E}$ is due to the different vegetation parameters near the sensors than are used as the grid cell average. In particular, the non-irrigated agricultural grassland and crop land have a lower leaf-area-index than the assumed 3.4 m^{2} m^{-2}. Due to the small urban fraction at these site, the values of $\lambda\mathcal{E}$ differ only slightly between the simulations with the bulk scheme and DCEP.

In contrast to $\lambda\mathcal{E}$, the **sensible heat flux** $\mathcal{H}$ is larger in the centre of Basel than in the rural surrounding (fig. 4.17). The values measured at the urban stations are more than twice as large as the ones at the rural stations at noon. CCLM/DCEP captures the maximum $\mathcal{H}$ at the urban BSPR and BSPA well, whereas it is overestimated by approx. 80 W m^{-2} at ALLS (but reduced from on overestimation by 166 W m^{-2} by the bulk scheme). During the night, DCEP captures the slightly positive $\mathcal{H}$ of approx. 26 W m^{-2} at BSPR and of approx. 11 W m^{-2} at BSPA, while the bulk scheme produces a negative $\mathcal{H}$. Due to the increased heat storage in the urban surfaces (cf. section 3.3) and the radiation trapping in DCEP, the urban surfaces are warmer during the night than with the bulk scheme resulting in a positive sensible heat flux. At ALLS, $\mathcal{H}$ is about 0 W m^{-2}, which is reproduced by DCEP. In total, at BSPR the RMSE is reduced from 68 W m^{-2} with the bulk scheme to 54 W m^{-2} and the MBE is improved from −24 W m^{-2} to −8 W m^{-2}. At BSPA, however, although the RMSE is reduced from 68 W m^{-2} with DCEP to 58 W m^{-2} with the bulk scheme, the MBE worsens from 0 W m^{-2} to −14 W m^{-2}. This is due to the underestimation of $\mathcal{H}$ during the morning and the late afternoon. At the rural stations GRNZ and VLNF, the maximum $\mathcal{H}$ is overestimated by CCLM by approx. 50 W m^{-2}. Possible reasons for this are the overestimation of the wind velocity (see section 4.4.3) or the assumed grid cell average roughness lengths that does not correspond to the local conditions. In the simulation, a roughness length of about 0.2 m is used, which rather corresponds to high mature crops than to grassland with a roughness length of 0.008 m to 0.06 m depending on the height of the grass (Wieringa 1993).

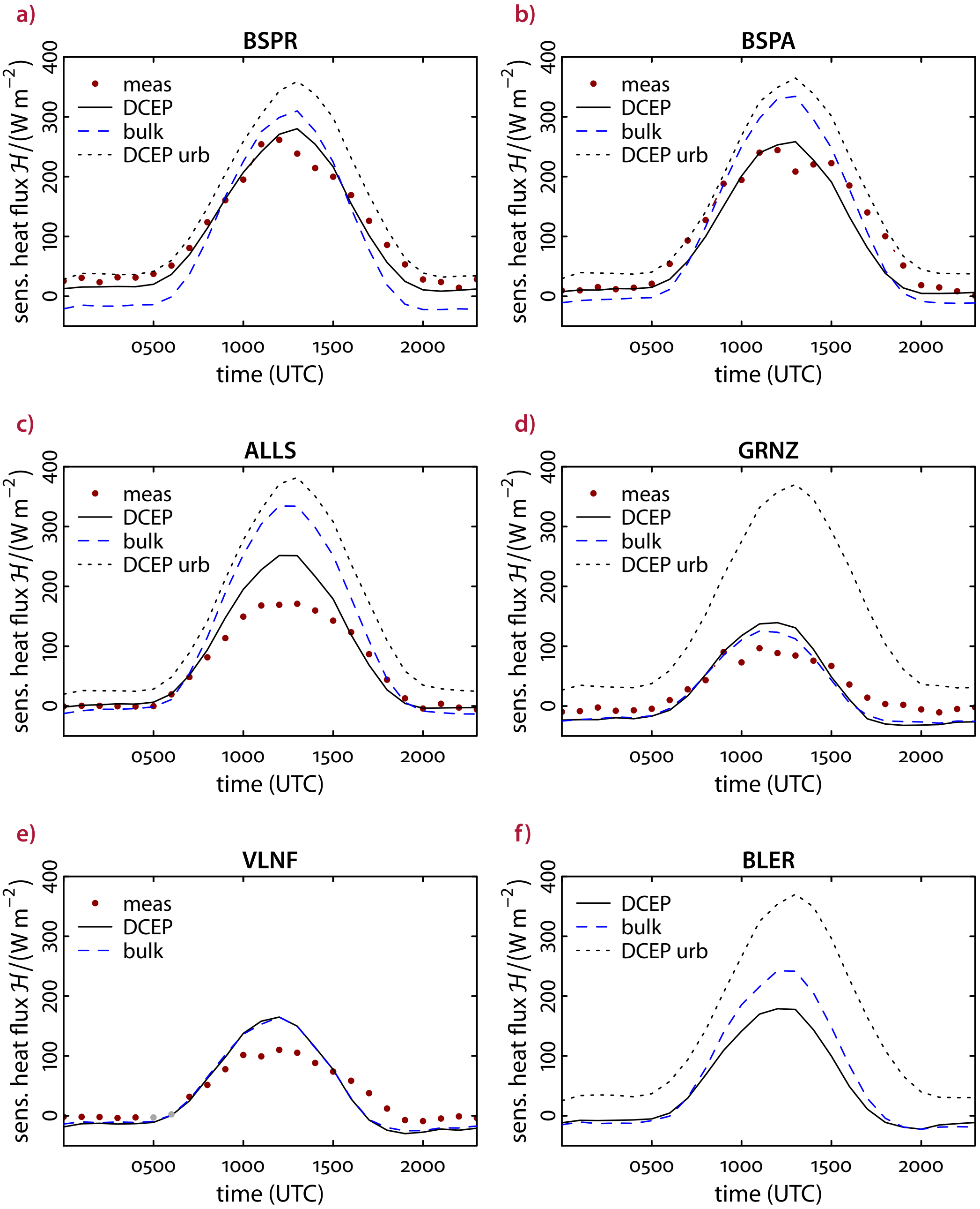

Figure 4.17. Measured and simulated average diurnal cycle of the sensible heat flux $\mathcal{H}$ between 20 June 2002 and 9 July 2002. The simulations are conducted with either the DCEP or the bulk scheme. The "DCEP urb" values represent only the sensible heat flux of the urban part of the corresponding mesoscale grid cell, H_{urb}; otherwise the simulated values represent the mesoscale grid cell average. At BLER, the sensible heat flux was not measured.

To formulate the energy budget of the *total* urban landscape, the energy fluxes are considered that flow into an imaginary volume which includes all important urban processes. This volume extends from the soil surface at a depth below which energy exchanges can be neglected at the time scale of interest up to a height of the roof level (Oke 1988; Arnfield 2003). Thus, in addition to the components of the energy budget of a soil surface or a single urban surface described in (3.55) on page 54, the energy budget of the total urban landscape incorporates further energy fluxes into the air volume (Oke 1988):

$$\mathcal{R}^* + \mathcal{H}_{\mathrm{anthr}} = \mathcal{H} + \lambda\mathcal{E} + \mathcal{G} + \mathcal{A}\,, \tag{4.12}$$

where $\mathcal{H}_{\mathrm{anthr}}$ is the anthropogenic heat flux, $\mathcal{G}$ the storage flux and $\mathcal{A}$ is the net advection through the sides of the volume. As discussed in the description of the set-up of the simulation in section 4.3, $\mathcal{H}_{\mathrm{anthr}}$ is neglected for the present summertime simulation. Despite the discussion at the beginning of this subsection, also the advection flux $\mathcal{A}$ is disregarded as proposed by Christen and Vogt (2004) for the BUBBLE results and was also done by Oke (1982), Oke et al. (1999), Grimmond and Oke (2002), Spronken-Smith (2002), Lemonsu et al. (2008) and Frey et al. (2011). Thus, the **storage flux** $\mathcal{G}$ can be calculated as the residual of the energy budget equation by

$$\mathcal{G} \approx \mathcal{R}^* - \mathcal{H} - \lambda\mathcal{E}\,. \tag{4.13}$$

Consequently, $\mathcal{G}$ accumulates all uncertainties of the other quantities in (4.13). The storage flux calculated from the measurements in that way represents, with the discussion above, an *upper* limit for the absolute value of the real storage flux. Furthermore, at the rural sites, direct measurements of the soil flux are available. This flux is part of the storage flux and can therefore be interpreted as a *lower* limit for the absolute value of the storage flux.

Typically, the heat storage is increased in urban areas compared to the rural surroundings during daytime (Grimmond and Oke 1999b) due to the increased surface area (Harman and Belcher 2006) and different thermal properties of the urban surfaces (Oke 1987). During nighttime, this additional stored energy is released maintaining a positive sensible heat flux (Oke 1988). By including additional vertical urban surfaces with specific urban surface parameters, DCEP simulates larger $\mathcal{G}$ during daytime and smaller (in absolute values larger) $\mathcal{G}$ during nighttime in the urban area of Basel than the bulk scheme (fig. 4.18). While this behaviour leads to a similar MBE of both schemes at BSPR, the RMSE is decreased with DCEP from 64 $\mathrm{W\,m^{-2}}$ to 57 $\mathrm{W\,m^{-2}}$. Similar improvements can be found at BSPA and ALLS.

At the rural sites GRNZ and VLNF, CCLM underestimates $\mathcal{G}$ during daytime when comparing with the residual storage flux but overestimates it when comparing with the directly measured flux. Thus, the simulated values lie between upper and the lower estimate. While the simulated storage fluxes at all sites and also most of the storage

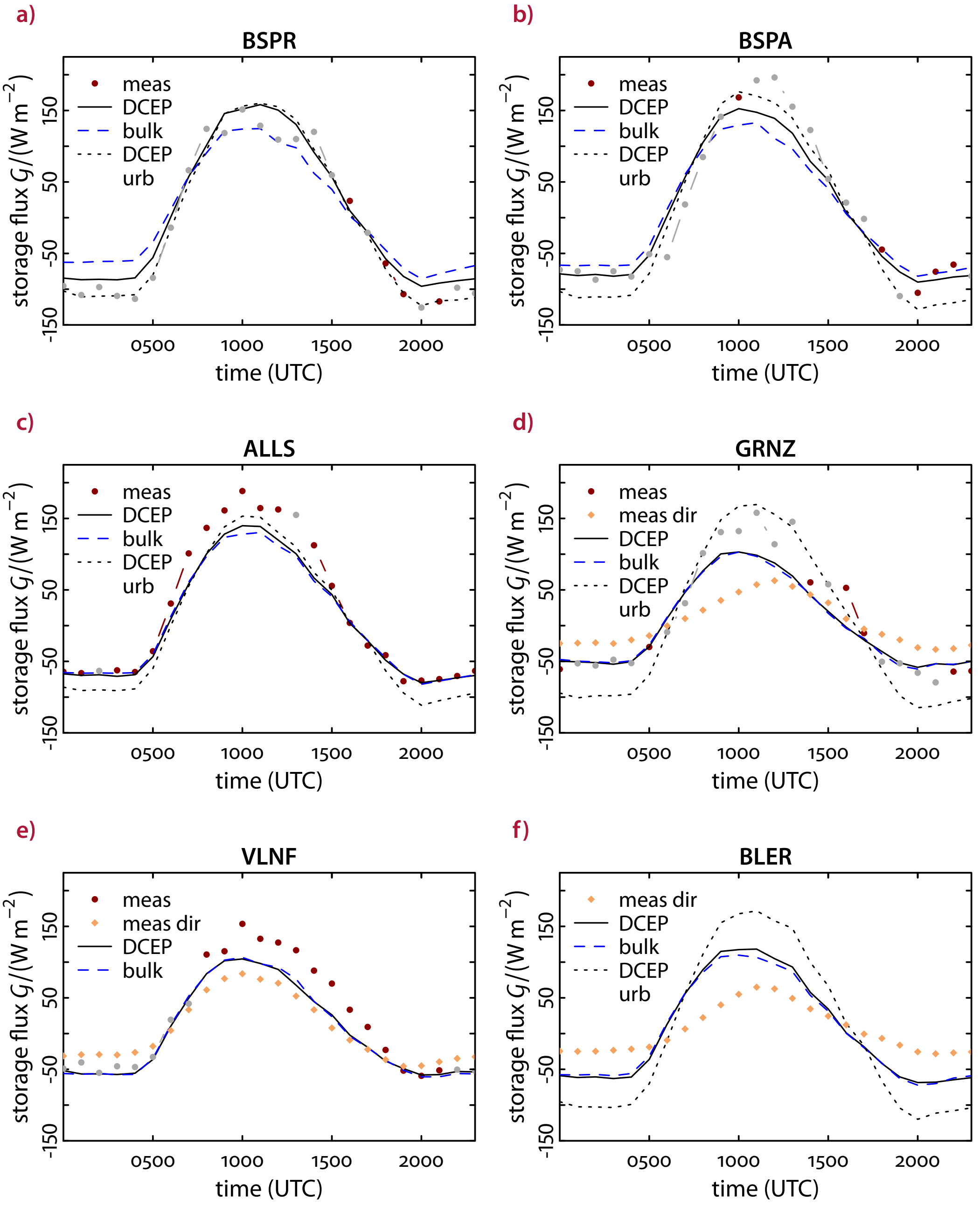

Figure 4.18. Average diurnal cycle of the storage flux G between 20 June 2002 and 9 July 2002 calculated from the net radiation, the sensible and the latent heat flux by means of (4.13). The simulations are conducted with either the DCEP or the bulk scheme. The "DCEP urb" values represent only the urban part of the storage flux of the corresponding mesoscale grid cell, G_{urb}; otherwise the simulated values represent the mesoscale grid cell average. In addition, "meas dir" shows the direct measurements at the rural sites. Since the sensible and latent heat fluxes were not measured at BLER, the storage flux calculated from measurements is not available there.

Site	$\lambda\mathcal{E}$		$\mathcal{H}$		$\mathcal{G}$	
	RMSEs (T/S/U)	MBE	RMSEs (T/S/U)	MBE	RMSEs (T/S/U)	MBE
BSPR	29 / 13 / 26	-2	54 / 14 / 52	-8	57 / 34 / 46	12
	30 / 19 / 23	*14*	*68 / 27 / 62*	*-24*	*64 / 52 / 37*	*12*
BSPA	52 / 27 / 44	15	58 / 26 / 52	-14	64 / 34 / 55	0
	49 / 45 / 20	*-8*	*68 / 12 / 67*	*0*	*67 / 47 / 48*	*-2*
ALLS	31 / 7 / 30	7	50 / 17 / 47	15	50 / 30 / 40	-12
	45 / 44 / 12	*-23*	*84 / 57 / 61*	*39*	*53 / 34 / 40*	*-14*
GRNZ	84 / 49 / 68	48	40 / 8 / 39	-6	58 / 43 / 40	-10
	90 / 54 / 71	*52*	*36 / 8 / 35*	*-8*	*58 / 44 / 38*	*-10*
VLNF	76 / 38 / 66	38	43 / 11 / 42	0	50 / 33 / 38	-18
	74 / 35 / 66	*35*	*42 / 9 / 41*	*1*	*50 / 32 / 38*	*-18*

Table 4.5. Root-mean-square errors (RMSE) and mean-bias errors (MBE) of the components of the energy budget at the surface between 20 June 2002 and 9 July 2002 calculated from the hourly grid cell averaged model output at the mesoscale grid cells in which the sites were situated. All values are in $\mathrm{W\,m^{-2}}$. In addition to the total RMSE listed first (T), the systematic RMSE (S) and the unsystematic RMSE (U) are listed. The values are given for the latent heat flux $\lambda\mathcal{E}$, the sensible heat flux $\mathcal{H}$ and the storage flux $\mathcal{G}$. The first row of each site in upright font gives the values for the coupled CCLM/DCEP simulation while the second row in italics lists the results of the default bulk scheme of CCLM. At BLER, the energy budget was not measured.

fluxes calculated as the energy residual show a pronounced temporal hysteresis pattern as found in all cities analysed by Grimmond and Oke (1999b) by peaking about 1 h to 2 h before the net radiation, only the directly measured soil flux at VLNF shows a similar behaviour. At both GRNZ and BLER, this effect is weaker or non-existent in the direct measurement.

4.4.3. Air temperature and wind velocity

In this subsection, the simulated air temperatures and wind velocities of both CCLM with DCEP and the bulk scheme are compared with the station measurements. At the urban and suburban stations, air temperature measurements are available at several heights so the height chosen for evaluation is the one closest to the first model level at about 10 m. Thus, the measurements can be compared to the simulated prognostic air temperature to avoid the influence of the calculation of the 2 m temperature in (3.91). Furthermore, the air temperature at this height might better represent the grid cell average temperature. The wind speed measurements are compared with the wind speed $\mathcal{U}^{\mathrm{h}}_{10\,\mathrm{m}}$ at a height of 10 m or with $\mathcal{U}^{\mathrm{h}}_{2}$ of the second main mesoscale model layer at a height of about 35 m, depending on the measurement height. This assignment works well for all stations except for VLNF where the wind speed was measured at a height of 2 m and is thus not comparable to the lowest simulated value at 10 m. All RMSE values and the MBE are listed in tab. 4.6 on page 117.

Rotach et al. (2005) compared temperature and wind profiles measured on 5 July 2002 by the Doppler SODAR / RASS at BKLH and by a tethered balloon 2.4 km further south in the centre of Basel. In addition, a wind profiler operated at BSPA. While the form of the temperature profiles were comparable showing an offset of about 2 K, and all systems agreed on the wind direction up to a height of about 700 m above sea level, the wind speed measurements differed by up to 4 m s^{-1} at certain heights. Up to a height of 600 m above sea level, the tethered balloon measured the highest wind speeds, the RASS up to 2 m s^{-1} lower wind speeds and the wind profiler again up to 1.2 m s^{-1} lower speeds than that. Here, Rotach et al. (2005) were uncertain as to how much of the differences can be attributed to spatial inhomogeneities in the wind field or measurement uncertainties of the various systems.

The **near-surface temperature** is depicted in fig. 4.19. At the rural stations, CCLM overestimates the 2 m temperature $\mathcal{T}_{2\,\mathrm{m}}$ by about 2.5 K during nighttime and by about 1 K at noon. Thus, the measurements show a stronger diurnal cycle than is simulated. The MBE is about 1 K and the RMSE is about 2.1 K whereas the simulation with DCEP is slightly worse than with the bulk scheme due to the slightly increased $\mathcal{T}_{2\,\mathrm{m}}$. At BSPR, CCLM with the bulk scheme captures the air temperature $\mathcal{T}_1$ at a height of approx. 10 m well during the late night till the afternoon and overestimates $\mathcal{T}_1$ by up to 1.8 K the rest of the time (total MBE of −0.4 K). The simulation with DCEP at BSPR is up to 2 K warmer during the night and early morning due to the increased sensible heat flux, and up to 1.5 K warmer at noon (total MBE of 0.6 K). Consequently, CCLM/DCEP overestimates $\mathcal{T}_1$ when CCLM with the bulk scheme captures it well and vice versa resulting in a similar RMSE of 1.7 K for both simulations. However, the bulk scheme captures the late night and morning temperatures only because two errors compensate each other: the CCLM is too warm in general and the bulk scheme does not reproduce the urban heat island of approx. 3 K. At BSPA and ALLS, both simulations overestimate $\mathcal{T}_1$ during the late night till the afternoon. Due to the increased temperature in the simulation with DCEP, the RMSE is approx. 0.5 K and the MBE 0.2 K larger with DCEP.

The **vertical profile of the potential temperature** θ calculated with (2.19) is shown for BKLH in fig. 4.20. A considerable difference between the CCLM simulations with the bulk scheme and DCEP can be found during the evening and night. Here, the simulation with DCEP is up to 0.75 K warmer on the lower levels and up to 0.2 K warmer at a height of 180 m due to the larger sensible heat flux near the surface resulting in a less stable atmosphere near the surface. Nonetheless, the simulated profile still indicates a statically stable boundary layer, while the measurements show a statically unstable atmosphere up to about 100 m. In the morning and in the afternoon, both simulations agree well with the measurements and at noon, both simulations overestimate θ by about 1 K up to a height of 500 m.

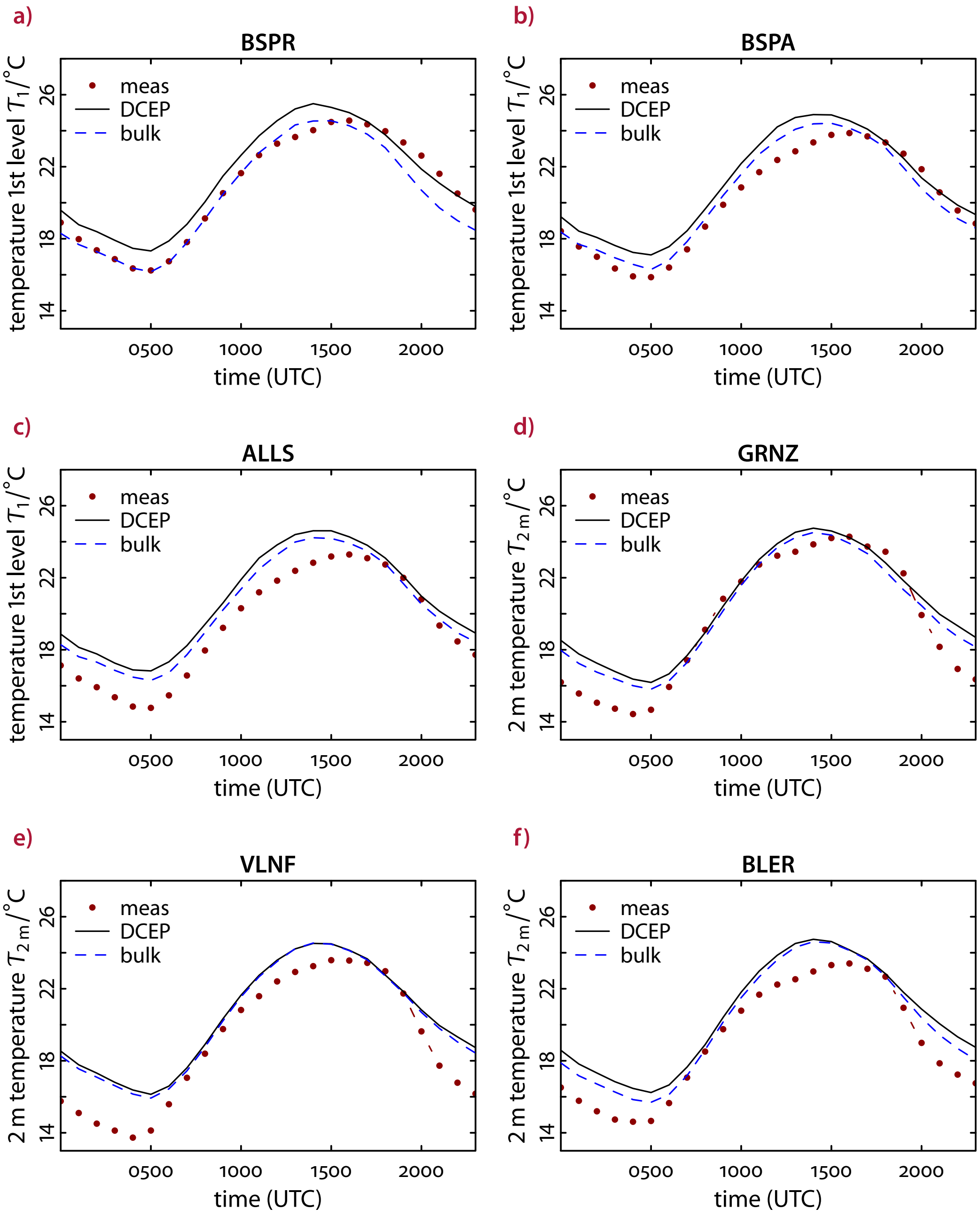

Figure 4.19. Measured and simulated average diurnal cycle of the air temperature T_1 at a height of about 10 m and $T_{2\,\text{m}}$ at a height of about 2 m between 20 June 2002 and 9 July 2002. The exact measurement heights are given in tab. 4.2. The simulations are conducted with either the DCEP or the bulk scheme and represent the mesoscale grid cell average.

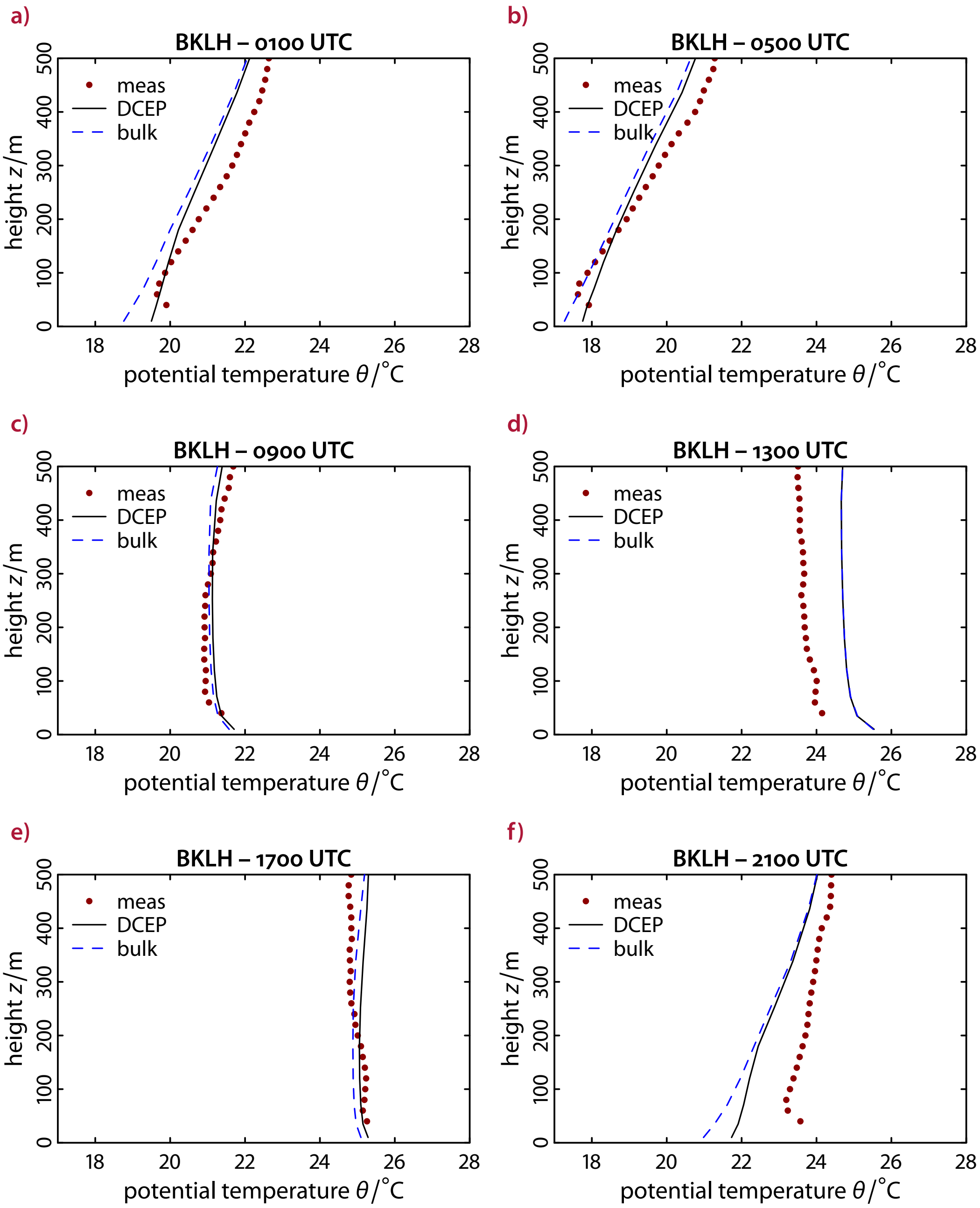

Figure 4.20. Measured and simulated average potential temperature θ profiles at Basel-Kleinhüningen for different times of the day. The simulations are conducted with either the DCEP or the bulk scheme and represent the mesoscale grid cell average.

The direct influence of the urban surfaces in DCEP causes the average **wind speed** to be reduced more strongly the higher the average wind speed is (see section 3.2). Nevertheless, the simulation with DCEP exhibits larger average wind speeds than the simulation with the bulk scheme (fig. 4.21). While the wind speed difference amounts to about 1 m s^{-1} at BSPR, the deviation is lower at the other stations. Thus, larger wind speeds are simulated with DCEP at the urban stations than at the rural GRNZ, and at the suburban ALLS than at the rural BLER. The effect that urbanization can increase the wind speed has also been found by Chandler (e.g. 1965), Bornstein and Johnson (1977), D. O. Lee (1979), Draxler (1986) and Fortuniak et al. (2006). Bornstein and Johnson (1977) reported a critical upwind rural wind velocity below which the air was effectively accelerated as it flowed over New York City (USA). This effect was due to the horizontal pressure gradient directed into the city induced by warmer near-surface temperatures in the city and due to a decreased stability of the atmosphere resulting in an increased downward flux of momentum. Above that critical wind speed the impact of the larger roughness elements in the city dominated resulting in a deceleration of the air. This critical value was found to be 3.6 m s^{-1} during daytime and 4.1 m s^{-1} during nighttime for observations from the period 1964–1967. While Chandler (1965) found respective values of 3.3 m s^{-1} and 5.6 m s^{-1} for London (UK) for 1961–1962, D. O. Lee (1979) reported lower values of 1.1 m s^{-1} and 2.3 m s^{-1}, respectively, for 1961–1970. Fortuniak et al. (2006) found an average critical wind speed of 1.13 m s^{-1} at Łódź (Poland), for the period 1997–2002. In the simulations, the bulk scheme includes the effects of the larger roughness elements by an increased roughness length of about 1 m. Under the assumption that this has a similar deceleration effect on the average wind speed as the parametrization with DCEP, DCEP necessarily results in larger wind speeds due to the increased near-surface temperature in the city. The locally higher near-surface temperatures induce larger pressure gradients in (2.14) and modify the stability functions in (2.29) and (2.30).

In the measurements, BSPR and BSPA show on average 0.59 m s^{-1} and 0.37 m s^{-1} lower wind speeds than GRNZ. This indicates that on average the wind velocity is slightly smaller in the city centre than in the rural surrounding. This is not reproduced by CCLM/DCEP and by CCLM with the bulk scheme only during nighttime. In general, both simulations overestimate the average wind velocity, especially during daytime. At BSPR, BSPA and ALLS, the bulk scheme captures the wind velocity better during nighttime; at GRNZ and BLER, DCEP captures the nighttime wind speed better. Nonetheless, at all stations (except VLNF), the RMSE is between 0.4 m s^{-1} and 0.7 m s^{-1} larger with DCEP than with the bulk scheme, and the MBE is between 0.3 m s^{-1} and 0.9 m s^{-1} larger.

The tendency to overestimate the wind speed is also seen in the **vertical wind profile** in fig. 4.22. In particular, at noon, CCLM/DCEP overestimates $\mathcal{U}^{\mathrm{h}}$ by more than 2 m s^{-1} at all depicted heights, the simulation with the bulk scheme overestimates $\mathcal{U}^{\mathrm{h}}$ by about 0.5 m s^{-1} less. While the bulk simulation agrees well with the measurement

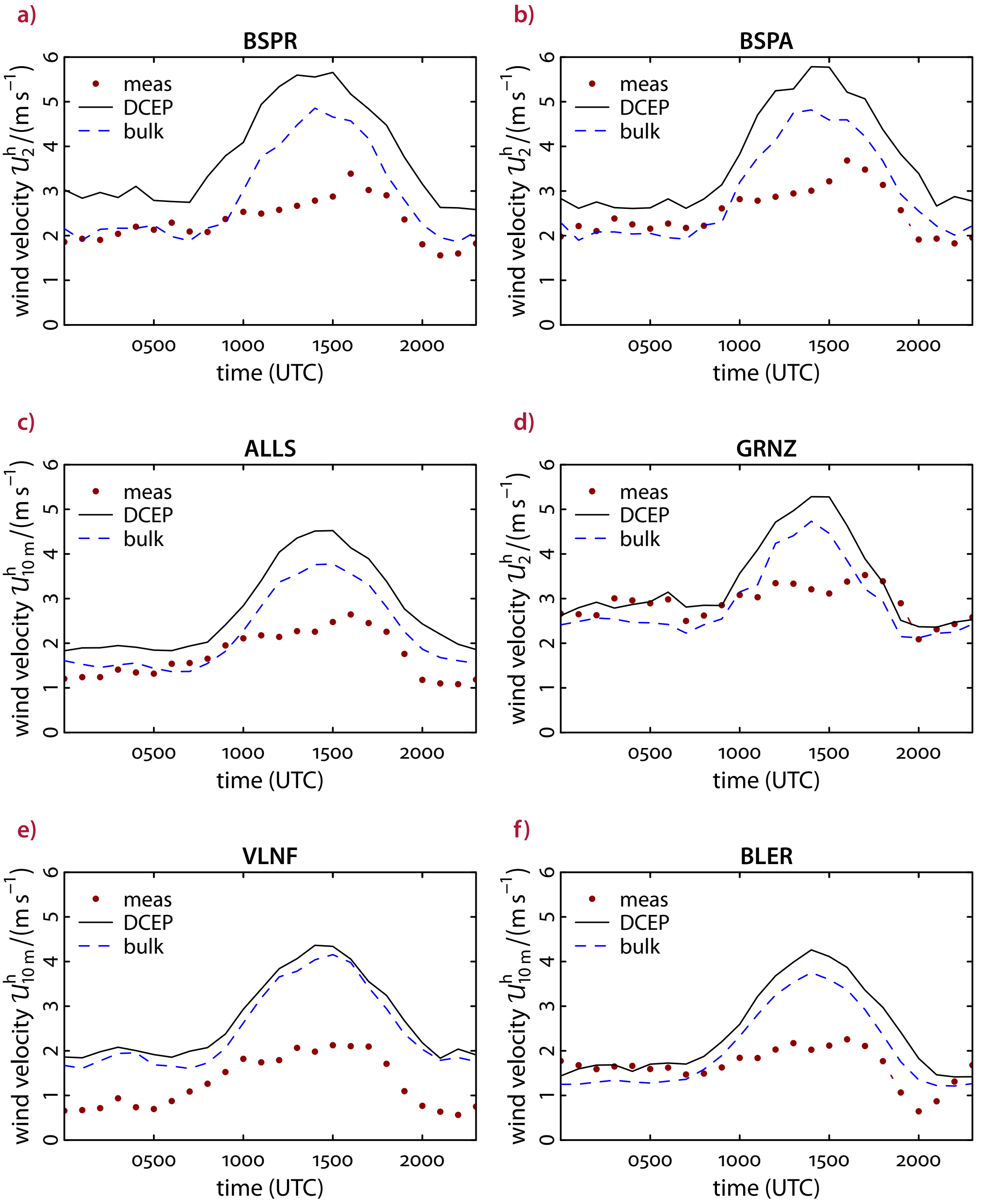

Figure 4.21. Measured and simulated average diurnal cycle of the wind velocity $\mathcal{U}_2^{\mathrm{h}}$ at the second mesoscale model layer at about 35 m and $\mathcal{U}_{10\,\mathrm{m}}^{\mathrm{h}}$ at a height of 10 m between 20 June 2002 and 9 July 2002. The simulations are conducted with either the DCEP or the bulk scheme. The simulated values represent the mesoscale grid cell average. At VLNF, the measurements took place at a height of 2 m and are thus not comparable with the simulated values at 10 m.

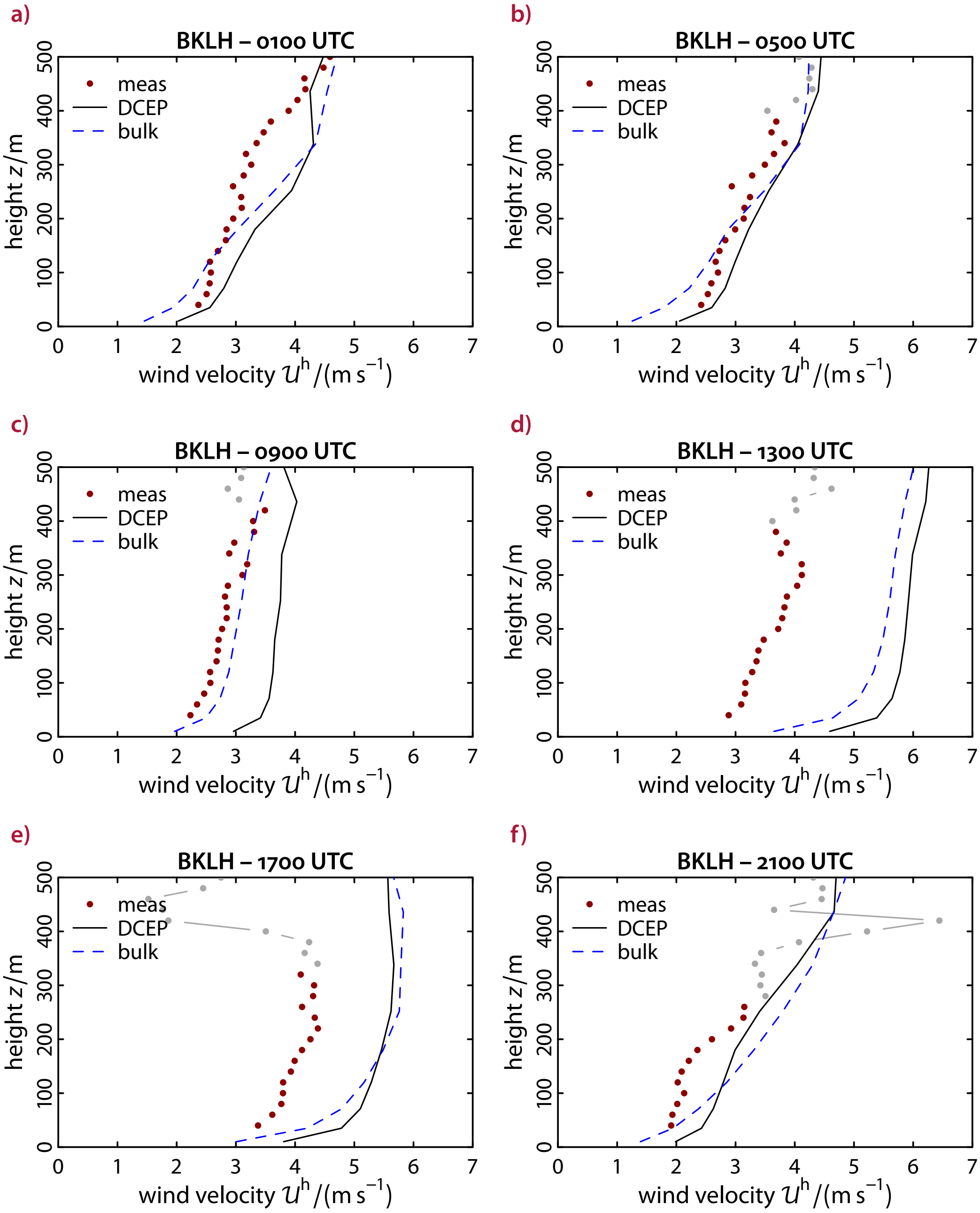

Figure 4.22. Measured and simulated average wind speed $\mathcal{U}^h$ profiles at Basel-Kleinhüningen for different times of the day between 20 June 2002 and 9 July 2002. The simulations are conducted with either the DCEP or the bulk scheme and represent the mesoscale grid cell average.

Site	$\mathcal{T}$		$\mathcal{U}$	
	RMSEs (T/S/U)	MBE	RMSEs (T/S/U)	MBE
BSPR	1.7 / 0.7 / 1.5	0.6	2.4 / 1.5 / 1.9	1.5
	1.7 / 0.5 / 1.6	*-0.4*	*1.7 / 0.6 / 1.5*	*0.6*
BSPA	1.7 / 0.9 / 1.4	0.9	2.2 / 1.2 / 1.9	1.2
	1.5 / 0.4 / 1.4	*0.3*	*1.6 / 0.4 / 1.6*	*0.4*
ALLS	2.0 / 1.5 / 1.4	1.4	1.6 / 1.0 / 1.3	1.0
	1.8 / 1.1 / 1.4	*0.9*	*1.2 / 0.5 / 1.1*	*0.5*
GRNZ	2.1 / 1.5 / 1.5	0.9	2.0 / 0.6 / 1.9	0.5
	2.1 / 1.2 / 1.5	*0.5*	*1.7 / 0.5 / 1.6*	*0.0*
VLNF	2.3 / 1.7 / 1.6	1.3	1.9 / 1.4 / 1.3	1.4
	2.2 / 1.5 / 1.6	*1.2*	*1.8 / 1.2 / 1.3*	*1.2*
BLER	2.0 / 1.4 / 1.4	1.2	1.8 / 0.8 / 1.6	0.7
	1.8 / 1.1 / 1.4	*0.9*	*1.4 / 0.4 / 1.3*	*0.4*

Table 4.6. Root-mean-square errors (RMSE) and mean-bias errors (MBE) of the air temperature and the wind velocity near the surface between 20 June 2002 and 9 July 2002, calculated from the hourly grid cell averaged model output at the mesoscale grid cells in which the sites were situated. The measurement heights are given in tab. 4.2. The observed temperatures are compared with the simulated air temperatures at the first main model level at a height of about 10 m (BSPR, BSPA, ALLS) or with the 2 m temperature (GRNZ, VLNF, BLER); the observed wind velocities are compared with the simulated wind velocities at the second main model level at a height of about 35 m (BSPR, BSPA, GRNZ) or with the 10 m wind velocity (ALLS, VLNF, BLER). Note that the measurement of the wind velocity at VLNF took place at a height of 2 m and is thus not comparable with the simulated value. All temperature values are in K and all wind velocities values are in m s^{-1}. In addition to the total RMSE listed first (T), the systematic RMSE (S) and the unsystematic RMSE (U) are listed. The first row of each site in upright font gives the values for the coupled CCLM/DCEP simulation while the second row in italics lists the results of the default bulk scheme of CCLM.

at 0900 UTC, CCLM/DCEP overestimates the wind speed by approx. 1 m s^{-1}. This difference between both simulations persists up to 450 m and is the biggest average one in the course of the day at heights that large. In the early morning and late night, $\mathcal{U}^{\mathrm{h}}$ lies between both simulations up to about 150 m. Above that, both simulations overestimate the wind speed. While both simulations also overestimate $\mathcal{U}^{\mathrm{h}}$ in the afternoon and early night, the simulated wind speed with DCEP is larger than the wind speed with the bulk scheme only up to 150 m. Above, the latter wind speed is slightly larger.

4.4.4. Comparison of the double-canyon with the single-canyon approach

In this subsection, the double-canyon approach of DCEP is compared with the single-canyon approach. The latter corresponds mainly to the original BEP scheme but with a closed radiative energy balance (cf. section 3.1). The corresponding simulation is called "corr" in accordance with the naming in the sensitivity study in section 3.6. Since the spreading of building heights in Basel is similar to that of γ^{min} of the sensitivity study or lower, only small differences are expected between both set-ups. Naturally, they are expected to be largest at both urban sites so they are analysed in the following.

The latent heat flux $\lambda\mathcal{E}$ of both approaches, depicted in figs. 4.23a and 4.23b, shows virtually no difference, which is due to neglecting the latent heat flux in the urban part of the grid cell. On the other hand, the sensible heat flux $\mathcal{H}$ in figs. 4.23c and 4.23d is slightly larger with the double-canyon approach, which reduces the MBE from $-17\,\mathrm{W\,m^{-2}}$ to $-8\,\mathrm{W\,m^{-2}}$ at BSPR and from $-21\,\mathrm{W\,m^{-2}}$ to $-14\,\mathrm{W\,m^{-2}}$ at BSPA. With a difference of $1\,\mathrm{W\,m^{-2}}$ at BSPR and $2\,\mathrm{W\,m^{-2}}$ at BSPA, the RMSE is slightly lower for the double-canyon approach; here, the reduction originates from the systematic RMSE. This tendency is also observed in the sensitivity study and is due to the increased wall temperatures in the urban canyon. Resembling the findings of the sensitivity study, the storage flux $\mathcal{G}$ is similar for both approaches (figs. 4.23e and 4.23f).

Likewise, the net radiation $\mathcal{R}^*$ in figs. 4.24a and 4.24b shows agreement of both approaches.

The total *grid cell mean* albedo α calculated from the ratio of $\mathcal{K}^{\uparrow}$ and $\mathcal{K}^{\Downarrow}$ and the total *urban* albedo α_{urb} calculated from the respective urban values are shown in figs. 4.24c and 4.24d. Due to the increased radiation capturing effect of the double-canyon approach, less radiation is reflected back into the sky in the urban part of the grid cell resulting in a lower α_{urb} in the "DCEP" run. Consequently, also the grid cell average albedo is lower in this run. The α of the double-canyon approach fits the measurements better during midday especially at BSPR. Both DCEP and corrected BEP, however, do not capture the higher total albedo at the beginning and end of the day. As discussed above, this is probably due to neglecting the zenith dependence of the urban surface albedos.

The simulated effective *urban* radiative temperature T_{urb} is determined by means of the urban longwave radiation budget in (3.62) and the urban emissivity ϵ_{urb} in (3.63), where the latter represents the average emissivity of the urban surfaces. Analogously, the simulated effective grid cell radiative temperature $\mathcal{T}_{\mathrm{rad}}$ is calculated from the grid cell longwave radiation budget in (3.67). Here, the emissivity ϵ represents the average of the urban emissivity ϵ_{urb} and the one of the natural surfaces, ϵ_{nat}, with the latter set to 0.996 in CCLM (cf. section 2.2.1). The same average emissivity is also assumed in the calculation of the radiative temperature from the *measured* longwave budget with its measured components $\mathcal{L}^{\downarrow}$ and $\mathcal{L}^{\uparrow}$. All temperatures are depicted in figs. 4.24e and 4.24f. For both urban sites, the simulated T_{urb} is on average slightly

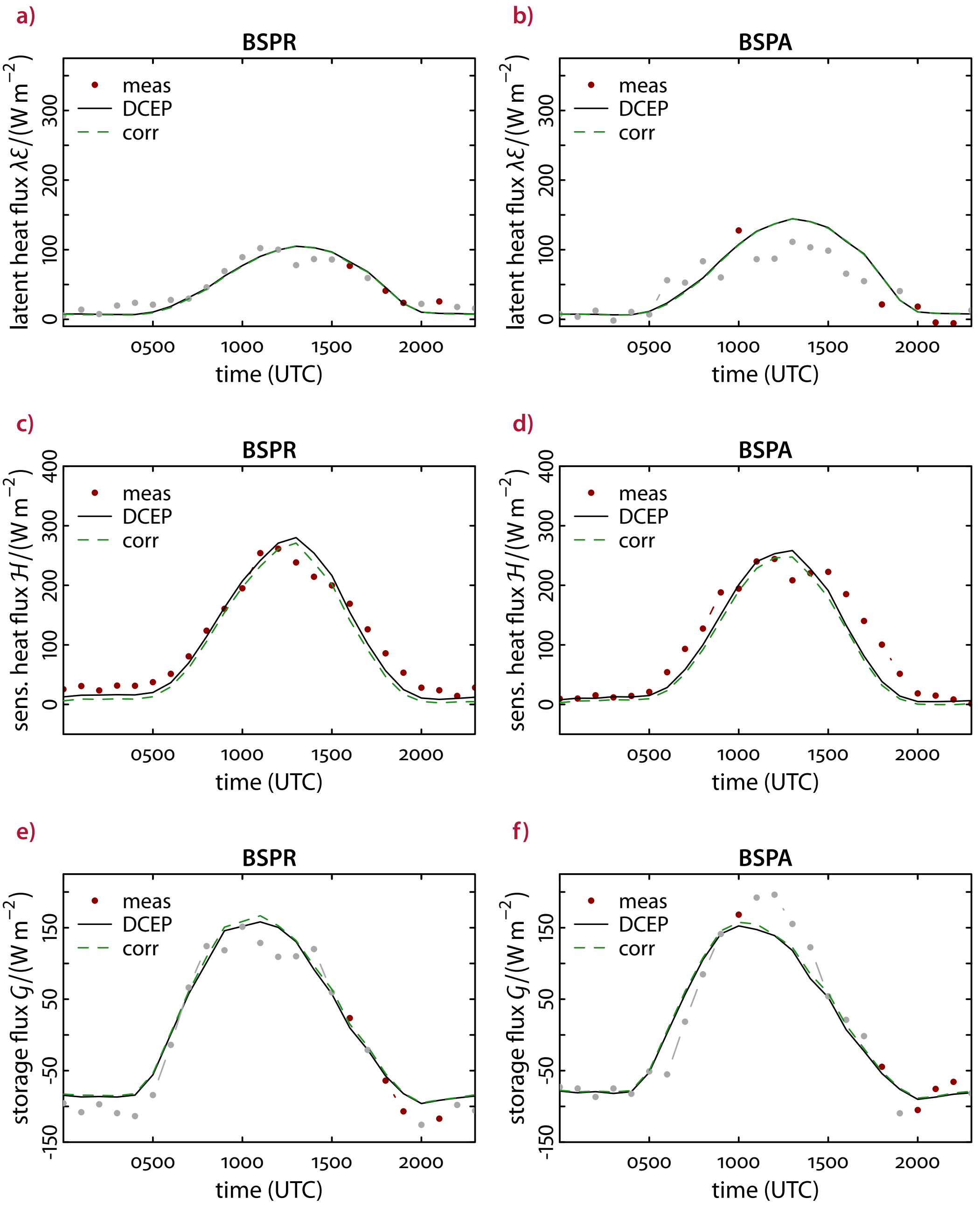

Figure 4.23. Measured and simulated average diurnal cycle of the heat fluxes at both urban stations between 20 June 2002 and 9 July 2002. The simulations are conducted with either the DCEP and double-canyon approach or the single-canyon approach in the corrected BEP scheme. The simulated values represent the mesoscale grid cell average.

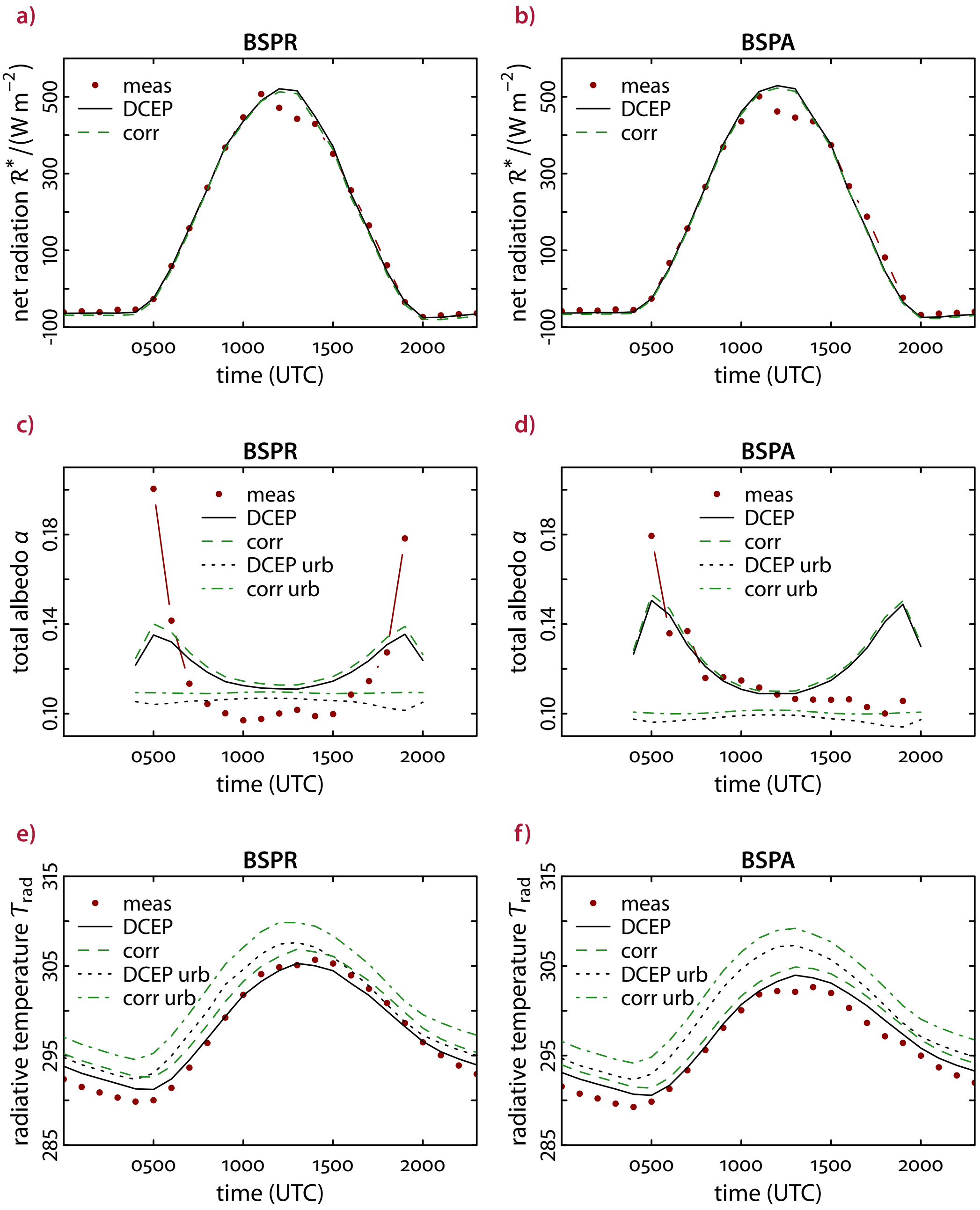

Figure 4.24. Measured and simulated average diurnal cycle of the radiation properties at both urban stations between 20 June 2002 and 9 July 2002. The simulations are conducted with either the DCEP and double-canyon approach or the single-canyon approach in the corrected BEP scheme. The simulated values represent the mesoscale grid cell average.

lower for DCEP than for the corrected BEP version (approx. 2.3 K and 1.9 K for BSPR and BSPA, respectively). Consequently, the simulated grid cell average T_{rad} is lower in the double-canyon approach than in the single-canyon approach (by 1.5 K and 0.9 K, respectively). At BSPR, DCEP reduces the RMSE of T_{rad} with respect to the "corr" run from 2.9 K to 2.2 K and also reduces the MBE from 1.8 K to 0.3 K. The reduction of the RMSE mainly originates from reducing the systematic RMSE. Similarly, at BSPA the RMSE is reduced from 2.7 K to 2.1 K and the MBE is reduced from 2.0 K to 1.1 K.

4.5. Summary

In this chapter, the evaluation of the fully online coupled CCLM/DCEP model with measurements from the Basel UrBan Boundary Layer Experiment (BUBBLE) was presented. This model was investigated in terms of the components of the radiation flux, the energy balance, the wind speed and the air temperature. Furthermore, this combined model was compared with CCLM using the bulk approach for the urban area of Basel and its surroundings.

The BUBBLE measurement sites used for the evaluation were depicted and the physical variables as well as their measurement conditions specified. In order to employ the DCEP scheme, urban canopy parameters were derived from 3-D building data and land-use data, and compared to the ones derived from the direct surroundings of each site by Christen and Vogt (2004).

The results of the evaluation show that the shortwave irradiance is simulated well by CCLM with a slight overestimation at noon, which is probably due to underestimating the cloud cover. Here, practically no difference between the simulations with the DCEP and the bulk scheme are seen, and also not between the sites. In contrast to this, the reflected shortwave radiation is improved by DCEP at the urban and suburban sites. This is due to the decreased albedo of the urban surfaces and the radiation capturing effect of the street canyon, a feature neglected by the bulk scheme. At the rural sites, the albedo is underestimated, where it remains unclear how this effect translates from the immediate site surroundings to the overall grid cell average. With respect to modelling the components of the longwave radiation both simulations perform reasonably well given the various uncertainties of these measurements. The observed values of the latent heat flux are captured well by the coupled CCLM/DCEP model at the urban and suburban sites. An improvement over the bulk scheme is mainly seen at the suburban station. This is caused by the better representations of the vegetation fraction in the DCEP set-up than in the bulk scheme's default land-use data. Analogously to the case of the albedo, the latent heat flux is overestimated at the rural sites. Again, this is due to the specifics of the local site settings possibly not being representative for all of the grid cell. In view of the sensible heat flux, DCEP considerably improves the performance at the urban and suburban sites: at nighttime, DCEP is able to produce the typical slightly positive heat flux at the urban site, the origin of the observed urban heat island in Basel. The bulk scheme, on the other hand, displays a negative sensible heat flux at all sites at night. One of the reasons for this better agreement of DCEP with the measurements is its higher storage flux during daytime at the urban and suburban sites, as compared to the bulk scheme. This allows for an increased nightly energy release. In summary, the accuracy of the flux simulations in terms of the root-mean-square error and the mean-bias error is comparable with that listed by Grimmond et al. (2010) and Grimmond et al. (2011) for the *offline* performance of a number of urban canopy models (UCMs) as well as the *offline* evaluation of the Noah UCM for Basel with site-specific input parameters tuned for optimal performance (Loridan and Grimmond 2012).

Furthermore, the near-surface air temperature and the wind velocity as well as air temperature and wind profiles were evaluated. As opposed to the investigation of urban radiation and energy fluxes, the full analysis of these quantities necessarily demands an online coupling of the DCEP scheme to CCLM.

It is found that the CCLM with the bulk scheme overestimates the near-surface air temperatures at the rural sites, and produces no urban heat island at the urban and suburban sites. The DCEP scheme, however, accounts for the urban heat island and consequently leads to an overestimation of the near-surface air temperatures. Here, the better agreement of the bulk scheme at the urban stations simply results from the cancellation of its mentioned shortcomings. Concerning the vertical potential temperature profile, the CCLM/DCEP model also provides a good description. It produces a less statically stable atmosphere in the lower boundary layer during the night than is obtained with the bulk approach. The unstable form of the measured profile in this region is not fully captured, though.

The near-surface wind velocity is overestimated by both simulations, especially during daytime. While the higher surface roughness of the city is accounted for in different ways in both, the DCEP and the bulk scheme, the overall wind velocities are higher in DCEP. This is due to the higher near-surface air temperatures resulting in a larger pressure gradient between urban and rural areas. In terms of the vertical wind profile, the findings are inconclusive. Whereas the form of the profile is captured well most of the time, both models overestimate the wind speed, particularly during daytime. In this context, possible measurement uncertainties need to be taken into account.

In addition, a comparison of the single-canyon approach of the corrected BEP scheme to the double-canyon approach of DCEP was performed. The findings confirm the results of the sensitivity study in section 3.6: In the urban areas, the double-canyon approach displays a slightly higher sensible heat flux, a lower albedo and a lower radiative temperature. The latter, in particular, agrees better with the measurements.

5. The influence of green areas and roof albedos on air temperatures during extreme heat events in Berlin, Germany

In this chapter, the influence of possible mitigation measures to extreme heat events (EHE) for the city of Berlin (Germany) is estimated. To this end, a reference simulation with the coupled CCLM/DCEP for EHEs in the years 2000–2009 is compared with simulations with modified vegetation fraction and roof albedo.

Berlin is the largest city of Germany with an area of 892 km^2 with 18 % woods and 12 % recreational area, and a population of about 3.4 million in the years 2000–2010 (Amt für Statistik Berlin-Brandenburg 2011). For the entire area of the city, a comprehensive 3-D building data set is used to calculate effective urban parameters for the respective mesoscale grid cells. Using these parameters, a reference simulation for the EHEs with a duration of at least 5 days is evaluated with observed 2 m temperatures from stations in Berlin and its surroundings; it is also compared to a simulation with the bulk scheme. In addition, the dependence of the simulated urban heat island (UHI) on the urban parameters is analysed.

In order to estimate the cooling effect of vegetation in Berlin, the 2 m temperatures of the reference simulation are compared with those from simulations with the same set-up except increased or decreased vegetation fractions. The findings are compared to the estimates derived from the UHI analysis. The application of high-albedo roof surface coatings (Bretz and Akbari 1997) is represented by simulations with an increased roof albedo. Analogously, these simulations are compared with the reference simulations.

First, the derivation of urban canopy parameters for the city of Berlin is described and second, the weather stations used for evaluation are depicted. Third, the model set-up is explained including a identification of the EHEs. Fourth, the model performance of the reference simulations is evaluated and the simulated urban heat islands are analysed. Last, results of simulations with the modified urban parameters are presented.

Note that the content of this chapter has been published in Schubert and Grossman-Clarke (2013a).

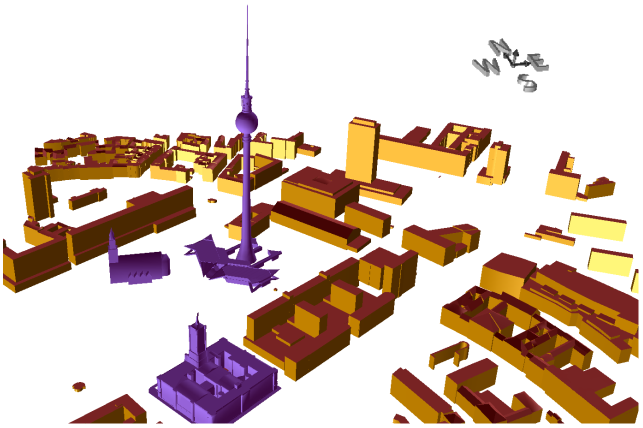

Figure 5.1. Rendered example of the 3-D data in CityGML format used to derive the urban parameters: Berlin Alexanderplatz and the TV tower

5.1. Derivation and analysis of urban canopy parameters in Berlin

For the reference simulation, various urban canopy parameters for every mesoscale grid cell are derived. For that an impervious surface data set of Berlin as well as a 3-D building data set with over 460 000 buildings (Jung 2009) in the City Geography Markup Language level of detail 2 format (CityGML LOD2) defined in OGC (2008) is used (fig. 5.1). In this format, buildings are modelled with polygons, which are semantically distinguished between ground, wall and roof surfaces. In the following, the derivation of the effective urban parameters is explained.

Since the urban part of the grid cell in DCEP represents a 100 % impervious surface, the urban fraction f_{urb} of a grid cell is set to the impervious surface coverage of the cell (fig. 5.2a), e.g. a grid cell with 70 % impervious surfaces is represented as 70 % urban and 30 % vegetated in the model. The fraction cover of buildings f_{b} is given by the area of the building's ground surfaces (fig. 5.2b). With that, the fraction cover of the street surfaces is given by $f_{\mathrm{str}} = f_{\mathrm{urb}} - f_{\mathrm{b}}$. For Berlin, maximum values of f_{urb} and f_{b} of 0.85 and 0.56 are found, respectively.

The street direction of the street canyon influences the shadowing of the urban surfaces and the drag forces on the walls (e.g. drag forces do not act on the walls if the street canyon is aligned with the direction of the average wind speed). Thus, all urban radiative properties and fluxes are averaged, weighted with the fraction f_{dir} of the corresponding street direction χ. In order to calculate f_{dir} of every mesoscale grid cell, the distribution of canyon angles of all wall polygons is weighted with their respective wall area. The canyon angle of a wall surface is defined by the normal of that surface projected onto the horizontal plane. For this study, every canyon angle is projected onto the four directions north-west–south-east, north–south, north-east–south-west and east–west. With these directions, the distribution of street directions is highly

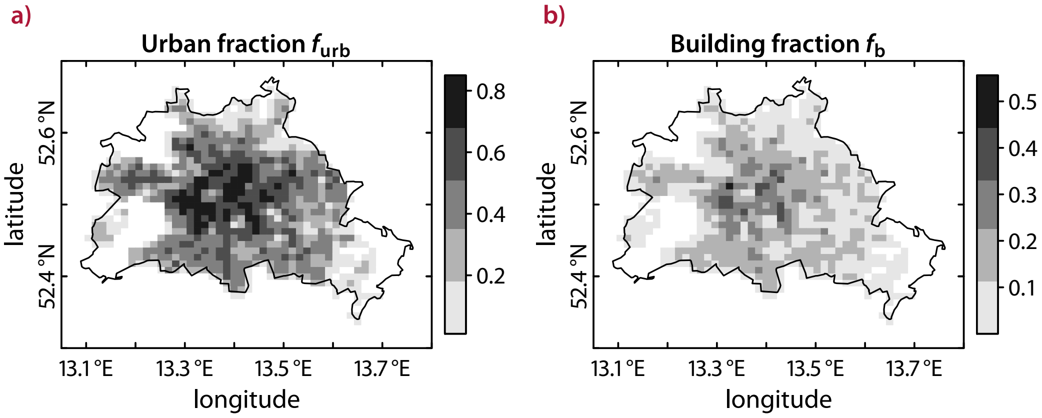

Figure 5.2. Urban fraction in a) and building fraction in b) of Berlin at a resolution of 1 km based on the impervious surface coverage and the 3-D building data set. The area of Berlin is outlined.

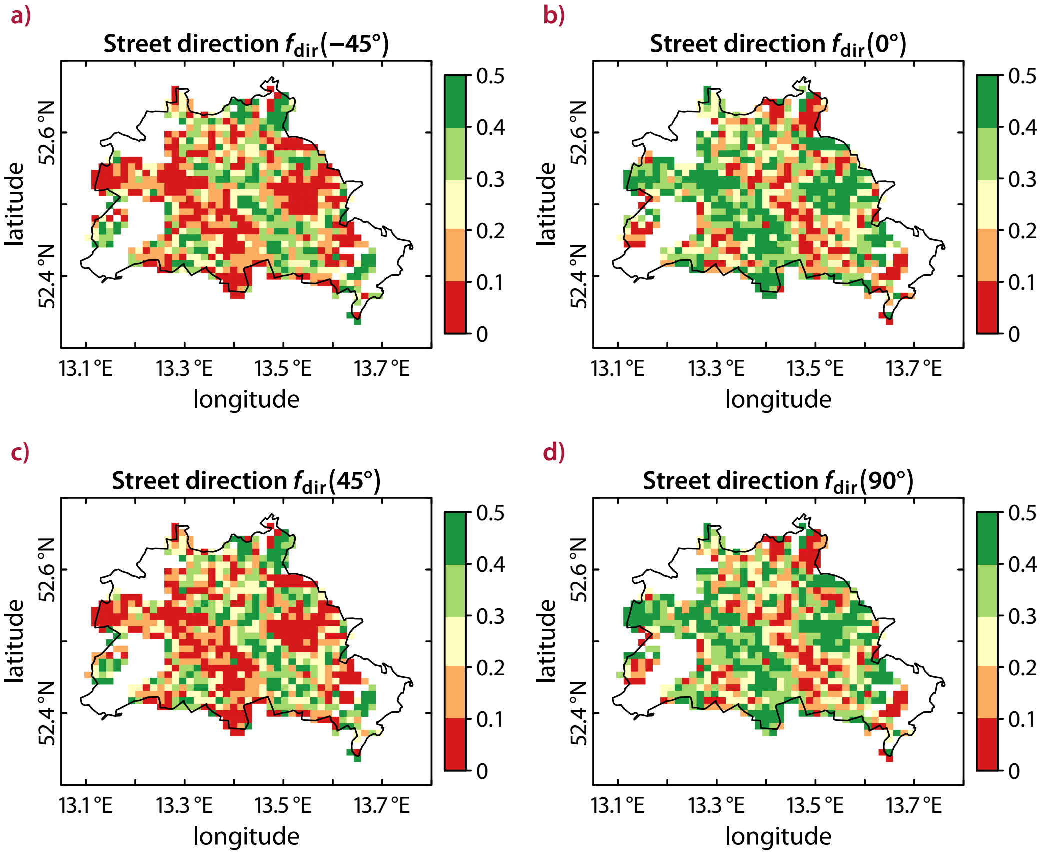

Figure 5.3. Distribution of street directions $f_{dir}(\zeta)$ of Berlin at a resolution of 1 km based on the 3-D building data set. The convention of the street canyon angle is explained in fig. 3.7a. A fraction of 0.25 for all directions corresponds to an equal distribution of directions. The area of Berlin is outlined.

correlated for directions that are perpendicular to each other (fig. 5.3). Defining the correlation coefficient between the fraction of direction a and b by

$$r(a,b) \equiv \frac{\overline{(a-\overline{a}^f)(b-\overline{b}^f)}^f}{s_a s_b} \quad \text{with} \quad s_i \equiv \sqrt{\overline{(i-\overline{i}^f)^2}^f}\,, \tag{5.1}$$

where $\overline{a}^f$ indicates the spatial average of a weighted with the urban fraction f_urb, the average r between perpendicular directions is 0.95 whereas it is −0.97 for directions not perpendicular.

The building height probability $\gamma(z)$ is determined by the distribution of building heights in the data set weighted by the respective wall area of the building. A building height is assigned to a street direction depending on the street direction of its wall surfaces. Here, the building height is defined as the average height of the roof surfaces. Figure 5.4 shows the spatial distribution of the fraction of buildings at the lowest heights averaged over all street directions. Each subfigure depicting $\gamma(z)$ includes buildings of heights $z \pm 2.5\,\text{m}$.

The street width assigned to a wall surface is the average distance to other wall surfaces. These single street widths of wall surfaces with the same street direction in a mesoscale grid cell are averaged weighted by the area of the respective wall surface. Thus, a street width of a larger building has a higher weight than that of a smaller one. The exact details are explained in the following: For each street direction in each grid cell, the street width W is the weighted average of the distances W_i:

$$W = \frac{1}{\sum_i A_i} \sum_i W_i A_i\,, \tag{5.2}$$

where A_i is the area of wall element i. W_i is the weighted average distance between wall i and the nearest visible walls j (see fig. 5.5):

$$W_i = \frac{1}{\sum_j A_j} \sum_{j=1}^{n_i} W_{ij} A_j \tag{5.3}$$

with n_i the smallest value fulfilling

$$\sum_{j=1}^{n_i} A_j \geq A_i \text{ and } W_{i1} \leq W_{i2} \leq \ldots \tag{5.4}$$

Here, the distance W_{ij} between two wall areas i and j is defined as the distance between their centroids if the line between the centroids is unobstructed. The specifications in (5.4) ensure that a sufficient number of nearest wall elements j is considered.

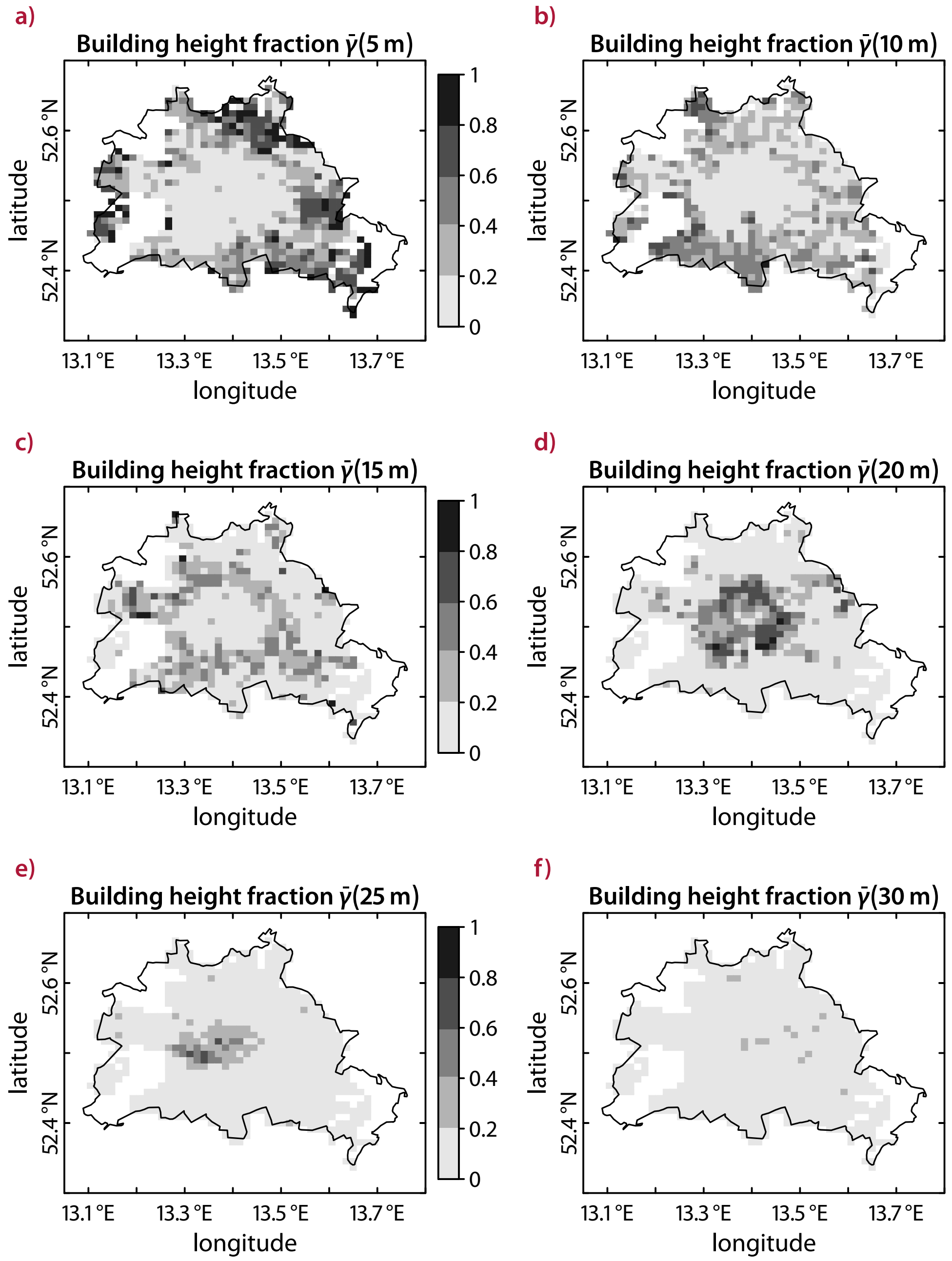

Figure 5.4. Building height distribution $\bar{\gamma}(z)$ of Berlin averaged over the four street directions for the lowest heights at a resolution of 1 km based on the 3-D building data set. The respective figures include buildings of a height $z \pm 2.5$ m. The area of Berlin is outlined.

Figure 5.6a shows the resulting street widths averaged over all street directions. The spatial average amounts to $\overline{W}^f = 18.7\,\mathrm{m}$. The building width B follows directly from the requirement that the total building and street surfaces of the simplified model equal that of the input data (Martilli 2009):

$$\frac{B}{W} = \frac{f_\mathrm{b}}{f_\mathrm{str}}\,. \tag{5.5}$$

This results in the spatial distribution shown in fig. 5.6b ($\overline{B}^f = 8.8\,\mathrm{m}$).

The street length D plays a minor role in the urban parametrization scheme presented here. The concrete value of D has negligible effect on the physical results because it is assumed that D is much larger than the street width W, the building width B or the maximum building height H. However, D should assume a value characterizing the mesoscale grid cell because it is used to calculate the total roof and building area in a grid cell. These areas should be equal to the actual areas (Martilli 2009). Thus, D is chosen to be equal to the average length fitting into a grid cell with a street canyon angle of ζ (fig. 5.7). The details of this approach are presented in the following.

First, the size of the grid cell is calculated. Starting from the line element for a spherical coordinate system,

$$\mathrm{d}s^2 = \mathrm{d}r^2 + r^2\,\mathrm{d}\varphi^2 + r^2\cos^2\varphi\,\mathrm{d}\lambda^2\,, \tag{5.6}$$

where r, λ and φ are the radius, longitude and latitude, the arc length l_λ in zonal direction with a spacing of $\Delta\lambda$ is given by

$$l_\lambda = \int_{\lambda-\Delta\lambda/2}^{\lambda+\Delta\lambda/2} r\cos\varphi\,\mathrm{d}\lambda = r\,\Delta\lambda\cos\varphi\,. \tag{5.7}$$

Similarly, the arc length l_φ in meridional direction with a spacing of $\Delta\varphi$ is given by

$$l_\varphi = \int_{\varphi-\Delta\varphi/2}^{\varphi+\Delta\varphi/2} r\,\mathrm{d}\varphi = r\,\Delta\varphi\,. \tag{5.8}$$

Along the meridional direction, l_λ varies with an average value of

$$\bar{l}_\lambda = \frac{1}{\Delta\varphi}\int_{\varphi-\Delta\varphi/2}^{\varphi+\Delta\varphi/2} r\,\Delta\lambda\cos\varphi\,\mathrm{d}\varphi = 2r\frac{\Delta\lambda}{\Delta\varphi}\sin(\Delta\varphi/2)\cos\varphi \xrightarrow{\Delta\varphi\to 0} r\,\Delta\lambda\cos\varphi\,. \tag{5.9}$$

l_φ is constant for different λ, thus

$$\bar{l}_\varphi = l_\varphi\,. \tag{5.10}$$

In the following, the area defined by $\Delta\lambda$ and $\Delta\varphi$ is assumed to be rectangular. CCLM

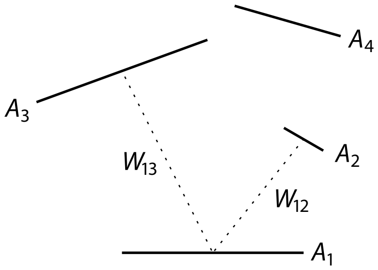

Figure 5.5. Calculation of the street width. The average street width W_1 for the surface A_1 is given by the area weighted average of W_{12} and W_{13}. The nearest area A_2 is not considered alone because A_2 is smaller than A_1. However, $A_2 + A_3 > A_1$, therefore area A_4 is not taken into account. Finally, the total grid cell average street width is given by the area weighted average of W_i of all areas A_i in that cell.

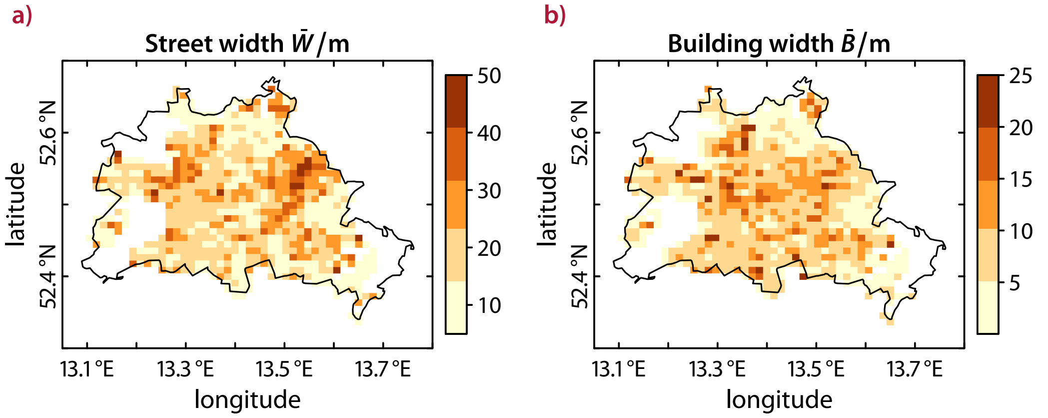

Figure 5.6. Street width in a) and building width in b) of Berlin averaged over the four street directions at a resolution of 1 km. The former is based on the 3-D building data set resulting with (5.5) in the latter. The area of Berlin is outlined.

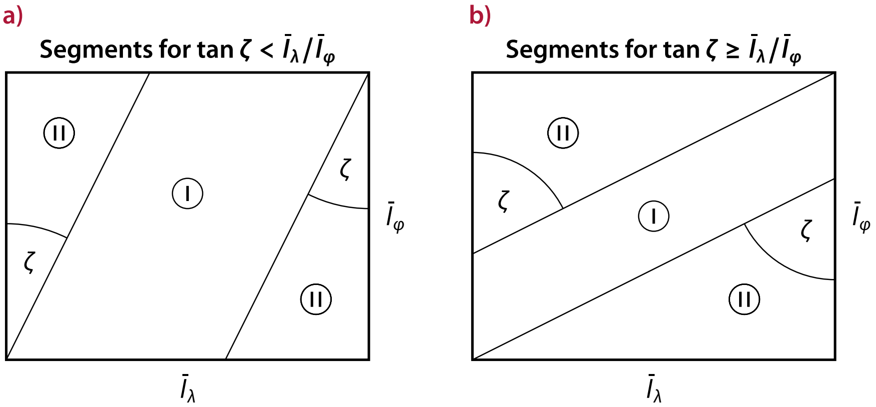

Figure 5.7. Calculation of the average street length. The mesoscale grid cell with side lengths $\bar{l}_\lambda$ and $\bar{l}_\varphi$ is divided into segments I and II depending on the street direction ζ. The maximum length with an angle ζ fitting into segment I is constant while it diminishes when approaching the boundaries in II. The average street length in the grid cell is the area weighted mean of these lengths.

works on a rotated grid that assumes the equator being located in the simulation region, thus the assumption is reasonable. The rectangle can be divided into three segments (fig. 5.7): the segment I with an area A_I in which the street length is constant and two segments II with an area A_II each in which the street length varies with the position in the grid cell. For $\tan\zeta < \bar{l}_\lambda/\bar{l}_\varphi$ (fig. 5.7a), the average street lengths of the two segments is given by

$$\bar{l}_{\mathrm{Ia)}} = \frac{\bar{l}_\varphi}{\cos\zeta}\,, \tag{5.11}$$

$$\bar{l}_{\mathrm{IIa)}} = \frac{1}{2}\frac{\bar{l}_\varphi}{\cos\zeta}\,, \tag{5.12}$$

with

$$A_{\mathrm{Ia)}} = \bar{l}_\varphi(\bar{l}_\lambda - \bar{l}_\varphi\tan\zeta)\,, \tag{5.13}$$

$$A_{\mathrm{IIa)}} = \frac{1}{2}\bar{l}_\varphi^2\tan\zeta\,. \tag{5.14}$$

Therefore, the average street width in the complete cell is given by

$$\bar{D}_{\mathrm{a)}} = \frac{1}{A_\mathrm{Ia} + 2A_\mathrm{IIa}}(\bar{l}_\mathrm{Ia}A_\mathrm{Ia} + 2\bar{l}_\mathrm{IIa}A_\mathrm{IIa}) = \frac{1}{\cos\zeta}\frac{\bar{l}_\varphi}{\bar{l}_\lambda}\left(\bar{l}_\lambda - \frac{1}{2}\bar{l}_\varphi\tan\zeta\right). \tag{5.15}$$

Similarly, for $\tan\zeta \geq \bar{l}_\lambda/\bar{l}_\varphi$ (fig. 5.7b), the average street length is given by

$$\bar{D}_{\mathrm{b)}} = \frac{1}{\sin\zeta}\frac{\bar{l}_\lambda}{\bar{l}_\varphi}\left(\bar{l}_\varphi - \frac{1}{2}\bar{l}_\lambda\cot\zeta\right). \tag{5.16}$$

5.2. Description of the weather stations

The CCLM/DCEP performance is evaluated by means of comparing simulated grid cell average air temperatures at 2 m above ground ($\mathcal{T}_{2\,\mathrm{m}}$) with observed temperatures from four surface weather stations located in Berlin, one station at the border of Berlin and one rural reference station at Lindenberg (fig. 5.8). Also all sensitivity runs are analysed at these stations.

The stations in Berlin are depicted in fig. 5.9. Urban parameters used in the model grid cells of the stations' locations are listed in tab. 5.1. The station at Berlin-Alexanderplatz (fig. 5.9a) was situated next to the TV tower in the centre of the city (cf. fig. 5.1) during all considered EHES. The very surrounding area consists of many small green patches and the building density apart from the TV tower is sparse resulting in a large street width. The station Berlin-Dahlem (fig. 5.9b) in the south-west is situated at the

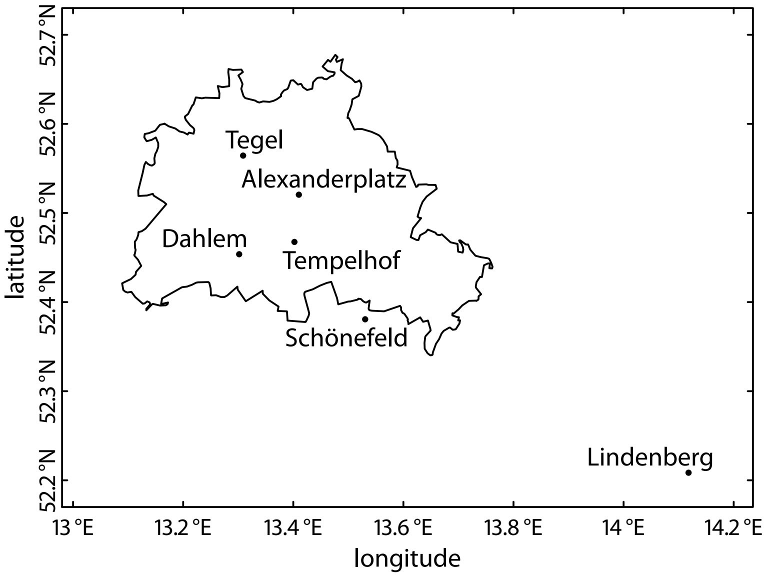

Figure 5.8. Locations of measurement sites in Berlin and vicinity from which 2 m temperature measurements are used for CCLM evaluation. The area of Berlin is outlined.

border of the Botanical Garden and is thus dominated by the large green area directly surrounding it.

The direct surroundings of the stations in figs. 5.9c and 5.9d at the (former) airports in Berlin are characterized by large open areas resulting in the very small building widths in tab. 5.1. For the simulations, the building width is set to 0 m in order to not unrealistically shadow the impervious surfaces in the respective areas. The station Berlin-Tegel is situated in the north-west and Berlin-Tempelhof in the southern centre of Berlin.

The station at the airport Schönefeld is located south-east of the border of Berlin and is characterized by similar conditions but is not considered *urban* in the simulation. Due to the close proximity to Berlin, Schönefeld is also affected by the urban area. The rural weather station at Lindenberg is approx. 60 km away from Berlin's centre.

The locations of all weather stations are indicated by black dots in the following spatial plots.

a) Former location of the station Berlin-Alexanderplatz in the centre of the city

b) Station Berlin-Dahlem in the Botanical Garden in the south-west of Berlin

c) Station Berlin-Tegel on the area of the airport in the north-west of Berlin

d) Station Berlin-Tempelhof in the southern centre of Berlin

Figure 5.9. Weather stations in Berlin. The picture in c) was taken by Jean Böhme.

Site	f_{urb}	$\bar{W}$/m	$\bar{B}$/m	$\bar{\gamma}$						
				0 m	5 m	10 m	15 m	20 m	25 m	30 m
Alexanderplatz	0.69	29.8	14.7	0.00	0.03	0.02	0.04	0.19	0.41	0.26
Dahlem	0.32	20.6	10.0	0.01	0.17	0.62	0.20	0.00	0.00	0.00
Tegel	0.26	25.2	3.4	0.01	0.37	0.29	0.29	0.04	0.00	0.00
Tempelhof	0.14	13.8	0.2	0.00	0.26	0.74	0.00	0.00	0.00	0.00

Table 5.1. Parameters of the grid cells that include Berlin measurement stations. The street width $\bar{W}$, the building width $\bar{B}$ and the height distribution $\bar{\gamma}$ are averages over all street directions.

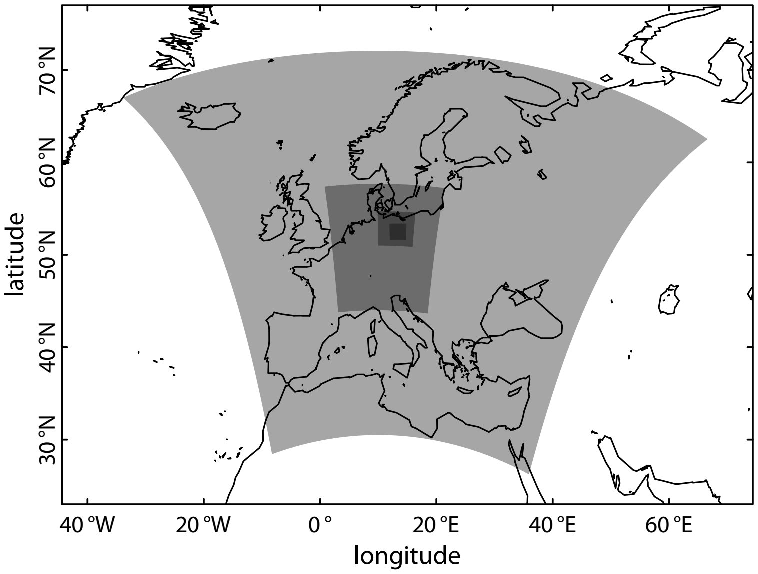

Figure 5.10. Nested domains of the downscaling for Berlin. The resolutions are with decreasing domain size 25 km, 7 km, 2.8 km and 1 km.

5.3. Identification of extreme heat events and set-up of simulations

In this sensitivity study the coupled CCLM/DCEP model is applied to the region around Berlin for EHES during the period 2000–2009. To identify the EHES, the criterion by Huth et al. (2000) and Meehl and Tebaldi (2004) is used. They defined an EHE as the longest period of consecutive days with (i) the daily maximum temperature larger than a threshold temperature T_1 for at least 3 days, (ii) the average daily maximum temperature above T_1 and (iii) the maximum temperature of every day above the threshold temperature T_2. For the application to Berlin, the choice of T_1 and T_2 is based on the statistics of the meteorological data obtained at two airport weather stations at Berlin-Tegel and Berlin-Tempelhof for the period 1970–1999 (see previous section for a description of the stations). T_1 and T_2 are defined as the 95th and 81st percentile, respectively, of the distribution, resulting in the same values for both weather stations: $T_1 = 30.9\,°\mathrm{C}$ and $T_2 = 27.3\,°\mathrm{C}$. The focus of this study lies on heat waves with a length of at least 5 days: 2002/07/28–2002/08/01, 2003/08/01–2003/08/13, 2006/07/01–2006/07/07 and 2006/07/17–2006/07/28 based on the statistics of both stations. An EHE is also identified for 2008, but depending on the station for a slightly different time period: 2008/07/25–2008/08/01 (Tegel) and 2008/07/24–2008/07/29 (Tempelhof).

Thus, 9 day CCLM simulations are conducted with one way nested grids of resolutions (fig. 5.10) of approx. 25 km (without DCEP), 7 km (without DCEP), 2.8 km (with and without DCEP) and 1 km (with and without DCEP) for the EHES listed above starting 2 days before the identified beginning of the EHE (see below for an analysis of the spin-up behaviour for different urban surface temperatures). The 25 km simulations cover Europe, the Mediterranean and Black Sea region; the 7 km simulation eastern France, the Alpine Region, Germany, Denmark, east Poland, Czech Republic; the 2.8 km simulation east Germany and west Poland with 150 × 150 grid points. The 1 km simulation is centred around Berlin with a domain size of approx. 195 km × 195 km.

The initial and six-hourly boundary conditions are provided by ERA-Interim reanalysis data (Dee et al. 2011). All nesting steps use spectral nudging (Rockel, Castro et al. 2008). Analogously to the simulation for Basel described in section 4.3, the initial soil water content for the 25 km resolution run is taken from a simulation with the same set-up as the 25 km run starting in January 1995. Without this spin up, CCLM simulations with the interpolated soil water content of ERA-Interim resulted in air temperatures that were considerably too low during the analysed EHEs.

The orography, monthly vegetation and soil parameters are provided by the preprocessor of CCLM (Smiatek et al. 2008). That data set provides vegetation parameters and roughness length in the area of Berlin appropriate for the bulk-transfer scheme. With DCEP, the preprocessor parameters represent the vegetation part in a grid cell only. Thus, the data in Berlin was substituted with parameters for July and August from the surroundings of Berlin: a leaf area index of $3.5\,\mathrm{m^2\,m^{-2}}$ and $2.9\,\mathrm{m^2\,m^{-2}}$; a plant cover fraction of 0.88 and 0.82; a root depth of 1.5 m; a roughness length of 0.13 m and 0.08 m.

The urban scheme DCEP is run with different set-ups for every simulation period:

1. The reference simulation represents the current state of Berlin. It uses the morphological input parameters derived in section 5.1 and urban surface parameters for roof (R), wall (W) and street surfaces (G) following the propositions by Martilli et al. (2002): an emissivity of $\epsilon_R = \epsilon_W = 0.90$, $\epsilon_G = 0.95$ and an thermal diffusivity of $k_R = k_W = 0.67 \times 10^{-6}\,\mathrm{m^2\,s^{-1}}$, $k_G = 0.29 \times 10^{-6}\,\mathrm{m^2\,s^{-1}}$. The albedo for roof and street surfaces is based on average values of a hyperspectral measurements (Roessner et al. 2011): $\alpha_R = 0.163$, $\alpha_G = 0.162$; in addition $\alpha_W = 0.162$ is assumed. Furthermore, an increased value of the volumetric specific heat capacity $c_R = c_W = c_G = 2.3 \times 10^6\,\mathrm{J\,m^{-3}\,K^{-1}}$ is used.

2. Compared to the reference simulation, the natural surface fraction $f_{\mathrm{nat}} \equiv 1 - f_{\mathrm{urb}}$ of each urban grid cell is modified by a certain amount $\delta f_{\mathrm{nat}} \equiv \Delta f_{\mathrm{nat}}/f_{\mathrm{nat}}$. The vegetation fraction f_{veg} of a grid cell, in turn, is given by f_{nat} multiplied by the plant cover fraction. Since an annual cycle of the plant cover fraction is assumed in CCLM, a constant δf_{nat} results in a varying absolute modification of f_{veg} but in a constant relative change: $\delta f_{\mathrm{nat}} = \delta f_{\mathrm{veg}}$. In the following, three different modifications of f_{nat} are analysed: $\delta f_{\mathrm{nat}} = -25\,\%$, $\delta f_{\mathrm{nat}} = +5\,\%$ and $\delta f_{\mathrm{nat}} = +15\,\%$. These model runs are named V-25, V+05 and V+15 in the following.

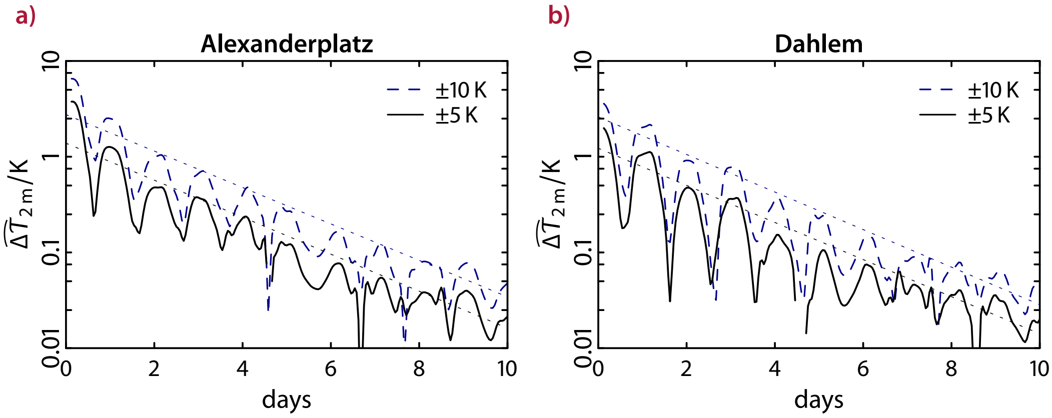

Figure 5.11. Difference of the 2 m temperature between simulations in which the temperatures of all urban surface layers were initialized by ±5 K or ±10 K relative to the default of 292 K

3. Based on the set-up of the reference simulation, the roof albedo is increased to 0.40 and 0.65 with the corresponding runs AR40 and AR65, respectively. Bretz and Akbari (1997) showed that even a large albedo of 0.65 is maintainable.

4. Combined V+15 and AR65, which is called VAR run.

In all set-ups, the temperature of all urban surface layers is initialized with 292 K at 0000 UTC, which roughly corresponds to the air temperature during the night. To estimate the time the urban surfaces need to adjust to the atmospheric conditions, simulations for the 2003 EHE with the settings of the reference simulations are conducted with perturbed urban surface temperatures of ±5 K and ±10 K. Figure 5.11 shows the resulting difference in the 2 m temperature, $\widehat{\Delta T}_{2\,\mathrm{m}}$, at the grid cells of the Berlin-Alexanderplatz and Dahlem station. The resulting time series have been smoothed with the binomial filter described in section 5.5. Both plots show an exponential decay of $\widehat{\Delta T}_{2\,\mathrm{m}}$ with a mean lifetime of approx. 2.25 days (indicated by the lines) overlaid with a diurnal cycle. Since the surface temperatures of the urban surfaces are more influenced by the temperature of the deeper layers during nighttime than during daytime (when the radiative forcing is dominating), $\widehat{\Delta T}_{2\,\mathrm{m}}$ is larger during nighttime than during daytime. For this study, a spin-up time of 2 days is used. After this time, the temperature difference due to the initialization of the urban surfaces is most likely less than 0.5 K (assuming that the initialized temperatures deviate not more than 10 K from the equilibrium temperatures).

Start date	Lindenberg	Alex.	Tegel	Tempelhof	Dahlem	Schönefeld
2002/07/28	2.3 / 0.0	2.0 / 0.0	2.0 / 0.3	2.5 / 0.5	2.5 / 1.4	2.2 / 0.8
	2.3 / 0.0	*2.4 / -1.0*	*2.1 / -0.1*	*2.2 / 0.2*	*2.0 / 0.7*	*2.2 / 0.7*
2003/08/01	1.1 / 0.6	0.9 / -0.3	1.2 / -0.3	1.2 / 0.1	2.1 / 1.0	1.4 / 0.8
	1.1 / 0.6	*1.7 / -1.3*	*1.4 / -0.8*	*1.0 / -0.4*	*1.3 / 0.0*	*1.3 / 0.7*
2006/07/01	2.4 / 1.7	2.5 / 1.4	2.5 / 1.4	2.6 / 1.4	3.7 / 2.9	3.0 / 2.1
	2.4 / 1.7	*2.5 / 0.5*	*2.4 / 0.9*	*2.5 / 1.3*	*3.2 / 2.5*	*2.9 / 2.0*
2006/07/17	1.9 / -0.2	1.6 / -0.5	1.9 / 0.0	1.7 / -0.2	2.9 / 1.6	2.2 / 0.4
	1.8 / -0.2	*2.2 / -1.4*	*1.9 / -0.4*	*1.6 / -0.5*	*2.3 / 1.0*	*2.1 / 0.3*
2008/07/24	2.3 / -1.2	2.1 / -1.6	2.1 / -1.7	2.2 / -1.5	1.8 / -0.3	2.1 / -1.2
	2.3 / -1.2	*2.9 / -2.4*	*2.5 / -2.1*	*2.3 / -1.7*	*1.9 / -1.1*	*2.2 / -1.3*

Table 5.2. Root-mean-square error (first columns) and mean-bias error (second columns) of the hourly 2 m temperature values in K based on a simulation period of one week. The values for the reference simulation with DCEP are written in an upright font while the corresponding values of simulations in which Berlin is only represented by the bulk approach is written italic.

5.4. Evaluation of the model performance and the simulated UHI characteristics

The performance of the coupled CCLM/DCEP model is assessed based on the root-mean-square error (RMSE) and the mean-bias error (MBE) (as defined in section 4.4) of the mesoscale grid cell average 2 m temperature $T_{2\,\mathrm{m}}$ for all introduced weather stations and EHEs (tab. 5.2). Here, the results for Lindenberg represent the quality of the pure CCLM model because the corresponding grid cell is practically not influenced by the urban modifications by DCEP applied in Berlin. With the chosen set-up, the quality of the CCLM simulations varies for the different periods. The model clearly performs best for the EHE of 2003 (RMSE of 1.1 and MBE of 0.6), while RMSE and MBE values as high as 2.4 and 1.7, respectively, were found for the other periods. For all analysed EHEs, the CCLM/DCEP performance in the urban region is similar to that at rural Lindenberg in terms of RMSE and MBE. This indicates that DCEP captures the urban effects well. If CCLM simulates the regional weather reasonably well, the coupled model shows good results for Berlin and vice versa. The deviations between observed and simulated values are larger for the Dahlem than for the other stations. This can be explained by the location of the Dahlem station in an extended park, whereas the model calculates the average grid cell $T_{2\,\mathrm{m}}$ comprising the influence of the urban and natural surfaces. This is confirmed when comparing the results with simulations in which Berlin is represented only by the bulk approach (also listed in tab. 5.2). While DCEP improves the MBE by approx. 1 K at the Alexanderplatz station*, the measurements at Tegel, Tempelhof and Schönefeld sites are slightly, and at the Dahlem site clearly better represented by the bulk scheme. The observations at the latter sites represent the natural surfaces and open areas in their immediate vicinity depicted in fig. 5.9 on page 132, and not the mix of urban and natural surfaces calculated by CCLM/DCEP as grid cell averages. Both temperatures can differ substantially. Eliasson (1996) for example found a difference of up to 2.5 K between temperatures measured in a street canyon and in an open area 400 m away from street canyon in the city centre of Göteborg (Sweden) during clear nights. Furthermore, Peterson (2003) analysed homogenized temperature measurements of 289 stations in the USA in the years 1989–1991 and found no statistically significant impact of urbanization over the contiguous USA. The author suggests that this is due to the dominance of the micro and local scale effects over the mesoscale urban heat island since urban meteorological observations are likely to be made within parks.

The bulk scheme, however, is not able to reproduce the urban heat island during the night. Figure 5.12 shows typical spatial distributions of $T_{2\,\mathrm{m}}$ simulated with the bulk approach of CCLM and with DCEP. While no considerably higher urban temperatures are simulated during the day by either approach, the urban area is on average clearly warmer than the surrounding rural area during the night with DCEP. The DCEP scheme generates UHI values of up to 5.5 K during the depicted night. The bulk scheme, however, features only a small urban heat island of up to 1 K. This scheme does not account for the additional heat capacity of the urban surfaces resulting in an underestimation of the storage flux during daytime. For example, DCEP simulates a grid cell average storage flux of up to 230 W m^{-2} in Berlin's centre during the day before the depicted UHI in fig. 5.12b whereas the bulk scheme shows only values up to 150 W m^{-2}. Thus, less energy can be released with the bulk scheme during nighttime, which results in an underestimation of the sensible heat flux. During the exemplary night 2003/08/05, DCEP produces a minimum storage flux of −170 W m^{-2} in the city centre with a sensible heat flux of up to 70 W m^{-2} whereas the bulk scheme shows a minimum storage flux of −85 W m^{-2}, which is accompanied by a smaller sensible heat flux of −20 W m^{-2} (cf. the evaluation with measurements in Basel in section 4.4.2).

In the following, results for the EHE in 2003 are analysed in detail. Figure 5.13 on page 140 shows a comparison of hourly values of measured and simulated 2 m temperatures for all weather stations for the first 7 days of the EHE. The CCLM/DCEP model captures the general behaviour at the stations well with a tendency to overestimate minimum air temperatures during the first nights. This is especially pronounced (up to 5 K) at the Dahlem station due to the reason stated above. Consequently, the

---

[*] except for the 2006 EHE where the model is generally to warm with a MBE 1.7 K at rural Lindenberg and the too cool temperatures of the bulk approach at the grid cell of Alexanderplatz compensate this

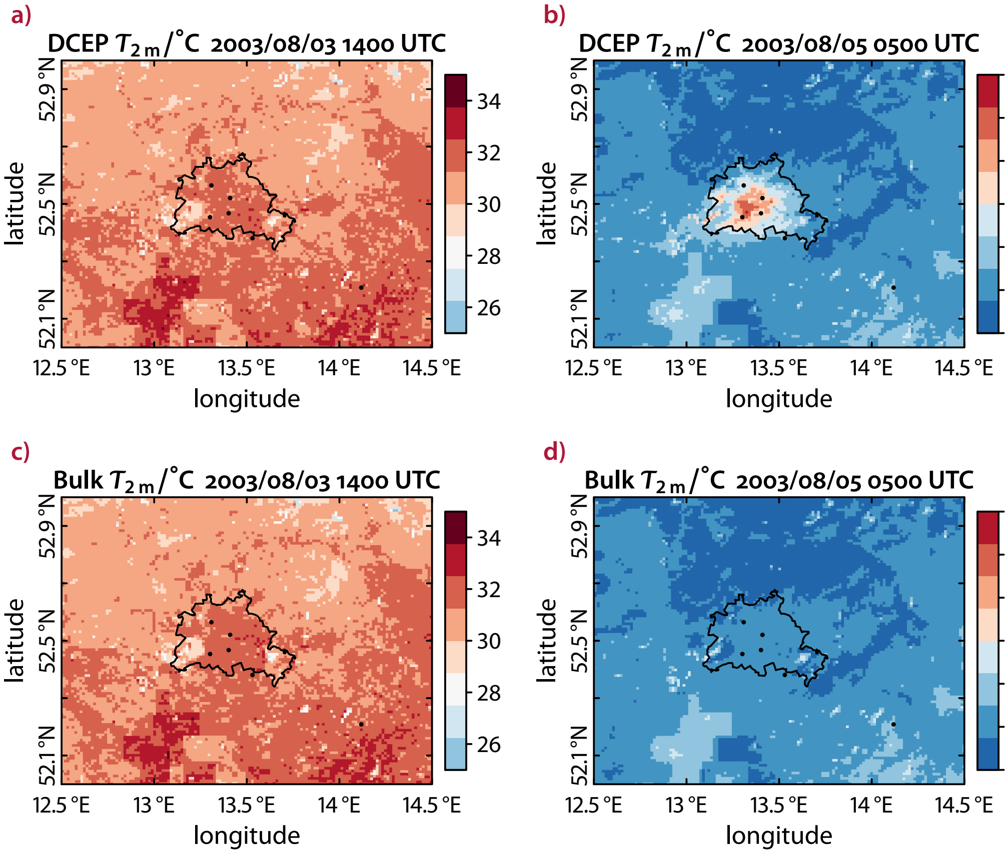

Figure 5.12. Typical spatial distributions of the simulated 2 m temperatures during the extreme heat event of 2003 at a resolution of 1 km simulated with the urban scheme DCEP in a) and b) as well as with the bulk approach in c) and d). The area of Berlin is outlined in black and the positions of the weather stations are indicated by black dots.

bulk approach describes the measurements of the Dahlem station better. Figure 5.14 depicts the over the 7 days averaged diurnal cycle of $\mathcal{T}_{2\,\mathrm{m}}$ at the different stations. While the largest difference between measurement and simulation with DCEP at Dahlem is approx. 3.2 K, the agreement at the other stations is better (see also tab. 5.2). In particular, the measurements at Alexanderplatz, which exemplify the urban heat island of Berlin, is much better represented by DCEP than by the bulk approach during the night. During the day, both approaches produce similar results.

In the following, the dependence of the *simulated* 2 m temperature in Berlin on the urban parameters is analysed. For that purpose, the UHI intensity $\Delta\mathcal{T}_{\mathrm{UHI}}$ for any grid cell in Berlin with $f_{\mathrm{urb}} > 0$ is defined as the difference in the 2 m temperature of that grid cell and that of the grid cell of Lindenberg:

$$\Delta\mathcal{T}_{\mathrm{UHI}} = \mathcal{T}_{2\,\mathrm{m}} - \mathcal{T}_{2\,\mathrm{m}}^{\mathrm{Lindenberg}}\,. \tag{5.17}$$

For every EHE and every specific hour of the day, ΔT_{UHI} is averaged over the analysed days of the EHE. The resulting distributions of the averaged ΔT_{UHI} are fitted to different regression models. The urban fraction f_{urb} is expected to be the most important parameter because it directly influences the averaging of urban and natural fluxes (cf. section 3.5); with increasing f_{urb} the heat island intensity is expected to increase. Furthermore, the urban effects should be more pronounced for larger buildings and narrower streets. Oke (1981) found for Australian, European and North American cities that the *maximum* urban heat island intensity increases with $\ln \lambda_{\mathrm{s}}$, where λ_{s} is the typical building-height-to-canyon-width ratio for the city with $\lambda_{\mathrm{s}} \equiv h/W$. Thus, the following models are used to fit the distributions by a least squares method, weighting each point with its variance resulting from the hourly average:

$$\Delta T_{\mathrm{UHI}} = \Delta T^{(\mathrm{a})}_{\mathrm{UHI}}(f_{\mathrm{urb}}) = m^{(\mathrm{a})}_{f} f_{\mathrm{urb}} + n^{(\mathrm{a})}\,, \tag{5.18a}$$

$$\Delta T_{\mathrm{UHI}} = \Delta T^{(\mathrm{b})}_{\mathrm{UHI}}(f_{\mathrm{urb}}, h) = m^{(\mathrm{b})}_{f} f_{\mathrm{urb}} + m^{(\mathrm{b})}_{h} h + n^{(\mathrm{b})}\,, \tag{5.18b}$$

$$\Delta T_{\mathrm{UHI}} = \Delta T^{(\mathrm{c})}_{\mathrm{UHI}}(f_{\mathrm{urb}}, 1/W) = m^{(\mathrm{c})}_{f} f_{\mathrm{urb}} + m^{(\mathrm{c})}_{W} \frac{1}{W} + n^{(\mathrm{c})}\,, \tag{5.18c}$$

$$\Delta T_{\mathrm{UHI}} = \Delta T^{(\mathrm{d})}_{\mathrm{UHI}}(f_{\mathrm{urb}}, \ln \lambda_{\mathrm{s}}) = m^{(\mathrm{d})}_{f} f_{\mathrm{urb}} + m^{(\mathrm{d})}_{\ln \lambda} \ln \lambda_{\mathrm{s}} + n^{(\mathrm{d})}\,, \tag{5.18d}$$

$$\Delta T_{\mathrm{UHI}} = \Delta T^{(\mathrm{e})}_{\mathrm{UHI}}(f_{\mathrm{urb}}, \lambda_{\mathrm{s}}) = m^{(\mathrm{e})}_{f} f_{\mathrm{urb}} + m^{(\mathrm{e})}_{\lambda} \lambda_{\mathrm{s}} + n^{(\mathrm{e})}\,, \tag{5.18e}$$

where $m^{(\mathrm{i})}_{\psi}$ is the slope of ψ and $n^{(\mathrm{i})}$ is the intercept of model (i). Figure 5.15a on page 142 compares the coefficients of determination, R^2, of all models for the 2003 EHE. All models explain the variance in the data reasonably well at nighttime ($R^2 > 0.6$) while the fit is rather inconclusive at daytime ($R^2 < 0.3$ at 1000 UTC). This is due to the fact that at that time of the day the UHI is less pronounced and the 2 m temperature depends less on the local urban parameters due to increased advection of air masses by higher wind speeds. Furthermore, the largest increase in R^2 relative to the simplest model in (5.18a) is reached with the model in (5.18e). Figure 5.15b shows the results of an F-test with the null hypothesis that the sum of the squared residuals of the enhanced model in (5.18e) is equal to that of the basic model in (5.18a) and the alternative hypothesis that this sum is lower for the enhanced model than for the basic model. The null hypothesis is rejected (i.e. the enhanced model reduces this sum significantly) throughout the day except at 0800 UTC, and at 1700 UTC and at 1800 UTC. Thus, the model in (5.18e) is studied in more detail.

The value of the slopes $m_f \equiv m^{(\mathrm{e})}_{f}$ and $m_\lambda \equiv m^{(\mathrm{e})}_{\lambda}$ as well as the intercept $n \equiv n^{(\mathrm{e})}$ of the 2003 EHE are shown in fig. 5.16 on page 143. Also depicted are the results of t-tests of the null hypothesis that m_f, m_λ or n, respectively, are equal to zero.

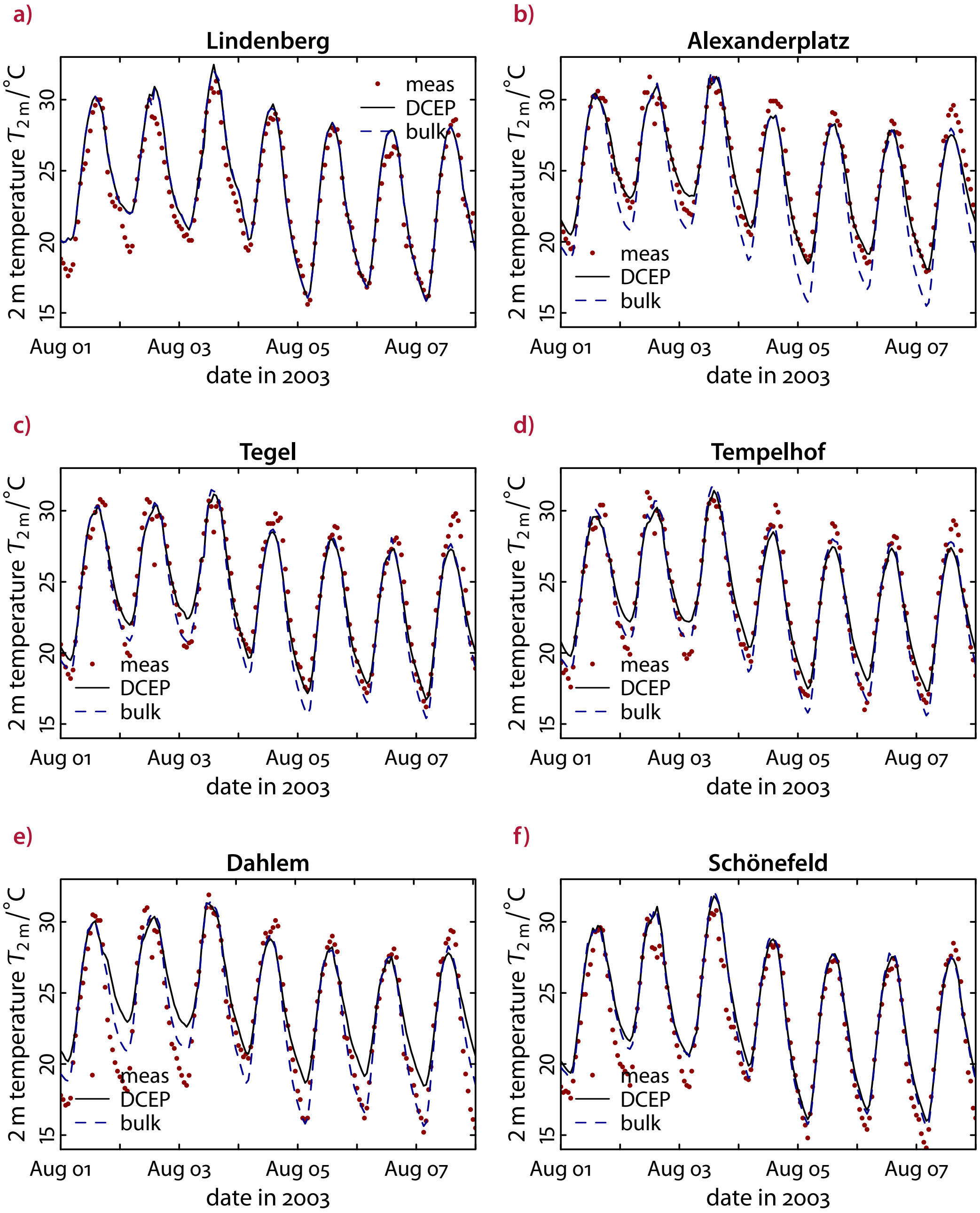

Figure 5.13. Comparison of hourly values of simulated (with DCEP or the bulk approach) and observed 2 m temperatures for the different surface weather stations during the extreme heat event of 2003

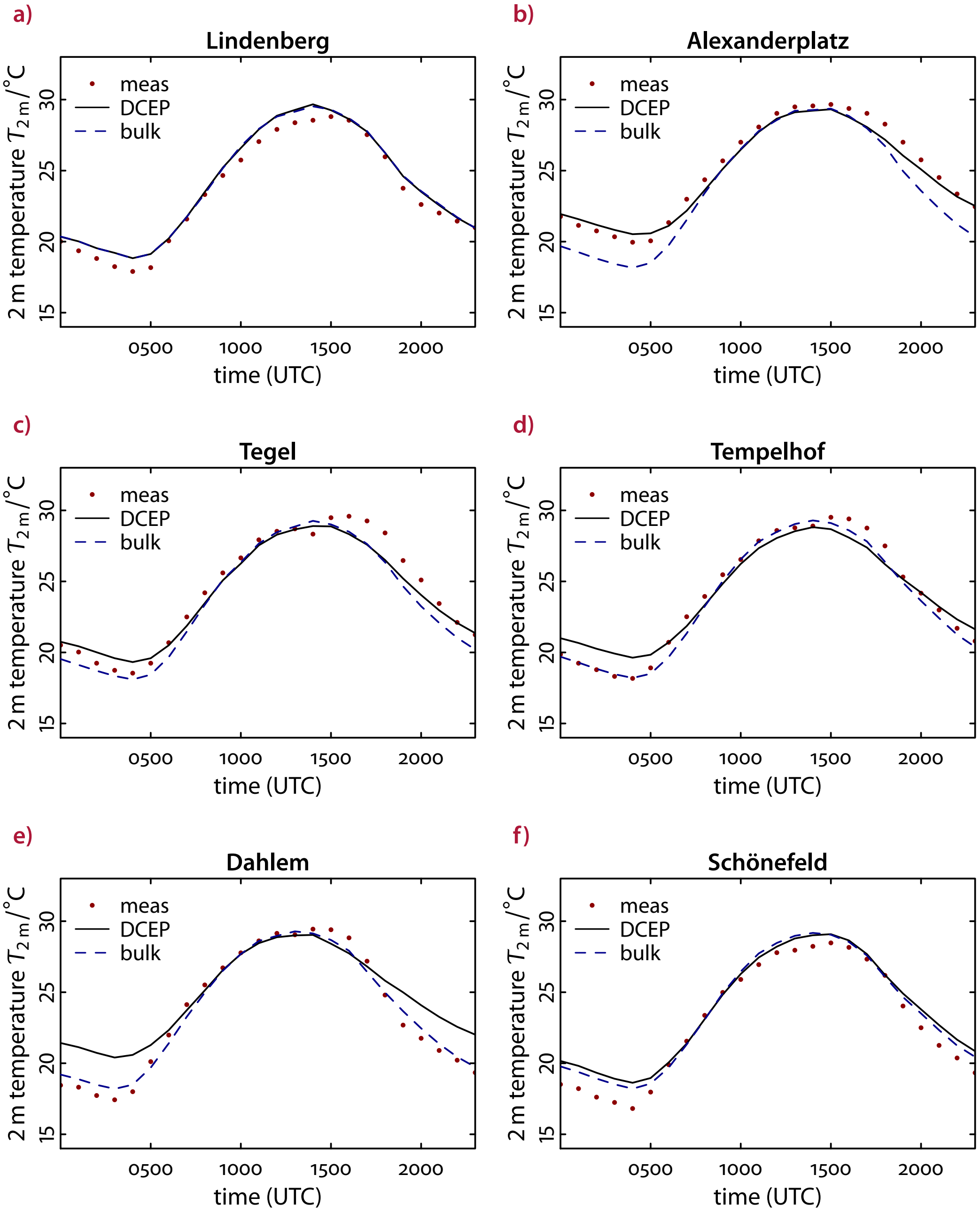

Figure 5.14. Comparison of the average diurnal course of simulated (with DCEP or the bulk approach) and observed 2 m temperatures for the different surface weather stations during the extreme heat event of 2003

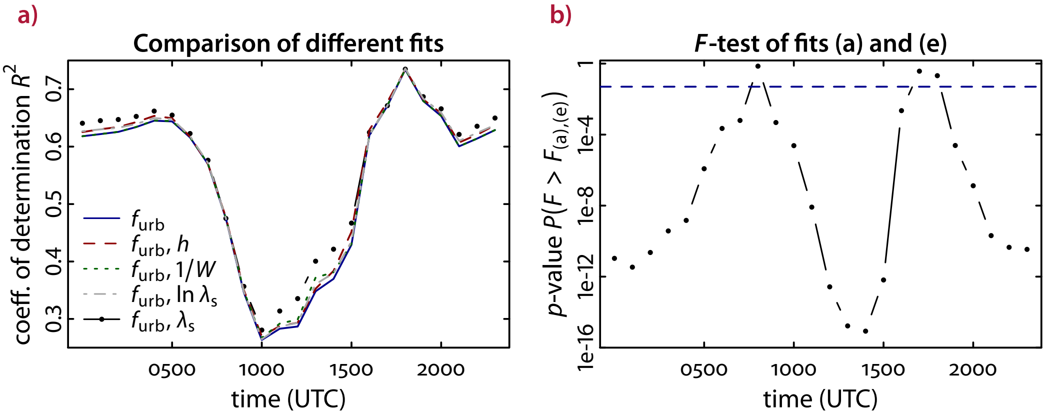

Figure 5.15. Comparison of the different fit models in (5.18) for the 2003 EHE. In a), the coefficient of determination, R^2, for all models is compared. The legend names the respective regressors of the models. In b), the results of an F-test is depicted with the null hypothesis that the sum of the squared residuals of the enhanced model in (5.18e) is equal to that of the basic model in (5.18a) and the alternative hypothesis that this sum is lower for the enhanced model than for the basic model. Shown is the probability of a more extreme F-value than the one computed for the two models (p-value). The significance level of 5 % is marked with a blue, dashed line. A p-value below that line indicates that (5.18e) is a significant improvement of (5.18a).

Since, in general, the UHI intensity is greatest at night (e.g. Oke and Maxwell 1975; Unwin 1980; Adebayo 1987; Magee et al. 1999; Fortuniak et al. 2006), m_f is larger during the night (approx. 3 K) than during the day (less then 1.5 K). Throughout the whole day, m_f is significantly different from zero.

Interestingly, the slope m_λ changes the sign during the day. At nighttime, m_λ is positive, thus, the UHI intensity increases with λ_s due to the increased amount of heat stored in the urban surfaces and due to the reduced sky visibility inside the street canyon. At noon, however, m_λ is negative indicating that temperatures are lower at the 2 m level with larger λ_s. This is due to the fact that more energy is being stored in the urban surface and the shadowing effect of the urban lower level surfaces is increased. m_λ is significantly different from zero except at the times of its zero crossing. Since the enhanced model in (5.18e) with $m_\lambda = 0$ corresponds to the basic model in (5.18a), the results of the corresponding t-test in fig. 5.16d is equivalent to the F-test in fig. 5.15b. Furthermore, the general behaviour of m_λ agrees with the results of the sensitivity studies of Hamdi and Schayes (2008) and Marciotto et al. (2010). Instead of the analysis of the spatial distribution of the UHI, both papers analysed the effect of varying λ_s for one street canyon. Hamdi and Schayes (2008) used a mesoscale model with BEP in a 1-D column mode forced with measurements from the Basel-Sperrstraße station between 17 June to 19 June 2002 (see section 4.2 for a description of the station). At nighttime, they found up to 0.8 K cooler canyon temperatures with $\lambda_s = 0.43$ and up to 0.25 K warmer canyon temperatures with

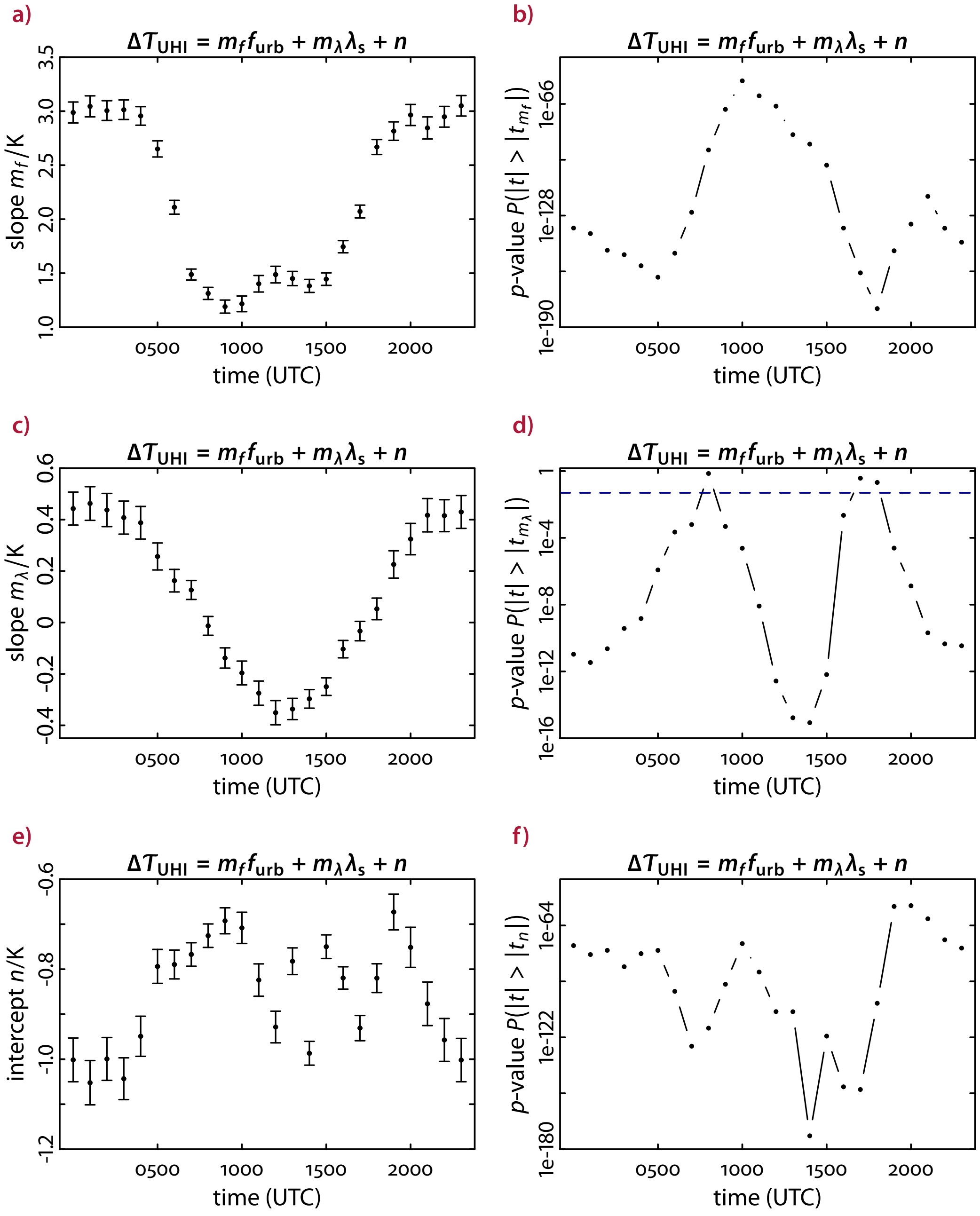

Figure 5.16. Results of the fit of the average urban heat island intensity ΔT_{UHI} to the model in (5.18e) for the 2003 EHE. Figure a), c) and e) show the regression coefficients with the respective standard deviation marked with error bars. Figure b), d) and f) show the results of a t-test with the null hypothesis that the respective regression coefficient is zero. Where appropriate, the significance level of 5 % is indicated by a blue, dashed line.

a) Averaged at 0100 UTC

Start date	m_f/K	m_λ/K	n/K	R^2	$P(F > F_{(a),(e)})$
2002/07/28	2.47±0.05	0.22±0.04	-0.54±0.03	0.78	0.00
2003/08/01	3.04±0.10	0.46±0.07	-1.05±0.05	0.65	0.00
2006/07/01	2.66±0.07	0.55±0.05	-0.25±0.04	0.75	0.00
2006/07/17	2.89±0.09	0.47±0.05	-0.38±0.04	0.70	0.00
2008/07/24	2.73±0.10	0.43±0.07	-0.56±0.05	0.58	0.00

b) Averaged at 1200 UTC

Start date	m_f/K	m_λ/K	n/K	R^2	$P(F > F_{(a),(e)})$
2002/07/28	1.63±0.06	-0.19±0.04	0.16±0.03	0.54	0.00
2003/08/01	1.49±0.08	-0.35±0.05	-0.93±0.04	0.34	0.00
2006/07/01	1.25±0.10	-0.17±0.06	-0.38±0.05	0.20	0.01
2006/07/17	1.28±0.09	-0.26±0.06	-0.22±0.04	0.23	0.00
2008/07/24	1.12±0.08	-0.06±0.05	-0.23±0.04	0.23	0.30

Table 5.3. Results of the linear regression with the model in (5.18e) for all analysed extreme heat events. Listed are the regression coefficients m_f, m_λ and n with their respective standard deviations as well as the coefficient of determination, R^2, and the p-value of the F-test described in the caption of fig. 5.15. Not shown is that all regression coefficients are significantly different from zero except m_λ for the 2008 EHE at 1200 UTC (as indicated by the equivalent p-value of the F-test).

$\lambda_s = 1.5$ compared with a simulation of $\lambda_s = 1$. At daytime, the results were reversed with an increase of up to 0.62 K for $\lambda_s = 0.43$ and a decrease of up to 0.4 K for $\lambda_s = 1.5$ in the canyon temperature. Marciotto et al. (2010) used a similar approach with an independent implementation of the TEB scheme (Masson 2000) forced with typical summer measurements at a micrometeorological station at the University of São Paulo, Brazil, and varied λ_s from 0.5 to 10. At 1200 local time, they found a decrease of the canyon temperature corresponding to a slope of $m_\lambda \approx -0.55$ K for $\lambda_s \leq 5$ and a slightly smaller m_λ for higher λ_s. At 0000 local time, they found $m_\lambda \approx 1$ K for $\lambda_s \leq 3$; for large $\lambda_s \geq 5$, they found a decrease of canyon temperatures as λ_s increases further similar to the night with $m_\lambda \approx -0.4$.

The intercept n is negative and significantly different from zero throughout the day. Its value depends mainly on the chosen reference grid cell. Lindenberg, located south-west of Berlin, is usually warmer than the rural area north of Berlin (cf. fig. 5.12 on page 138) resulting in the negative value of n.

As an example, fig. 5.17 shows the distribution of the average ΔT_{UHI} as a function of f_{urb} and λ_s for the 2003 EHE at 0100 UTC. Furthermore, tab. 5.3 lists the results of the fit for all other analysed EHEs at 0100 UTC (nighttime with $m_\lambda > 0$) and at 1200 UTC (daytime with $m_\lambda < 0$). These results support the findings for the 2003 EHE.

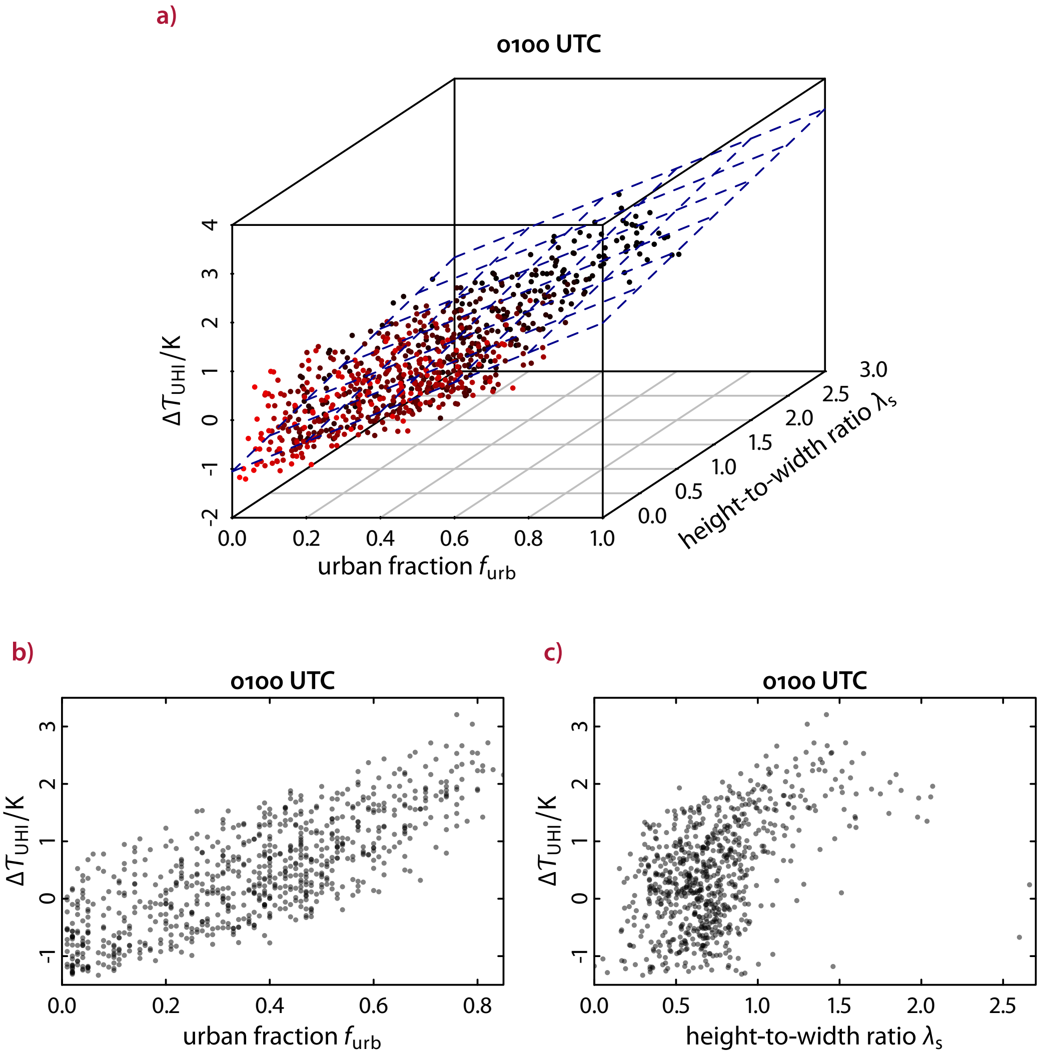

Figure 5.17. Distribution of the average simulated urban heat island intensity ΔT_{UHI} as a function of the urban fraction f_{urb} and the height-to-width ratio λ_s for the 2003 EHE at 0100 UTC. In a), light red dots correspond to low λ_s and darker dots to larger λ_s.

5.5. Assessment of the parameter influence

In this section, the effect of the modifications of the natural surface fraction f_{nat} and the roof albedo α_{R} on the 2 m temperature is analysed. In order to provide a better context for these findings, the corresponding changes in the urban fraction f_{urb} and in the total, grid cell averaged albedo α are determined beforehand.

The spatial distribution of the change in the urban fraction, Δf_{urb}, resulting from a modified natural surface fraction f_{nat} can be derived directly from the spatial distribution of f_{urb}: A relative change of the natural surface fraction by δf_{nat} implies a change in the urban fraction of

$$\Delta f_{\mathrm{urb}}(\delta f_{\mathrm{nat}}) = -\,\Delta f_{\mathrm{nat}}(\delta f_{\mathrm{nat}}) = -(1 - f_{\mathrm{urb}})\,\delta f_{\mathrm{nat}}\,. \tag{5.19}$$

Thus, the larger f_{urb} in fig. 5.2a the smaller Δf_{urb}. The calculation of the change in the grid cell averaged albedo, $\Delta\alpha$, due to an increased roof albedo α_{R} is slightly more complicated. A larger α_{R} increases the *urban* albedo for diffuse and direct radiation separately (cf. (3.61)) depending on the urban canopy parameters. Consequently, the respective grid cell averaged values are modified as given in (3.65) and (3.66). Furthermore, due to the effect of these changes on the meteorological state variables, the soil water content is modified by a small amount, which results in a slightly different albedo of natural surfaces as well (see (2.23) and (2.24)). Figure 5.18a depicts the average spatial distribution of the change of the total urban albedo, $\Delta\alpha_{\mathrm{urb}}$, at 1200 UTC for the 2003 EHE and fig. 5.18c shows the respective histogram of $\Delta\alpha_{\mathrm{urb}}$. Analogously, figs. 5.18b and 5.18d depict the corresponding values of the grid cell averaged total albedo. While $\Delta\alpha_{\mathrm{urb}}$ is relatively homogeneously distributed over the area of Berlin, $\Delta\alpha$ is clearly larger in the city centre due to the larger urban fraction there. The average $\Delta\alpha$ of the urban grid cells of Berlin is about 0.07. Similar results are found for other times of the day with large insolation and also for the other EHEs.

The impact of the f_{nat} and α_{R} changes is measured with the difference in the 2 m temperature, $\Delta T_{2\,\mathrm{m}}$, between the respective sensitivity run and the reference simulation. The time series of $\Delta T_{2\,\mathrm{m}}$ have been smoothed with a binomial filter of a length of 7 h to suppress high frequency noise. The binomial filter is a symmetrical weighted moving average in which the filtered value of the series x_t,

$$\widehat{x}_t \equiv \sum_{i=-n}^{n} w_i x_{t+i}\,, \tag{5.20}$$

includes n backward and n forward data points as well as the central data point at time t. The weights w_i are set proportional to binomial coefficients to prevent a

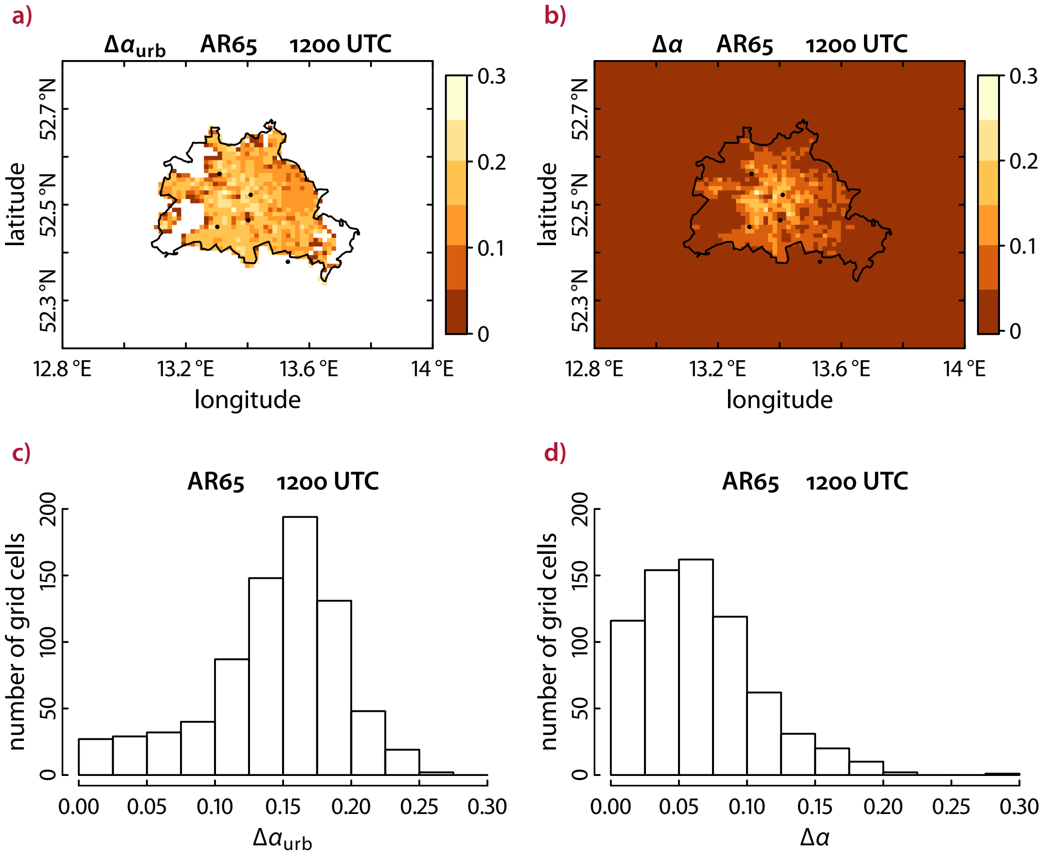

Figure 5.18. Average increase of the total albedo in the AR65 run compared to the reference simulation at 1200 UTC during the 2003 EHE. In a) and c), the albedo difference in the urban part of the grid cell, $\Delta\alpha_{urb}$, is depicted, while in b) and d), the average albedo difference of the complete mesoscale grid cell, $\Delta\alpha$, is shown.

negative frequency response (Mitchell et al. 1966):

$$w_i = 4^{-n}\binom{2n}{i+n} \qquad \text{with} \qquad \binom{n}{k} = \frac{n!}{k!(n-k)!}, \tag{5.21}$$

where the factor 4^{-n} ensures that the weights add up to one. Averaging over $2n+1=7$ hourly time steps, frequencies with a period of more than 7.3 h are suppressed by more than 50 %.

Figures 5.19 and 5.21 show $\widehat{\Delta T}_{2\,\mathrm{m}}$ in response to V-25, V+05, V+15, AR40, AR65 and VAR for the first 7 days of the 2003 EHE at the grid cells of the urban stations and Schönefeld. Furthermore, each fig. a) shows a spatial distribution of $\Delta T_{2\,\mathrm{m}}$ of the respective single parameter sensitivity run with the largest cooling effect.

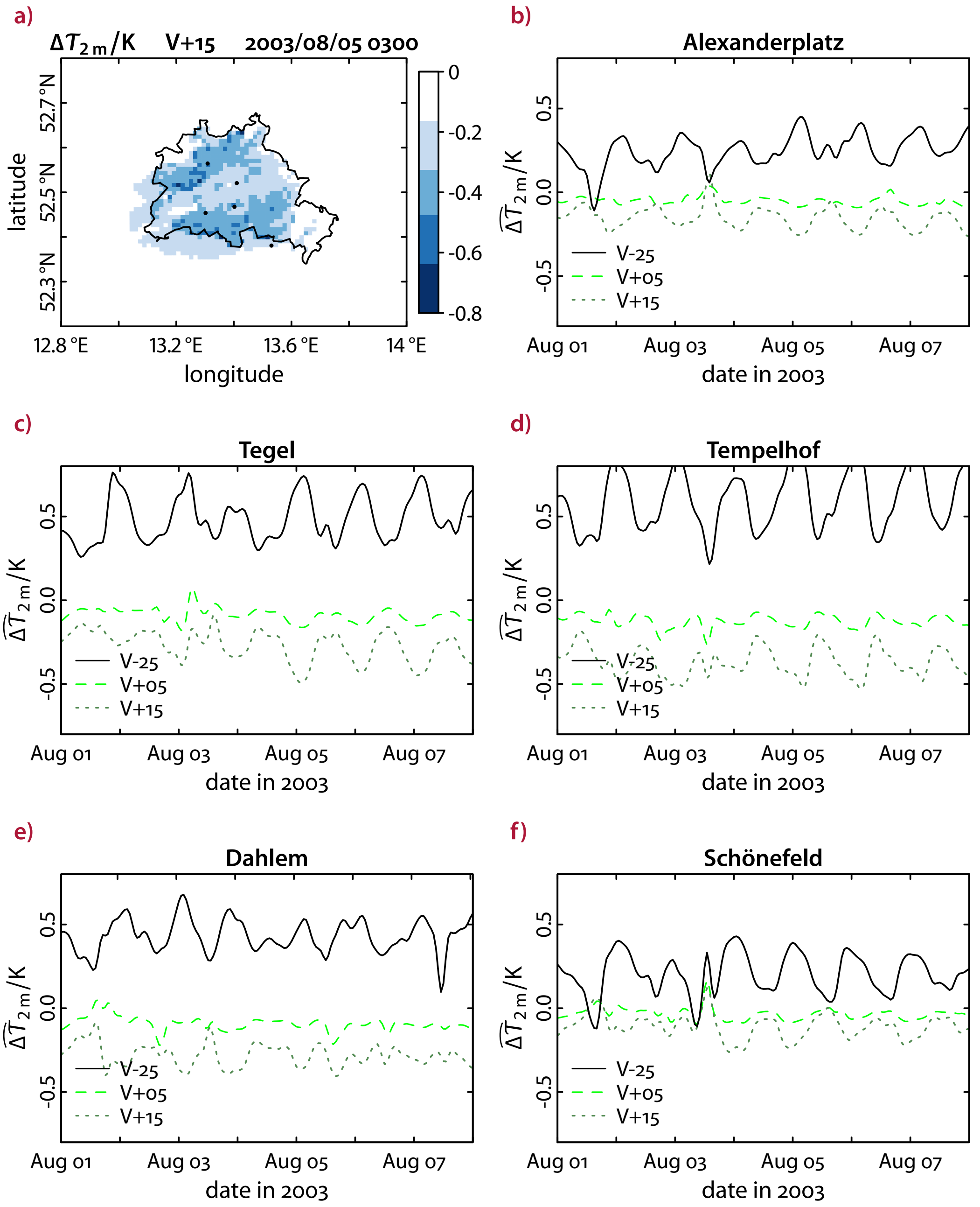

Figure 5.19. Effect of the modified natural surface fraction on the 2 m temperature relative to the reference run for the first 7 days of the extreme heat event in 2003 depicted in fig. 5.13. a) Spatial distribution of $\Delta T_{2\,m}$ in the V+15 run; b)–f) filtered $\Delta T_{2\,m}$ for the urban weather stations and Schönefeld.

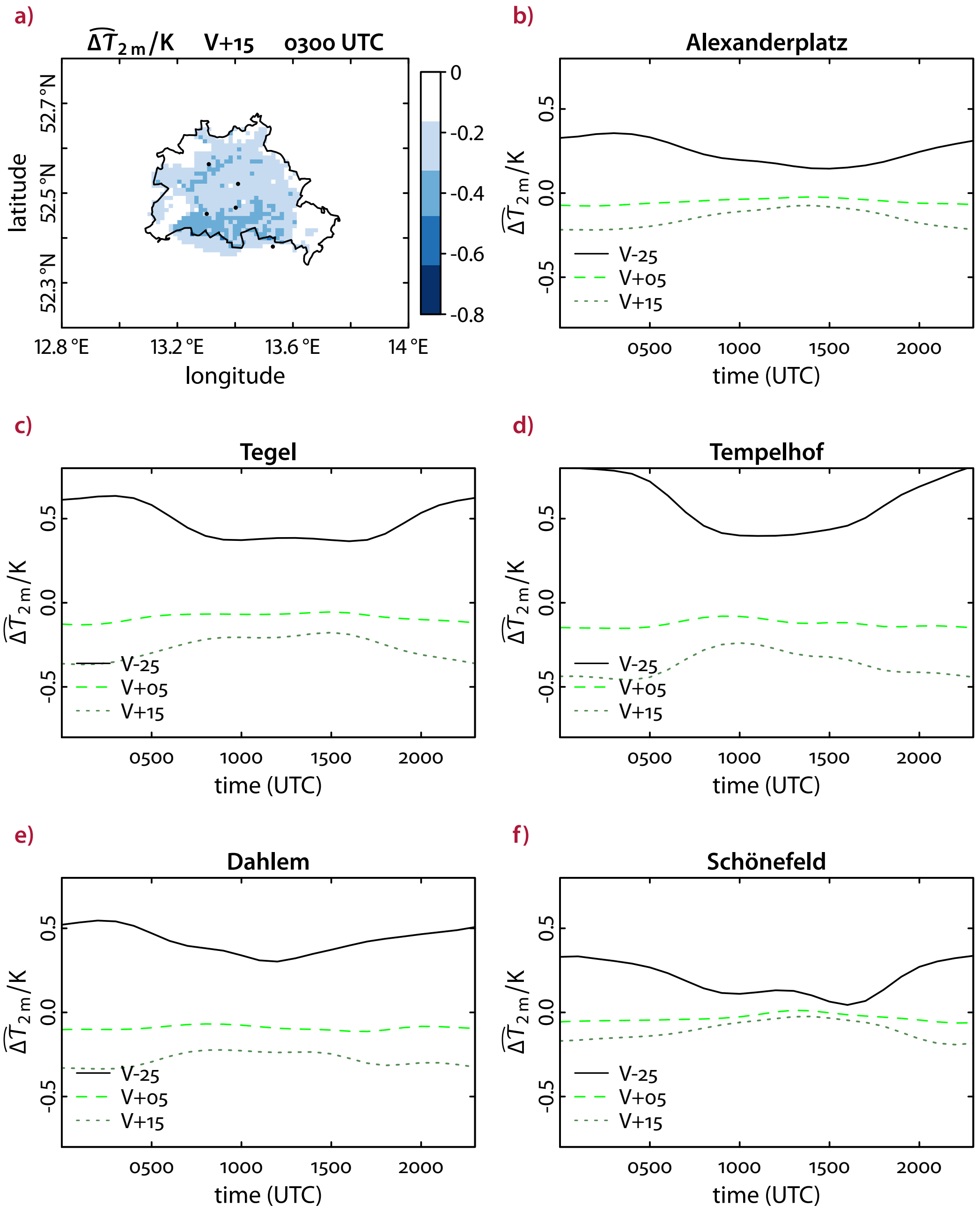

Figure 5.20. Average diurnal cycle of the effect of the modified natural surface fraction on the 2 m temperature relative to the reference run for the first 7 days of the extreme heat event in 2003 depicted in fig. 5.14. a) Spatial distribution of the averaged $\widehat{\Delta T}_{2\,\mathrm{m}}$ in the V+15 run; b)–f) averaged $\widehat{\Delta T}_{2\,\mathrm{m}}$ for the urban weather stations and Schönefeld.

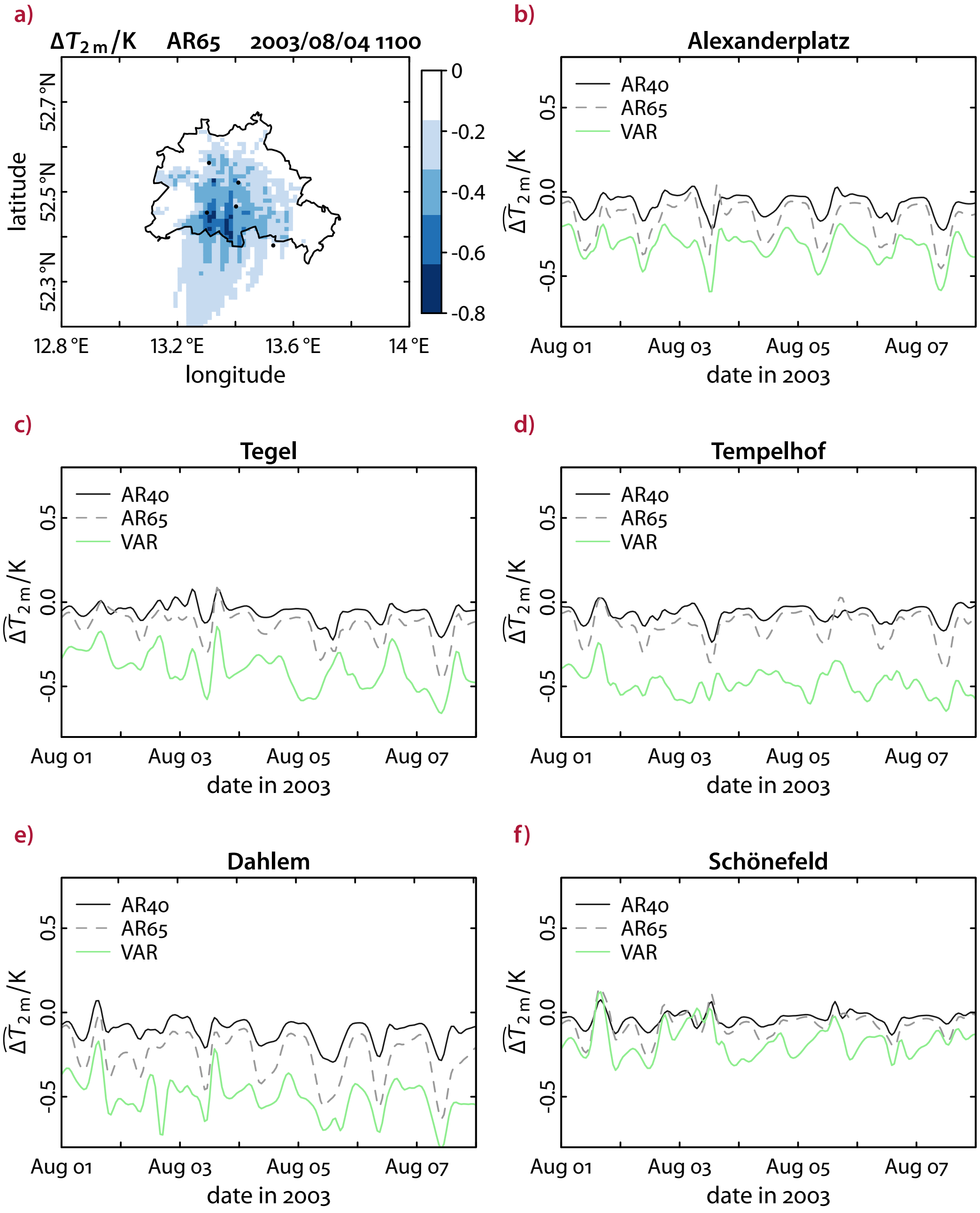

Figure 5.21. Effect of the increased roof albedo and the VAR settings on the 2 m temperature relative to the reference run for the first 7 days of the extreme heat event in 2003 depicted in fig. 5.13. a) Spatial distribution of $\Delta T_{2\,\mathrm{m}}$ in the AR65 run; b)–f) filtered $\Delta T_{2\,\mathrm{m}}$ for the urban weather stations and Schönefeld.

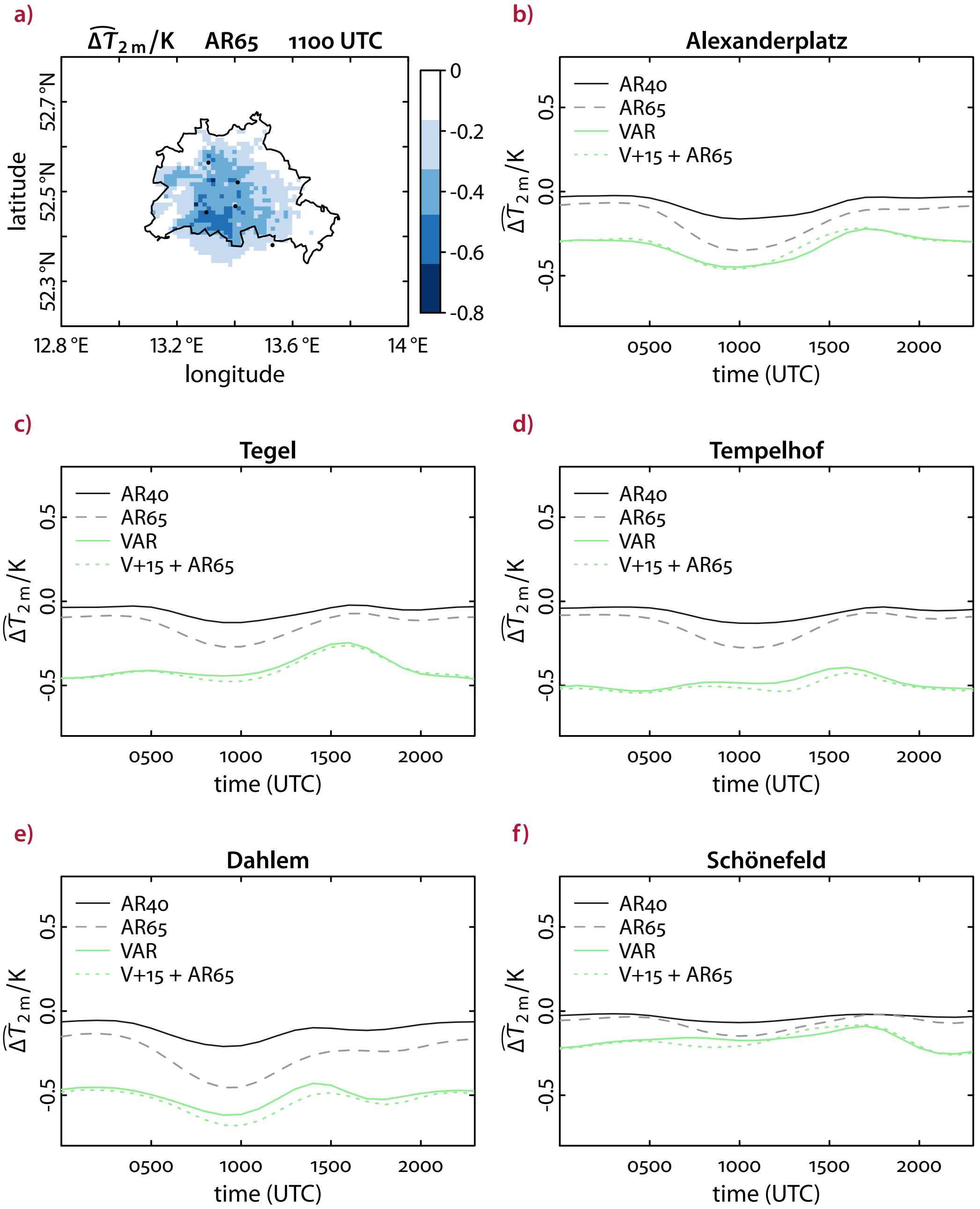

Figure 5.22. Average diurnal cycle of the effect of the increased roof albedo and the VAR settings on the 2 m temperature relative to the reference run for the first 7 days of the extreme heat event in 2003 depicted in fig. 5.14. a) Spatial distribution of the averaged $\widehat{\Delta T}_{2\,\mathrm{m}}$ in the AR65 run; b)–f) averaged $\widehat{\Delta T}_{2\,\mathrm{m}}$ for the urban weather stations and Schönefeld. Also shown is the summed average of $\widehat{\Delta T}_{2\,\mathrm{m}}$ of V+15 and AR65.

Start date	Alexanderplatz				Tegel			
	V-25	V+15	AR65	VAR	V-25	V+15	AR65	VAR
2002/07/28	0.38	-0.20	-0.35	-0.46	0.63	-0.32	-0.30	-0.46
2003/08/01	0.36	-0.22	-0.35	-0.45	0.64	-0.37	-0.27	-0.45
2006/07/01	0.46	-0.27	-0.42	-0.55	0.62	-0.38	-0.39	-0.60
2006/07/17	0.37	-0.22	-0.42	-0.53	0.55	-0.35	-0.26	-0.46
2008/07/24	0.32	-0.23	-0.34	-0.43	0.58	-0.38	-0.29	-0.51

Tempelhof				Dahlem				Schönefeld			
V-25	V+15	AR65	VAR	V-25	V+15	AR65	VAR	V-25	V+15	AR65	VAR
0.76	-0.41	-0.24	-0.51	0.53	-0.31	-0.38	-0.53	0.20	-0.13	-0.07	-0.17
0.80	-0.46	-0.28	-0.53	0.55	-0.34	-0.45	-0.62	0.34	-0.19	-0.15	-0.25
0.82	-0.48	-0.24	-0.58	0.60	-0.38	-0.46	-0.63	0.16	-0.11	-0.06	-0.15
0.78	-0.45	-0.30	-0.56	0.53	-0.32	-0.34	-0.53	0.25	-0.19	-0.14	-0.25
0.74	-0.45	-0.23	-0.55	0.46	-0.32	-0.50	-0.62	0.26	-0.17	-0.06	-0.20

Table 5.4. Maximum average change in 2 m temperature in K derived from the average diurnal course of $\widehat{\Delta T}_{2\,\mathrm{m}}$ for each urban station. Rows represent the five analysed extreme heat events in order of their occurrence.

In the considered model grid cells, VAR has the largest cooling effect on $T_{2\,\mathrm{m}}$ (up to 0.81 K at Dahlem). For the single parameter runs, AR65 causes the largest cooling (up to 0.63 K at Dahlem) while V-25 leads to an increase in $T_{2\,\mathrm{m}}$ of up to 0.80 K at Tempelhof. The effects of AR40 and AR65 are stronger for the Dahlem than for the Alexanderplatz grid cell, which is characterized by a larger f_{urb} value and therefore roof area. This can be explained by the predominant simulated wind direction. During the EHEs in 2003 and 2008, the wind direction is mainly north to northeast; in 2002 and 2006, this is the case about half of the time. The Dahlem station, which is located in the southern part of the city, benefits from the accumulated effect of $\Delta T_{2\,\mathrm{m}}$ in a large part of the urban area. Figure 5.21a shows a clear north south gradient along the wind direction and advection of the cooler air into the rural area south of the city.

The average diurnal course of $\widehat{\Delta T}_{2\,\mathrm{m}}$ for V-25, V+05 and V+15 is shown in fig. 5.20 while AR40, AR65 and VAR are depicted in fig. 5.22. Consequently, each fig. a) shows the averaged spatial distribution of $\widehat{\Delta T}_{2\,\mathrm{m}}$ of the sensitivity run depicted on the left-hand side. The maximum average changes in $T_{2\,\mathrm{m}}$ derived from the average diurnal course of $\widehat{\Delta T}_{2\,\mathrm{m}}$ for each urban station and EHE is shown in tab. 5.4.

The largest average $\widehat{\Delta T}_{2\,\mathrm{m}}$ of the runs with increased natural surface fraction is simulated during the night. A higher natural surface fraction implies a lower urban fraction and, consequently, a reduction of the *total* heat storage capacity as well as a

Start date	Alexanderplatz		Tegel		Tempelhof		Dahlem	
	V-25	V+15	V-25	V+15	V-25	V+15	V-25	V+15
2002/07/28	0.19	-0.11	0.46	-0.27	0.53	-0.32	0.42	-0.25
2003/08/01	0.24	-0.14	0.56	-0.34	0.65	-0.39	0.52	-0.31
2006/07/01	0.21	-0.12	0.49	-0.30	0.57	-0.34	0.45	-0.27
2006/07/17	0.22	-0.13	0.53	-0.32	0.62	-0.37	0.49	-0.29
2008/07/24	0.21	-0.13	0.51	-0.30	0.59	-0.35	0.46	-0.28

Table 5.5. Expected maximum average change in 2 m temperature in K derived from the slope m_f of reference simulation for each urban station.

reduction of radiation trapping. During daytime, the latent heat flux is larger implying that less energy is available to heat the near-surface air. This behaviour is similar to the UHI effect in Berlin which is stronger during the night than during the day. In particular, it can be compared to the temperature change derived from the UHI analysis of the reference simulation in the previous section. With (5.19), the UHI model in (5.18e) would result in a change of temperature of

$$\Delta T_{2\,\mathrm{m}}^{\mathrm{estimate}} = \Delta f_{\mathrm{urb}} m_f = -(1 - f_{\mathrm{urb}})\, \delta f_{\mathrm{nat}}\, m_f\,. \tag{5.22}$$

Table 5.5 lists the corresponding temperature changes. These values underestimate the simulated changes for V-25 and V+15 in tab. 5.4. Especially, at the Alexanderplatz station, the simulated temperature change is about twice as large as the one estimated with (5.22). Here, the small local absolute change Δf_{nat} of the mesoscale grid cell at the Alexanderplatz station is accompanied by larger changes of the surrounding grid cells, which increases the effect. Δf_{urb} is larger at the other stations, thus yielding a better estimate there.

As expected, the largest effect of the increased roof albedo is detected during midday when the incoming solar radiation is largest. Interestingly, the averaged $\widehat{\Delta T}_{2\,\mathrm{m}}$ of the VAR run is similar to the sum of $\widehat{\Delta T}_{2\,\mathrm{m}}$ of the V+15 and AR65 runs (also shown in fig. 5.22). This indicates that the cooling effects of an increased vegetation fraction and an increased roof albedo add up when measured at a height of 2 m.

5.6. Summary and conclusion

This chapter was devoted to estimating the effect of green areas and roof albedos on air temperatures in Berlin (Germany) during extreme heat events (EHE). Five EHEs were identified in the considered years 2000–2009. For each EHE, a reference simulation with CCLM/DCEP was conducted representing the meteorology at that time. To this end, urban canopy parameters were derived based on highly detailed

3-D building and land surface data. As opposed to relying on land-use data only, this method produces urban parameters of higher spatial resolution and circumvents a rough assignment to classes. Thus, it is likely to produce a more realistic description of the ensemble of urban surfaces.

From the reference simulations, it was concluded that the CCLM/DCEP model performs well in terms of the root-mean-square error (RMSE) and the mean-bias error (MBE) of the 2 m temperature. Both error measures behave similarly at the rural station Lindenberg (which is practically not influenced by DCEP) and the urban station Alexanderplatz in the centre of Berlin. This indicates a consistent interplay of DCEP with CCLM since these two stations are representative of the rural and urban characteristics, respectively. At the other urban stations, however, the bulk scheme performs better due to large green areas dominating the station's surroundings. Therefore, these station measurements are not comparable with the simulated grid cell average temperature of urban and natural surfaces. An extreme example is the Dahlem station measurement for the EHE of 2003 displaying a temperature even lower than at the Lindenberg site. Furthermore, the bulk scheme does not produce an urban heat island (UHI).

Within the DCEP reference simulations, the UHI was analysed employing a linear dependence on the urban fraction and the height-to-width ratio. At nighttime, this linear model describes the UHI well. As expected, the UHI increases with rising urban fraction and height-to-width ratio. At daytime, in contrast, the UHI effect is very weak and the linear model is insufficient in describing the temperature distribution. Still, the findings indicate a small increase of temperature with rising urban fraction but a decrease of temperature with rising height-to-width ratio. With higher buildings and narrower streets, the shadowing of the lower urban surfaces is increased leading to lower near-surface air temperatures.

By varying the natural surface fraction, the influence of green areas on the 2 m temperatures is investigated. A natural surface fraction decreased by 25 % for all mesoscale grid cells of Berlin results in an up to 0.82 K larger 2 m temperature at the urban stations. An increase of the natural surface fraction by 15 % shows a cooling of up to 0.48 K. This effect is more pronounced at nighttime due to the difference in the total heat storage capacity and the radiation trapping capability associated with a change of the urban fraction. In general, a stronger effect is observed than the reference simulation would imply by a change of the urban fraction in the linear model. This is because the linear model only considers the local urban parameters whereas for the variation of the natural surface fraction all urban grid cells were modified. Hence, a modification of the natural surface fraction of only one grid cell might be better represented by the linear model.

An increased albedo of roof surfaces directly reproduces the effect of high-albedo surface coatings. In the simulation with a roof albedo of 0.65, up to 0.5 K lower 2 m temperatures were detected at the urban stations compared with the reference simulation with a roof albedo of about 0.16. This effect is stronger during daytime, as is expected. However, the largest change was not detected in the city centre but in the outskirts due to the advection of cool air towards that region. This advection of cool air was also seen in the study by Taha (2008) for Sacramento (California, USA). Due to the larger insolation at Sacramento, and an increase of the albedo not only of the roofs but also of wall and street surfaces, a lower 2 m temperature of up to 3 K was found. Rosenzweig et al. (2009), in turn, found temperature changes similar to this analysis of up to 0.6 K in their study for New York City (USA). Krayenhoff and Voogt (2010) summarized further studies and found a peak daytime air temperature reduction on the order of 0.5 K for typical clear-sky midlatitude summer conditions for a 0.1 average increase in the neighbourhood-scale albedo. In this study, however, a grid cell dependent temperature change results from grid cell dependent albedo increases, but also taking advection into consideration. It is therefore difficult to spatially correlate a specific temperature change with a corresponding albedo increase. Nonetheless, the simulation with a roof albedo of 0.65 can be interpreted to yield a cooling that is roughly consistent with the estimate in Krayenhoff and Voogt (2010).

Combining both, the increased natural surface fractions and higher roof albedos, results in temperature differences comparable to the sum of those of the single modifications. The maximum effects of the single modifications do not simply add up because they occur at different times of the day. Thus, the maximum cooling at the urban stations was found to be 0.63 K. Even though these grid cell average changes appear small relative to the large scale natural surface fraction and albedo modifications assumed in the simulations, it needs to be pointed out that subgrid scale temperature changes can be more intense.

6. Outlook and overall conclusion

This chapter concludes this work with an outlook for possible extensions of DCEP as well as future research questions, and gives an overall summary that puts the results of the main chapters 3 to 5 into context.

6.1. Further model developments

In all simulations in this work, anthropogenic heat emissions are neglected. As argued for Basel in section 4.3, this can be justified with the choice of the analysed episodes (summertime) and the cities in which e.g. air-conditioning systems are not widely used. In a model system that should be applicable to a large variety of cities and simulation periods, however, anthropogenic heat emissions have to be taken into account. Taha (1997), for example, lists anthropogenic heat emissions of up to 210 W m^{-2} in wintertime. In order to estimate these emissions, Sailor (2011), in his review paper, proposes to combine the so-called “inventory approach” for industrial and transportation sector emissions with a “building energy modelling approach” for the building sector. In the former approach, energy consumption data is mapped onto diurnal and spatial allocation profiles, usually assuming the consumption to equal the emissions without time lag. Due to the complexity of anthropogenic heat emissions from buildings, such an inventory approach can overestimate or underestimate heat emissions depending on the season and on the type of buildings (Sailor 2011). Thus, building energy models (e.g. Crawley et al. 2001; Salamanca et al. 2010) are employed to estimate these kinds of emissions. Especially when coupled to an urban canopy scheme like DCEP, estimates for a specific time period become possible. In general, the exact methodology for each approach depends on the available input data; refer to Sailor (2011) for a list of former studies and concrete strategies.

Furthermore, the effect of water and snow on the urban surfaces has not yet been considered in this work. For the analysed summer periods and extreme heat events, this can be justified by the small number of days with precipitation as well as the low water storage capacity of the urban surfaces and a consequently large surface runoff (Grimmond and Oke 1991). Therefore, the total depletion of these reservoirs by evaporation requires only a few hours of daytime conditions (Masson 2000). However, to be applicable to a larger variety of meteorological conditions, the effect of precipitation and evaporation has to be considered for the urban surfaces. During wintertime, for example, the snow cover changes the surface energy partitioning considerably (e.g. Lemonsu et al. 2008).

To this end, the generalization and implementation of the snow model and evaporation approaches of the soil model TERRA_ML of CCLM (Doms, Förstner et al. 2011) and the single-layer urban canopy scheme TEB (Masson 2000) is planned. The TEB scheme has been successfully evaluated for Montreal (Canada) in snowy conditions (Lemonsu et al. 2010). Thus, it is proposed to add a water and a snow reservoir with a limited storage capacity to every horizontal urban surface element (roof or ground surfaces). For every water reservoir, a budget equation is solved taking into account the rain rate and the evaporation. Excess water is lost as runoff. For every snow reservoir, a snow model is used to calculate its evolution. Depending on the respective reservoir, the surface is assumed to be partly wet or partly snow-covered. In the case of the water reservoir, the wet part of the surface is saturated, while the other part is assumed to be dry. In the case of the snow reservoir, the emissivity, albedo, surface temperature, and the sensible and latent heat flux from the snow-free part of the surface are given as described in sections 3.1 and 3.2, while these quantities of the snow-covered part are given by the respective quantities of the snow model. For further computation in the snow case, the average value of the snow-covered and not snow-covered parts is used, which implies, for example, that the albedo of the urban surfaces is no longer constant: with increasing snow cover, the albedo also increases. This also means that the radiation budget equations (3.4) and (3.5) have to be solved again when the urban radiative surface properties values have changed.

For the simulations for both, Basel and Berlin, urban canopy parameters are derived specific to every mesoscale grid cell from digital building data (sections 4.1 and 5.1). As in other studies (e.g. Lemonsu et al. 2004; Hamdi and Schayes 2007; H. Zhang et al. 2008; Salamanca et al. 2011), however, only typical or average urban surface parameters of roofs, walls and streets, respectively, are used for the whole simulation region. Loridan et al. (2010) analysed which urban canopy parameters are most important for estimating the urban surface energy balance for the dense European city centre of Marseille (France). For this purpose they used the offline version of the single-layer urban canopy scheme by Kusaka et al. (2001) that is implemented in the Weather Research and Forecasting (WRF) model. They found the model to display the largest sensitivity to the roof's albedo and heat conductivity.

In further simulations for the area of Berlin, it is therefore planned to use hyperspectral surface reflection and absorption measurements (Roessner et al. 2011) to calculate average surface parameters for every mesoscale grid cell. Due to the high spectral resolution, the specific surface material can be identified. With this information, roof and street surfaces can be recognized and dedicated parameters derived. So far, in the simulation for Berlin in chapter 5, only the *average* albedo obtained from the measurement data depicted in fig. 6.1 is used for the complete simulation region. Since these measurements are not available for the complete area of Berlin, though, urban surface parameters will be assigned to urban structure types (Bochow et al. 2010) in the areas where data is available. It will be explored whether these values can

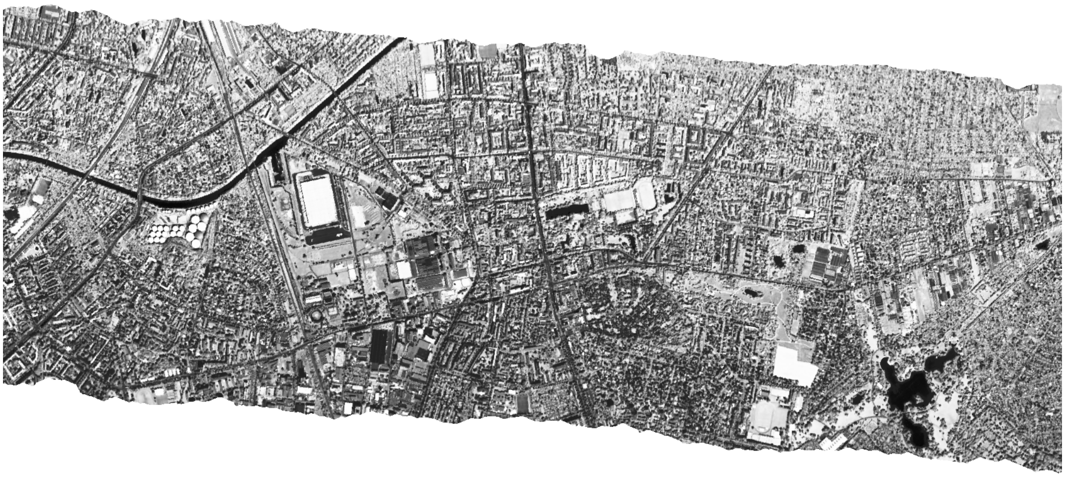

Figure 6.1. Surface albedo resulting from averaging over hyperspectral surface reflection and absorption measurements in the south-east of Berlin (Germany). Pure black pixels correspond to a minimum albedo of 0 and white to a maximum of 0.9.

be translated to the rest of Berlin by using the same urban surface parameters for the same urban structure type.

The integration of vegetation into the street canyon element is another interesting but demanding task. Such an extension considers radiation interactions of buildings and vegetation as well as different environmental conditions for plants. In addition, the geometry of the real canyon is better represented in the model: If the ground surface in a real canyon consists of vegetation as well as impervious surfaces but the canyons in the model are only made up of impervious surfaces, the street width in the model can be chosen to reflect the real impervious surface or to represent the actual distance between the buildings' walls. The first solution employed by Lemonsu et al. (2012) for the original formulation of TEB necessarily resulted in too narrow canyons. This underestimation of the distance between buildings had a considerable effect on the radiation trapping and, therefore, on the radiative temperatures of the urban surfaces. In this work, the latter option was chosen (see (5.2) to (5.4)), which together with (5.5) ensures equal building and street fractions in reality and in the model. However, vegetation and buildings can cast shadows on each other (S.-H. Lee and Park 2008; Lemonsu et al. 2012), which is not considered here so far. Furthermore, vegetation within a street canyon is exposed to different climatic conditions than vegetation in larger parks. Single-layer UCMs that separately calculate the atmospheric conditions within the street canyon can easily take that into account (e.g. S.-H. Lee and Park 2008; Lemonsu et al. 2012). In contrast, multi-layer models such as DCEP, which interact with the vegetation via the grid cell's average atmosphere, do not calculate the conditions within the canyon separately and, thus, cannot distinguish between in-canyon vegetation and a separate vegetated part of the grid cell.

Either way, the soil and vegetation model has to run twice to represent the two kinds of vegetation. In addition, the radiative interaction within the canyon is more complex and, thus, computationally more demanding. Also, further urban canopy parameters are required, which increases the need for more highly detailed urban data sets.

From a technical point of view, the computational requirements of DCEP analysed in section 3.5.3 can be further reduced. On a system with several computational nodes, the calculation of the urban properties and fluxes can be distributed among all nodes. By this, nodes that do not have urban grid cells in their domain would not have to wait for the nodes that do have urban grid cells. Depending on the set-up, the advantage of this approach might be negligible, though, because the communication between nodes is time-consuming. Furthermore, the memory management can be modified such that the urban fields are allocated only for urban grid cells. While CCLM's input and output routines including the routines for restart files[*] have been extended for this work to cope with up to 7-dimensional fields, fields that are not allocated at all grid cells would require an extensive rewrite of these routines.

6.2. Subsequent studies

The coupled CCLM/DCEP model aims to be applicable to a variety of cities, weather conditions and climates (currently, this excludes days dominated by precipitation or anthropogenic heat, as discussed above). Therefore, the evaluation and application of CCLM/DCEP in situations different to the ones analysed in this work will help to further assess the model. For instance, simulations for cities with a large building height variability such as New York City (USA) will help to establish a comparison of the double-canyon approach and the single-canyon approach (see next section).

Other weather conditions include situations that are, for example, dominated by high wind speeds or extensive cloud covers. The urban heat island decreases with the increase of each of these properties (cf. Eliasson 1996; Unger et al. 2001; Morris et al. 2001). Strong winds advect the urban heat downwind and, therefore, increase air temperatures in the downwind rural areas. This can be reproduced by the online coupling of DCEP to CCLM. In cloudy conditions, the typical urban surface characteristics such as low albedo, radiation trapping and increased heat storage are still present but produce a smaller effect on the atmosphere due to less insolation. Since this situation is not qualitatively different to the conditions analysed in this study, these effects can also be captured by DCEP. In both cases, simulations will show to what extent the detailed representation of the urban surface still yields results superior to simpler schemes.

---

[*] A restart file includes the complete model state that allows to stop the model run and continue the calculation later. The support of such a restart is necessary for long-term simulations.

Furthermore, the extension of DCEP to include anthropogenic heat fluxes and precipitation (outlined in the preceding section) is expected to enable CCLM/DCEP to capture all meteorological conditions. This allows to apply the model to long-term periods, and, therefore, to study climatological research questions: Does DCEP correct a possible bias of CCLM in urban areas and their surroundings? How do the modifications of the urban properties of chapter 5 change the near-surface temperature on a climatological scale? And, more generally, what is the impact of more complex urban development scenarios for a metropolitan area?

6.3. Summary and conclusion

In this work, the development of the Double-Canyon Effect parametrization scheme (DCEP) and the full online coupling with the mesoscale climate model COSMO-CLM (CCLM) was presented. Furthermore, the coupled CCLM/DCEP was evaluated with measurements from the Basel UrBan Boundary Layer Experiment (BUBBLE) and CCLM/DCEP was applied to assess the effect of possible mitigation strategies in Berlin (Germany) during extreme heat events (EHEs).

The DCEP scheme is a multi-layer urban canopy model (UCM) based on the Building Effect Parametrization (BEP) by Martilli et al. (2002). The main difference between DCEP and BEP lies in the formulation of the radiation scheme. The DCEP scheme differentiates between direct and diffuse shortwave radiation and ensures the closure of the radiative energy balance. In BEP, the total diffuse radiation that is received from the sky is overestimated in general, which leads to errors in the calculation of the effective radiative temperature and to unphysical values of the effective urban albedo for diffuse radiation. Furthermore, DCEP includes the roof surface into the radiation exchange, i.e. roof surfaces exchange radiation with the other urban surfaces, and shadowing effects on roofs are taken into account. This is done by extending the basic street canyon element to span two canyons. A sensitivity analysis has shown that the effect of the closure of the energy balance and the inclusion of roofs into the radiation exchange is most important for grid cells with a large building height variability; this is, for example, the case for New York City (USA) at a resolution of 1 km × 1 km. For the typical height distributions of Basel and Berlin, though, only small differences were found in the simulated meteorological fields. Thus, a conclusive assessment of the double-canyon approach in comparison with the single-canyon approach is not possible with the evaluation in this study. The evaluation of additional simulations for cities with a larger building height spread like New York City are needed. Ensuring the closure of the energy balance, however, is important from a physical point of view and might have noticeable effects also for cities like Berlin and Basel. Especially in long-term simulations, a constant overestimation of diffuse sky radiation of 10 % and more can change the results considerably.

The extensive evaluation of CCLM/DCEP with measurements from the Basel UrBan Boundary Layer Experiment (BUBBLE) showed good performance of the coupled model in simulating energy fluxes; thus, this online coupled model provides a quality comparable to that of offline simulations by other models. While an offline evaluation of BEP for the BUBBLE data was successfully done before (Hamdi and Schayes 2007), this present online evaluation showed the quality of a UCM coupled to a mesoscale model including the interaction of both models. The latter is the method of choice for predictive purposes.

The analysed heat island mitigation strategies – an increased natural surface fraction and high albedo roof coatings – during extreme heat events in Berlin showed little cooling of the near-surface air temperature. The increase of the natural surface fraction in every urban grid cell in Berlin by 15 % produced an average cooling of up to 0.48 K during the night whereas the high roof albedo of 0.65 reduced the temperature by up to 0.5 K. In particular, the results of the latter scenario of an albedo change confirm the findings of other groups. Combining both scenarios a cooling of up to 0.63 K was found. Since all of these values represent the changes of the grid cell average temperature, local changes are expected to be more intense. In general, field experiments analysing the local scale effects of city-scale urban heat island mitigation approaches cannot be performed due to costs and logistics as well as the difficulty of creating a comparable reference scenario (Krayenhoff and Voogt 2010). Therefore, although UCMs might not exactly quantify the processes in the urban roughness layer, UCMs coupled to mesoscale models such as the CCLM are the best available tools for this kind of analysis due to the variety of scales involved (Krayenhoff and Voogt 2010). The online coupled CCLM/DCEP represents such a tool. Since DCEP is formulated in terms of physically explicit urban canopy parameters directly reflecting the real world, modified real world conditions like the building morphologies or the roof albedo can be directly implemented without having to propagate the effects to derived quantities such as the roughness length or albedo of the whole city.

While CCLM/DCEP was primarily analysed on a 1 km scale and was developed with extensive urban building data-sets in mind, the application of DCEP on larger grids can also be preferable depending on the size of the city and the aim of the simulation. In order to analyse intra-urban temperature differences, the city should obviously occupy as many grid cells as possible. However, to study the average effect of cities on the mesoscale, simulations with large grid cells can be conducted with DCEP and the implemented tile approach. Simpler schemes with less input parameters might be better suited for these calculations, though. Georgescu et al. (2013), for example, studied the climatic impacts of the megapolitan expansion in Arizona (USA) on a 20 km grid with a single-layer UCM coupled with the WRF model. Another single-layer UCM was used in a global climate model at a resolution of 1.9° × 2.5° (Oleson et al. 2010).

Analogously, an extended DCEP including the developments discussed in section 6.1 can be used for operational weather prediction. However, here, the computing requirements have to be kept in mind, in particular the additional memory space needed for large domains with several urban regions. Also, if only an approximation of the effect of the urban surface on meteorological fields is desired, simpler models with less computing demands may suffice.

The quality of the CCLM/DCEP simulation of the urban near-surface air temperatures crucially depends on the performance of the driving model outside of the urban area, as seen in the studies for Basel and Berlin. Especially in Berlin, the simulation errors with respect to the absolute values of the 2 m temperature were similar at the rural reference station and in the city centre. However, this also indicates that the relative difference between the urban and rural environment can be caught by CCLM/DCEP in principle, even if there are systematic errors in CCLM's forcing. The latter statement, naturally, can be expected to hold to a degree depending on the size and type of the deviation of CCLM.

In all simulations of Basel and Berlin, the employed urban canopy parameters (UCPs) were derived from urban morphological data-sets. In particular for Berlin, the combination of an impervious surface data-set with an extensive building data-set in the CityGML format allowed for the derivation of realistic UCPs, which are not based on coarse land-use data. This resulted in a more realistic representation of the urban surfaces in DCEP and consequently in CCLM/DCEP, permitting the analysis of the simulated urban heat island in terms of grid cell dependent UCPs. In the future, building data-sets for an increasing number of cities will likely be available. The approaches presented here can be further adjusted to these data-sets to provide UCPs for future high resolution mesoscale simulations.

A. The radiation budget equations of the urban surfaces

For reference, the complete equations that describe the incoming diffuse longwave and shortwave radiation on the ith west and east wall, on the ith roof and on the ground surface are listed in the following. The terms in blue have been added to include the roofs in the radiation exchange. In the first lines, an approach including the roofs in the interaction can be chosen (blue) or one neglecting the roof part (black). The correction factor introduced in section 3.1.1 is marked in red. Restricting oneself to the black terms, the original formulation by Martilli et al. (2002) is recovered.

A.1. Incoming longwave radiation

$$
\begin{aligned}
L_{\mathrm{W}i} = {} & \left\{ \begin{matrix} \mathcal{L}^{\downarrow} \tilde{\Psi}_{\mathrm{Ss}\to i} + \sum_{j=1}^{n} c \mathcal{L}^{\downarrow} \tilde{\Psi}_{j\to i} (1 - \Gamma_j) \\ \sum_{k=0}^{n} \gamma_k \mathcal{L}^{\downarrow} \tilde{\Psi}_{\mathrm{Sd} \xrightarrow{k} i} + \sum_{k=0}^{n} \gamma_k \sum_{j=1}^{n} c \mathcal{L}^{\downarrow} \tilde{\Psi}_{j \xrightarrow{k} i} (1 - \Gamma_j) \end{matrix} \right\} \\
& + \epsilon_{\mathrm{G}} \sigma T_{\mathrm{G}}^4 \tilde{\Psi}_{\mathrm{G}\to i} + (1 - \epsilon_{\mathrm{G}}) L_{\mathrm{G}} \tilde{\Psi}_{\mathrm{G}\to i} \\
& + \sum_{k=0}^{n} \gamma_k \epsilon_{\mathrm{G}} \sigma T_{\mathrm{G}}^4 \tilde{\Psi}_{\mathrm{G} \xrightarrow{k} i} + \sum_{k=0}^{n} \gamma_k (1 - \epsilon_{\mathrm{G}}) L_{\mathrm{G}} \tilde{\Psi}_{\mathrm{G} \xrightarrow{k} i} \\
& + \sum_{j=1}^{n} \epsilon_{\mathrm{W}} \sigma T_{\mathrm{E}j}^4 \tilde{\Psi}_{j\to i} \Gamma_j + \sum_{j=1}^{n} (1 - \epsilon_{\mathrm{W}}) L_{\mathrm{E}j} \tilde{\Psi}_{j\to i} \Gamma_j \\
& + \sum_{k=0}^{n} \gamma_k \sum_{j=1}^{n} \epsilon_{\mathrm{W}} \sigma T_{\mathrm{E}j}^4 \tilde{\Psi}_{j \xrightarrow{k} i} \Gamma_j + \sum_{k=0}^{n} \gamma_k \sum_{j=1}^{n} (1 - \epsilon_{\mathrm{W}}) L_{\mathrm{E}j} \tilde{\Psi}_{j \xrightarrow{k} i} \Gamma_j \\
& + \sum_{k=0}^{i-1} \epsilon_{\mathrm{R}} \sigma T_{\mathrm{R}k}^4 \tilde{\Psi}_{\mathrm{R}k\to i} \gamma_k + \sum_{k=0}^{i-1} (1 - \epsilon_{\mathrm{R}}) L_{\mathrm{R}k} \tilde{\Psi}_{\mathrm{R}k\to i} \gamma_k
\end{aligned} \tag{A.1}
$$

$$\begin{aligned}
L_{\mathrm{E}i} = {} & \left\{\begin{matrix}
\mathcal{L}^{\downarrow}\tilde{\Psi}_{\mathrm{Ss}\rightarrow i} + \sum_{j=1}^{n} c\mathcal{L}^{\downarrow}\tilde{\Psi}_{j\rightarrow i}(1-\mathit{\Gamma}_j) \\
\sum_{k=0}^{n}\gamma_k\mathcal{L}^{\downarrow}\tilde{\Psi}_{\mathrm{Sd}\xrightarrow{k} i} + \sum_{k=0}^{n}\gamma_k\sum_{j=1}^{n} c\mathcal{L}^{\downarrow}\tilde{\Psi}_{j\xrightarrow{k} i}(1-\mathit{\Gamma}_j)
\end{matrix}\right\} \\
& + \epsilon_{\mathrm{G}}\sigma T_{\mathrm{G}}^4\tilde{\Psi}_{\mathrm{G}\rightarrow i} + (1-\epsilon_{\mathrm{G}})L_{\mathrm{G}}\tilde{\Psi}_{\mathrm{G}\rightarrow i} \\
& + \sum_{k=0}^{n}\gamma_k\epsilon_{\mathrm{G}}\sigma T_{\mathrm{G}}^4\tilde{\Psi}_{\mathrm{G}\xrightarrow{k} i} + \sum_{k=0}^{n}\gamma_k(1-\epsilon_{\mathrm{G}})L_{\mathrm{G}}\tilde{\Psi}_{\mathrm{G}\xrightarrow{k} i} \\
& + \sum_{j=1}^{n}\epsilon_{\mathrm{W}}\sigma T_{\mathrm{W}j}^4\tilde{\Psi}_{j\rightarrow i}\mathit{\Gamma}_j + \sum_{j=1}^{n}(1-\epsilon_{\mathrm{W}})L_{\mathrm{W}j}\tilde{\Psi}_{j\rightarrow i}\mathit{\Gamma}_j \\
& + \sum_{k=0}^{n}\gamma_k\sum_{j=1}^{n}\epsilon_{\mathrm{W}}\sigma T_{\mathrm{W}j}^4\tilde{\Psi}_{j\xrightarrow{k} i}\mathit{\Gamma}_j + \sum_{k=0}^{n}\gamma_k\sum_{j=1}^{n}(1-\epsilon_{\mathrm{W}})L_{\mathrm{W}j}\tilde{\Psi}_{j\xrightarrow{k} i}\mathit{\Gamma}_j \\
& + \sum_{k=0}^{i-1}\epsilon_{\mathrm{R}}\sigma T_{\mathrm{R}k}^4\tilde{\Psi}_{\mathrm{R}k\rightarrow i}\gamma_k + \sum_{k=0}^{i-1}(1-\epsilon_{\mathrm{R}})L_{\mathrm{R}k}\tilde{\Psi}_{\mathrm{R}k\rightarrow i}\gamma_k
\end{aligned} \tag{A.2}$$

$$\begin{aligned}
L_{\mathrm{G}} = {} & \left\{\begin{matrix}
\mathcal{L}^{\downarrow}\tilde{\Psi}_{\mathrm{Ss}\rightarrow \mathrm{G}} + 2\sum_{j=1}^{n} c\mathcal{L}^{\downarrow}\tilde{\Psi}_{j\rightarrow \mathrm{G}}(1-\mathit{\Gamma}_j) \\
\sum_{k=0}^{n}\gamma_k\mathcal{L}^{\downarrow}\tilde{\Psi}_{\mathrm{Sd}\xrightarrow{k} \mathrm{G}} + \sum_{j=1}^{n} c\mathcal{L}^{\downarrow}\tilde{\Psi}_{j\rightarrow \mathrm{G}}(1-\mathit{\Gamma}_j) + \sum_{k=0}^{n}\gamma_k\sum_{j=1}^{n} c\mathcal{L}^{\downarrow}\tilde{\Psi}_{j\xrightarrow{k} \mathrm{G}}(1-\mathit{\Gamma}_j)
\end{matrix}\right\} \\
& + \sum_{j=1}^{n}\epsilon_{\mathrm{W}}\sigma(T_{\mathrm{E}j}^4 + T_{\mathrm{W}j}^4)\tilde{\Psi}_{j\rightarrow i}\mathit{\Gamma}_j + \sum_{j=1}^{n}(1-\epsilon_{\mathrm{W}})(L_{\mathrm{E}j} + L_{\mathrm{W}j})\tilde{\Psi}_{j\rightarrow i}\mathit{\Gamma}_j \\
& + \sum_{k=0}^{n}\gamma_k\sum_{j=1}^{n}\epsilon_{\mathrm{W}}\sigma(T_{\mathrm{E}j}^4 + T_{\mathrm{W}j}^4)\tilde{\Psi}_{j\rightarrow i}\mathit{\Gamma}_j + \sum_{k=0}^{n}\gamma_k\sum_{j=1}^{n}(1-\epsilon_{\mathrm{W}})(L_{\mathrm{E}j} + L_{\mathrm{W}j})\tilde{\Psi}_{j\rightarrow i}\mathit{\Gamma}_j
\end{aligned} \tag{A.3}$$

$$\begin{aligned}
L_{\mathrm{R}i} = {} & \left\{\begin{matrix}
\mathcal{L}^{\downarrow} \\
\mathcal{L}^{\downarrow}\tilde{\Psi}_{\mathrm{Sd}\rightarrow \mathrm{R}i} + 2\sum_{j=i+1}^{n} c\mathcal{L}_{\mathrm{R}i}\tilde{\Psi}_{j\rightarrow \mathrm{R}i}(1-\mathit{\Gamma}_j)
\end{matrix}\right\} \\
& + \sum_{j=i+1}^{n}\epsilon_{\mathrm{W}}\sigma(T_{\mathrm{E}j}^4 + T_{\mathrm{W}j}^4)\tilde{\Psi}_{j\rightarrow \mathrm{R}i}\mathit{\Gamma}_j + \sum_{j=i+1}^{n}(1-\epsilon_{\mathrm{W}})(L_{\mathrm{E}j} + L_{\mathrm{W}j})\tilde{\Psi}_{j\rightarrow \mathrm{R}i}\mathit{\Gamma}_j
\end{aligned} \tag{A.4}$$

A.2. Incoming shortwave radiation

$$\begin{aligned} K_{\mathrm{W}i} = {} & \left\{ \begin{aligned} & S^{\mathrm{k},\Downarrow}_{\mathrm{W}i} + \mathcal{K}^{\downarrow}\tilde{\varPsi}_{\mathrm{Ss}\to i} + \sum_{j=1}^{n} c\mathcal{K}^{\downarrow}\tilde{\varPsi}_{j\to i}(1-\varGamma_j) \\ & S^{\mathrm{k},\Downarrow}_{\mathrm{W}i} + \sum_{k=0}^{n}\gamma_k\mathcal{K}^{\downarrow}\tilde{\varPsi}_{\mathrm{Sd}\xrightarrow{k} i} + \sum_{k=0}^{n}\gamma_k\sum_{j=1}^{n} c\mathcal{K}^{\downarrow}\tilde{\varPsi}_{j\xrightarrow{k} i}(1-\varGamma_j) \end{aligned} \right\} \\ & + (1-\epsilon_{\mathrm{G}})K_{\mathrm{G}}\tilde{\varPsi}_{\mathrm{G}\to i} + \sum_{k=0}^{n}\gamma_k(1-\epsilon_{\mathrm{G}})K_{\mathrm{G}}\tilde{\varPsi}_{\mathrm{G}\xrightarrow{k} i} \\ & + \sum_{j=1}^{n}(1-\epsilon_{\mathrm{W}})K_{\mathrm{E}j}\tilde{\varPsi}_{j\to i}\varGamma_j + \sum_{k=0}^{n}\gamma_k\sum_{j=1}^{n}(1-\epsilon_{\mathrm{W}})K_{\mathrm{E}j}\tilde{\varPsi}_{j\xrightarrow{k} i}\varGamma_j \\ & + \sum_{k=0}^{i-1}(1-\epsilon_{\mathrm{R}})K_{\mathrm{R}k}\tilde{\varPsi}_{\mathrm{R}k\to i}\gamma_k \end{aligned} \tag{A.5}$$

$$\begin{aligned} K_{\mathrm{E}i} = {} & \left\{ \begin{aligned} & S^{\mathrm{k},\Downarrow}_{\mathrm{E}i} + \mathcal{K}^{\downarrow}\tilde{\varPsi}_{\mathrm{Ss}\to i} + \sum_{j=1}^{n} c\mathcal{K}^{\downarrow}\tilde{\varPsi}_{j\to i}(1-\varGamma_j) \\ & S^{\mathrm{k},\Downarrow}_{\mathrm{E}i} \sum_{k=0}^{n}\gamma_k\mathcal{K}^{\downarrow}\tilde{\varPsi}_{\mathrm{Sd}\xrightarrow{k} i} + \sum_{k=0}^{n}\gamma_k\sum_{j=1}^{n} c\mathcal{K}^{\downarrow}\tilde{\varPsi}_{j\xrightarrow{k} i}(1-\varGamma_j) \end{aligned} \right\} \\ & + (1-\epsilon_{\mathrm{G}})K_{\mathrm{G}}\tilde{\varPsi}_{\mathrm{G}\to i} + \sum_{k=0}^{n}\gamma_k(1-\epsilon_{\mathrm{G}})K_{\mathrm{G}}\tilde{\varPsi}_{\mathrm{G}\xrightarrow{k} i} \\ & + \sum_{j=1}^{n}(1-\epsilon_{\mathrm{W}})K_{\mathrm{W}j}\tilde{\varPsi}_{j\to i}\varGamma_j + \sum_{k=0}^{n}\gamma_k\sum_{j=1}^{n}(1-\epsilon_{\mathrm{W}})K_{\mathrm{W}j}\tilde{\varPsi}_{j\xrightarrow{k} i}\varGamma_j \\ & + \sum_{k=0}^{i-1}(1-\epsilon_{\mathrm{R}})K_{\mathrm{R}k}\tilde{\varPsi}_{\mathrm{R}k\to i}\gamma_k \end{aligned} \tag{A.6}$$

$$\begin{aligned} K_{\mathrm{G}} = {} & \left\{ \begin{aligned} & S^{\mathrm{k},\Downarrow}_{\mathrm{G}} + \mathcal{K}^{\downarrow}\tilde{\varPsi}_{\mathrm{Ss}\to \mathrm{G}} + 2\sum_{j=1}^{n} c\mathcal{K}^{\downarrow}\tilde{\varPsi}_{j\to \mathrm{G}}(1-\varGamma_j) \\ & S^{\mathrm{k},\Downarrow}_{\mathrm{G}} + \sum_{k=0}^{n}\gamma_k\mathcal{K}^{\downarrow}\tilde{\varPsi}_{\mathrm{Sd}\xrightarrow{k} \mathrm{G}} + \sum_{j=1}^{n} c\mathcal{K}^{\downarrow}\tilde{\varPsi}_{j\to \mathrm{G}}(1-\varGamma_j) + \sum_{k=0}^{n}\gamma_k\sum_{j=1}^{n} c\mathcal{K}^{\downarrow}\tilde{\varPsi}_{j\xrightarrow{k} \mathrm{G}}(1-\varGamma_j) \end{aligned} \right\} \\ & + \sum_{j=1}^{n}(1-\epsilon_{\mathrm{W}})(K_{\mathrm{E}j}+K_{\mathrm{W}j})\tilde{\varPsi}_{j\to i}\varGamma_j + \sum_{k=0}^{n}\gamma_k\sum_{j=1}^{n}(1-\epsilon_{\mathrm{W}})(K_{\mathrm{E}j}+K_{\mathrm{W}j})\tilde{\varPsi}_{j\to i}\varGamma_j \end{aligned} \tag{A.7}$$

$$K_{\mathrm{R}i} = \left\{ \begin{array}{l} \mathcal{K}^{\Downarrow} + \mathcal{K}^{\downarrow} \\ S_{\mathrm{R}i}^{\mathrm{k},\Downarrow} + \mathcal{K}^{\downarrow} \tilde{\Psi}_{\mathrm{Sd}\to\mathrm{R}i} + 2 \sum_{j=i+1}^{n} c \mathcal{K}_{\mathrm{R}i} \tilde{\Psi}_{j\to\mathrm{R}i} (1 - \Gamma_j) \end{array} \right\} + \sum_{j=i+1}^{n} (1 - \epsilon_{\mathrm{W}}) (K_{\mathrm{E}j} + K_{\mathrm{W}j}) \tilde{\Psi}_{j\to\mathrm{R}i} \Gamma_j \tag{A.8}$$

B. View factors

This chapter introduces the concept of view factors and sketches how the view factors used by Martilli et al. (2002) for the single-canyon approach are obtained. Furthermore, a method to calculate the additional view factors used in the double-canyon approach of DCEP is presented.

B.1. Definition and usage of view factors

This description of the basic properties of view factors is based on D. C. Hamilton and Morgan (1952) and Sparrow and Cess (1978). If the view between two surfaces is partially obstructed, the view factor between them has to be modified; here, a special treatment of these cases is added.

A view factor describes the fraction of energy that a surface receives from a diffusively radiating source. Let E_j be the energy received by a surface of area A_j emanating from a diffusively radiating source of area A_i with radiosity R_i. Furthermore, let $\Psi_{i\to j}$ be the view factor from surface i to j, then

$$E_j = R_i A_i \Psi_{i\to j}\,. \tag{B.1}$$

Due to energy conservation, the sum of all view factors from A_i is unity:

$$\sum_j \Psi_{i\to j} = 1\,. \tag{B.2}$$

The effective view factor $\tilde{\Psi}_{i\to j}$ relates now the emitted and received radiosity:

$$R_j \equiv \frac{E_j}{A_j} = R_i \frac{A_i}{A_j} \Psi_{i\to j} \equiv R_i \tilde{\Psi}_{i\to j}\,. \tag{B.3}$$

The view factor is given by (see fig. B.1 for definition of variables)

$$\Psi_{i\to j} = \frac{1}{A_i} \int_{A_i} \int_{A_j} \nu_{\hat{\imath}\hat{\jmath}} \frac{\cos\beta_{\hat{\imath}} \cos\beta_{\hat{\jmath}}}{\pi r_{\hat{\imath}\hat{\jmath}}^2} \, \mathrm{d}A_{\hat{\jmath}} \, \mathrm{d}A_{\hat{\imath}}\,, \tag{B.4}$$

where $\nu_{\hat{\imath}\hat{\jmath}}$ is 1 if the view between the surface elements $\mathrm{d}A_{\hat{\imath}}$ and $\mathrm{d}A_{\hat{\jmath}}$ is unobstructed

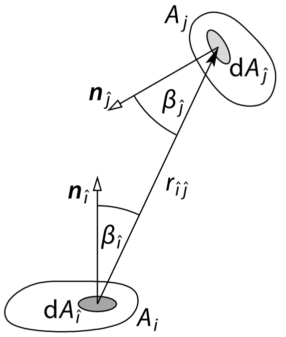

Figure B.1. Calculation of view factor between surface A_i and A_j by integrating over A_i and A_j. $\boldsymbol{n}_{\hat{\imath}}$ and $\boldsymbol{n}_{\hat{\jmath}}$ are the respective normal vectors of the surface elements $\mathrm{d}A_{\hat{\imath}}$ and $\mathrm{d}A_{\hat{\jmath}}$, which are $r_{\hat{\imath}\hat{\jmath}}$ apart.

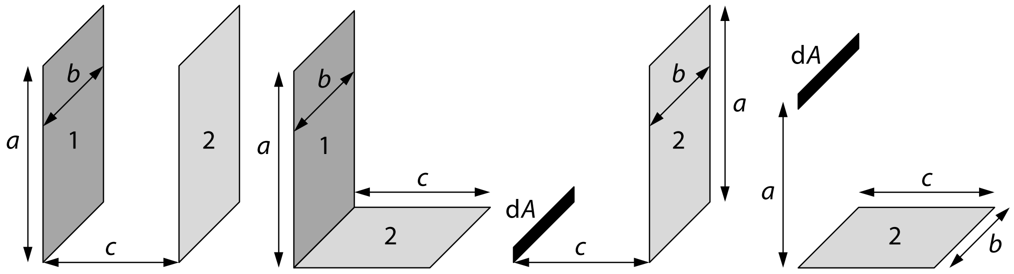

a) Parallel **b)** Perpendicular **c)** Parallel **d)** Perpendicular

Figure B.2. Basic configurations whose analytic expressions of view factors (Sparrow and Cess 1978) are used to derive other view factors

and 0 otherwise. With that, the reciprocity rule is obvious:

$$A_i \Psi_{i\to j} = A_j \Psi_{j\to i}. \tag{B.5}$$

Dividing by A_i yields

$$\tilde{\Psi}_{j\to i} = \Psi_{i\to j} \tag{B.6}$$

and – multiplying with A_i – the reciprocity rule for effective view factors reads

$$A_i \tilde{\Psi}_{j\to i} = A_j \tilde{\Psi}_{i\to j}\,. \tag{B.7}$$

B.2. Derivation of the view factors used in DCEP

Instead of solving (B.4) for every configuration, unknown view factors can be computed from known ones. The view factor for radiation from a surface A_i to A_j with $A_j = A'_j + A''_j$ is given by

$$A_i \Psi_{A_i\to A_j} = A_i \Psi_{A_i\to A'_j} + A_i \Psi_{A_i\to A''_j}\,. \tag{B.8}$$

Furthermore, switching sending and receiving surfaces,

$$A_j \Psi_{A_j\to A_i} = A'_j \Psi_{A'_j\to A_i} + A''_j \Psi_{A''_j\to A_i} . \tag{B.9}$$

However, analytic expressions for basic view factors must be given to start with. Figure B.2 shows the configurations of which the analytic expressions of view factors were provided, which, in turn, are used to calculate view factors of more complex cases. The factor of fig. B.2a is given by

$$\begin{aligned}\Psi^{\mathrm{a})}_{1\to 2} &\equiv \Psi_{\mathrm{prl}}(a,b,c)\\ &= \frac{2}{\pi XY}\Bigg[\frac{1}{2}\ln\left(\frac{(1+X^2)(1+Y^2)}{1+X^2+Y^2}\right) + Y\sqrt{1+X^2}\arctan\left(\frac{Y}{\sqrt{1+X^2}}\right)\\ &\qquad + X\sqrt{1+Y^2}\arctan\left(\frac{X}{\sqrt{1+Y^2}}\right) - Y\arctan Y - X\arctan X\Bigg]\end{aligned} \tag{B.10a}$$

with $X = a/c$ and $Y = b/c$, $c \neq 0$. Since $\lim_{c\to 0} \Psi_{\mathrm{prl}}(a,b,c) = 1$, it is set

$$\Psi_{\mathrm{prl}}(a,b,0) \equiv 1 \tag{B.10b}$$

for $a \neq 0$ and $b \neq 0$. The view factor for two perpendicular rectangles (fig. B.2b) is given by

$$\begin{aligned}\Psi^{\mathrm{b})}_{1\to 2} &\equiv \Psi_{\mathrm{nrm}}(a,b,c)\\ &= \frac{1}{\pi X}\Bigg\{\frac{1}{4}\Bigg[\ln\left(\frac{(1+X^2)(1+Y^2)}{1+Z^2}\right) + X^2\ln\left(\frac{X^2(1+Z^2)}{Z^2(1+X^2)}\right) + Y^2\ln\left(\frac{Y^2(1+Z^2)}{Z^2(1+Y^2)}\right)\Bigg]\\ &\qquad + X\arctan\left(\frac{1}{X}\right) + Y\arctan\left(\frac{1}{Y}\right) - Z\arctan\left(\frac{1}{Z}\right)\Bigg\}\end{aligned} \tag{B.11a}$$

with $X = a/b$, $Y = c/b$, $b \neq 0$, and $Z^2 = X^2 + Y^2$, $Z > 0$. Here, a and c have been exchanged for a more consistent formulation, and Z has been redefined slightly compared to Sparrow and Cess (1978). Since $\lim_{b\to 0} \Psi_{\mathrm{nrm}}(a,b,c) = 0$,

$$\Psi_{\mathrm{nrm}}(a,0,c) \equiv 0 \tag{B.11b}$$

is set for $a \neq 0$ and $c \neq 0$. Given the view factor algebra in (B.8) and (B.9), (B.10) and (B.11) are used to calculate the view factors in appendices B.2.1 and B.2.2.

However, the view factors in appendix B.2.3 needed for including roofs in the radiation exchange cannot be calculated with the above approach. The visibility between the two surfaces in question is partly obstructed, which is not taken into account by the view factors analysed so far. Instead, the view factors for an infinitesimal area to a finite area in figs. B.2c and B.2d are used to numerically integrate the view factor:

$$\Psi_{A_1 \to A_2} = \frac{1}{A_1} \int_{A_1} \Psi_{\mathrm{d}A_1 \to A_2} \, \mathrm{d}A_1 \, . \tag{B.12}$$

This saves one integration in (B.4). In the numerical implementation of this integral, Gauss' formula is employed (Abramowitz and Stegun 1972), with roots of Legendre polynomials acting as the nodes of integration. The view factor in fig. B.2c is given by

$$\begin{aligned} \Psi^{\mathrm{c})}_{\mathrm{d}A \to 2} &\equiv \Psi^{\mathrm{d}}_{\mathrm{prl}}(a, b, c) \\ &= \frac{1}{\pi X} \left[\sqrt{1 + X^2} \arctan\left(\frac{Y}{\sqrt{1 + X^2}} \right) - \arctan Y + \frac{XY}{\sqrt{1 + Y^2}} \arctan\left(\frac{X}{\sqrt{1 + Y^2}} \right) \right] \end{aligned} \tag{B.13a}$$

with $X = b/c$, $Y = a/c$ and $c \neq 0$. For $a, b > 0$, the limit $\lim_{c \to 0} \Psi^{\mathrm{d}}_{\mathrm{prl}}(a, b, c)$ becomes $1/2$, so that

$$\Psi^{\mathrm{d}}_{\mathrm{prl}}(a, b, 0) \equiv \frac{1}{2} \tag{B.13b}$$

is defined. Furthermore, the view factor depicted in fig. B.2d is given by

$$\begin{aligned} \Psi^{\mathrm{d})}_{\mathrm{d}A \to 2} &\equiv \Psi^{\mathrm{d}}_{\mathrm{nrm}}(a, b, c) \\ &= \frac{1}{\pi} \left\{ \arctan\left(\frac{1}{X} \right) + \frac{X}{2} \ln\left[\frac{X^2 (Z^2 + 1)}{(X^2 + 1) Z^2} \right] - \frac{X}{Z} \arctan\left(\frac{1}{Z} \right) \right\} \end{aligned} \tag{B.14}$$

with $X = a/b$, $Y = c/b$, $Z^2 = X^2 + Y^2$, $Z > 0$ and $b \neq 0$. Again, a and c have been exchanged, and Z slightly redefined. With (B.13) and (B.14), the view factors in appendix B.2.3 are calculated. This is only necessary once, thus practically not increasing the total run-time of the model.

In the following, the explicit derivation of view factors used in this work is shown. For that, the respective urban surface configuration is reduced to an equivalent schematic configuration in which only the surface elements are named with numbers from 1 to 8 that are necessary for the derivation. Here, several numbers in an index indicate that several surface elements are taken together, e.g. A_{345} indicates the area of the surface consisting of the elements 3, 4 and 5.

B.2.1. View factors between surfaces inside a single canyon

This subsection outlines the derivation of the view factors in fig. B.3 on the next page used in the single-canyon approach. Martilli et al. (2002) only lists the final expressions of the view factors.

Wall element to ground element

With the nomenclature in fig. B.3a and the decomposition

$$A_{12}\Psi_{12\to3} = A_1\Psi_{1\to3} + A_2\Psi_{2\to3}\,, \tag{B.15}$$

it immediately follows that

$$\Psi_{1\to3} = \frac{1}{A_1}\left(A_{12}\Psi_{12\to3} - A_2\Psi_{2\to3}\right), \tag{B.16}$$

$$\tilde{\Psi}_{1\to3} = \frac{1}{A_3}\left(A_{12}\Psi_{12\to3} - A_2\Psi_{2\to3}\right), \tag{B.17}$$

resulting in the effective view factor for radiation from wall element i to the ground surface G

$$\tilde{\Psi}_{i\to\mathrm{G}} = \frac{1}{W}\left[z_{i+1/2}\Psi_{\mathrm{nrm}}(z_{i+1/2}, D, W) - z_{i-1/2}\Psi_{\mathrm{nrm}}(z_{i-1/2}, D, W)\right] \tag{B.18}$$

and, when applying the reciprocity rule (B.5), in

$$\tilde{\Psi}_{\mathrm{G}\to i} = \frac{1}{\Delta z_i}\left[z_{i+1/2}\Psi_{\mathrm{nrm}}(z_{i+1/2}, D, W) - z_{i-1/2}\Psi_{\mathrm{nrm}}(z_{i-1/2}, D, W)\right]. \tag{B.19}$$

Wall element to wall element

Applying the decomposition rules (B.8) and (B.9) in fig. B.3b yields the view factors

$$A_{123}\Psi_{123\to456} = A_{12}\Psi_{12\to6} + A_{12}\Psi_{12\to45} + A_3\Psi_{3\to45} + A_3\Psi_{3\to6}\,, \tag{B.20}$$

$$A_{12}\Psi_{12\to6} = A_1\Psi_{1\to6} + A_2\Psi_{2\to6}\,, \tag{B.21}$$

$$A_3\Psi_{3\to45} = A_3\Psi_{3\to4} + A_3\Psi_{3\to5}\,, \tag{B.22}$$

$$A_{23}\Psi_{23\to56} = A_2\Psi_{2\to5} + A_2\Psi_{2\to6} + A_3\Psi_{3\to5} + A_3\Psi_{3\to6}\,. \tag{B.23}$$

Furthermore, one gets

$$A_1\Psi_{1\to6} = A_3\Psi_{3\to4} \tag{B.24}$$

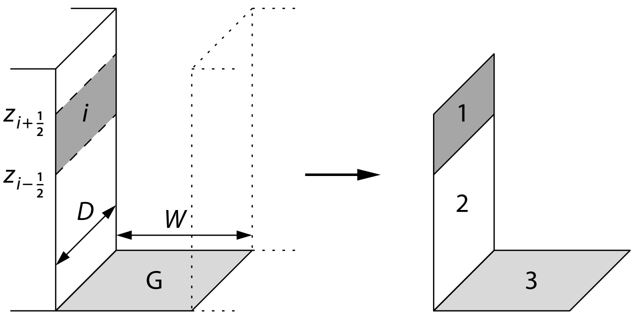

a) Wall element to ground element

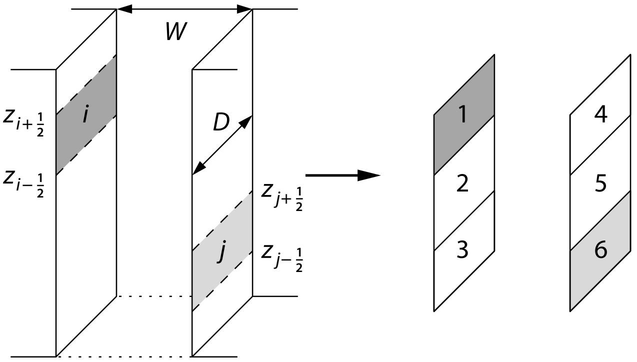

b) Wall element to wall element

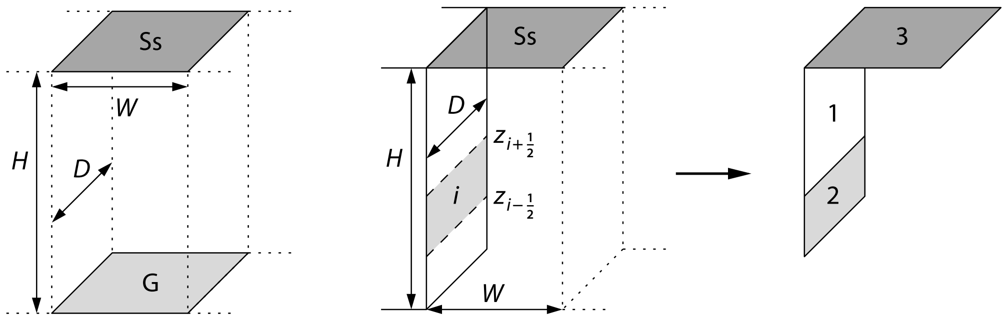

c) Sky element to ground element

d) Sky element to wall element

Figure B.3. Surface configuration entering the single-canyon view factors used in the single-canyon approach by Martilli et al. (2002). For each figure except c), the surfaces shaded in dark and light grey on the left-hand side are assigned to the schematic configuration on the right-hand side, which is used in the derivation of the analytic expression for the view factor. The view factor in c) is already given by the view factor in fig. B.2a.

due to symmetry and the reciprocity rule (B.5). Thus,

$$\Psi_{1\to6} = \frac{1}{2}\frac{1}{A_1}\left(A_{123}\Psi_{123\to456} - A_{12}\Psi_{12\to45} - A_{23}\Psi_{23\to56} + A_2\Psi_{2\to5}\right), \tag{B.25}$$

$$\tilde{\Psi}_{1\to6} = \frac{1}{2}\frac{1}{A_6}\left(A_{123}\Psi_{123\to456} - A_{12}\Psi_{12\to45} - A_{23}\Psi_{23\to56} + A_2\Psi_{2\to5}\right), \tag{B.26}$$

yielding the final expression for the effective view factor for radiation from the wall element i to the wall element j:

$$\begin{aligned}\tilde{\Psi}_{i\to j} = \frac{1}{2}\frac{1}{\Delta z_j}\Big[&|z_{i+1/2} - z_{j-1/2}|\Psi_{\text{prl}}\left(|z_{i+1/2} - z_{j-1/2}|, D, W\right)\\ &-|z_{i+1/2} - z_{j+1/2}|\Psi_{\text{prl}}\left(|z_{i+1/2} - z_{j+1/2}|, D, W\right)\\ &-|z_{i-1/2} - z_{j-1/2}|\Psi_{\text{prl}}\left(|z_{i-1/2} - z_{j-1/2}|, D, W\right)\\ &+|z_{i-1/2} - z_{j+1/2}|\Psi_{\text{prl}}\left(|z_{i-1/2} - z_{j+1/2}|, D, W\right)\Big].\end{aligned} \tag{B.27}$$

Note, that although derived for $i > j$, (B.27) is also valid for $j \geq i$.

Sky element to ground element

The effective view factor for radiation from the single-canyon sky element to the ground element and vice versa (fig. B.3c) is directly given by the factor for two parallel rectangles in (B.10a):

$$\tilde{\Psi}_{\text{Ss}\to\text{G}} = \Psi_{\text{prl}}(W, D, H), \tag{B.28}$$

$$\tilde{\Psi}_{\text{G}\to\text{Ss}} = \Psi_{\text{prl}}(W, D, H). \tag{B.29}$$

Sky element to wall element

With the decomposition in fig. B.3d

$$A_3\Psi_{3\to12} = A_3\Psi_{3\to1} + A_3\Psi_{3\to2}, \tag{B.30}$$

it immediately follows that

$$\Psi_{3\to2} = \Psi_{3\to12} - \Psi_{3\to1}, \tag{B.31}$$

$$\tilde{\Psi}_{3\to2} = \frac{A_3}{A_2}\left(\Psi_{3\to12} - \Psi_{3\to1}\right). \tag{B.32}$$

Thus, the effective view factor for radiation from the single-canyon sky element Ss to the wall element i is

$$\tilde{\Psi}_{\mathrm{Ss}\to i} = \frac{W}{\Delta z_i}\left[\Psi_{\mathrm{nrm}}(W, D, H - z_{i-1/2}) - \Psi_{\mathrm{nrm}}(W, D, H - z_{i+1/2})\right]. \tag{B.33}$$

With the reprocity rule, the view factor for the opposite direction is given by

$$\tilde{\Psi}_{i\to\mathrm{Ss}} = \Psi_{\mathrm{nrm}}(W, D, H - z_{i-1/2}) - \Psi_{\mathrm{nrm}}(W, D, H - z_{i+1/2}). \tag{B.34}$$

B.2.2. View factors including the surface at the far end of the canyon and roofs

In this subsection, expressions for the view factors in fig. B.4 describing the interaction with the canyon end and the roof surfaces are derived. The radiative interaction of the canyon elements with the canyon end is neglected in section 3.1.1 because it is assumed that the canyon length D is much larger than the canyon width W or the maximum canyon height H. The resulting small error is compensated for by introducing the correction factor c in (3.13) and (3.22). Nonetheless, the view factors including the canyon end surface are useful to test the consistency of the implementation of the single-canyon view factors with (B.2) resulting in e.g.

$$\Psi_{i\to\mathrm{G}} + \Psi_{i\to\mathrm{Ss}} + 2\Psi_{i\to\mathrm{E}} + \sum_{j=1}^{n} \Psi_{i\to j} = 1, \quad \forall i, \tag{B.35}$$

$$\Psi_{\mathrm{G}\to\mathrm{Ss}} + 2\Psi_{\mathrm{G}\to\mathrm{E}} + 2\sum_{j=1}^{n} \Psi_{\mathrm{G}\to\mathrm{Ss}} = 1. \tag{B.36}$$

The view factors depicted in figs. B.4c and B.4d are used to model the radiative interaction of roofs with their surroundings in the double-canyon approach.

Wall element to canyon end element

From the decomposition in fig. B.4a,

$$A_{12}\Psi_{12\to 45} = A_1\Psi_{1\to 45} + A_2\Psi_{2\to 45}, \tag{B.37}$$

$$A_1\Psi_{1\to 45} = A_1\Psi_{1\to 4} + A_1\Psi_{1\to 5}, \tag{B.38}$$

$$A_2\Psi_{2\to 45} = A_2\Psi_{2\to 4} + A_2\Psi_{2\to 5} \tag{B.39}$$

and, due to symmetry,

$$A_1\Psi_{1\to 5} = A_2\Psi_{2\to 4}, \tag{B.40}$$

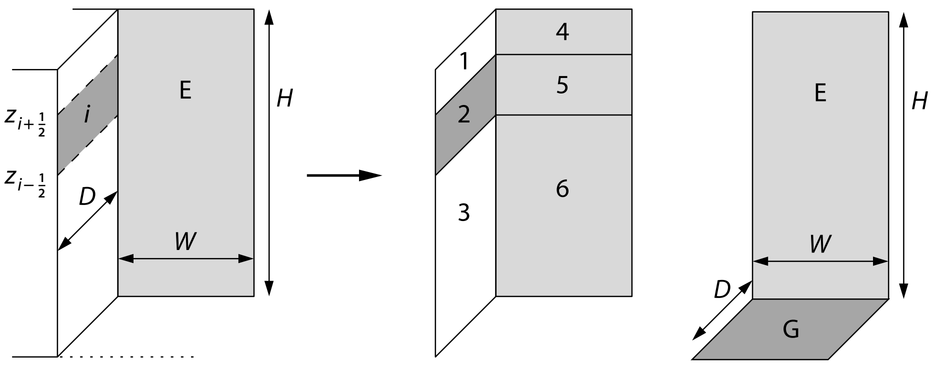

a) Wall element to far end of canyon

b) Ground element to far end of canyon side

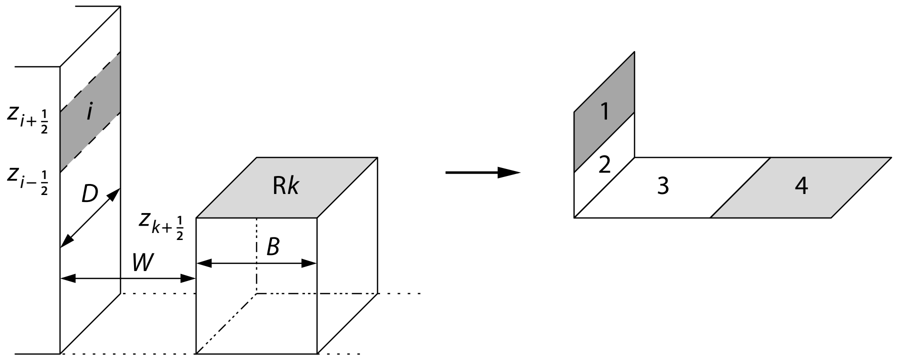

c) Wall element to roof element

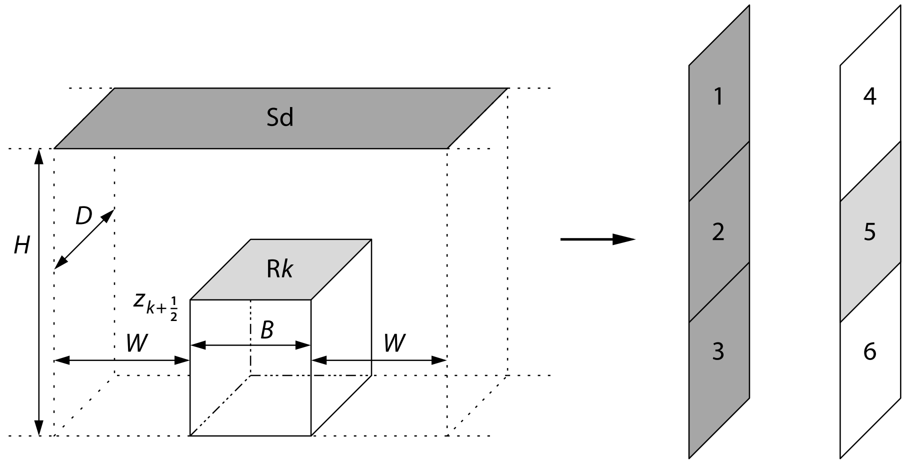

d) Sky element to roof element

Figure B.4. Additional view factors. The view factor configurations depicted in a) and b) can be used to test the consistency of the implementation of single-canyon view factors (cf. (B.35) and (B.36)) but are not used in the final model. The view factors in c) and d) are unique to the double-canyon approach.

it follows

$$A_2 \Psi_{2\to 4} = \frac{1}{2}\left(A_{12} \Psi_{12\to 45} - A_1 \Psi_{1\to 4} - A_2 \Psi_{2\to 5}\right) \tag{B.41}$$

and analogously

$$A_2 \Psi_{2\to 6} = \frac{1}{2}\left(A_{23} \Psi_{23\to 56} - A_3 \Psi_{3\to 6} - A_2 \Psi_{2\to 5}\right) . \tag{B.42}$$

Inserting this into

$$A_2 \Psi_{2\to 456} = A_2 \Psi_{2\to 4} + A_2 \Psi_{2\to 5} + A_2 \Psi_{2\to 6} \tag{B.43}$$

yields

$$\Psi_{2\to 456} = \frac{1}{2}\frac{1}{A_2}\left(A_{12} \Psi_{12\to 45} - A_1 \Psi_{1\to 4} + A_{23} \Psi_{23\to 56} - A_3 \Psi_{3\to 6}\right) , \tag{B.44}$$

$$\tilde{\Psi}_{2\to 456} = \frac{1}{2}\frac{1}{A_{456}}\left(A_{12} \Psi_{12\to 45} - A_1 \Psi_{1\to 4} + A_{23} \Psi_{23\to 56} - A_3 \Psi_{3\to 6}\right) , \tag{B.45}$$

which result in the effective view factors between the ith wall element and the canyon end surface E:

$$\begin{aligned}\tilde{\Psi}_{i\to \mathrm{E}} = \frac{1}{2}\frac{1}{HW}\Big[&(H - z_{i-1/2}) D \Psi_{\mathrm{nrm}}(D, H - z_{i-1/2}, W)\\ &-(H - z_{i+1/2}) D \Psi_{\mathrm{nrm}}(D, H - z_{i+1/2}, W)\\ &+z_{i+1/2} D \Psi_{\mathrm{nrm}}(D, z_{i+1/2}, W)\\ &-z_{i-1/2} D \Psi_{\mathrm{nrm}}(D, z_{i-1/2}, W)\Big]\end{aligned} \tag{B.46}$$

and

$$\begin{aligned}\tilde{\Psi}_{\mathrm{E}\to i} = \frac{1}{2}\frac{1}{\Delta z_i}\Big[&(H - z_{i-1/2}) D \Psi_{\mathrm{nrm}}(D, H - z_{i-1/2}, W)\\ &-(H - z_{i+1/2}) D \Psi_{\mathrm{nrm}}(D, H - z_{i+1/2}, W)\\ &+z_{i+1/2} D \Psi_{\mathrm{nrm}}(D, z_{i+1/2}, W)\\ &-z_{i-1/2} D \Psi_{\mathrm{nrm}}(D, z_{i-1/2}, W)\Big] .\end{aligned} \tag{B.47}$$

Ground element to canyon end

The effective view factor depicted fig. B.4b is simply given by the view factor in fig. B.2b:

$$\tilde{\Psi}_{\mathrm{G}\to\mathrm{E}} = \frac{D}{H}\Psi_{\mathrm{nrm}}(H, W, D) \tag{B.48}$$

and consequently

$$\tilde{\Psi}_{\mathrm{E}\to\mathrm{G}} = \Psi_{\mathrm{nrm}}(H, W, D)\,. \tag{B.49}$$

Wall element to roof element

In fig. B.4c, from the decompositions

$$A_{12}\Psi_{12\to34} = A_{12}\Psi_{12\to3} + A_{12}\Psi_{12\to4}\,, \tag{B.50}$$

$$A_{12}\Psi_{12\to4} = A_1\Psi_{1\to4} + A_2\Psi_{2\to4}\,, \tag{B.51}$$

$$A_2\Psi_{2\to34} = A_2\Psi_{2\to3} + A_2\Psi_{2\to4}\,, \tag{B.52}$$

it follows that

$$\Psi_{1\to4} = \frac{1}{A_1}\left(A_{12}\Psi_{12\to34} - A_{12}\Psi_{12\to3} - A_2\Psi_{2\to34} + A_2\Psi_{2\to3}\right), \tag{B.53}$$

$$\tilde{\Psi}_{1\to4} = \frac{1}{A_4}\left(A_{12}\Psi_{12\to34} - A_{12}\Psi_{12\to3} - A_2\Psi_{2\to34} + A_2\Psi_{2\to3}\right). \tag{B.54}$$

Inserting the model variables from fig. B.4c into (B.54) results in a valid expression only for $i > j$:

$$\begin{aligned}\tilde{\Psi}_{i\to\mathrm{R}k} = \frac{1}{B}\Big[&(z_{k+1/2} - z_{j-1/2})\Psi_{\mathrm{nrm}}(z_{i+1/2} - z_{k-1/2}, D, W + B)\\ &-(z_{k+1/2} - z_{j-1/2})\Psi_{\mathrm{nrm}}(z_{i+1/2} - z_{k-1/2}, D, W)\\ &-(z_{k-1/2} - z_{j-1/2})\Psi_{\mathrm{nrm}}(z_{i-1/2} - z_{k-1/2}, D, W + B)\\ &+(z_{k-1/2} - z_{j-1/2})\Psi_{\mathrm{nrm}}(z_{i-1/2} - z_{k-1/2}, D, W)\Big]\end{aligned} \tag{B.55}$$

The wall element i is not visible from roof level j for $i \le j$, thus

$$\tilde{\Psi}_{i\to\mathrm{R}j} = 0 \quad \text{for} \quad i \le j\,. \tag{B.56}$$

Analogously, for $i > j$,

$$\begin{aligned}\tilde{\Psi}_{\mathrm{R}k\to i} = \frac{1}{\Delta z_i}\Big[&(z_{i+1/2} - z_{k-1/2})\Psi_{\mathrm{nrm}}(z_{i+1/2} - z_{k-1/2}, D, W + B)\\ &-(z_{i+1/2} - z_{k-1/2})\Psi_{\mathrm{nrm}}(z_{i+1/2} - z_{k-1/2}, D, W)\\ &-(z_{i-1/2} - z_{k-1/2})\Psi_{\mathrm{nrm}}(z_{i-1/2} - z_{k-1/2}, D, W + B)\\ &+(z_{i-1/2} - z_{k-1/2})\Psi_{\mathrm{nrm}}(z_{i-1/2} - z_{k-1/2}, D, W)\Big]\end{aligned} \tag{B.57}$$

and

$$\tilde{\Psi}_{\mathrm{R}k\to i} = 0 \quad \text{for} \quad i \le j\,. \tag{B.58}$$

Sky element to roof element

In fig. B.4d, after decomposing and utilizing symmetry,

$$\begin{aligned}A_{123}\Psi_{123\to5} &= A_2\Psi_{2\to5} + A_1\Psi_{1\to5} + A_3\Psi_{3\to5}\\ &= A_2\Psi_{2\to5} + 2A_1\Psi_{1\to5}\,,\end{aligned} \tag{B.59}$$

$$A_{12}\Psi_{12\to45} = A_1\Psi_{1\to45} + A_2\Psi_{2\to45}\,, \tag{B.60}$$

$$A_1\Psi_{1\to45} = A_1\Psi_{1\to4} + A_1\Psi_{1\to5}\,, \tag{B.61}$$

$$A_2\Psi_{2\to45} = A_2\Psi_{2\to5} + A_2\Psi_{2\to4}\,. \tag{B.62}$$

Furthermore, due to reciprocity and symmetry:

$$A_2\Psi_{2\to4} = A_4\Psi_{4\to2} = A_1\Psi_{1\to5}\,. \tag{B.63}$$

Thus,

$$\Psi_{123\to5} = \frac{1}{A_{123}}(A_{12}\Psi_{12\to45} - A_1\Psi_{1\to4})\,, \tag{B.64}$$

$$\tilde{\Psi}_{123\to5} = \frac{1}{A_5}(A_{12}\Psi_{12\to45} - A_1\Psi_{1\to4})\,, \tag{B.65}$$

which results in

$$\tilde{\Psi}_{\mathrm{Sd}\to\mathrm{R}k} = \frac{1}{B}\big[(W + B)\Psi_{\mathrm{prl}}(W + B, D, H - z_{k-1/2}) - W\Psi_{\mathrm{prl}}(W, D, H - z_{k-1/2})\big]\,. \tag{B.66}$$

With (B.10b), the view factor for the highest level n is given by $\tilde{\Psi}_{\mathrm{Sd}\to\mathrm{R}n} = 1$. From reciprocity rule and (B.64) follows

$$\tilde{\Psi}_{\mathrm{R}k\to\mathrm{Sd}} = \frac{1}{B+2W}\left[(W+B)\Psi_{\mathrm{prl}}(W+B, D, H-z_{k-1/2}) - W\Psi_{\mathrm{prl}}(W, D, H-z_{k-1/2})\right]. \tag{B.67}$$

Analogously, $\tilde{\Psi}_{\mathrm{R}n\to\mathrm{Sd}} = B/(B+2W)$.

B.2.3. View factors between the surfaces of two canyons

In order to include roofs in the radiative exchange between urban surfaces, the extension to a double canyon is necessary. The remaining view factors of this extension that were not given in the previous subsections are described here. Since the urban surfaces involved are distributed over two canyons, the sight between the surfaces is partially obstructed by the building in the centre of the configuration and, thus, the view factors are to be integrated numerically as explained in the introduction of this section.

Let A and B be the sending and receiving area, respectively, of every configuration depicted in subfigure a) in figs. B.5 to B.8 on pages 182–185. The respective sending area A of the full configuration shown is split into two parts, A_1 and A_2, yielding the two schematic configurations in fig. b) and c). A_1 is defined such that the view from A_1 to the receiving area B is not obstructed. Thus, the corresponding view factor $\Psi_{A_1\to B}$ is derived analytically analogously to the procedure above (both A_1 and B are shown in fig. b)). From A_2, B is only partially visible depending on the position on A_2. Figure c) shows an infinitesimal area element $\mathrm{d}A$ on A_2 together with the fraction of the receiving area, $\Delta B(\mathrm{d}A)$, that is visible from $\mathrm{d}A$. The corresponding view factor $\Psi_{\mathrm{d}A\to\Delta B(\mathrm{d}A)}$ is derived in the following based on the infinitesimal view factors in (B.13) and (B.14). The view factor for radiation from A_2 to B is then given by the (numerically solved) integral of $\Psi_{\mathrm{d}A\to\Delta B(\mathrm{d}A)}$ (cf. (B.12)). Finally, the total view factor $\Psi_{A\to B}$ is calculated with (B.7) and (B.9).

Ground element to double-canyon sky element

In fig. B.5b, the decompositions

$$A_{12}\Psi_{12\to34} = A_1\Psi_{1\to34} + A_2\Psi_{2\to34}, \tag{B.68}$$

$$A_1\Psi_{1\to34} = A_1\Psi_{1\to3} + A_1\Psi_{1\to4}, \tag{B.69}$$

$$A_2\Psi_{2\to34} = A_2\Psi_{2\to3} + A_2\Psi_{2\to4}, \tag{B.70}$$

and the symmetry of the configuration,

$$A_1 \Psi_{1\to4} = A_2 \Psi_{2\to3} \,, \tag{B.71}$$

yield the following view factors:

$$\Psi_{1\to34} = \frac{1}{2A_1}\left(A_{12}\Psi_{12\to34} + A_1\Psi_{1\to3} - A_2\Psi_{2\to4}\right), \tag{B.72}$$

$$\tilde{\Psi}_{1\to34} = \frac{1}{2A_{34}}\left(A_{12}\Psi_{12\to34} + A_1\Psi_{1\to3} - A_2\Psi_{2\to4}\right). \tag{B.73}$$

The view factor in fig. B.5c is simply given by

$$\Psi_{\mathrm{d}A\to23} = \Psi_{\mathrm{d}A\to2} + \Psi_{\mathrm{d}A\to3} \,. \tag{B.74}$$

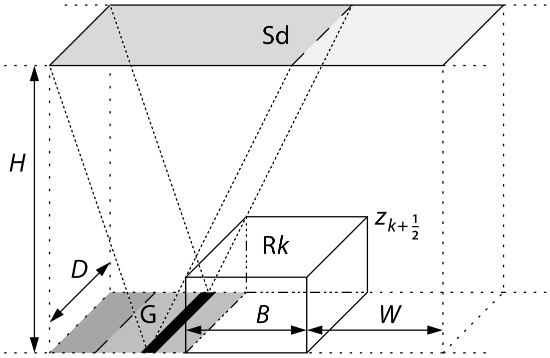

a) Full configuration

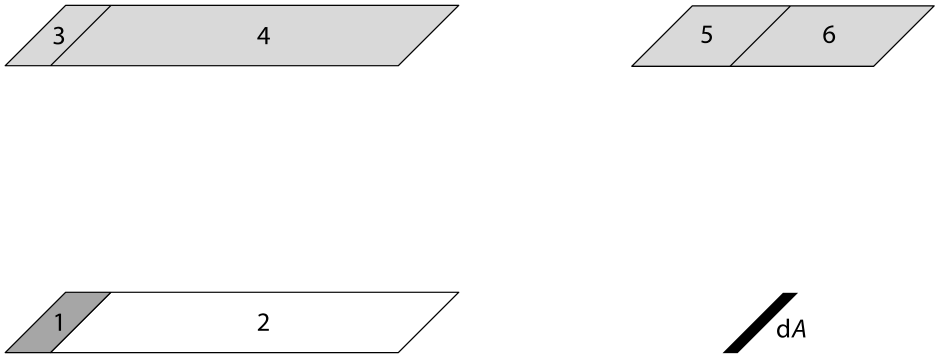

b) The sky element (divided into the elements 3 and 4) is fully visible from element 1

c) Elements 5 and 6 are the from dA visible fraction of the sky element

Figure B.5. Configurations entering the view factor for radiation from a ground element to the sky element of a double canyon. The full configuration in a) is divided into the two parts in b) and c).

Ground element to wall element of a neighbouring canyon

The configuration in fig. B.6b is similar to the simplified configuration of $\tilde{\Psi}_{i\to\mathrm{R}k}$ in fig. B.4c. Therefore, the view factor depicted in fig. B.6b is given by (B.54). The view factor depicted in fig. B.6c is given by

$$\Psi_{\mathrm{d}A\to 6} = \Psi_{\mathrm{d}A\to 56} - \Psi_{\mathrm{d}A\to 5}\,. \tag{B.75}$$

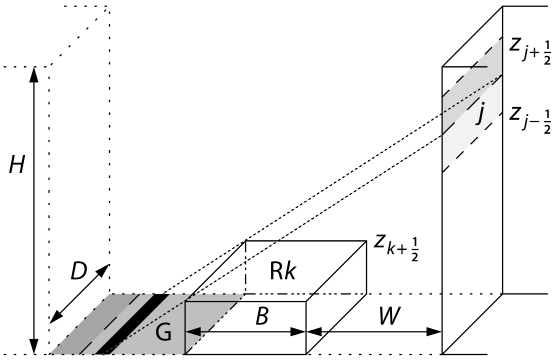

a) Full configuration

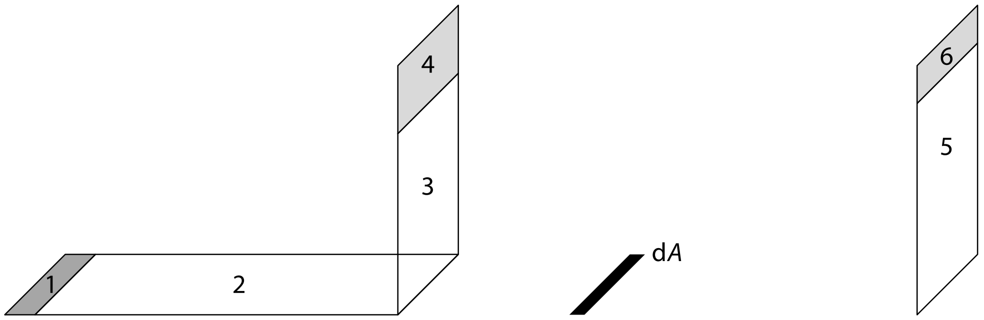

b) The wall element (element 4) is fully visible from surface element 1

c) Surface element 6 is the from dA visible fraction of the wall element

Figure B.6. Configurations entering the view factor for radiation from a ground element to a wall element of a neighbouring canyon. The full configuration in a) is divided into the two parts in b) and c).

Wall element to sky element of a double canyon

The view factor depicted in fig. B.7b is similar to the view factor in fig. B.3d and is given by

$$\tilde{\Psi}_{2\to3} = \Psi_{3\to12} - \Psi_{3\to1}\,. \tag{B.76}$$

The view factor in fig. B.7c is directly given by (B.14).

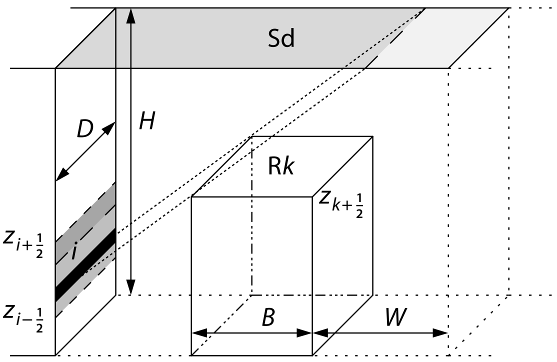

a) Full setup

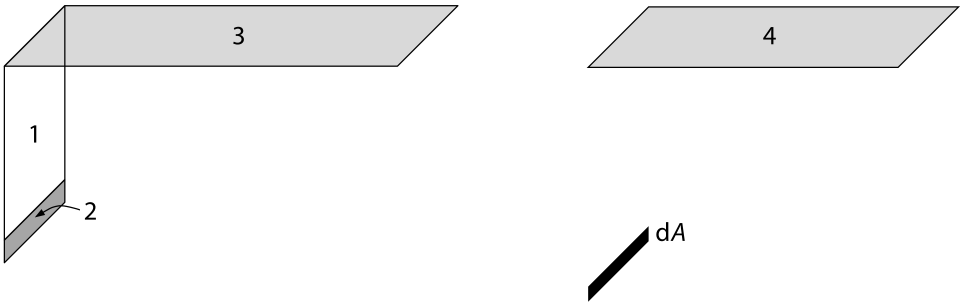

b) The sky element (element 3) is fully visible from surface element 2

c) Surface element 4 is the from dA visible fraction of the sky element

Figure B.7. Configurations entering the view factor for radiation from a wall element to the sky element of a double canyon. The full configuration in a) is divided into the two parts in b) and c).

Wall element to wall element of a neighbouring canyon

The view factor in fig. B.8b is analogue to the view factor in fig. B.3b and is therefore given by (B.26). The view factor in fig. B.8c is similar to (B.75) and, therefore, given by

$$\Psi_{\mathrm{d}A\to 7} = \Psi_{\mathrm{d}A\to 78} - \Psi_{\mathrm{d}A\to 8}\,. \tag{B.77}$$

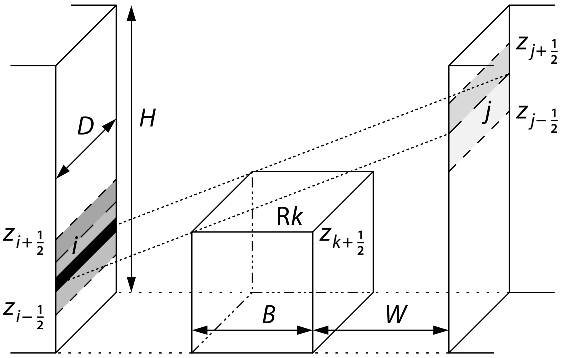

a) Full configuration

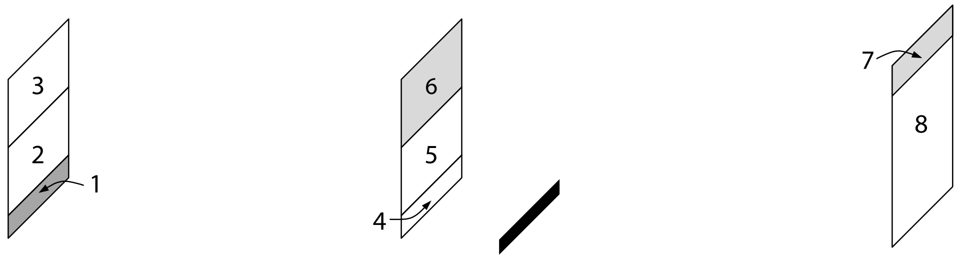

b) The wall element (element 6) is fully visible from surface element 1

c) Surface element 7 is the from dA visible fraction of the wall element

Figure B.8. Configurations entering the view factor for radiation from a wall element to a wall element of a neighbouring canyon. The full configuration in a) is divided into the two parts in b) and c).

Bibliography

The bibliography is divided into two sections: While the first section lists all entries that are connected with the content of this work, the second section includes references to style guides and software employed.

Primary sources

3D-Stadtmodelle Basel-Stadt (2012). Grundbuch- und Vermessungsamt Basel-Stadt. URL: `http://www.gva.bs.ch/produkte_dienstleistungen/3d-stadtmodelle.cfm` (visited on 21/08/2012) (cit. on p. 80).

Abramowitz, M. and I. A. Stegun (1972). *Handbook of mathematical functions with formulas, graphs, and mathematical tables*. Dover publications, p. 1046 (cit. on p. 172).

Adebayo, Y. R. (1987). 'A note on the effect of urbanization on temperature in Ibadan'. In: *Journal of Climatology* 7.2, pp. 185–192 (cit. on p. 142).

Aida, M. (1982). 'Urban albedo as a function of the urban structure – A model experiment'. In: *Boundary-Layer Meteorology* 23.4 (4), pp. 405–413 (cit. on p. 97).

Aida, M. and M. Yaji (1979). 'Observations of atmospheric downward radiation in the Tokyo area'. In: *Boundary-Layer Meteorology* 16.4 (4), pp. 453–465 (cit. on p. 99).

Amt für Statistik Berlin-Brandenburg (2011). *Statistisches Jahrbuch 2011*. Kulturbuch-Verlag, p. 561 (cit. on p. 123).

Arnfield, A. J. (2003). 'Two decades of urban climate research: a review of turbulence, exchanges of energy and water, and the urban heat island'. In: *International Journal of Climatology* 23.1, pp. 1–26 (cit. on pp. 17, 54, 108).

Best, M. J. (2005). 'Representing urban areas within operational numerical weather prediction models'. In: *Boundary-Layer Meteorology* 114.1, pp. 91–109 (cit. on pp. 18, 19).

Best, M. J., C. S. B. Grimmond and M. Villani (2006). 'Evaluation of the Urban Tile in MOSES using Surface Energy Balance Observations'. In: *Boundary-Layer Meteorology* 118.3 (3), pp. 503–525 (cit. on pp. 19, 21, 36).

Blackadar, A. K. (1962). 'The vertical distribution of wind and turbulent exchange in a neutral atmosphere'. In: *Journal of Geophysical Research* 67.8, pp. 3095–3102 (cit. on p. 31).

Bochow, M., H. Taubenböck, K. Segl and H. Kaufmann (2010). 'An automated and adaptable approach for characterizing and partitioning cities into urban structure types'. In: *2010 IEEE International Geoscience and Remote Sensing Symposium (IGARSS)*. (Honolulu, Hawaii, USA, 25th–30th July 2010). IEEE, pp. 1796–1799 (cit. on p. 158).

Böhm, U., M. Kücken, W. Ahrens, A. Block, D. Hauffe, K. Keuler, B. Rockel and A. Will (2006). 'CLM – The Climate Version of LM: Brief Description and Long-Term Applications'. In: *COSMO Newsletter*. Ed. by U. Schättler, A. Montani and M. Milelli. 6. Deutscher Wetterdienst, pp. 225–235 (cit. on p. 25).

Bornstein, R. D. and D. S. Johnson (1977). 'Urban-rural wind velocity differences'. In: *Atmospheric Environment* 11.7, pp. 597–604 (cit. on p. 114).

Boussinesq, J. (1897). *Théorie de l'écoulmnent tourbillonnant et tumultuex des liquides dans les lits rectilignes à grande section*. Gauthier-Villars et fils (cit. on p. 31).

Bretz, S. E. and H. Akbari (1997). 'Long-term performance of high-albedo roof coatings'. In: *Energy and Buildings* 25.2, pp. 159–167 (cit. on pp. 22, 123, 135).

Brown, M. (2000). 'Urban parameterizations for mesoscale meteorological models'. In: *Mesoscale Atmospheric dispersion*. Ed. by Z. Boybeyi. WIT Press London, pp. 193–255 (cit. on p. 19).

Bruse, M. and H. Fleer (1998). 'Simulating surface–plant–air interactions inside urban environments with a three dimensional numerical model'. In: *Environmental Modelling & Software* 13.3–4, pp. 373–384 (cit. on p. 17).

BUBBLE (2004). *Basel Urban Boundary Layer Experiment*. University of Basel. URL: `http://pages.unibas.ch/geo/mcr/Projects/BUBBLE/` (visited on 19/08/2012) (cit. on pp. 85–87).

Bueno, B., L. Norford, G. Pigeon and R. Britter (2011). 'Combining a Detailed Building Energy Model with a Physically-Based Urban Canopy Model'. In: *Boundary-Layer Meteorology* 140.3 (3), pp. 471–489 (cit. on p. 21).

Burian, S., N. Augustus, I. Jeyachandran and M. Brown (2008). *National Building Statistics Database: Version 2*. Tech. rep. University of Utah, Department of Civil, Environmental Engineering and Los Alamos National Laboratory, p. 78 (cit. on pp. 23, 67).

Burian, S. and C. Jason (2009). *Development of Gridded Fields of Urban Canopy Parameters for Advanced Urban Meteorological and Air Quality Models*. Report. Environmental Protection Agency, USA, p. 73 (cit. on p. 23).

Büttner, G., K. B., G. Maucha and R. Pataki (2012). *Implementation and achievements of CLC2006*. Tech. rep. European Environment Agency, p. 65 (cit. on pp. 23, 80).

Chandler, T. J. (1965). *The Climate of London*. Hutchinson, p. 292 (cit. on p. 114).

Chen, F., H. Kusaka, R. Bornstein, J. Ching, C. S. B. Grimmond, S. Grossman-Clarke, T. Loridan, K. W. Manning, A. Martilli, S. Miao, D. Sailor, F. P. Salamanca, H. Taha, M. Tewari, X. Wang, A. A. Wyszogrodzki and C. Zhang (2011). 'The integrated WRF/urban modelling system: development, evaluation, and applications to urban environmental problems'. In: *International Journal of Climatology* 31.2, pp. 273–288 (cit. on p. 23).

Chin, H.-N. S., M. J. Leach, G. A. Sugiyama, J. M. Leone, H. Walker, J. S. Nasstrom and M. J. Brown (2005). 'Evaluation of an Urban Canopy Parameterization in a Mesoscale Model Using VTMX and URBAN 2000 Data'. In: *Monthly Weather Review* 133.7, pp. 2043–2068 (cit. on p. 22).

Ching, J., M. Brown, T. McPherson, S. Burian, F. Chen, R. Cionco, A. Hanna, T. Hultgren, D. Sailor, H. Taha and D. Williams (2009). 'National Urban Database and Access Portal Tool'. In: *Bulletin of the American Meteorological Society* 90.8, pp. 1157–1168 (cit. on p. 23).

Christen, A. and R. Vogt (2004). 'Energy and radiation balance of a central European city'. In: *International Journal of Climatology* 24.11, pp. 1395–1421 (cit. on pp. 21, 79, 85, 88, 89, 92, 95, 97, 99, 104, 108, 121).

Clarke, J. A. (1985). *Energy Simulation in Building Design*. Adam Hilger, p. 388 (cit. on p. 52).

Cotton, W. R. and R. A. Pielke Sr (2007). *Human impacts on weather and climate*. 2nd ed. Cambridge University Press, p. 304 (cit. on p. 17).

Crank, J. and P. Nicolson (1947). 'A practical method for numerical evaluation of solutions of partial differential equations of the heat-conduction type'. In: *Mathematical Proceedings of the Cambridge Philosophical Society* 43.01, pp. 50–67 (cit. on p. 52).

Crawley, D. B., L. K. Lawrie, F. C. Winkelmann, W. Buhl, Y. J. Huang, C. O. Pedersen, R. K. Strand, R. J. Liesen, D. E. Fisher, M. J. Witte and J. Glazer (2001). 'EnergyPlus: creating a new-generation building energy simulation program'. In: *Energy and Buildings* 33.4, pp. 319–331 (cit. on p. 157).

Deardorff, J. W. and G. Sommeria (1977). 'Subgrid-Scale Condensation in Models of Nonprecipitating Clouds'. In: *Journal of the Atmospheric Sciences* 34.2, pp. 344–355 (cit. on p. 31).

Dee, D. P., S. M. Uppala, A. J. Simmons, P. Berrisford, P. Poli, S. Kobayashi, U. Andrae, M. A. Balmaseda, G. Balsamo, P. Bauer, P. Bechtold, A. C. M. Beljaars, L. van de Berg, J. Bidlot, N. Bormann, C. Delsol, R. Dragani, M. Fuentes, A. J. Geer, L. Haimberger, S. B. Healy, H. Hersbach, E. V. Hólm, L. Isaksen, P. Kållberg, M. Köhler, M. Matricardi, A. P. McNally, B. M. Monge-Sanz, J.-J. Morcrette, B.-K. Park, C. Peubey, P. de Rosnay, C. Tavolato, J.-N. Thépaut and F. Vitart (2011). 'The ERA-

Interim reanalysis: configuration and performance of the data assimilation system'. In: *Quarterly Journal of the Royal Meteorological Society* 137.656, pp. 553–597 (cit. on pp. 90, 134).

Doll, D., J. K. S. Ching and J. Kaneshiro (1985). 'Parameterization of subsurface heating for soil and concrete using net radiation data'. In: *Boundary-Layer Meteorology* 32.4 (4), pp. 351–372 (cit. on p. 54).

Doms, G., J. Förstner, E. Heise, H.-J. Herzog, D. Mironov, M. Raschendorfer, T. Reinhardt, B. Ritter, R. Schrodin, J.-P. Schulz and G. Vogel (2011). *A Description of the Nonhydrostatic Regional COSMO Model. Physical Parameterization*. Deutscher Wetterdienst, p. 154 (cit. on pp. 29, 32, 158).

Doms, G., U. Schättler and M. Baldauf (2011). *A Description of the Nonhydrostatic Regional COSMO Model. Dynamics and Numerics*. Deutscher Wetterdienst, p. 147 (cit. on pp. 25, 28, 29).

Draxler, R. R. (1986). 'Simulated and Observed Influence of the Nocturnal Urban Heat Island on the Local Wind Field'. In: *Journal of Climate and Applied Meteorology* 25.8, pp. 1125–1133 (cit. on p. 114).

Dupont, S., T. L. Otte and J. K. S. Ching (2004). 'Simulation of Meteorological Fields Within and Above Urban and Rural Canopies with a Mesoscale Model'. In: *Boundary-Layer Meteorology* 113.1 (1), pp. 111–158 (cit. on pp. 19, 22, 23).

Eliasson, I. (1996). 'Intra-urban nocturnal temperature differences: a multivariate approach'. In: *Climate Research* 7, pp. 21–30 (cit. on pp. 137, 160).

Estournel, C., R. Vehil, D. Guedalia, J. Fontan and A. Druilhet (1983). 'Observations and Modeling of Downward Radiative Fluxes (Solar and Infrared) in Urban/Rural Areas'. In: *Journal of Applied Meteorology* 22.1, pp. 134–142 (cit. on p. 99).

Fan, H., L. Meng and M. Jahnke (2009). 'Generalization of 3D Buildings Modelled by CityGML'. In: *Advances in GIScience*. Ed. by M. Sester, L. Bernard, V. Paelke, W. Cartwright, G. Gartner, L. Meng and M. P. Peterson. Lecture Notes in Geoinformation and Cartography. Springer, pp. 387–405 (cit. on p. 23).

Favre, A. (1965). 'Équations des gaz turbulents compressibles'. In: *Journal de Mécanique* 4, pp. 361–421 (cit. on p. 26).

Fisher, B., J. Kukkonen and M. Schatzmann (2001). 'Meteorology applied to urban air pollution problems: COST 715'. In: *International Journal of Environment and Pollution* 16.1, pp. 560–570 (cit. on p. 79).

Foken, T. (2008). 'The energy balance closure problem: an overview'. In: *Ecological Applications* 18.6, pp. 1351–1367 (cit. on p. 104).

Fortuniak, K., K. Kłysik and J. Wibig (2006). 'Urban–rural contrasts of meteorological parameters in Łódź'. In: *Theoretical and Applied Climatology* 84.1–3 (1), pp. 91–101 (cit. on pp. 114, 142).

Frank, W. M. (1983). 'The Cumulus Parameterization Problem'. In: *Monthly Weather Review* 111.9, pp. 1859–1871 (cit. on p. 27).

Frey, C. M., E. Parlow, R. Vogt, M. Harhash and M. M. Abdel Wahab (2011). 'Flux measurements in Cairo. Part 1: in situ measurements and their applicability for comparison with satellite data'. In: *International Journal of Climatology* 31.2, pp. 218–231 (cit. on pp. 99, 104, 108).

Friedrich, M., A. Grätz and G. Jendritzky (2001). 'Further development of the urban bioclimate model UBIKLIM, taking local wind systems into account'. In: *Meteorologische Zeitschrift* 10.4, pp. 267–272 (cit. on p. 17).

Fuhrer, O. (22nd June 2012). *[CLM_CRCS] Only missing values in 0.009° CCLM output after 1st hour*. Message on the COSMO-CLM CRCS mailing list (cit. on p. 90).

Galmarini, S., F. Michelutti and P. Thunis (2000). 'Estimating the Contribution of Leonard and Cross Terms to the Subfilter Scale from Atmospheric Measurements'. In: *Journal of the Atmospheric Sciences* 57.17, pp. 2968–2976 (cit. on p. 26).

Galmarini, S. and P. Thunis (1999). 'On the Validity of Reynolds Assumptions for Running-Mean Filters in the Absence of a Spectral Gap'. In: *Journal of the Atmospheric Sciences* 56.12, pp. 1785–1796 (cit. on p. 26).

Garratt, J. R. (1992). *The atmospheric boundary layer*. Cambridge University Press, p. 316 (cit. on p. 27).

geo.bl (2012). GIS-Fachstelle Kanton Basel-Landschaft. URL: `http://www.geo.bl.ch/` (visited on 21/08/2012) (cit. on p. 80).

Georgescu, M., M. Moustaoui, A. Mahalov and J. Dudhia (2013). 'Summer-time climate impacts of projected megapolitan expansion in Arizona'. In: *Nature Climate Change* 3.1, pp. 37–41 (cit. on p. 162).

Grimmond, C. S. B., M. Blackett, M. J. Best, J.-J. Baik, S. E. Belcher, J. Beringer, S. I. Bohnenstengel, I. Calmet, F. Chen, A. Coutts, A. Dandou, K. Fortuniak, M. L. Gouvea, R. Hamdi, M. Hendry, M. Kanda, T. Kawai, Y. Kawamoto, H. Kondo, E. S. Krayenhoff, S.-H. Lee, T. Loridan, A. Martilli, V. Masson, S. Miao, K. Oleson, R. Ooka, G. Pigeon, A. Porson, Y.-H. Ryu, F. Salamanca, G. Steeneveld, M. Tombrou, J. A. Voogt, D. T. Young and N. Zhang (2011). 'Initial results from Phase 2 of the international urban energy balance model comparison'. In: *International Journal of Climatology* 31.2, pp. 244–272 (cit. on pp. 19–21, 92, 122).

Grimmond, C. S. B., M. Blackett, M. J. Best, J. Barlow, J.-J. Baik, S. E. Belcher, S. I. Bohnenstengel, I. Calmet, F. Chen, A. Dandou, K. Fortuniak, M. L. Gouvea, R.

Hamdi, M. Hendry, T. Kawai, Y. Kawamoto, H. Kondo, E. S. Krayenhoff, S.-H. Lee, T. Loridan, A. Martilli, V. Masson, S. Miao, K. Oleson, G. Pigeon, A. Porson, Y.-H. Ryu, F. Salamanca, L. Shashua-Bar, G.-J. Steeneveld, M. Tombrou, J. A. Voogt, D. Young and N. Zhang (2010). 'The International Urban Energy Balance Models Comparison Project: First results from Phase 1'. In: *Journal of Applied Meteorology and Climatology* 49.6, pp. 1268–1292 (cit. on pp. 17, 19–21, 73, 92, 122).

Grimmond, C. S. B., H. A. Cleugh and T. R. Oke (1991). 'An objective urban heat storage model and its comparison with other schemes'. In: *Atmospheric Environment. Part B. Urban Atmosphere* 25.3, pp. 311–326 (cit. on p. 19).

Grimmond, C. S. B. and T. R. Oke (1991). 'An Evapotranspiration-Interception Model for Urban Areas'. In: *Water Resources Research* 27.7, pp. 1739–1755 (cit. on p. 157).

– (1999a). 'Aerodynamic Properties of Urban Areas Derived from Analysis of Surface Form'. In: *Journal of Applied Meteorology* 38.9, pp. 1262–1292 (cit. on p. 89).

– (1999b). 'Heat Storage in Urban Areas: Local-Scale Observations and Evaluation of a Simple Model'. In: *Journal of Applied Meteorology* 38.7, pp. 922–940 (cit. on pp. 108, 110).

– (2002). 'Turbulent Heat Fluxes in Urban Areas: Observations and a Local-Scale Urban Meteorological Parameterization Scheme (LUMPS)'. In: *Journal of Applied Meteorology* 41.7, pp. 792–810 (cit. on pp. 19, 108).

Grossman-Clarke, S., J. A. Zehnder, T. Loridan and C. S. B. Grimmond (2010). 'Contribution of Land Use Changes to Near-Surface Air Temperatures during Recent Summer Extreme Heat Events in the Phoenix Metropolitan Area'. In: *Journal of Applied Meteorology and Climatology* 49.8, pp. 1649–1664 (cit. on pp. 22, 23).

gva.bs (2012). Grundbuch- und Vermessungsamt Basel-Stadt. URL: `http://www.gva.bs.ch/` (visited on 21/08/2012) (cit. on p. 80).

Hamdi, R. and V. Masson (2008). 'Inclusion of a Drag Approach in the Town Energy Balance (TEB) Scheme: Offline 1D Evaluation in a Street Canyon'. In: *Journal of Applied Meteorology and Climatology* 47.10, pp. 2627–2644 (cit. on p. 21).

Hamdi, R. and G. Schayes (2007). 'Validation of Martilli's urban boundary layer scheme with measurements from two mid-latitude European cities'. In: *Atmospheric Chemistry and Physics* 7.17, pp. 4513–4526 (cit. on pp. 20–22, 36, 73, 77, 92, 158, 162).

– (2008). 'Sensitivity study of the urban heat island intensity to urban characteristics'. In: *International Journal of Climatology* 28.7, pp. 973–982 (cit. on p. 142).

Hamilton, D. C. and W. R. Morgan (1952). 'Radiant-interchange configuration factors'. In: *National Advisory Committee For Aeronautics* 2836, p. 110 (cit. on p. 169).

Hamilton, I. G., M. Davies, P. Steadman, A. Stone, I. Ridley and S. Evans (2009). 'The significance of the anthropogenic heat emissions of London's buildings: A comparison against captured shortwave solar radiation'. In: *Building and Environment* 44.4, pp. 807–817 (cit. on p. 92).

Harman, I. N. and S. E. Belcher (2006). 'The surface energy balance and boundary layer over urban street canyons'. In: *Quarterly Journal of the Royal Meteorological Society* 132.621, pp. 2749–2768 (cit. on p. 108).

Heusinkveld, B. G., A. F. G. Jacobs, A. A. M. Holtslag and S. M. Berkowicz (2004). 'Surface energy balance closure in an arid region: role of soil heat flux'. In: *Agricultural and Forest Meteorology* 122.1–2, pp. 21–37 (cit. on p. 104).

Högström, U. (1996). 'Review of some basic characteristics of the atmospheric surface layer'. In: *Boundary-Layer Meteorology* 78.3–4 (3), pp. 215–246 (cit. on p. 32).

Holman, J. P. (1986). *Heat Transfer*. Ed. by A. Murphy, M. Eichberg and S. Tenney. 6th ed. McGraw-Hill Book Company, p. 676 (cit. on p. 53).

Huth, R., J. Kyselý and L. Pokorná (2000). 'A GCM Simulation of Heat Waves, Dry Spells, and Their Relationships to Circulation'. In: *Climatic Change* 46.1-2 (1), pp. 29–60 (cit. on p. 133).

Iqbal, M. (1983). *An Introduction to Solar Radiation*. Academic Press, p. 390 (cit. on p. 45).

Jung, I. (2009). *Building Reconstruction Berlin*. Reference report. virtualcitySYSTEMS, p. 2 (cit. on p. 124).

Kabat, P., M. Claussen, P. A. Dirmeyer, J. H. C. Gash, L. Bravo de Guenni, M. Meybeck, R. A. Pielke Sr, C. J. Vörösmarty, R. W. A. Hutjes and S. Lütkemeier, eds. (2004). *Vegetation, water, humans and the climate: A new perspective on an interactive system*. Springer, p. 566 (cit. on p. 17).

Kato, T. (1997). 'Hydrostatic and non-hydrostatic simulations of moist convection: Review and further study'. English. In: *Meteorology and Atmospheric Physics* 63.1–2 (1-2), pp. 39–51 (cit. on p. 17).

Keller, L. and A. Friedmann (1924). 'Differentialgleichungen für die turbulente Bewegung einer kompressiblen Flüssigkeit'. In: *Proceedings of the First International Congress on Applied Mechanics, Delft*, pp. 395–405 (cit. on p. 30).

Kessler, E. (1969). *On the Distribution and Continuity of Water Substance in Atmospheric Circulations*. Vol. 10. Meteorological monographs 32. American Meteorological Society, p. 84 (cit. on p. 29).

Kikegawa, Y., Y. Genchi, H. Yoshikado and H. Kondo (2003). 'Development of a numerical simulation system toward comprehensive assessments of urban warming countermeasures including their impacts upon the urban buildings' energy-demands'. In: *Applied Energy* 76.4, pp. 449–466 (cit. on p. 22).

Kłysik, K. (1996). 'Spatial and seasonal distribution of anthropogenic heat emissions in Łódź, Poland'. In: *Atmospheric Environment* 30.20, pp. 3397–3404 (cit. on p. 92).

Kondo, H., Y. Genchi, Y. Kikegawa, Y. Ohashi, H. Yoshikado and H. Komiyama (2005). 'Development of a Multi-Layer Urban Canopy Model for the Analysis of Energy Consumption in a Big City: Structure of the Urban Canopy Model and its Basic Performance'. In: *Boundary-Layer Meteorology* 116.3 (3), pp. 395–421 (cit. on pp. 19, 22).

Koppe, C., S. Kovats, G. Jendritzky, B. Menne, J. Baumüller, A. Bitan, J. Díaz Jiménez, K. L. Ebi, G. Havenith, C. López Santiago, P. Michelozzi, F. Nicol, A. Matzarakis, G. McGregor, P. Jorge Nogueira, S. Sheridan and T. Wolf (2004). *Heat waves: risks and responses*. Tech. rep. World Health Organization, p. 123 (cit. on p. 17).

Krayenhoff, E. S. and J. A. Voogt (2010). 'Impacts of Urban Albedo Increase on Local Air Temperature at Daily-Annual Time Scales: Model Results and Synthesis of Previous Work'. In: *Journal of Applied Meteorology and Climatology* 49.8, pp. 1634–1648 (cit. on pp. 22, 155, 162).

Kusaka, H., H. Kondo, Y. Kikegawa and F. Kimura (2001). 'A Simple Single-Layer Urban Canopy Model For Atmospheric Models: Comparison With Multi-Layer And Slab Models'. In: *Boundary-Layer Meteorology* 101.3 (3), pp. 329–358 (cit. on pp. 19, 36, 158).

Kuttler, W. (2004). 'Stadtklima. Teil 1: Grundzüge und Ursachen'. In: *Umweltwissenschaften und Schadstoff-Forschung* 16.3 (3), pp. 187–199 (cit. on pp. 17, 53, 95).

Lee, D. O. (1979). 'The influence of atmospheric stability and the urban heat island on urban-rural wind speed differences'. In: *Atmospheric Environment* 13.8, pp. 1175–1180 (cit. on p. 114).

Lee, S.-H. and S.-U. Park (2008). 'A Vegetated Urban Canopy Model for Meteorological and Environmental Modelling'. In: *Boundary-Layer Meteorology* 126.1 (1), pp. 73–102 (cit. on pp. 20, 21, 159).

Lemonsu, A., S. Bélair, J. Mailhot, M. Benjamin, G. Morneau, B. Harvey, F. Chagnon, M. Jean and J. Voogt (2008). 'Overview and First Results of the Montreal Urban Snow Experiment 2005'. In: *Journal of Applied Meteorology and Climatology* 47.1, pp. 59–75 (cit. on pp. 108, 157).

Lemonsu, A., S. Bélair, J. Mailhot and S. Leroyer (2010). 'Evaluation of the Town Energy Balance Model in Cold and Snowy Conditions during the Montreal Urban Snow Experiment 2005'. In: *Journal of Applied Meteorology and Climatology* 49.3, pp. 346–362 (cit. on pp. 21, 158).

Lemonsu, A., C. S. B. Grimmond and V. Masson (2004). 'Modeling the Surface Energy Balance of the Core of an Old Mediterreanean City: Marseille'. In: *Journal of Applied Meteorology* 43.2, pp. 312–327 (cit. on pp. 21, 158).

Lemonsu, A., V. Masson, L. Shashua-Bar, E. Erell and D. Pearlmutter (2012). 'Inclusion of vegetation in the Town Energy Balance model for modelling urban green areas'. In: *Geoscientific Model Development* 5.6, pp. 1377–1393 (cit. on pp. 20, 159).

Liu, Y., F. Chen, T. Warner and J. Basara (2006). 'Verification of a mesoscale data-assimilation and forecasting system for the Oklahoma City area during the Joint Urban 2003 field project'. In: *Journal of Applied Meteorology* 45.7, pp. 912–929 (cit. on p. 19).

Loridan, T., C. S. B. Grimmond, S. Grossman-Clarke, F. Chen, M. Tewari, K. Manning, A. Martilli, H. Kusaka and M. Best (2010). 'Trade-offs and responsiveness of the single-layer urban canopy parametrization in WRF: An offline evaluation using the MOSCEM optimization algorithm and field observations'. In: *Quarterly Journal of the Royal Meteorological Society* 136.649, pp. 997–1019 (cit. on p. 158).

Loridan, T. and C. S. B. Grimmond (2012). 'Multi-site evaluation of an urban land-surface model: intra-urban heterogeneity, seasonality and parameter complexity requirements'. In: *Quarterly Journal of the Royal Meteorological Society* 138.665, pp. 1094–1113 (cit. on pp. 21, 91, 93, 122).

Louis, J. F. (1979). 'A parametric model of vertical eddy fluxes in the atmosphere'. In: *Boundary-Layer Meteorology* 17.2, pp. 187–202 (cit. on pp. 49–51).

Magee, N., J. Curtis and G. Wendler (1999). 'The Urban Heat Island Effect at Fairbanks, Alaska'. In: *Theoretical and Applied Climatology* 64 (1), pp. 39–47 (cit. on p. 142).

Mahmood, R., R. A. Pielke Sr, K. G. Hubbard, D. Niyogi, G. Bonan, P. Lawrence, B. Baker, R. McNider, C. McAlpine, A. Etter et al. (2010). 'Impacts of land use land cover change on climate and future research priorities'. In: *Bulletin of the American Meteorological Society* 91.1, pp. 37–46 (cit. on p. 17).

Marciotto, E. R., A. P. Oliveira and S. R. Hanna (2010). 'Modeling study of the aspect ratio influence on urban canopy energy fluxes with a modified wall-canyon energy budget scheme'. In: *Building and Environment* 45.11, pp. 2497–2505 (cit. on pp. 142, 144).

Markowski, P. and Y. Richardson (2010). *Mesoscale Meteorology in Midlatitudes*. Wiley-Blackwell, p. 407 (cit. on p. 31).

Martilli, A. (2007). 'Current research and future challenges in urban mesoscale modelling'. In: *International Journal of Climatology* 27.14, pp. 1909–1918 (cit. on p. 19).

Martilli, A. (2009). 'On the Derivation of Input Parameters for Urban Canopy Models from Urban Morphological Datasets'. In: *Boundary-Layer Meteorology* 130.2, pp. 301–306 (cit. on pp. 56, 82, 89, 128).

Martilli, A., A. Clappier and M. W. Rotach (2002). 'An urban surface exchange parameterisation for mesoscale models'. In: *Boundary-Layer Meteorology* 104.2, pp. 261–304 (cit. on pp. 19, 20, 33–36, 39, 45, 47, 49, 53, 55, 69, 75, 91, 134, 161, 165, 169, 173, 174).

Martilli, A., Y.-A. Roulet, M. Junier, F. Kirchner, M. W. Rotach and A. Clappier (2003). 'On the impact of urban surface exchange parameterisations on air quality simulations: the Athens case'. In: *Atmospheric Environment* 37.30, pp. 4217–4231 (cit. on pp. 22, 73, 77).

Martine, G., D. Deligiorgis, C. Fuersich, L. Leon and A. Odelius (2007). *State of the World Population 2007: Unleashing the Potential of Urban Growth*. Report. United Nations Population Fund (UNFPA), p. 99 (cit. on p. 17).

Masson, V. (2006). 'Urban surface modeling and the meso-scale impact of cities'. In: *Theoretical and Applied Climatology* 84.1, pp. 35–45 (cit. on pp. 18, 19, 21).

Masson, V., C. S. B. Grimmond and T. R. Oke (2002). 'Evaluation of the Town Energy Balance (TEB) Scheme with Direct Measurements from Dry Districts in Two Cities'. In: *Journal of Applied Meteorology* 41.10, pp. 1011–1026 (cit. on pp. 21, 92).

Masson, V., Y. Lion, A. Peter, G. Pigeon, J. Buyck and E. Brun (2012). '"Grand Paris": regional landscape change to adapt city to climate warming'. In: *Climatic Change* (cit. on p. 22).

Masson, V. (2000). 'A Physically-Based Scheme For The Urban Energy Budget In Atmospheric Models'. In: *Boundary-Layer Meteorology* 94.3 (3), pp. 357–397 (cit. on pp. 19, 21, 36, 144, 157, 158).

Meehl, G. A. and C. Tebaldi (2004). 'More Intense, More Frequent, and Longer Lasting Heat Waves in the 21st Century'. In: *Science* 305.5686, pp. 994–997 (cit. on p. 133).

Mellor, G. L. and T. Yamada (1982). 'Development of a turbulence closure model for geophysical fluid problems'. In: *Reviews of Geophysics and Space Physics* 20.4, pp. 851–875 (cit. on p. 30).

Meyers, T. P. and S. E. Hollinger (2004). 'An assessment of storage terms in the surface energy balance of maize and soybean'. In: *Agricultural and Forest Meteorology* 125.1–2, pp. 105–115 (cit. on p. 104).

Michelozzi, P., G. Accetta, M. De Sario, D. D'Ippoliti, C. Marino, M. Baccini, A. Biggeri, H. R. Anderson, K. Katsouyanni, F. Ballester, L. Bisanti, E. Cadum, B. Forsberg, F. Forastiere, P. G. Goodman, A. Hojs, U. Kirchmayer, S. Medina, A. Paldy,

C. Schindler, J. Sunyer and C. A. Perucci (2009). 'High Temperature and Hospitalizations for Cardiovascular and Respiratory Causes in 12 European Cities'. In: *American Journal of Respiratory and Critical Care Medicine* 179.5, pp. 383–389 (cit. on p. 17).

Mitchell Jr., J. M., B. Dzerdzeevskii, H. Flohn, W. L. Hofmeyr, H. H. Lamp, K. N. Rao and C. C. Wallén (1966). *Climatic Change*. Technical Note 79. World Meteorological Organization, p. 75 (cit. on p. 147).

Moncrieff, J. B., J. M. Massheder, H. de Bruin, J. Elbers, T. Friborg, B. Heusinkveld, P. Kabat, S. Scott, H. Soegaard and A. Verhoef (1997). 'A system to measure surface fluxes of momentum, sensible heat, water vapour and carbon dioxide'. In: *Journal of Hydrology* 188–189, pp. 589–611 (cit. on p. 104).

Monin, A. S. and A. M. Obukhov (1954). 'Basic laws of turbulent mixing in the atmosphere near the ground'. In: *Tr. Akad. Nauk SSSR Geofiz. Inst* 24.151, pp. 163–87 (cit. on p. 49).

Monin, A. S. and A. M. Yaglom (1971). *Statistical Fluid Mechanics. Mechanics of Turbulence*. Ed. by J. L. Lumley. Vol. 1. The MIT Press, p. 782 (cit. on p. 26).

Morris, C. J. G., I. Simmonds and N. Plummer (2001). 'Quantification of the Influences of Wind and Cloud on the Nocturnal Urban Heat Island of a Large City'. In: *Journal of Applied Meteorology* 40.2, pp. 169–182 (cit. on p. 160).

Muthers, S., A. Matzarakis and E. Koch (2010). 'Climate Change and Mortality in Vienna—A Human Biometeorological Analysis Based on Regional Climate Modeling'. In: *International Journal of Environmental Research and Public Health* 7.7, pp. 2965–2977 (cit. on p. 17).

Neunhäuserer, L., B. Fay and M. Raschendorfer (2007). 'Towards urbanisation of the non-hydrostatic numerical weather prediction model Lokalmodell (LM)'. In: *Boundary-Layer Meteorology* 124.1 (1), pp. 81–97 (cit. on p. 23).

Offerle, B., C. S. B. Grimmond and K. Fortuniak (2005). 'Heat storage and anthropogenic heat flux in relation to the energy balance of a central European city centre'. In: *International Journal of Climatology* 25.10, pp. 1405–1419 (cit. on pp. 92, 104).

Offerle, B., C. S. B. Grimmond, K. Fortuniak and W. Pawlak (2006). 'Intraurban Differences of Surface Energy Fluxes in a Central European City'. In: *Journal of Applied Meteorology and Climatology* 45.1, pp. 125–136 (cit. on p. 104).

Offerle, B., C. S. B. Grimmond and T. R. Oke (2003). 'Parameterization of Net All-Wave Radiation for Urban Areas'. In: *Journal of Applied Meteorology* 42.8, pp. 1157–1173 (cit. on p. 19).

OGC (2008). *OpenGIS City Geography Markup Language (CityGML) Encoding Standard*. Ed. by G. Gröger, T. H. Kolbe, A. Czerwinski and C. Nagel. Open Geospatial Consortium Inc., p. 218 (cit. on p. 124).

Oke, T. R. (1981). 'Canyon geometry and the nocturnal urban heat island: Comparison of scale model and field observations'. In: *Journal of Climatology* 1.3, pp. 237–254 (cit. on p. 139).

– (1982). 'The energetic basis of the urban heat island'. In: *Quarterly Journal of the Royal Meteorological Society* 108.455, pp. 1–24 (cit. on p. 108).

– (1987). *Boundary Layer Climates*. 2nd ed. Taylor & Francis, p. 435 (cit. on p. 108).

– (1988). 'The urban energy balance'. In: *Progress in Physical Geography* 12.4, pp. 471–508 (cit. on p. 108).

Oke, T. R. and R. Fuggle (1972). 'Comparison of urban/rural counter and net radiation at night'. In: *Boundary-Layer Meteorology* 2.3 (3), pp. 290–308 (cit. on p. 99).

Oke, T. R. and G. B. Maxwell (1975). 'Urban heat island dynamics in Montreal and Vancouver'. In: *Atmospheric Environment* 9.2, pp. 191–200 (cit. on p. 142).

Oke, T. R., R. A. Spronken-Smith, E. Jáuregui and C. S. B. Grimmond (1999). 'The energy balance of central Mexico City during the dry season'. In: *Atmospheric Environment* 33.24–25, pp. 3919–3930 (cit. on p. 108).

Oleson, K. W., G. B. Bonan and J. Feddema (2010). 'Effects of white roofs on urban temperature in a global climate model'. In: *Geophysical Research Letters* 37.3 (cit. on p. 162).

Oncley, S., T. Foken, R. Vogt, W. Kohsiek, H. DeBruin, C. Bernhofer, A. Christen, E. Gorsel, D. Grantz, C. Feigenwinter, I. Lehner, C. Liebethal, H. Liu, M. Mauder, A. Pitacco, L. Ribeiro and T. Weidinger (2007). 'The Energy Balance Experiment EBEX-2000. Part I: overview and energy balance'. In: *Boundary-Layer Meteorology* 123.1 (1), pp. 1–28 (cit. on p. 104).

Orlanski, I. (1975). 'A Rational Subdivision of Scales for Atmospheric Processes'. In: *Bulletin of the American Meteorological Society* 56.5, pp. 527–530 (cit. on p. 25).

– (1981). 'The Quasi-Hydrostatic Approximation'. In: *Journal of the Atmospheric Sciences* 38.3, pp. 572–582 (cit. on p. 17).

Peterson, T. C. (2003). 'Assessment of Urban Versus Rural In Situ Surface Temperatures in the Contiguous United States: No Difference Found'. In: *Journal of Climate* 16.18, pp. 2941–2959 (cit. on p. 137).

Pielke Sr, R. A. (2002). *Mesoscale Meteorological Modeling*. 2nd ed. International Geophysics Series 78. Academic Press, p. 676 (cit. on p. 45).

Pielke Sr, R. A., G. Marland, R. A. Betts, T. N. Chase, J. L. Eastman, J. O. Niles, D. S. Niyogi and S. W. Running (2002). 'The influence of land-use change and landscape dynamics on the climate system: relevance to climate-change policy beyond the radiative effect of greenhouse gases'. In: *Philosophical Transactions A* 360.1797, p. 1705 (cit. on p. 17).

Press, W. H., S. A. Teukolsky, W. T. Vetterling and B. P. Flannery (1992). *Numerical Recipes in Fortran 77. The Art of Scientific Computing*. 2nd ed. Cambridge University Press, p. 933 (cit. on p. 38).

Raschendorfer, M. (2012). *Surface to atmosphere transfer: by vertical integration of effective gradient flux densities throughout the near surface transfer layer*. URL: `http://www.clm-community.eu/index.php?menuid=171&downloadid=959&reporeid=0` (cit. on p. 32).

Ratti, C., S. Di Sabatino, R. Britter, M. Brown, F. Caton and S. Burian (2002). 'Analysis of 3-D urban databases with respect to pollution dispersion for a number of European and American cities'. In: *Water, Air, & Soil Pollution: Focus* 2.5, pp. 459–469 (cit. on p. 23).

Raupach, M. R. (1992). 'Drag and drag partition on rough surfaces'. In: *Boundary-Layer Meteorology* 60.4, pp. 375–395 (cit. on p. 52).

Raupach, M. R., R. A. Antonia and S. Rajagopalan (1991). 'Rough-wall turbulent boundary layers'. In: *Applied Mechanics Reviews* 44.1, pp. 1–25 (cit. on p. 51).

Raupach, M. R. and R. H. Shaw (1982). 'Averaging procedures for flow within vegetation canopies'. In: *Boundary-Layer Meteorology* 22.1, pp. 79–90 (cit. on pp. 26, 51).

Reynolds, O. (1895). 'On the dynamical theory of incompressible viscous fluids and the determination of the criterion'. In: *Philosophical Transactions of the Royal Society of London. A* 186, pp. 123–164 (cit. on p. 26).

Ritter, B. and J. F. Geleyn (1992). 'A comprehensive radiation scheme for numerical weather prediction models with potential applications in climate simulations'. In: *Monthly Weather Review* 120.2, pp. 303–325 (cit. on p. 29).

Rockel, B., C. L. Castro, R. A. Pielke Sr, H. von Storch and G. Leoncini (2008). 'Dynamical downscaling: Assessment of model system dependent retained and added variability for two different regional climate models'. In: *Journal of Geophysical Research* 113, p. D21107 (cit. on pp. 90, 134).

Rockel, B., A. Will and A. Hense (2008). 'The regional climate model COSMO-CLM (CCLM)'. In: *Meteorologische Zeitschrift* 17.4, pp. 347–348 (cit. on pp. 17, 25).

Roessner, S., K. Segl, M. Bochow, U. Heiden, W. Heldens and H. Kaufmann (2011). 'Potential of hyperspectral remote sensing for analyzing the urban environment'. In: *Urban Remote Sensing. Monitoring, Synthesis and Modeling in the Urban Environment*. Ed. by X. Yang. Wiley-Blackwell (cit. on pp. 134, 158).

Rosenzweig, C., W. D. Solecki, J. Cox, S. Hodges, L. Parshall, B. Lynn, R. Goldberg, S. Gaffin, R. B. Slosberg, P. Savio, M. Watson and F. Dunstan (2009). 'Mitigating New York City's Heat Island: Integrating Stakeholder Perspectives and Scientific Evaluation'. In: *Bulletin of the American Meteorological Society* 90.9, pp. 1297–1312 (cit. on pp. 22, 155).

Rotach, M. W. (1993). 'Turbulence close to a rough urban surface part I: Reynolds stress'. In: *Boundary-Layer Meteorology* 65.1, pp. 1–28 (cit. on p. 50).

– (1999). 'On the influence of the urban roughness sublayer on turbulence and dispersion'. In: *Atmospheric Environment* 33.24-25, pp. 4001–4008 (cit. on p. 87).

– (2002). 'The siting, choice, and operation of surface instrumentation in urban areas'. In: *Surface energy balance in urban areas.* COST 715 Working Group 2 Meeting. (Antwerp, Belgium, 12th Apr. 2000). Ed. by M. Piringer, pp. 5–15 (cit. on p. 87).

Rotach, M. W., E. Batchvarova, R. Berkowicz, J. Brechler, Z. Janour, P. Kastner-Klein, D. Middleton, V. Prior, C. Sacré and C. Soriano (2001). 'Wind input data for urban dispersion modelling'. In: *Preparation of meteorological input data for urban site studies.* COST 715 Workshop. (Prague, Czech Republic, 15th June 2000). Ed. by M. Schatzmann, J. Brechler and B. Fisher, pp. 77–86 (cit. on p. 88).

Rotach, M. W., S. E. Gryning, E. Batchvarova, A. Christen and R. Vogt (2004). 'Pollutant dispersion close to an urban surface–the BUBBLE tracer experiment'. In: *Meteorology and Atmospheric Physics* 87.1, pp. 39–56 (cit. on p. 21).

Rotach, M. W., R. Vogt, C. Bernhofer, E. Batchvarova, A. Christen, A. Clappier, B. Feddersen, S. E. Gryning, G. Martucci, H. Mayer, V. Mitev, T. R. Oke, E. Parlow, H. Richner, M. Roth, Y.-A. Roulet, D. Ruffieux, J. A. Salmond, M. Schatzmann and J. A. Voogt (2005). 'BUBBLE–an urban boundary layer meteorology project'. In: *Theoretical and Applied Climatology* 81.3, pp. 231–261 (cit. on pp. 21, 79, 90, 111).

Roth, M. (2000). 'Review of atmospheric turbulence over cities'. In: *Quarterly Journal of the Royal Meteorological Society* 126.564, pp. 941–990 (cit. on p. 88).

Rummukainen, M. (2010). 'State-of-the-art with regional climate models'. In: *Wiley Interdisciplinary Reviews: Climate Change* 1.1, pp. 82–96 (cit. on p. 17).

Sailor, D. J. (2011). 'A review of methods for estimating anthropogenic heat and moisture emissions in the urban environment'. In: *International Journal of Climatology* 31.2, pp. 189–199 (cit. on p. 157).

Sailor, D. J. and N. Dietsch (2007). 'The urban heat island Mitigation Impact Screening Tool (MIST)'. In: *Environmental Modelling & Software* 22.10, pp. 1529–1541 (cit. on p. 22).

Salamanca, F., A. Krpo, A. Martilli and A. Clappier (2010). 'A new building energy model coupled with an urban canopy parameterization for urban climate simulations—part I. formulation, verification, and sensitivity analysis of the model'. In: *Theoretical and Applied Climatology* 99 (3), pp. 331–344 (cit. on pp. 21, 73, 157).

Salamanca, F. and A. Martilli (2010). 'A new Building Energy Model coupled with an Urban Canopy Parameterization for urban climate simulations—part II. Validation with one dimension off-line simulations'. In: *Theoretical and Applied Climatology* 99 (3), pp. 345–356 (cit. on pp. 21, 73).

Salamanca, F., A. Martilli and C. Yagüe (2011). 'A numerical study of the Urban Heat Island over Madrid during the DESIREX (2008) campaign with WRF and an evaluation of simple mitigation strategies'. In: *International Journal of Climatology* (cit. on pp. 22, 23, 158).

Schmid, H. P. and T. R. Oke (1990). 'A model to estimate the source area contributing to turbulent exchange in the surface layer over patchy terrain'. In: *Quarterly Journal of the Royal Meteorological Society* 116.494, pp. 965–988 (cit. on p. 104).

Schubert, S. and S. Grossman-Clarke (2013a). 'The Influence of Green Areas and Roof Albedos on Air Temperatures during Extreme Heat Events in Berlin, Germany'. In: *Meteorologische Zeitschrift* 22.2, pp. 131–143 (cit. on pp. 123, 208).

– (2013b). 'Evaluation of the coupled COSMO-CLM/DCEP model with observations from BUBBLE'. Submitted (cit. on p. 208).

Schubert, S., S. Grossman-Clarke and A. Martilli (2010). *Implementation and Testing of the Building Energy Parameterization Model (BEP) in the Climate Local Model (CLM)*. Presented at the Ninth Symposium on the Urban Environment, Keystone, CO, USA (cit. on p. 23).

– (2012). 'A Double-Canyon Radiation Scheme for Multi-Layer Urban Canopy Models'. In: *Boundary-Layer Meteorology* 145.3, pp. 439–468 (cit. on pp. 36, 45, 208).

Skamarock, W. C., J. B. Klemp, J. Dudhia, D. O. Gill, D. M. Barker, M. G. Duda, X.-Y. Huang, W. Wang and J. G. Powers (2008). *A Description of the Advanced Research WRF Version 3*. Technical Note. National Center for Atmospheric Research (cit. on p. 25).

Smiatek, G., B. Rockel and U. Schättler (2008). 'Time invariant data preprocessor for the climate version of the COSMO model (COSMO-CLM)'. In: *Meteorologische Zeitschrift* 17.4, pp. 395–405 (cit. on pp. 68, 91, 134).

Sparrow, E. M. and R. D. Cess (1978). *Radiation heat transfer*. Augmented Edition. Hemisphere Publishing Corporation, p. 366 (cit. on pp. 169–171).

Spronken-Smith, R. A. (2002). 'Comparison of summer- and winter-time suburban energy fluxes in Christchurch, New Zealand'. In: *International Journal of Climatology* 22.8, pp. 979–992 (cit. on p. 108).

Steppeler, J., G. Doms, U. Schättler, H. W. Bitzer, A. Gassmann, U. Damrath and G. Gregoric (2003). 'Meso-gamma scale forecasts using the nonhydrostatic model LM'. In: *Meteorology and Atmospheric Physics* 82.1, pp. 75–96 (cit. on p. 25).

Stull, R. B. (1988). *An Introduction to Boundary Layer Meteorology*. Atmospheric Sciences Library. Kluwer Academic Publishers, p. 684 (cit. on pp. 30, 31).

Suckling, P. (1981). 'Nocturnal observations of incoming longwave radiation and the urban heat island for a small prairie city'. In: *Meteorology and Atmospheric Physics* 29 (1), pp. 23–27 (cit. on p. 99).

Taha, H. (1997). 'Urban climates and heat islands: albedo, evapotranspiration, and anthropogenic heat'. In: *Energy and Buildings* 25.2, pp. 99–103 (cit. on p. 157).

– (1999). 'Modifying a Mesoscale Meteorological Model to Better Incorporate Urban Heat Storage: A Bulk-Parameterization Approach'. In: *Journal of Applied Meteorology* 38.4, pp. 466–473 (cit. on p. 19).

– (2008). 'Meso-urban meteorological and photochemical modeling of heat island mitigation'. In: *Atmospheric Environment* 42.38, pp. 8795–8809 (cit. on pp. 22, 155).

Unger, J., Z. Sümeghy and J. Zoboki (2001). 'Temperature cross-section features in an urban area'. In: *Atmospheric Research* 58.2, pp. 117–127 (cit. on p. 160).

United Nations: Population Division of the Department of Economic and Social Affairs (2011). *World Population Prospects: The 2010 Revision and World Urbanization Prospects: The 2011 Revision*. Research rep. (cit. on p. 17).

Unwin, D. J. (1980). 'The Synoptic Climatology of Birmingham's Urban Heat Island, 1965–74'. In: *Weather* 35.2, pp. 43–50 (cit. on p. 142).

Wieringa, J. (1993). 'Representative roughness parameters for homogeneous terrain'. In: *Boundary-Layer Meteorology* 63.4 (4), pp. 323–363 (cit. on p. 106).

Willmott, C. J. (1981). 'On the validation of models'. In: *Physical Geography* 2.2, pp. 184–194 (cit. on p. 93).

Wilson, K., A. Goldstein, E. Falge, M. Aubinet, D. Baldocchi, P. Berbigier, C. Bernhofer, R. Ceulemans, H. Dolman, C. Field, A. Grelle, A. Ibrom, B. E. Law, A. Kowalski, T. Meyers, J. Moncrieff, R. Monson, W. Oechel, J. Tenhunen, R. Valentini and S. Verma (2002). 'Energy balance closure at FLUXNET sites'. In: *Agricultural and Forest Meteorology* 113.1–4, pp. 223–243 (cit. on p. 104).

Wong, G. S. K. and T. F. W. Embleton (1984). 'Variation of specific heats and of specific heat ratio in air with humidity'. In: *The Journal of the Acoustical Society of America* 76.2, pp. 555–559 (cit. on p. 28).

Wright, A. J., A. N. Young and S. Natarajan (2005). 'Dwelling temperatures and comfort during the August 2003 heat wave'. In: *Building Services Engineering Research and Technology* 26.4, pp. 285–300 (cit. on p. 53).

Yi, C., K. J. Davis, P. S. Bakwin, B. W. Berger and L. C. Marr (2000). 'Influence of advection on measurements of the net ecosystem-atmosphere exchange of CO_2 from a very tall tower'. In: *Journal of Geophysical Research* 105.D8, pp. 9991–9999 (cit. on p. 30).

Zhang, C. L., F. Chen, S. G. Miao, Q. C. Li, X. A. Xia and C. Y. Xuan (2009). 'Impacts of urban expansion and future green planting on summer precipitation in the Beijing metropolitan area'. In: *Journal of Geophysical Research* 114.D2, p. D02116 (cit. on p. 17).

Zhang, H., N. Sato, T. Izumi, K. Hanaki and T. Aramaki (2008). 'Modified RAMS-Urban Canopy Model for Heat Island Simulation in Chongqing, China'. In: *Journal of Applied Meteorology and Climatology* 47.2, pp. 509–524 (cit. on pp. 23, 158).

Secondary sources and software

Bringhurst, R. (2005). *The Elements of Typographic Style*. 3.1. Hartley & Marks, p. 382 (cit. on p. 207).

Eaton, J. W., D. Bateman and S. Hauberg (2008). *GNU Octave Manual Version 3*. Network Theory Limited, p. 568 (cit. on pp. 64, 207).

Harrower, M. and C. A. Brewer (2003). 'Colorbrewer.org: An Online Tool for Selecting Colour Schemes for Maps'. In: *The Cartographic Journal* 40.1, pp. 27–37 (cit. on p. 207).

Hornby, A. S. (2010). *Oxford Advanced Learner's Dictionary of Current English*. Ed. by J. Turnbull. 8th ed. Oxford University Press (cit. on p. 207).

International Bureau of Weights and Measures (2006). *The International System of Units (SI)*. 8th ed., p. 180 (cit. on p. 207).

Neteler, M. and H. Mitasova (2008). *Open Source GIS: A GRASS GIS Approach*. 3rd ed. The International Series in Engineering and Computer Science 773. Springer, p. 406 (cit. on p. 207).

Quantum GIS Development Team (2009). *Quantum GIS Geographic Information System*. Open Source Geospatial Foundation (cit. on p. 207).

R Core Team (2012). *R: A Language and Environment for Statistical Computing*. R Foundation for Statistical Computing. Vienna, Austria (cit. on p. 207).

Thompson, A. and B. N. Taylor (2008). *Guide for the Use of the International System of Units (SI)*. National Institute of Standards and Technology, p. 75 (cit. on p. 207).

Acknowledgements

First of all, I would like to thank Friedrich-Wilhelm Gerstengarbe for the opportunity of writing my PhD thesis at the Potsdam Institute for Climate Impact Research and for the constant support to work freely on such an interesting topic. I am also very grateful to Uwe Ulbrich for the regular meetings and fruitful discussions as well as the possibility to do a doctorate under his supervision. I am highly indebted to Susanne Grossman-Clarke for her continuous support on a daily basis, her ideas and comments, her hospitality during my stay at the Arizona State University as well as for an introduction into the urban climate community. I am also very grateful to Matthias Lüdeke for his support and patience during the last phase of this work.

I want to thank the International Max Planck Research School on Earth System Modelling for their financial support as well as for the scientific and generic courses. In particular, I am grateful to Antje Weitz and Cornelia Kampmann for their constant guidance and commitment to organization.

Furthermore, I would like to thank Alberto Martilli, Oliver Fuhrer, Kristina Trusilova, Mathias Bochow, Uwe Böhm, Barbara Früh, Andreas Will, Thomas Loridan and Fred Meier as well as all anonymous reviewers for suggestions, discussions and comments. Many thanks also to Andreas Christen, Roland Vogt and James Voogt for the supply and description of the BUBBLE data. The BUBBLE campaign was made possible by a large number of grants and resources from many institutions and individuals. The core project was financed by the Swiss Federal Office for Education and Science (Grant C00.0068). Furthermore, the University of Basel, the Swiss Federal Institute of Technology (ETH) Zurich, the Technical University of Dresden, and the Bulgarian National Institute of Meteorology and Hydrology contributed to the data set.

Moreover, I would like to thank the city of Berlin for making available the 3-D building data as well as the European Union for supporting the creation of this data through the European Regional Development Fund. Furthermore, the map of the impervious surface coverage of Berlin is based on data from the Urban and Environmental Information System of the Senate Department for Urban Development of Berlin. In this context I am very grateful to Martin Wodinski and Ylva Hauf for the creation of gridded maps as well as their help with GIS software, and to Claus Nagel for his introduction to the technicalities of CityGML.

Representative of the whole working group, I would also like to acknowledge the people in my room, Jan Volkholz, Matthias Büchner and Julia Lutz, for the help with smaller and larger daily problems. Moreover, I am very grateful to Susanne Grossman-Clarke, Ruth Herrberg-Schubert, Jan Volkholz and Thomas Clarke for proofreading

and helping with matters of the English language. Many thanks also to Jean Böhme for the pictures of the weather station at the airport Berlin-Tegel.

Last but not least, I wish to thank my family and friends for their moral support, not only during the work on this study but also throughout my entire life.

Vielen Dank!

be Berlin
Berlin Business Location Center

Selbständigkeitserklärung

Hiermit erkläre ich, die vorliegende Arbeit selbständig und nur mit der angegebenen Hilfe verfasst zu haben. Die verwendete Literatur ist im Literaturverzeichnis und die technischen Hilfsmittel unten angegeben. Weiterhin sind die (veröffentlichten und geplanten) Publikationen, auf deren Grundlage diese Arbeit erstellt wurde, im Folgenden aufgeführt.

Sebastian Schubert

Technische Hilfsmittel:

- Intel Fortran Compiler zur Übersetzung von cosmo-clm und dcep
- Oracle Java-Compiler zur Übersetzung des CityGML Analyseprogramms
- gnu Octave (Eaton u. a. 2008) und R (R Core Team 2012) für die Analyse der Simulationsergebnisse und weitergehende Berechnungen
- grass gis (Neteler und Mitasova 2008) and Quantum gis (Quantum gis Development Team 2009) für die Visualiserung und Aufbereitung der Geodaten von Berlin und Basel
- diverse Linux-Systeme als grundlegende Arbeitsumgebung mit typischen Hilfsmitteln wie Bash, Eclipse, gnu Emacs, git and LaTeX 2_ε

Sprach- und Stilleitfäden:

- einsprachiges Englisch-Wörterbuch (Hornby 2010)
- allgemeine Typographierichtlinien (Bringhurst 2005)
- Farbschemata für Karten (Harrower und Brewer 2003)
- Verwendung von si-Einheiten (bipm 2006; Thompson und Taylor 2008)

Veröffentlichungen:

- Teile von Kapitel 3 wurden in Schubert u. a. (2012)* veröffentlicht.
- Der Inhalt von Kapitel 5 wurde in Schubert und Grossman-Clarke (2013a)† veröffentlicht.
- Eine Veröffentlichung des Kapitels 4 befindet sich im Review-Prozess (Schubert und Grossman-Clarke 2013b)‡.

---

[*] S. Schubert, S. Grossman-Clarke und A. Martilli (2012). ‘A Double-Canyon Radiation Scheme for Multi-Layer Urban Canopy Models’. In: *Boundary-Layer Meteorology* 145.3, S. 439–468. DOI: `10.1007/s10546-012-9728-3`.

[†] S. Schubert und S. Grossman-Clarke (2013a). ‘The Influence of Green Areas and Roof Albedos on Air Temperatures during Extreme Heat Events in Berlin, Germany’. In: *Meteorologische Zeitschrift* 22.2, S. 131–143. DOI: `10.1127/0941-2948/2013/0393`.

[‡] S. Schubert und S. Grossman-Clarke (2013b). ‘Evaluation of the coupled COSMO-CLM/DCEP model with observations from BUBBLE’. Eingereicht.